Hadron Production and Freeze-Out Dynamics at $\sqrt{s_{NN}} = 3.0$ GeV Au+Al and $\sqrt{s_{NN}} = 19.6$ GeV Au+Au Collisions as Measured at STAR

By

SAMANTHA GAIL BROVKO
B.S. (University of California, Davis) 2008
M.S. (University of California, Davis) 2010

DISSERTATION

Submitted in partial satisfaction of the requirements for the degree of

DOCTOR OF PHILOSOPHY

in

Physics

in the

OFFICE OF GRADUATE STUDIES

of the

UNIVERSITY OF CALIFORNIA

DAVIS

Approved:

Professor Daniel A. Cebra, Chair

Professor Manuel Calderón De La Barca Sánchez

Professor Ramona Vogt

Committee in Charge

2014

Samantha Gail Brovko
May 2014
Physics

Hadron Production and Freeze-Out Dynamics at $\sqrt{s_{NN}} = 3.0$ GeV Au+Al and $\sqrt{s_{NN}} = 19.6$ GeV Au+Au Collisions as Measured at STAR

Abstract

The Beam Energy Scan program at RHIC was commissioned to search for the critical point and the turn-off of QGP signatures. The program has completed collisions of Au+Au at energies from 7.7 to 62.4 GeV per nucleon pair in 2010 and 2011. The addition of a full-coverage Time-of-Flight detector at STAR had extended momentum range for clean particle identification. Mid-rapidity ($|y| < 0.5$) hadron spectra will be used to determine the freeze-out dynamics of the system. Particle spectra for π, K, p and $\bar{p}$ as a function of $m_T - m_0$ will be presented and these will be used to discuss in particular the source's Coulombic effect on soft pions, as well as three of the four signs of the onset of deconfinement: the "Kink," the "Horn," and the "Step." Comparisons will be made to $\sqrt{s_{NN}}$ = 7.7 GeV, 11.5 GeV, 19.6 GeV (from 2001), 27 GeV, 39 GeV $Au + Au$ data from STAR, and $\sqrt{s_{NN}} = 17.3$ GeV $Pb + Pb$ data from the SPS heavy ion program. Collisions between gold ions in the RHIC beam with aluminum nuclei in the beam pipe allow us to analyze fixed target interactions with the STAR detector at RHIC. These lower energy fixed target collisions may allow us to extend the low energy reach of the RHIC beam energy scan and possibly improve the chance of finding the critical point of the hadronic to quark matter phase boundary. In this thesis, we will present preliminary results of spectra analysis for a fixed target collision system at $\sqrt{s_{NN}}$ = 3.0 GeV. Also, the viability of doing fixed target experiments with a collider detector will be discussed. Comparisons to simulation, using UrQMD, will also be made. The analysis provides a good reference to study excitation functions of strangeness production, net baryon, and collective flow inside heavy ion collisions.

Dedication

This document is dedicated to my father.

Dad, you have always believed in me; look where I am now.

Acknowledgments

Nam dui ligula, fringilla a, euismod sodales, sollicitudin vel, wisi. Morbi auctor lorem non justo. Nam lacus libero, pretium at, lobortis vitae, ultricies et, tellus. Donec aliquet, tortor sed accumsan bibendum, erat ligula aliquet magna, vitae ornare odio metus a mi. Morbi ac orci et nisl hendrerit mollis. Suspendisse ut massa. Cras nec ante. Pellentesque a nulla. Cum sociis natoque penatibus et magnis dis parturient montes, nascetur ridiculus mus. Aliquam tincidunt urna. Nulla ullamcorper vestibulum turpis. Pellentesque cursus luctus mauris.

Contents

Abstract ii

Acknowledgments iv

List of Figures viii

List of Tables xv

1 Introduction 1

1.1 Overview . . . 1

1.2 The States of Nuclear Matter . . . 2

1.3 The Beam Energy Scan Program . . . 4

1.4 Fixed Target Collisions Measured with the STAR Experiment . . . 7

2 Ultra-Relativistic Heavy Ion Physics 9

2.1 Introduction . . . 9

2.2 Signatures of the Quark-Gluon Plasma . . . 13

2.2.1 Strangeness Enhancement . . . 14

2.2.2 J/ψ Suppression . . . 15

2.2.3 Direct Photons and Dileptons . . . 17

2.2.4 Azimuthal Anisotropy or Flow . . . 21

2.2.5 Jets, High p_T Probes . . . 26

2.3 Particle Spectra . . . 28

2.3.1 Blastwave Model . . . 30

2.4 Particle Ratios and the Coulomb Source . . . 32
2.4.1 The Coulomb Source Effect . . . 38

3 The STAR Experiment **41**
3.1 Introduction to the STAR Experiment . . . 41
3.2 The Time Projection Chamber . . . 41
3.2.1 Event Reconstruction . . . 46
3.2.2 Particle Identification (PID) of the TPC via dE/dx . . . 48
3.3 The Time Of Flight Detector . . . 50
3.3.1 Particle Identification (PID) of the TOF via $1/\beta$ . . . 54
3.4 The Trigger Detectors . . . 55
3.4.1 Beam–Beam Counters . . . 55
3.4.2 Zero Degree Calorimeter . . . 56
3.5 Software and Detector Acceptance and Efficiency . . . 58
3.5.1 TPC Tracking Efficiency . . . 58
3.5.2 TOF Matching Efficiency . . . 59

4 Analysis Methods **61**
4.1 Introduction . . . 61
4.2 Modifications to the STAR Vertexing Algorithm . . . 61
4.3 Fixed Target Interactions . . . 67
4.3.1 A Fixed Target Geometry . . . 67
4.3.2 Understanding Centrality and Event Selection . . . 70
4.3.3 Fitting Methods . . . 78
4.3.4 Corrections, Systematics and Errors . . . 83
4.4 Beam–Beam Collisions . . . 86
4.4.1 Trigger Requirements . . . 86
4.4.2 Event and Track Selection . . . 87

4.4.3 Fitting Methods . . . 90
4.4.4 Corrections, Systematics and Errors . . . 93

5 Results and Discussion **99**
5.1 Fixed Target Interactions . . . 99
5.2 Beam–Beam Collisions . . . 105

6 Conclusion **114**

Appendices **117**

A $\sqrt{s_{\rm NN}} = 19.6$ GeV $Au + Au$ Gaussian Fits **117**
A.1 The 70%-80% Centrality Class . . . 117
A.2 The 60%-70% Centrality Class . . . 124
A.3 The 50%-60% Centrality Class . . . 131
A.4 The 40%-50% Centrality Class . . . 138
A.5 The 30%-40% Centrality Class . . . 145
A.6 The 20%-30% Centrality Class . . . 152
A.7 The 10%-20% Centrality Class . . . 159
A.8 The 5%-10% Centrality Class . . . 166
A.9 The 0%-5% Centrality Class . . . 173

B Global Properties of Nucleus-Nucleus Collisions **180**
B.1 The Glauber Model . . . 180

Curriculum Vitæ **185**

Publications **188**

References **196**

List of Figures

1.1 A sketch of the Nuclear Matter Phase Diagram with anticipated Beam Energy Scan data points . . . 3

1.2 A reconstructed fixed-target interaction as measured at STAR . . . 7

2.1 Heavy quark potential versus temperature . . . 17

2.2 Nuclear Modification Factor at RHIC and SPS . . . 18

2.3 Schematic of expected sources of photons . . . 19

2.4 Schematic of expected sources of dileptons, invariant mass spectrum . . . 20

2.5 Cartoon of the Overlap Region in A+A collisions . . . 22

2.6 Particle identified elliptic flow . . . 24

2.7 Constituent-quark scaling of particle-identified elliptic flow . . . 25

2.8 Suppression of the away-side jet peak . . . 27

2.9 The Kink . . . 35

2.10 The Horn . . . 36

2.11 The Step . . . 36

2.12 The Dale . . . 37

3.1 A 3D Picture of STAR . . . 42

3.2 A schematic picture of the TPC . . . 43

3.3 The TPC MWPC of an outer sector. . . . 44

3.4 Schematic of a full sector (inner and outer) of the TPC . . . 45

3.5 TPC Event Reconstruction . . . 46

3.6 Ionization energy loss as a function of momentum . . . 49

3.7 A cut-out of the STAR detector identifying the position of the pVPD 50
3.8 pVPD module construction schematic 51
3.9 Full assembly of the pVPD detectors of the TOF 51
3.10 Detailed cut-out of the TOFr trays 53
3.11 A sample of particle identification using the TOF 55
3.12 The BBC scintillator array 56
3.13 ZDC module construction 57
3.14 TOFr tray pick-up pad layout 60

4.1 A cartoon of three types of pile-up vertices at STAR 62
4.2 Reconstructed Vertex Locations for (R, Z, N) = (6, 6, 2) 64
4.3 A reconstructed shadow vertex 65
4.4 An example of a fixed target vertex in the STAR detector 68
4.5 The STAR fixed target geometry 69
4.6 Particle acceptances for the STAR fixed target geometry 70
4.7 Cartoon of Au and Al nuclei to emphasize scale 71
4.8 Woods-Saxon populated nuclei for Au and Al 72
4.9 Total Multiplicity Correlation with Impact Parameter 73
4.10 Pion Multiplicity and TPC Multiplicity Correlation with Impact Parameter . 74
4.11 Pion and Proton Multiplicity Correlation with Impact Parameter 74
4.12 Pion Multiplicity fit with a Glauber Monte Carlo 75
4.13 Vertex position distributions before analysis cuts for $Au + Al$ $\sqrt{s_{NN}} = 3.0$ GeV 77
4.14 Vertex position distributions after analysis cuts for $Au + Al$ $\sqrt{s_{NN}} = 3.0$ GeV 78
4.15 Energy Loss versus Momentum for $Au + Al$ $\sqrt{s_{NN}} = 3.0$ GeV 80
4.16 Positive pion fits for $Au + Al\sqrt{s_{NN}} = 3.0$ GeV 81
4.17 Positive pion fits for $Au + Al\sqrt{s_{NN}} = 3.0$ GeV 82
4.18 Negative pion fits for $Au + Al\sqrt{s_{NN}} = 3.0$ GeV 83
4.19 Negative pion fits for $Au + Al\sqrt{s_{NN}} = 3.0$ GeV 84

4.20 Simulated event processed with STARSim for $Au + Al\sqrt{s_{NN}} = 3.0$ GeV . . . 85
4.21 Vertex position distributions for $Au + Au$ $\sqrt{s_{NN}} = 19.6$ GeV 88
4.22 Event Quality: V_Z Distribution and Reference Multiplicity 89
4.23 Energy Loss versus Rigidity and $1/\beta$ versus Rigidity for Au+Au $\sqrt{s_{NN}} = 19.6$ GeV 91
4.24 Efficiency for $\pi^{\pm}$ in Au+Au $\sqrt{s_{NN}} = 19.6$ GeV 94
4.25 Efficiency for $K^{\pm}$ in Au+Au $\sqrt{s_{NN}} = 19.6$ GeV 94
4.26 Efficiency for p and $\bar{p}$ in Au+Au $\sqrt{s_{NN}} = 19.6$ GeV 95
4.27 Energy loss correction for $Au + Au$ $\sqrt{s_{NN}} = 19.6$ GeV 96
4.28 TOF Efficiency for $Au + Au$ $\sqrt{s_{NN}} = 19.6$ GeV 97

5.1 Pion Spectra for $Au + Al$ $\sqrt{s_{NN}} = 3.0$ GeV 100
5.2 Proton Spectra for $Au + Al$ $\sqrt{s_{NN}} = 3.0$ GeV 101
5.3 Pion Ratio and Coulomb Fit for $Au + Al$ $\sqrt{s_{NN}} = 3.0$ GeV 102
5.4 Coulomb Potential and (anti)Proton Yield for $Au + Al$ $\sqrt{s_{NN}} = 3.0$ GeV . . 103
5.5 Mid-rapidity ($|y - y_{CM}| < 0.1$) dN/dy yields for $Au + Al$ $\sqrt{s_{NN}} = 3.0$ GeV . 104
5.6 Identified Particle Spectra for $Au + Au$ $\sqrt{s_{NN}} = 19.6$ GeV 105
5.7 Proton dN/dy versus Center-of-Mass Energy for $Au + Au$ $\sqrt{s_{NN}} = 19.6$ GeV 107
5.8 Proton dN/dy and Coulomb Potential versus Center-of-Mass Energy for Au+ Au $\sqrt{s_{NN}} = 19.6$ GeV 108
5.9 Pion dN/dy versus Center-of-Mass Energy for $Au + Au$ $\sqrt{s_{NN}} = 19.6$ GeV . 109
5.10 Pion dN/dy versus Center of Mass Energy, the Kink, for Au+Au $\sqrt{s_{NN}} = 19.6$ GeV 111
5.11 Kaon dN/dy versus Center of Mass Energy, the Horn, for $Au + Au$ $\sqrt{s_{NN}} =$ 19.6 GeV 112
5.12 Positively Charged Kaon Temperature versus Center of Mass Energy, the Step, for $Au + Au$ $\sqrt{s_{NN}} = 19.6$ GeV 113

A.1 Positive pion TPC fits for 70%-80% central events $Au + Au\sqrt{s_{NN}} = 19.6$ GeV 117
A.2 Positive pion TOF fits for 70%-80% central events $Au + Au\sqrt{s_{NN}} = 19.6$ GeV 118
A.3 Negative pion TPC fits for 70%-80% central events $Au + Au\sqrt{s_{NN}} = 19.6$ GeV 118
A.4 Negative pion TOF fits for 70%-80% central events $Au + Au\sqrt{s_{NN}} = 19.6$ GeV 119
A.5 Positive kaon TPC fits for 70%-80% central events $Au + Au\sqrt{s_{NN}} = 19.6$ GeV 119
A.6 Positive kaon TOF fits for 70%-80% central events $Au + Au\sqrt{s_{NN}} = 19.6$ GeV 120
A.7 Negative kaon TPC fits for 70%-80% central events $Au + Au\sqrt{s_{NN}} = 19.6$ GeV 120
A.8 Negative kaon TOF fits for 70%-80% central events $Au + Au\sqrt{s_{NN}} = 19.6$ GeV 121
A.9 Positive proton TPC fits for 70%-80% central events $Au + Au\sqrt{s_{NN}} = 19.6$ GeV 121
A.10 Positive proton TOF fits for 70%-80% central events $Au + Au\sqrt{s_{NN}} = 19.6$ GeV 122
A.11 Negative proton TPC fits for 70%-80% central events $Au + Au\sqrt{s_{NN}} = 19.6$ GeV 122
A.12 Negative proton TOF fits for 70%-80% central events $Au + Au\sqrt{s_{NN}} = 19.6$ GeV 123
A.13 Positive pion TPC fits for 60%-70% central events $Au + Au\sqrt{s_{NN}} = 19.6$ GeV 124
A.14 Positive pion TOF fits for 60%-70% central events $Au + Au\sqrt{s_{NN}} = 19.6$ GeV 125
A.15 Negative pi1n TPC fits for 60%-70% central events $Au + Au\sqrt{s_{NN}} = 19.6$ GeV 125
A.16 Negative pion TOF fits for 60%-70% central events $Au + Au\sqrt{s_{NN}} = 19.6$ GeV 126
A.17 Positive kaon TPC fits for 60%-70% central events $Au + Au\sqrt{s_{NN}} = 19.6$ GeV 126
A.18 Positive kaon TOF fits for 60%-70% central events $Au + Au\sqrt{s_{NN}} = 19.6$ GeV 127
A.19 Negative kaon TPC fits for 60%-70% central events $Au + Au\sqrt{s_{NN}} = 19.6$ GeV 127
A.20 Negative kaon TOF fits for 60%-70% central events $Au + Au\sqrt{s_{NN}} = 19.6$ GeV 128
A.21 Positive proton TPC fits for 60%-70% central events $Au + Au\sqrt{s_{NN}} = 19.6$ GeV 128

A.22 Positive proton TOF fits for 60%-70% central events $Au + Au\sqrt{s_{NN}} = 19.6$ GeV . . . 129
A.23 Negative proton TPC fits for 60%-70% central events $Au + Au\sqrt{s_{NN}} = 19.6$ GeV . . . 129
A.24 Negative proton TOF fits for 60%-70% central events $Au + Au\sqrt{s_{NN}} = 19.6$ GeV . . . 130
A.25 Positive pion TPC fits for 50%-60% central events $Au + Au\sqrt{s_{NN}} = 19.6$ GeV 131
A.26 Positive pion TOF fits for 50%-60% central events $Au + Au\sqrt{s_{NN}} = 19.6$ GeV 132
A.27 Negative pion TPC fits for 50%-60% central events $Au + Au\sqrt{s_{NN}} = 19.6$ GeV 132
A.28 Negative pion TOF fits for 50%-60% central events $Au + Au\sqrt{s_{NN}} = 19.6$ GeV 133
A.29 Positive kaon TPC fits for 50%-60% central events $Au + Au\sqrt{s_{NN}} = 19.6$ GeV 133
A.30 Positive kaon TOF fits for 50%-60% central events $Au + Au\sqrt{s_{NN}} = 19.6$ GeV 134
A.31 Negative kaon TPC fits for 50%-60% central events $Au + Au\sqrt{s_{NN}} = 19.6$ GeV 134
A.32 Negative kaon TOF fits for 50%-60% central events $Au + Au\sqrt{s_{NN}} = 19.6$ GeV 135
A.33 Positive proton TPC fits for 50%-60% central events $Au + Au\sqrt{s_{NN}} = 19.6$ GeV . . . 135
A.34 Positive proton TOF fits for 50%-60% central events $Au + Au\sqrt{s_{NN}} = 19.6$ GeV . . . 136
A.35 Negative proton TPC fits for 50%-60% central events $Au + Au\sqrt{s_{NN}} = 19.6$ GeV . . . 136
A.36 Negative proton TOF fits for 50%-60% central events $Au + Au\sqrt{s_{NN}} = 19.6$ GeV . . . 137
A.37 Positive pion TPC fits for 40%-50% central events $Au + Au\sqrt{s_{NN}} = 19.6$ GeV 138
A.38 Positive pion TOF fits for 40%-50% central events $Au + Au\sqrt{s_{NN}} = 19.6$ GeV 139
A.39 Negative pi1n TPC fits for 40%-50% central events $Au + Au\sqrt{s_{NN}} = 19.6$ GeV 139
A.40 Negative pion TOF fits for 40%-50% central events $Au + Au\sqrt{s_{NN}} = 19.6$ GeV 140
A.41 Positive kaon TPC fits for 40%-50% central events $Au + Au\sqrt{s_{NN}} = 19.6$ GeV 140

A.42 Positive kaon TOF fits for 40%-50% central events $Au + Au\sqrt{s_{NN}} = 19.6$ GeV 141
A.43 Negative kaon TPC fits for 40%-50% central events $Au + Au\sqrt{s_{NN}} = 19.6$ GeV 141
A.44 Negative kaon TOF fits for 40%-50% central events $Au + Au\sqrt{s_{NN}} = 19.6$ GeV 142
A.45 Positive proton TPC fits for 40%-50% central events $Au + Au\sqrt{s_{NN}} = 19.6$ GeV . . . 142
A.46 Positive proton TOF fits for 40%-50% central events $Au + Au\sqrt{s_{NN}} = 19.6$ GeV . . . 143
A.47 Negative proton TPC fits for 40%-50% central events $Au + Au\sqrt{s_{NN}} = 19.6$ GeV . . . 143
A.48 Negative proton TOF fits for 40%-50% central events $Au + Au\sqrt{s_{NN}} = 19.6$ GeV . . . 144
A.49 Positive pion TPC fits for 30%-40% central events $Au + Au\sqrt{s_{NN}} = 19.6$ GeV 145
A.50 Positive pion TOF fits for 30%-40% central events $Au + Au\sqrt{s_{NN}} = 19.6$ GeV 146
A.51 Negative pi1n TPC fits for 30%-40% central events $Au + Au\sqrt{s_{NN}} = 19.6$ GeV 146
A.52 Negative pion TOF fits for 30%-40% central events $Au + Au\sqrt{s_{NN}} = 19.6$ GeV 147
A.53 Positive kaon TPC fits for 30%-40% central events $Au + Au\sqrt{s_{NN}} = 19.6$ GeV 147
A.54 Positive kaon TOF fits for 30%-40% central events $Au + Au\sqrt{s_{NN}} = 19.6$ GeV 148
A.55 Negative kaon TPC fits for 30%-40% central events $Au + Au\sqrt{s_{NN}} = 19.6$ GeV 148
A.56 Negative kaon TOF fits for 30%-40% central events $Au + Au\sqrt{s_{NN}} = 19.6$ GeV 149
A.57 Positive proton TPC fits for 30%-40% central events $Au + Au\sqrt{s_{NN}} = 19.6$ GeV . . . 149
A.58 Positive proton TOF fits for 30%-40% central events $Au + Au\sqrt{s_{NN}} = 19.6$ GeV . . . 150
A.59 Negative proton TPC fits for 30%-40% central events $Au + Au\sqrt{s_{NN}} = 19.6$ GeV . . . 150
A.60 Negative proton TOF fits for 30%-40% central events $Au + Au\sqrt{s_{NN}} = 19.6$ GeV . . . 151

A.61 Positive pion TPC fits for 20%-30% central events $Au + Au\sqrt{s_{NN}} = 19.6$ GeV 152
A.62 Positive pion TOF fits for 20%-30% central events $Au + Au\sqrt{s_{NN}} = 19.6$ GeV 153
A.63 Negative pi1n TPC fits for 20%-30% central events $Au + Au\sqrt{s_{NN}} = 19.6$ GeV 153
A.64 Negative pion TOF fits for 20%-30% central events $Au + Au\sqrt{s_{NN}} = 19.6$ GeV 154
A.65 Positive kaon TPC fits for 20%-30% central events $Au + Au\sqrt{s_{NN}} = 19.6$ GeV 154
A.66 Positive kaon TOF fits for 20%-30% central events $Au + Au\sqrt{s_{NN}} = 19.6$ GeV 155
A.67 Negative kaon TPC fits for 20%-30% central events $Au + Au\sqrt{s_{NN}} = 19.6$ GeV 155
A.68 Negative kaon TOF fits for 20%-30% central events $Au + Au\sqrt{s_{NN}} = 19.6$ GeV 156
A.69 Positive proton TPC fits for 20%-30% central events $Au + Au\sqrt{s_{NN}} = 19.6$ GeV 156
A.70 Positive proton TOF fits for 20%-30% central events $Au + Au\sqrt{s_{NN}} = 19.6$ GeV 157
A.71 Negative proton TPC fits for 20%-30% central events $Au + Au\sqrt{s_{NN}} = 19.6$ GeV 157
A.72 Negative proton TOF fits for 20%-30% central events $Au + Au\sqrt{s_{NN}} = 19.6$ GeV 158
A.73 Positive pion TPC fits for 10%-20% central events $Au + Au\sqrt{s_{NN}} = 19.6$ GeV 159
A.74 Positive pion TOF fits for 10%-20% central events $Au + Au\sqrt{s_{NN}} = 19.6$ GeV 160
A.75 Negative pion TPC fits for 10%-20% central events $Au + Au\sqrt{s_{NN}} = 19.6$ GeV 160
A.76 Negative pion TOF fits for 10%-20% central events $Au + Au\sqrt{s_{NN}} = 19.6$ GeV 161
A.77 Positive kaon TPC fits for 10%-20% central events $Au + Au\sqrt{s_{NN}} = 19.6$ GeV 161
A.78 Positive kaon TOF fits for 10%-20% central events $Au + Au\sqrt{s_{NN}} = 19.6$ GeV 162
A.79 Negative kaon TPC fits for 10%-20% central events $Au + Au\sqrt{s_{NN}} = 19.6$ GeV 162
A.80 Negative kaon TOF fits for 10%-20% central events $Au + Au\sqrt{s_{NN}} = 19.6$ GeV 163
A.81 Positive proton TPC fits for 10%-20% central events $Au + Au\sqrt{s_{NN}} = 19.6$ GeV 163

A.82 Positive proton TOF fits for 10%-20% central events $Au + Au\sqrt{s_{NN}} = 19.6$ GeV . . . 164
A.83 Negative proton TPC fits for 10%-20% central events $Au + Au\sqrt{s_{NN}} = 19.6$ GeV . . . 164
A.84 Negative proton TOF fits for 10%-20% central events $Au + Au\sqrt{s_{NN}} = 19.6$ GeV . . . 165
A.85 Positive pion TPC fits for 5%-10% central events $Au + Au\sqrt{s_{NN}} = 19.6$ GeV 166
A.86 Positive pion TOF fits for 5%-10% central events $Au + Au\sqrt{s_{NN}} = 19.6$ GeV 167
A.87 Negative pion TPC fits for 5%-10% central events $Au + Au\sqrt{s_{NN}} = 19.6$ GeV 167
A.88 Negative pion TOF fits for 5%-10% central events $Au + Au\sqrt{s_{NN}} = 19.6$ GeV 168
A.89 Positive kaon TPC fits for 5%-10% central events $Au + Au\sqrt{s_{NN}} = 19.6$ GeV 168
A.90 Positive kaon TOF fits for 5%-10% central events $Au + Au\sqrt{s_{NN}} = 19.6$ GeV 169
A.91 Negative kaon TPC fits for 5%-10% central events $Au + Au\sqrt{s_{NN}} = 19.6$ GeV 169
A.92 Negative kaon TOF fits for 5%-10% central events $Au + Au\sqrt{s_{NN}} = 19.6$ GeV 170
A.93 Positive proton TPC fits for 5%-10% central events $Au + Au\sqrt{s_{NN}} = 19.6$ GeV 170
A.94 Positive proton TOF fits for 5%-10% central events $Au + Au\sqrt{s_{NN}} = 19.6$ GeV 171
A.95 Negative proton TPC fits for 5%-10% central events $Au + Au\sqrt{s_{NN}} = 19.6$ GeV 171
A.96 Negative proton TOF fits for 5%-10% central events $Au + Au\sqrt{s_{NN}} = 19.6$ GeV 172
A.97 Positive pion TPC fits for 0%-5% central events $Au + Au\sqrt{s_{NN}} = 19.6$ GeV 173
A.98 Positive pion TOF fits for 0%-5% central events $Au + Au\sqrt{s_{NN}} = 19.6$ GeV 174
A.99 Negative pion TPC fits for 0%-5% central events $Au + Au\sqrt{s_{NN}} = 19.6$ GeV 174
A.100 Negative pion TOF fits for 0%-5% central events $Au + Au\sqrt{s_{NN}} = 19.6$ GeV 175
A.101 Positive kaon TPC fits for 0%-5% central events $Au + Au\sqrt{s_{NN}} = 19.6$ GeV 175
A.102 Positive kaon TOF fits for 0%-5% central events $Au + Au\sqrt{s_{NN}} = 19.6$ GeV 176
A.103 Negative kaon TPC fits for 0%-5% central events $Au + Au\sqrt{s_{NN}} = 19.6$ GeV 176
A.104 Negative kaon TOF fits for 0%-5% central events $Au + Au\sqrt{s_{NN}} = 19.6$ GeV 177
A.105 Positive proton TPC fits for 0%-5% central events $Au + Au\sqrt{s_{NN}} = 19.6$ GeV 177

A.106 Positive proton TOF fits for 0%-5% central events $Au + Au\sqrt{s_{NN}} = 19.6$ GeV 178
A.107 Negative proton TPC fits for 0%-5% central events $Au + Au\sqrt{s_{NN}} = 19.6$ GeV 178
A.108 Negative proton TOF fits for 0%-5% central events $Au + Au\sqrt{s_{NN}} = 19.6$ GeV 179

B.1 Schematic of Spectator-Participant Model 182
B.2 Relating Overlap Region, Glauber Quantities and Event Multiplicity 183

List of Tables

4.1 Vertex Finding Efficiency for Three Different Parameter Sets 66

4.2 A summary of the analysis event cuts for the fixed target data 78

4.3 A summary of the analysis event cuts and track cuts for the beam-beam collision data 87

4.4 A summary of the systematic errors for the beam-beam collision data 98

Chapter 1

Introduction

1.1 Overview

This dissertation presents a summary of extensive analysis of charged light particle production in 3.0 GeV per nucleon pair central $Au+Al$ interactions as well as 19.6 GeV per nucleon pair $Au + Au$ collisions of several centrality classes. The goal of this work is to analyze a particular energy between nominal SPS energies and nominal RHIC energies to search for interesting physics including a possible phase transition, and to compare the systematics between RHIC and SPS for similar energies. By studying the interactions of the Au-like nucleus with the Al nucleus of the beam pipe material, we determine the feasibility of analyzing fixed target collisions with a center-of-mass designed detector. Knowing such an analysis is possible can further studies of the beam energy dependence of the temperature and baryon chemical potential and place other results on the nuclear matter phase diagram. By studying the collisions of two Au nuclei we can place on the nuclear matter phase diagram an energy with some possible interesting physics and further characterize the nuclear matter phase diagram.

The dissertation is organized as follows: Chapter 1 presents a focused overview of the field of Ultra-Relativistic Heavy Ion Physics and motivates the analysis; Chapter 2 provides a brief introduction to the necessary theory required to understand the analysis and the physics goals of the analysis; Chapter 3 describes in some detail the experimental setup and

an adequate description of the detector operation; Chapter 4 describes the analysis methods from initial data production to data refinement, particle identification and extraction of raw yields, as well as the corrections and systematic studies of the analysis; Chapter 5 concisely presents the results of the analysis and discusses the physical significance and relevance of those results by comparing to theoretical calculations and other world experiments; and finally in Chapter 6 a summary and conclusion are presented with future work in mind.

1.2 The States of Nuclear Matter

In ultra-relativistic heavy ion collisions a partonic state of matter is inferred from measurements made at energies of 200 GeV per nucleon pair. The Quark-Gluon Plasma (QGP) has been established based on two very important results [1]. First, the result describing the suppression of the away-side jet peak in central $Au + Au$ collisions [2] [3]. The observed suppression indicates the existence of a dense medium in which hadrons interact strongly with the medium early in the collision history. Second, the the result describing the hydrodynamic fit of the elliptic flow as a function of transverse momentum. Additionally, when scaling kinetic energy and elliptic flow by constituent-quark number, the separation of mesons from baryons disappears and all particles follow the same hydrodynamic curve. This property indicates degrees of freedom at the partonic level, i.e. the flow of quarks rather than hadrons. These, and other signatures of the QGP, will be discussed in further detail in Section 2.2. Once the QGP was supported by these strong pieces of evidence, characterization of the medium and determination of the baryon chemical potentials and temperatures where the QGP could exist became the next step.

The phase diagram of nuclear matter as it is today, see Figure 1.1, is mostly a schematic with only two known points: nuclear matter at room temperature [5] and the transition temperature ($\sim$175 MeV) at μ_B of zero [6]. For reference, room temperature is $\frac{1}{40}$ eV. The large black dot in the figure represents the proton at room temperature. The muave/pink

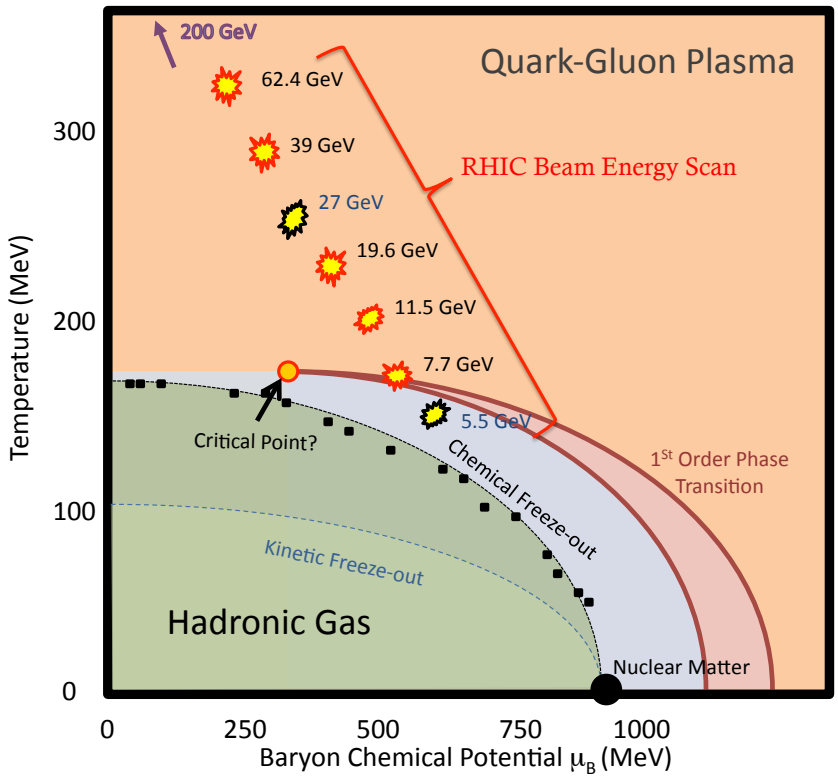

Figure 1.1: Nuclear matter phase diagram schematic with temperature versus baryon chemical potential μ_B. For reference, room temperature is $\frac{1}{40}$ eV. The large black dot represents the proton at room temperature. The muave/pink area wedged by thick dark red lines represents the possible region where the first order phase transition [4] may occur. The blue region represents the thermal production of hadrons before chemical freeze-out. The green regions represent elastic collisions above the kinetic freeze-out curve, and below the kinetic freeze-out curve, the final state of hadrons with fixed momenta. After chemical freeze-out, only particle decay contributes to changes particle number.

area wedged by thick dark red lines represents the possible region where the first order phase transition [4] may occur. The blue region represents the thermal production of hadrons before chemical freeze-out. The chemical freeze-out curve represents the temperature and baryon chemical potential at which the thermal production of hadrons has ceased [7]. After chemical freeze-out, only particle decay contributes to changes in particle number. The green regions represent elastic collisions above the kinetic freeze-out curve, and below the kinetic freeze-out curve, the final state of hadrons with fixed momenta. The kinetic freeze-out curve defines the temperatures and baryon chemical potentials at which elastic collisions and momentum transfer have ceased [7]. It is expected that the chemical freeze-out temperatures are always greater than the kinetic freeze-out temperatures [7]. The diagram displays the temperature versus baryon chemical potential and qualitatively illustrates the trends we see from theoretical calculations of the various transition curves [4] and an approximate region for the location of the critical point [8] — the point where the cross-over phase transition is expected to change order — and onset of deconfinement [9]. The Beam Energy Scan's (see section 1.3) program of collision energies is thought to create equilibrated systems whose initial states are near the T and μ_B of the onset of deconfinement; however, we are unable to measure directly these initial state variables for the corresponding collision energies. The diagram will be better understood when the phase transition curve, the freeze-out curves and the critical point are determined.

1.3 The Beam Energy Scan Program

At the heart of ultra-relativistic heavy ion physics is mapping the nuclear matter phase diagram. And, at the forefront of current research in QCD theory and experiment is the search for evidence of a critical point and/or its associated first order phase transition in the phase diagram. Though recent progress in lattice QCD and model calculations has been great, an exact location of the phase boundaries between the QGP and hadronic gas

as well as the postulated critical point are still unknown [10–12]. Observational evidence of these two features must then be found by heavy ion experiments [13–16] such as those at the Relativistic Heavy Ion Collider (RHIC) due to the facility's collision energy range corresponding to the prime search region of the phase diagram.

Theory has predicted several signatures of a first order phase transition and signatures for the critical point (for example [17–23] and references therein). The majority of these results indicate an increase in fluctuations when the freeze-out trajectory passes through the critical point or some dependence of the fluctuations on center of mass energy near the range in μ_B where the critical point lies [23] [24]. Because the critical point may act as an attractor [25] (a phenomena discussed in reference [26] in the context of nuclear liquid-gas transitions) as long as the thermalized initial conditions fall within this range of μ_B the evolution of the system with time will pass through the critical point; passing through the critical point would provide evidence for its existence without the problems precise theoretical calculations encounter. Establishing the validity of the hypothesized critical point, or even bounding the region where it lies by proving the existence of both a cross-over AND a first/second order transition, would begin to concretely define the phase diagram. This result would be as groundbreaking as proving the formation of the QGP.

The nuclear matter phase diagram (see Figure 1.1) is currently incomplete. Determining chemical freeze-out points, kinetic freeze-out points and the order of the phase transition all require multiple energies to be run with one given species of ion as well as running different species with similar energies [9] [27]. Experiments like the Super Proton Synchrotron (SPS) at CERN and the Alternating Gradient Synchrotron (AGS) at Brookhaven National Laboratory (BNL) were already running heavy-ion collisions at high μ_B. In RHIC also at BNL, several species of ions are collided to determine properties of the QGP and to look for its signatures in data with small μ_B.

In 2001 and 2008 test beams of lower center-of-mass energies of 19.6 GeV per nucleon pair and 9.2 GeV per nucleon pair, respectively, were run to demonstrate the readiness

of the detectors at RHIC to collect data at these sub-injection energies. While neither of these runs were long enough to improve on the physics measurements reported by the SPS experiments many checks have been performed. With the results from these tests published in references [28–30], a well-designed program suitable for both heavy ion experiments at RHIC with the goals of mapping the phase diagram was created.

In 2009, the STAR collaboration (Solenoidal Tracker At RHIC) proposed to run a beam energy scan (BES) to find the energies where QGP signatures could no longer be observed as well as to identify a softest point indicative of a first-order phase transition [31]. The BES program has three main goals and intends to achieve them by colliding Au beams in a range of energies from 5.5 GeV per nucleon pair (below the onset of deconfinement [9] and the supposed critical point) to 62.4 GeV per nucleon pair (above the supposed critical point) [31]. First it will search for the turn-off of each of the signatures of the QGP discussed in Section 2.2. Second it will search for a first-order phase transition and further map the kinetic and chemical freeze-out curves. And finally, it intends to search for evidence of a critical point [8].

In 2010, the majority of the proposed energies for $Au + Au$ collisions were run (62.4, 39, 11.5, 7.7) with two energies (27, 19.6) postponed for the following year, 2011. A test of the 5.5 GeV beams occurred in 2010 and at the time accelerator experts were unable to tune the beams for circulation in the RHIC rings nor to bring them into collision at any interaction region. Thus the only proposed BES energy below the energy identified as the onset of deconfinement [9] could not be run nor could data be collected. However, the STAR detector was able to record data from the beam halo (Au-like) colliding with the beam pipe (Al) with vertices inside the main detector, the Time Projection Chamber (TPC see section 3.2), during the 19.6, 11.5, and 7.7 GeV per nucleon pair beams. These beam-halo+pipe collisions have allowed the STAR collaboration to study interactions with center-of-mass energies below the requested 5.5 GeV energy and to extend the low energy reach of the BES program. The STAR collaboration can compare the beam-halo+pipe results with data from

previous experimental programs, namely the fixed target heavy-ion program of the AGS.

1.4 Fixed Target Collisions Measured with the STAR Experiment

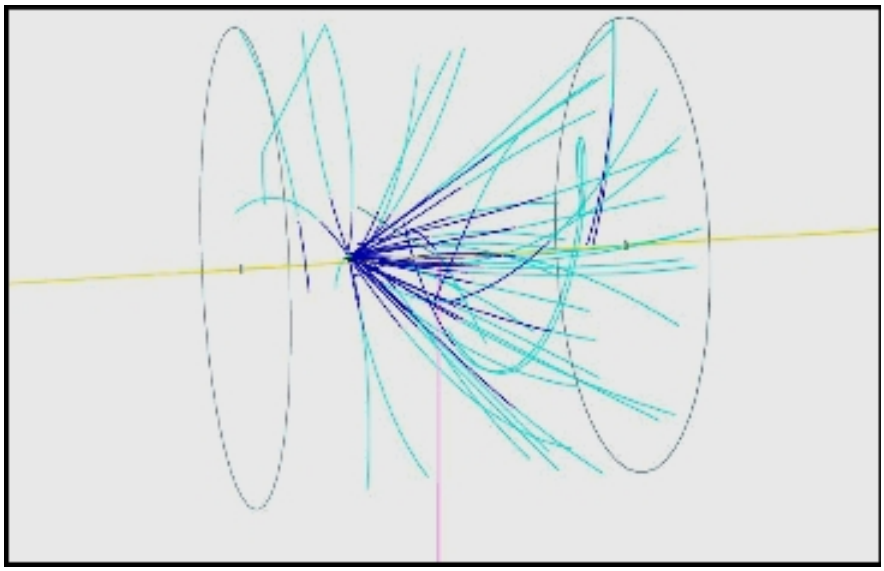

Figure 1.2: Fixed target interaction as reconstructed by the STAR detector. Note that the vertex is displaced from the beam axis (the yellow line) and also displaced from the center of the detector (denoted by the pink line). All of the tracks are to one side of the vertex (to the right) as would be expected from a projectile on a target at rest rather than being symmetric about the collision point as is typical of collider events.

During data collection of previous low energy beam test runs at RHIC, the STAR collaboration found a large number of beam-halo+pipe interactions that were recorded in addition to the good $Au + Au$ collisions. An example of a reconstructed fixed target interaction is shown in Figure 1.2. The yellow line denotes the beam axis and the two black rings represent the TPC end-caps. The pink line shows the center of the TPC. All of the tracks reconstruct and extrapolate to a point near the left TPC end-cap where the light blue indicates the part of a track that was reconstructed with hits and the dark blue indicates the extrapolation of that track to the vertex. A few attempts were made to exclude beam-halo+pipe collisions from data collection before the BES program began. However, those studies demonstrated

the importance of recording the data of these interactions. And further studies indicate the necessity of reconstructing the Au-like+Al vertices and tracks in addition to the Au+Au collisions for the entire BES program. By accurately reconstructing events like these, end-users could easily reject events of this type from their analyses without the risk of mis-associated tracks to a vertex nor shadow vertices (this is described in further detail in Section 4.2).

In the summer of 2010 the UCD group began in earnest to analyze the beam-halo+pipe events and to determine if physics extraction was possible. This required, among many other things, determining the energy at which the interactions occurred. The beam pipe 'target' (Al) is parallel to the Au ion beam axis and the Au-like projectile nucleus experiences energy loss while traveling through the metal of the pipe prior to experiencing a nuclear interaction. Additionally, considerations of the detector geometry to determine acceptance and efficiency of tracking were made. Careful evaluation of variables for determining collision centrality with comparisons to an analytic Glauber model [32] [33] (a model to estimate the number of particles produced based on the number of nucleons participating in an inelastic collision) as well as a Glauber Monte Carlo [34] was one of the largest challenges of the initial study. After diligent analysis of the data described in Section 4.3, a determination of the collision energy and centrality definition allowed for particle spectra to be produced.

Ultimately being able to use STAR as a fixed target experiment as well as a colliding beam experiment has allowed the Beam Energy Scan (BES) to reach further into the high baryon chemical potential and low temperature region of the nuclear matter phase diagram as the program intended. Currently, a fixed target program is under development to more accurately compare systematics between the colliding beam energies and the fixed target energies [35].

Chapter 2

Ultra-Relativistic Heavy Ion Physics

Systematic experimental studies with relativistic heavy ions began in the 1970's at laboratories in Berkeley, California, USA and Dubna, Russia. The early experiments broke ground with a better understanding of the strong force leading to a string of hypotheses requiring high temperatures and energy densities for the formation of a new phase, a quark-gluon plasma (QGP) [36–38], and thus generated some excitement and momentum for experiments with more energy per nucleon. For a QGP to exist required a phase transition and it would be characterized by free quarks and gluons. During these early years, quantum chromo-dynamics (QCD) was developed to describe the strongly interacting matter at said high energy densities and temperatures. This chapter will summarize the key concepts of QCD, highlight key features of the Quark-Gluon Plasma that can be experimentally quantified, discuss particle spectra analysis, and detail the Coulomb analysis to be presented in Chapter 5.

2.1 Introduction

The theory of quantum chromodynamics (QCD) was developed using the basis and methodology of quantum electrodynamics (QED). The success and precision of calculations in QED help promise for predictions in QCD. However, as QCD theory furthered, key differences affected the ability to make as precise predictions as the electromagnetic counterpart. In

QED, the Lagrangian is:

$$\mathcal{L} = -\frac{1}{4}F_{\mu\nu}^2 \tag{2.1}$$

where,

$$F_{\mu\nu} = \partial_\mu A_\nu - \partial_\nu A_\mu \tag{2.2}$$

and A_μ describes the vector potential of the electromagnetic field. The coupling constant $\alpha_s = \frac{1}{137}$ allows for convergence of calculations for interactions, including diagrams containing a large number of vertices.

In QCD, the Lagrangian is:

$$\mathcal{L} = -\frac{1}{4}\sum_i F_{\mu\nu}^\alpha F^{\mu\nu\ \alpha} + i\sum_q \bar{\psi}_q^i \gamma^\mu (D_\mu)_{ij} \psi_q^j - \sum_q m_q \bar{\psi}_q^i \psi_{q\ i} \tag{2.3}$$

where in the first term, the gluon-only term, $\alpha = 1, 2, \ldots, 8$ indicates the color indices of gluons, and

$$F_{\mu\nu}^\alpha = \partial_\mu A_\nu^\alpha - \partial_\nu A_\mu^\alpha + g_s [A_\mu, A_\nu]^\alpha \tag{2.4}$$

A_μ^α are the eight vector potentials of the gluon field, with g_s being the color charge, and the last term in equation 2.4 represents the self-interaction of gluons due to their non-zero color charge (very unlike photons in QED since photons have no electromagnetic charge). The second term in the lagrangian describes the interaction of quarks with gluons where each of the ψ_q^i are four-component Dirac spinors of the quark fields with color i and flavor q, and

$$(D_\mu)_{ij} = \delta_{ij}\partial_\mu + i\frac{g_s}{2}\sum_\alpha \lambda_{i,j}^\alpha A_\mu^\alpha \tag{2.5}$$

The $\lambda_{i,j}$ are 3×3 matrices in equation 2.5 are SU(3) group representations. The third and last term in the lagrangian describes the self-interaction of quarks. Finally, the coupling

constant in QCD is calculated with the following:

$$\alpha_s(Q^2) = \frac{4\pi}{\beta_0 \ln(Q^2/\Lambda^2)}\big(1 + \text{higher logarithmic terms}\big) \tag{2.6}$$

In equation 2.6, Λ is a scale constant, $\beta_0 = 11 - \frac{2}{3}n_f$ where n_f denotes the number of light quarks. Typically α_s is calculated at the mass of the Z^0 boson and $\alpha_s = 0.118 \pm 0.002$ giving $\Lambda = 217^{+25}_{-23}$ MeV [39]. For large values of Q^2 perturbative methods are used for calculations. But, because the value of α_s is large in the case of small Q^2, and sometimes greater than 1, analytical calculations do not always converge. Thus, more complex numerical methods are needed, namely lattice QCD methodology, and was introduced in 1974 [40] and continues to be developed.

Lattice QCD relies on the computation strength of computers and has pushed the development of parallel processing. Because finite-temperature lattice QCD is challenging and complex, only a brief discussion of the main findings will be presented here. An introduction to the theory can be found in Ref. [41] while more detailed information can be found in Refs. [42–47].

Calculations using lattice QCD begin with deconfinement starting with the Polyakov loop [48–50]

$$L(T) \sim \lim_{r\to\infty} e^{(-V(r)/T)} \tag{2.7}$$

where $V(r)$ is the potential between a static quark-antiquark ($q\bar{q}$) pair separated by distance r, and T is the temperature. The potential, $V(r) \sim \sigma r$, where σ is the string tension for pure gauge theory and in the limit of Eqn 2.7 $V(r) \to \infty$ meaning $L = 0$. $L(T)$ then becomes similar to an order parameter because color screening causes the string to melt forcing the potential to be finite and L to be non-vanishing. Thus for the temperature range $0 < T < T_c$, $L = 0$ and quarks are in confinement, but for temperatures $T > T_c$, L is finite and non-vanishing, meaning quarks are in deconfinement. The temperature T_c has the significance of being the temperature for the onset of deconfinement and an indicator of a first-order phase

transition [41]. This rapid change in L is not as easily seen with light quark masses as it is with heavy quark masses [45].

The effective quark mass can be determined using lattice methods by calculating the expectation value of $\langle\bar{\psi}\psi\rangle(T)$. The quantity $\langle\bar{\psi}\psi\rangle(T)$ is the order parameter of the chirally symmetric Lagrangian that occurs when taking the limit of vanishing current quark mass. Chiral symmetry is broken in the confined phase with finite consituent quark masses, and it is expected that at high enough temperature, the symmetry will be restored. At vanishing baryon number density, the shift from constituent quark mass to current quark mass and deconfinement are expected to occur simultaneously [51]. Physically, however, quark masses are neither infinite nor massless but rather have a finite current quark mass, thus the symmetry is only approximate.

Next, lattice QCD characterizes the behavior of the energy density and the pressure at deconfinement. Bulk thermodynamic properties are indicative of the number of degrees of freedom in the system in the high temperature limit. For example, pressure tends to the ideal gas value as the temperature becomes very high. The pressure of the ideal system

$$\frac{P_\pi}{T^4} = \frac{3\pi^2}{90} \qquad T \to 0 \tag{2.8}$$

$$\frac{P_{\text{qgp}}}{T^4} = (16 + \frac{21}{2}n_f)\frac{\pi^2}{90} \qquad T \to \infty \tag{2.9}$$

when the baryon chemical potential $\mu = 0$. Classically the free energy density is calculated from the difference between two temperatures, and in lattice QCD this is approximated by

$$\epsilon \sim \frac{\partial(\ln(Z)/T^4)}{\partial T} \tag{2.10}$$

where Z is the QCD partition function. By taking the derivative with respect to the gauge coupling instead, Eqn 2.10 becomes the difference between the expectation values of the

Euclidean action,

$$\epsilon \sim N_\pi^4 \int_{\beta_0}^{\beta} d\beta' \Big(\langle \hat{S}_E \rangle - \langle \hat{S}_E(T=0) \rangle \Big) \tag{2.11}$$

which is calculable on the lattice. An abrupt increase in the value of energy density is observed at the critical temperature when plotting ϵ/T^4 as a function of the temperature in units of the critical temperature, T/T_c. It increases from a small hadronic value to a large value approximately 10% below the value of a Stefan-Boltzmann ideal gas [52]. And with some manipulation, one can obtain a value for P/T^4 which is indicative of the number of degrees of freedom in the system. The value of the transition temperature must be calculated by fixing other observables on the lattice, such as the proton or ρ-meson mass, since there are no dimensions in the equations of QCD for massless quarks. Addidtionally, the value of the temperature depends on the number of quark flavors present in the theory. For example, 2-flavor calculations yield $T_c = 173 \pm 4$ MeV while 3-flavor calculations obtain $T_c = 154 \pm 8$ MeV [45]; or if using the ρ-meson mass as the point of reference, $T_c \sim 150$ MeV or if using the string tension σ then $T_c \sim 200$ MeV. All points of reference, either using quark numbers or a particular observable, obtain $\epsilon = 1 - 2$ GeV/fm^3 for the energy density in order to produce deconfined quarks and gluons.

Lattice calculations show that a transition from hadrons to deconfined quarks and gluons does exist and that the transition coincides with chiral symmetry restoration. The calculations also demonstrate that the transition occurs at a critical temperature and is observed when a sudden increase in the energy density occurs and shifts to a large value that is ∼10% lower than the Stefan-Boltzmann ideal gas value.

2.2 Signatures of the Quark-Gluon Plasma

Nucleus-nucleus collisions, A+A, have three main stages of evolution. Beginning at the point of collision, $t = 0$, a very hot, very energy dense region is created. The energy density of the initial collision can be estimated by the Björken formula, which is the rapidity independent

Lorentz formula:

$$\epsilon = \frac{1}{\tau_f S}\frac{dE_T}{dy} \simeq \frac{3}{2}\frac{\langle m_T \rangle}{\tau_f S}\frac{dN_{ch}}{dy} \tag{2.12}$$

where ϵ is the initial energy density, τ_f the formation time, S the overlap region, $\frac{dE_T}{dy}$ the transverse energy density, $\langle m_T \rangle$ the average transverse mass, and $\frac{dN_{ch}}{dy}$ the density of charged particles. This stage is characterized by large momenta exchanges, jets, heavy quark pairs ($c\bar{c}$ and $b\bar{b}$) and interactions at the parton level.

Next, these partons interact to achieve chemical and thermal equilibrium. This stage is characterized by a rapid expansion and cooling of the locally statistically equilibrated system to the critical temperature, T_c [53]. The quark-gluon plasma has an expected lifetime of between 1 to 10 fm/c and a size of at most a few femtometers in diameter; it must equilibrate and expand within these dimensional restrictions. Equilibration allows for further evolution to be calculable using relativistic hydrodynamics. Questions still remain in regard to the equilibration time, whether it occurs instantaneously [54] or over a long (10 fm/c)/short (1 fm/c) period of time [55] [56]. This time is also where direct photons are produced and the start of collective flow begins.

Finally, hadronization and chemical and kinetic freeze-out occur. In the subsequent hot hadronic gas phase following hadronization, global observables like centrality (the overlap region), initial volume, number of participants and more must be interpreted to determine, after the fact, the initial conditions of the collision. From these observables, the signals of the quark-gluon plasma must be distinguished from the hadron background. Even these signals are modified by final-state interactions in the hadronic phase. Some of the key signatures are discussed in the following sections.

2.2.1 Strangeness Enhancement

A feature of the QGP is an enhancement in strangeness content. Typically in hadronic interactions, production of strangeness is suppressed due to the higher mass of the strange

quark as compared to the up and down quarks. However, in the QGP environment, not only are quarks and gluons produced in abundance, but also the energy density and temperature are high (on the order of the strange quark mass $m_s = 101^{+29}_{-21}$ MeV [39]). As u and d quarks are the most easily produced and most abundant quarks at the initial stage of the QGP fireball, the available phase space is quickly filled; thus strangeness becomes the favored produced particle pair [57]. Furthermore, the u and d quarks annihilate with the $\bar{u}$ and $\bar{d}$ antiquarks, respectively, while $s\bar{s}$ annihilation occurs less frequently until the saturation of s and $\bar{s}$ abundances.

The two main production channels for $s\bar{s}$ pairs are $q\bar{q} \rightarrow s\bar{s}$ and $g\bar{g} \rightarrow s\bar{s}$. Considering production of $s\bar{s}$ pairs by only the $q\bar{q}$ channel, chemical equilibrium in strangeness would only be reached after about eight times the natural lifespan of the QGP fireball. Rafelski and others proposed that the quark-antiquark pairs are created dominantly by the gluon-gluon fusion channel [57] [58] and this would be reflected in the enhancement of strange- and multi-strange baryons compared to purely hadronic interactions at the same temperature.

Strangeness enhancement is measured in terms of the strangeness enhancement factor. It is experimentally defined as the yield per participating nucleon of a given type of strange particle in heavy ion collisions (at RHIC, Au+Au, for example) relative to the same strange particle yield in a lighter reference collision system (at RHIC, p+p, for example). Strangeness fugacity, γ_s, is introduced to thermochemical models to account for possible incomplete chemical equilibration of strangeness.

2.2.2 J/ψ Suppression

In the presence of a QGP, the bound state of $c\bar{c}$, the J/ψ, will be suppressed with increasing temperature due to a weakening of the heavy quark effective potential [59]. This is Debye screening of free color charges in the QGP and explains the long-range Coulomb-type term in the effective potential. At small distances, the strong coupling constant $\alpha_s \sim Q^2$, the momentum transfer, while at large distances $\alpha_s \sim \frac{1}{Q^2}$. This leads to the effective potential

rising linearly with distance, r, and thus the effective potential between two heavy quarks is calculable on the lattice. This phenomenon adds the string-like term in the effective potential. The effective potential(also called "Cornell" potential) then looks like,

$$V(r) = \sigma r - \frac{\alpha}{r} \tag{2.13}$$

and describes the color interaction between c and $\bar{c}$ without the presence of a QGP medium (i.e. vacuum). This potential will turn into a short-range Yukawa-type

$$V(r) = \sigma r \frac{1 - e^{-\mu(T)r}}{\mu(T)r} - \frac{\alpha e^{-\mu(T)r}}{r} \tag{2.14}$$

interaction in the presence of a QGP medium (see Fig 2.1), with the range given by the Debye screening length, λ_D, related to the inverse of $\mu(T)$ the temperature dependent screening mass. This potential can be plugged into the Schrödinger equation, since it is non-relativistic, in order to determine the disassociating temperature of each state of J/ψ (and also the Υ family).

The potentials mentioned above are rather simplified to what may actually occur during a heavy-ion collision. By looking at Fig 2.2 the magnitude of the observed suppression at both RHIC and SPS facilities indicates more than Debye screening as the dominant cause of suppression. The figure, taken from Ref. [61] shows the nuclear modification factor, R_{AA}, for J/ψ's with low rapidity from the PHENIX experiment using Au+Au and Cu+Cu collisions as a function of the number of participants, N_{part}, in the initial collision. Also on the plot are similar results derived from measurements from other experiments with lower energies and different collision systems (Pb+Pb, In+In, S+U) at CERN. The nuclear modification factor (R_{AA} or R_{AB}) is again plotted as a function of the number of participants corresponding to the centrality bins made in each of the different analyses. The pattern showcased is similar for all colliding systems despite the colliding systems being in different energy (and therefore shadowing/anti-shadowing) regimes [61]. The original potential is too simplistic and we

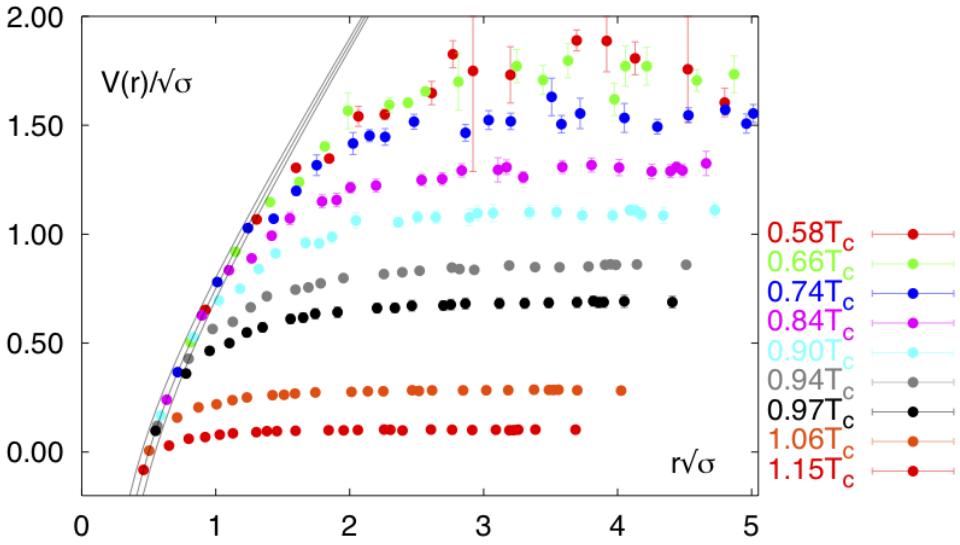

Figure 2.1: Taken from Ref. [60]. Temperature dependence of the heavy quark potential for three flavor QCD with a quark mass $m_q = 0.1$. The band of lines gives the Cornell-potential in units of the square root of the string tension, $V(r)/\sqrt{\sigma} = -(\alpha/r)\sqrt{\sigma} + r\sqrt{\alpha}$ with $\alpha = 0.25 \pm 0.05$. The gauge couplings corresponding to the different temperatures are $\beta = 3.25$, 3.30, 3.35, 3.40, 3.43, 3.45, 3.46, 3.50, 3.54. The string tension values used to set the scale are based on the interpolation formula given in Ref. [52]. The potentials have been normalized at short distances such that they agree with the zero temperature Cornell potential at $r = 1/4T$.

must look for additional modification factors such as those from cold nuclear matter effects to heavy quark suppression [61].

2.2.3 Direct Photons and Dileptons

Two signals that can provide information about the earliest times of the collision without much interference from the colored medium are the direct photon production and dilepton production. These two radiated signals are proposed as both the most promising and efficient signals for characterizing the initial state of a heavy ion collision.

Photons are produced at every stage of the fireball evolution, see Figure 2.3. Direct photons refer to photons that are produced from particle collisions. These photons have a large mean-free path compared to they system size (∼10 fm) and traverse the colored medium without participating in a collision or interaction since photons interact electromagnetically. Thus, direct photons can carry information about the QGP, like temperature at their pro-

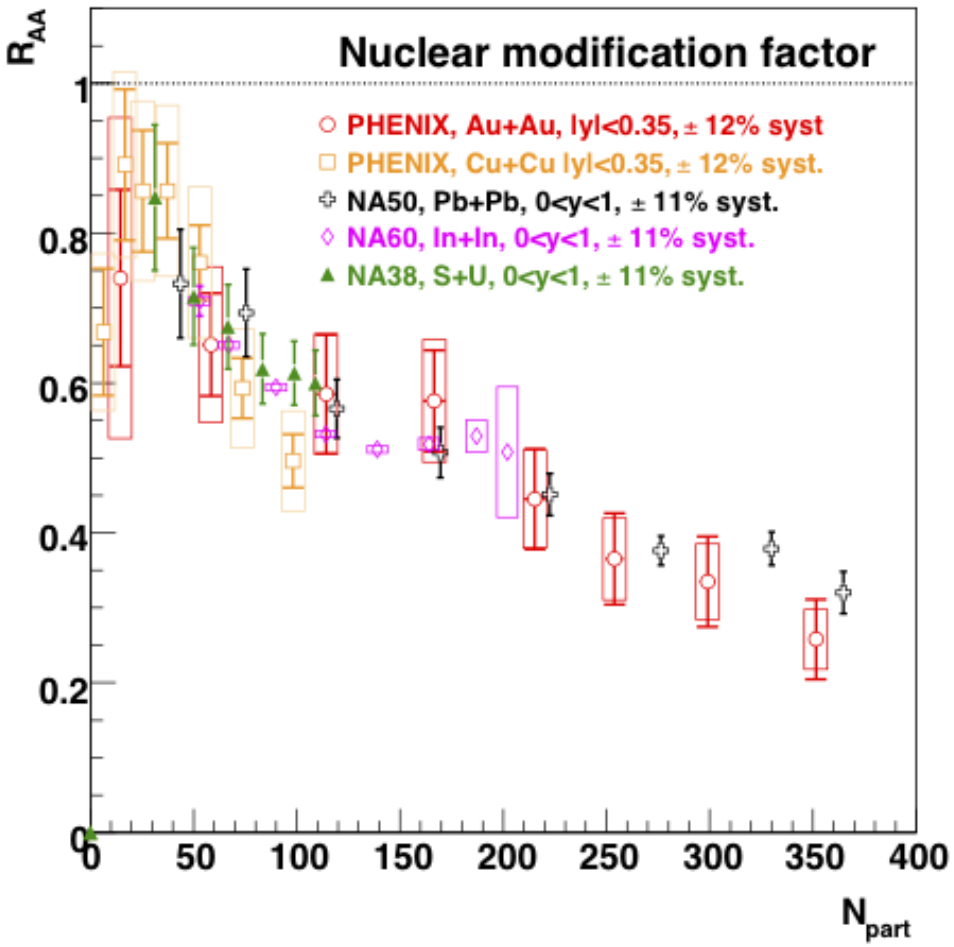

Figure 2.2: Taken from Ref. [61]. J/ψ nuclear modification factors for Au-Au, Pb-Pb, In-In and S-U colliding systems at their respective energies (200, 19 and 17.3 GeV) as a function of the number of participants, N_{part}.

duction, and serve as a signal for QGP formation and early stages of the collision [63]. This broad category can be further subdivided by stages of the collision evolution into prompt photons, pre-equilibrium photons, thermal photons and jet conversion photons. Prompt photons are created in the early stages of the collision (initial hard scatterings) through gluon channels such as $q\bar{q} \rightarrow \gamma\bar{g}$, $g\bar{q} \rightarrow \gamma g$, or the dominant gluon-photon Compton Scattering process $gq \rightarrow \gamma q$. Pre-equilibrium photons are produced before the plasma is thermalized. Thermal photons are produced thermally from both hadronic reactions (certain types of Compton scatters like $\pi\rho \rightarrow \gamma\rho$ [64] [65]) and the QGP environment. Jet conversion photons are produced from the passage of jets through the plasma [62].

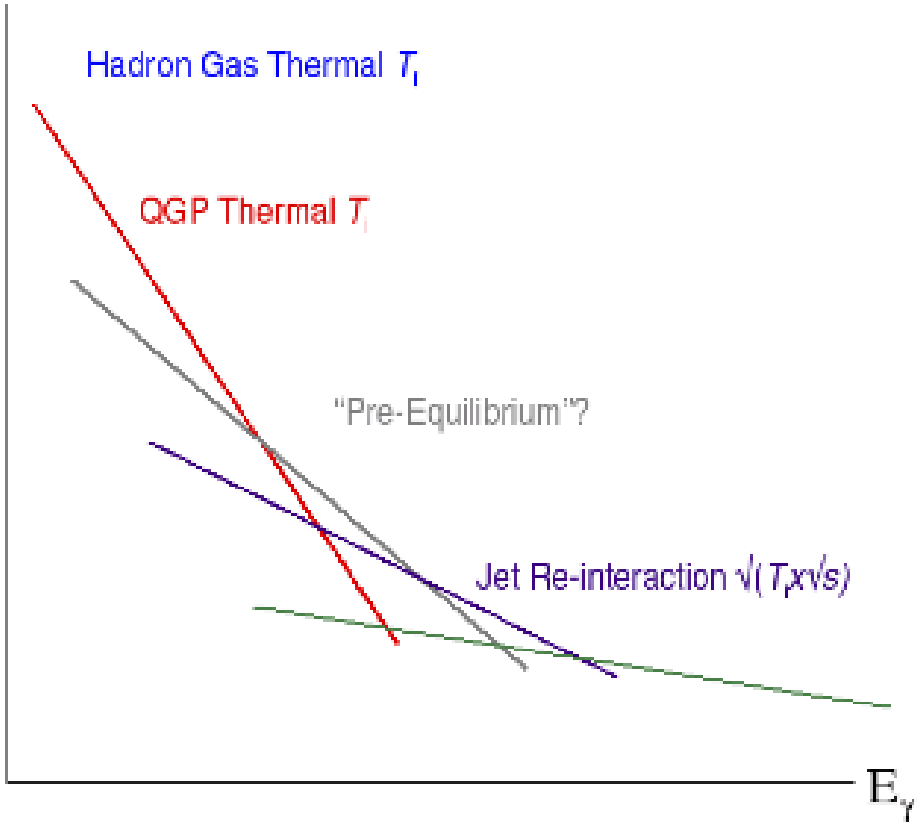

Figure 2.3: Schematic of expected sources of photons as a function of energy [62]. The red line is the contribution from QGP Thermal emission, the grey line represents the contribution from emission on pre-equilibrium, the purple line denotes contributions from jet re-interactions, the green line is not labeled but describes the photons emitted during the pQCD prompt $x\sqrt{s}$ phase, and the blue label for Hadron Gas Thermal is for contributions to the low energy side of emission which decreases rapidly as energy increases; it has a much steeper slope than thermal QGP emission.

Direct photon production, however, has a relatively small cross section in addition to the signal being washed out by the large number of additional sources of photons throughout the fireball's lifetime. An example of other such sources of photons include hadronic decays (like pions $\pi^0 \rightarrow \gamma\gamma$). These backgrounds are typically subtracted using the invariant mass spectrum method established by the WA98 Collaboration [66] and then perfected by the PHENIX Collaboration [67].

Dileptons are massive, unlike the massless real direct photons, and allow for parameters like invariant mass and transverse momentum to be utilized to examine properties at each stage of the fireball [68]. Dileptons with high transverse momentum and/or high invariant

mass are produced at the earlier stages of the fireball whereas dileptons with low transverse momentum and/or small invariant mass are produced later. Production mechanisms for dilepton pairs are $q\bar{q} \rightarrow \gamma^* \rightarrow l^+l^-$ during the QGP phase while in the hadronic phase mechanisms include decays of particles like ρ, ω, ϕ, and J/ψ, interactions following $h^+h^- \rightarrow l^+l^-$ format as well as the Drell-Yan process (where a valence quark from one nucleus interacts with a sea quark from the other nucleus to produce a virtual photon which decays into a lepton pair) [62].

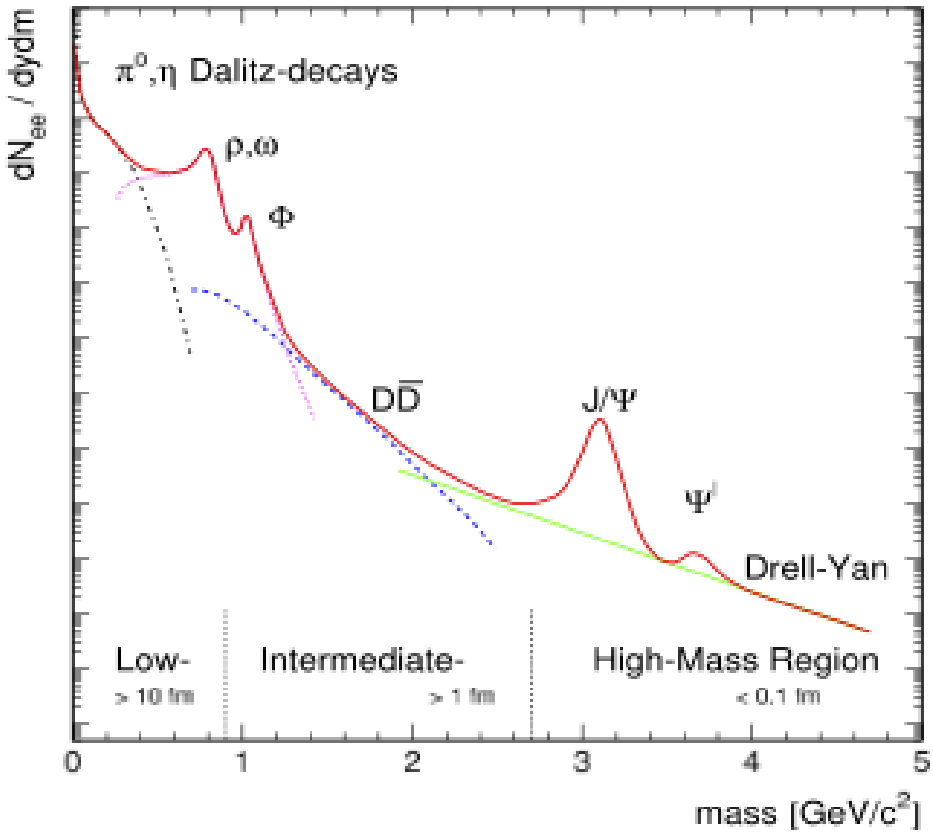

Figure 2.4: Schematic of expected sources of dileptons as a function of invariant mass [62]. The red line is the sum total of all contributions; the black dot-dashed line represents the contribution from Dalitz-decays of scalar mesons; the purple dotted curve is the ρ, ω, and ϕ vector mesons; the blue dashed line describes contributions from $c\bar{c}$; and the green line is the contribution from Drell-Yan processes.

Dileptons can be subdivided into three rough categories corresponding to the invariant mass of the produced pair, see Figure 2.4. These categories are the low-mass region (LMR)

where the invariant mass $M < M_\phi = 1.024$ GeV [39], the intermediate-mass region (IMR) where $M_\phi < M < M_{J/\psi} = 3.1$ GeV [39], and the high-mass region (HMR) where $M \geq M_{J/\psi}$. In the LMR, dilepton production is dominated by vector meson decays and the signal can illustrate the medium modification of vector mesons. Continuum radiation from the QGP dominates dilepton production in the IMR; thus they carry signatures of thermal radiation from the QGP. The HMR of dilepton invariant mass is dominated by heavy flavor decays from hadrons like Υ and J/ψ and carries valuable information regarding thermalization, elliptic flow, and energy loss of heavy quarks in the medium [62].

An example of an important confirmation of medium effects on particle decay is found when reviewing the history of the ρ meson and its production in heavy ion collisions. In the low-mass region, dilepton emission is mediated by the broad vector meson $\rho(770)$ since this meson couples strongly to the $\pi\pi$ channel and has a short lifetime. Hypotheses regarding the medium affecting the mass and/or width of mesons led to experiments CERES [69] and NA45 [70] at CERN SPS to produce dilepton invariant mass distributions to determine the validity of those hypotheses. Both experiments found evidence that the invariant mass distribution was in excess below the ϕ meson mass and that $\pi\pi$ annihilation could reproduce the data only if the intermediate ρ meson was modified [69] [70]. With the available statistics and resolution a differentiation between a larger width or change in mass was not possible and further studies by NA60 [71] with In+In definitively rules out models where the mass of the ρ meson was reduced, confirming a broadening of the width.

2.2.4 Azimuthal Anisotropy or Flow

Bulk behavior of the produced particles in a nucleus-nucleus collision can also relay information regarding early stages of evolution and the production of a QGP [72–76]. Particularly, when there is a non-central (not head-on) collision, the partons in the overlap region are subject to spatial anisotropy due to the random population of nucleons in the nucleus and the random orientation and magnitude of the impact parameter. The almond-shape of the

overlap region is highlighted by the orange object in Fig. 2.5. The beam line is represented

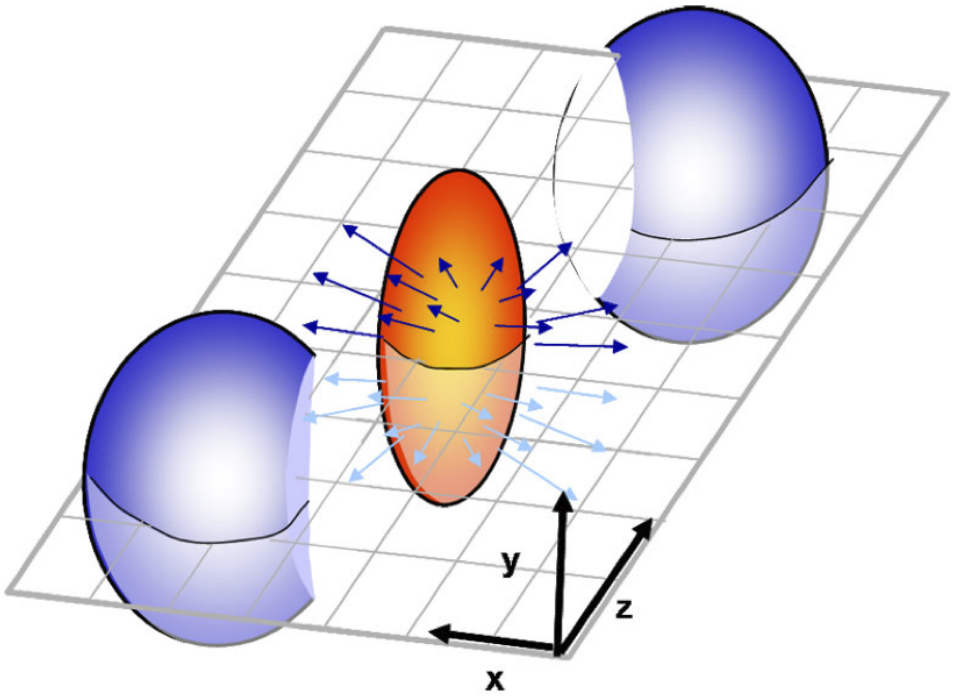

Figure 2.5: Cartoon of the overlap region in A+A collisions. The beam line is represented by the z-axis and the two blue-purple spheres are the spectator nucleons from the colliding nuclei. The orange almond-shape defines the region of participating nucleons in the collision, with all the arrows sizes emphasizing the magnitude of the pressure gradients. The grid bisecting the three objects denotes the reaction plane and is defined by the impact parameter along the x-axis and the beam line.

by the z-axis and the two blue-purple spheres are the spectator nucleons from the colliding nuclei. The grid bisecting the three objects denotes the reaction plane and is defined by the impact parameter along the x-axis and the beam line. The particles which are along the short axis are subject to the higher pressure gradient (all the arrows in the figure, where sizes denote the magnitude of the pressure gradient) as compared to particles along the long axis. As a result, the initial spatial anisotropy is converted into an anisotropy in momentum space. This momentum anisotropy will reflect the time evolution of pressure gradients generated in the system at early stages in the collision [77] [78].

The anisotropy in the momentum space can be calculated by looking at the azimuthal distribution of produced particles with respect to the reaction plane. The azimuthal distri-

bution of the produced particles can be decomposed into the Fourier series [79],

$$E\frac{d^3N}{d^3\mathbf{p}} = \frac{1}{2\pi}\frac{d^2N}{p_T dp_T dy}\left(1 + 2\sum_{n=1}^{\infty} v_n \cos(n[\phi - \Psi_r])\right) \tag{2.15}$$

where E is the energy of the particle, $\mathbf{p}$ is the magnitude of the momentum, p_T is the transverse momentum, ϕ is the azimuthal angle, y is the rapidity, and Ψ_r is the reaction plane angle [80]. The sine terms in the expansion vanish due to the reflection symmetry of the collision with respect to the reaction plane. The coefficients can be calculated as average values:

$$v_n = \langle \cos(n[\phi - \Psi_r]) \rangle \tag{2.16}$$

The first three harmonics hold some physical significance in heavy ion collisions; the first two are discussed in the following paragraphs while the third harmonic is discussed more in-depth below. Higher-order harmonics (v_6 or v_8 for example) are currently under scrutiny to determine if physics can be deduced from their signals.

The 'zeroth' coefficient in the above Fourier decomposition represents radial flow, a completely isotropic emission of particles representing the uniform expansion of the fireball [53]. Radial flow gives information regarding the kinetic equilibrium of the system before its rapid expansion [81]. The momentum distribution of matter that has reached kinetic equilibrium will be isotropic while un-equilibrated matter will have a Lorentz boosted momentum distribution [81]. There is an observed signal in the transverse momentum (p_T) spectra for heavier particles like the proton which can be experimentally measured via the blastwave model [82,83] (described later in Section 2.3.1): it is the shoulder at the low-p_T region of the spectra.

The first coefficient (v_1) represents directed flow. Directed flow describes the collective motion of produced particles from one nucleus being counterbalanced by the equal magnitude but opposite direction of produced particles from the other nucleus [53]. The directed flow signal can be seen significantly near beam rapidity, but vanishes near midrapidity; the loss

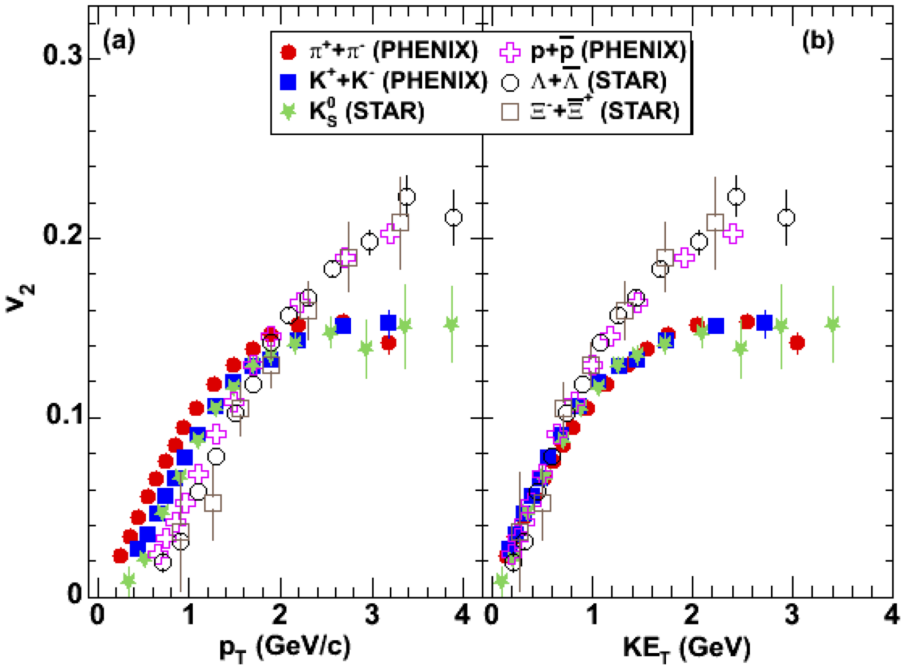

Figure 2.6: Second harmonic, v_2, plotted as a function of transverse momentum, p_T. Note that the baryons follow a different curve to mesons from Ref. [88]

of signal is due to the symmetry of the collision geometry [81]. Observing a minimum in the directed flow as a function of beam energy can mean a softening of the equation of state (EOS) [84–86]; a softening of the EOS illustrates the possible formation of a QGP in the early stages of the collision [87].

Elliptic Flow

The second harmonic (v_2) represents elliptic flow and characterizes the ellipticity of the azimuthal distribution of produced particles. Elliptic flow arises due to the spatial anisotropy of the overlap region in the initial collision and develops early in the collision evolution. Final state interactions should lead to a positive value of v_2 [89] due to differing path lengths in the medium at different azimuthal angles. Elliptic flow is an advantageous signature of QGP formation due to its ease of measurement and high statistical accuracy: elliptic flow affects

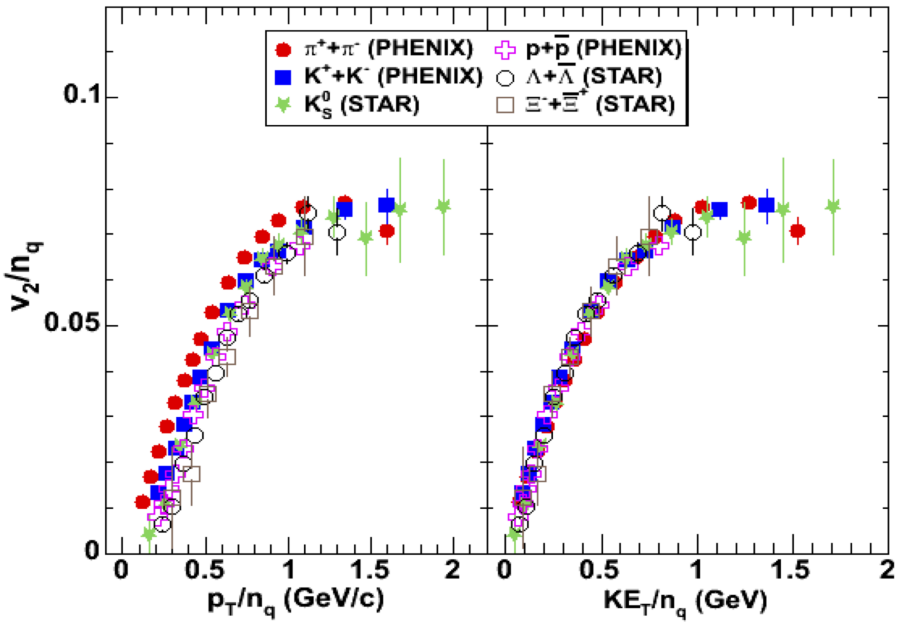

Figure 2.7: Number of quark (n_q) scaled v_2 as a function of scaled p_T on the left panel and scaled KE_T on the right panel. When each particle type is scaled by the number of constituent quarks (baryons by 3 and mesons by 2), all hadrons fall on the same curve. This is indicative of flow originating prior to hadronization. [88]

all final state particles.

Elliptic flow typically has its largest magnitude at midrapidity and falls off toward higher values of $|\eta|$. This pattern is found over a broad range of incident energies (and experiments) except for a study with Pb+Pb at the SPS [90] that demonstrates a flatter distribution.

Results from the STAR experiment show that elliptic flow as a function of p_T follows two distinct curves separated by hadron type and a non-zero elliptic flow for strange hadrons [91, 92]. These findings are confirmed later by the PHENIX collaboration in Ref. [88] and shown in Fig. 2.6. Here, the second harmonic, v_2, is plotted as a function of transverse momentum, p_T , on the left panel and again as a function of transverse kinetic energy, KE_T, on the right panel. Clearly visible in both panels is the separation of mesons from baryons in two curves.

The PHENIX collaboration further found when scaling both axes by the number of

constituent quarks (also called n_{cq} scaling) that all hadrons except for pions, fall on a common curve, see Fig. 2.7. Because multi-strange baryons are not as affected by the hadronic stage compared to lighter hadrons combined with the evidence that elliptic flow develops early in the collision evolution, the large magnitude of v_2 suggests that the s quark flows similarly to u and d quarks [22,93,94]. Recent results from PHENIX on flow of non-photonic electrons (in this case, D-mesons) extend constituent quark scaling to the charm quark [95]. Quark coalescence (recombination) models show such common scaling with the number of constituent quarks, meaning there is partonic collectivity.

2.2.5 Jets, High p_T Probes

Hard scattering processes that produce the majority of soft particles in heavy ion collisions also produce highly energetic particles. The manner in which these hard particles interact with the medium is a unique direct probe of the environment without disturbing the medium itself. Dihadron azimuthal correlations at high p_T are a way to reconstruct jet structure in particle collisions. For collisions like $p+p$, when reconstructing jets, the range or cone of the jet is narrow and fragments similarly to a charged particle through matter: via radiation or excitation of the medium. In QCD, gluon radiation and quark pair production are the mechanisms that a hard-scatter particle would lose energy. Once these hard-scatter particles are placed in the collision environment directly following a nucleus-nucleus interaction, one jet of the pair may have farther to traverse, or a longer interaction with, before exiting the medium. Then, the away-side jet would lose energy as it traversed the hot and dense medium, possibly losing all of its energy along the way; this is called jet quenching. Understanding the phenomenon of jet quenching helps to probe the color structure of QCD matter.

In Figure 2.8 correlations between high p_T hadrons for $p+p$, central d+Au and central Au+Au collisions (background subtracted) from STAR are shown [96]. The azimuthal distribution of hadrons have $p_T > 2$ GeV/c relative to a trigger hadron with $p_{T\ \mathrm{trig}} > 4$ GeV/c. A hadron pair from the same jet will have an enhanced correlation strength at $\Delta\phi \approx 0$,

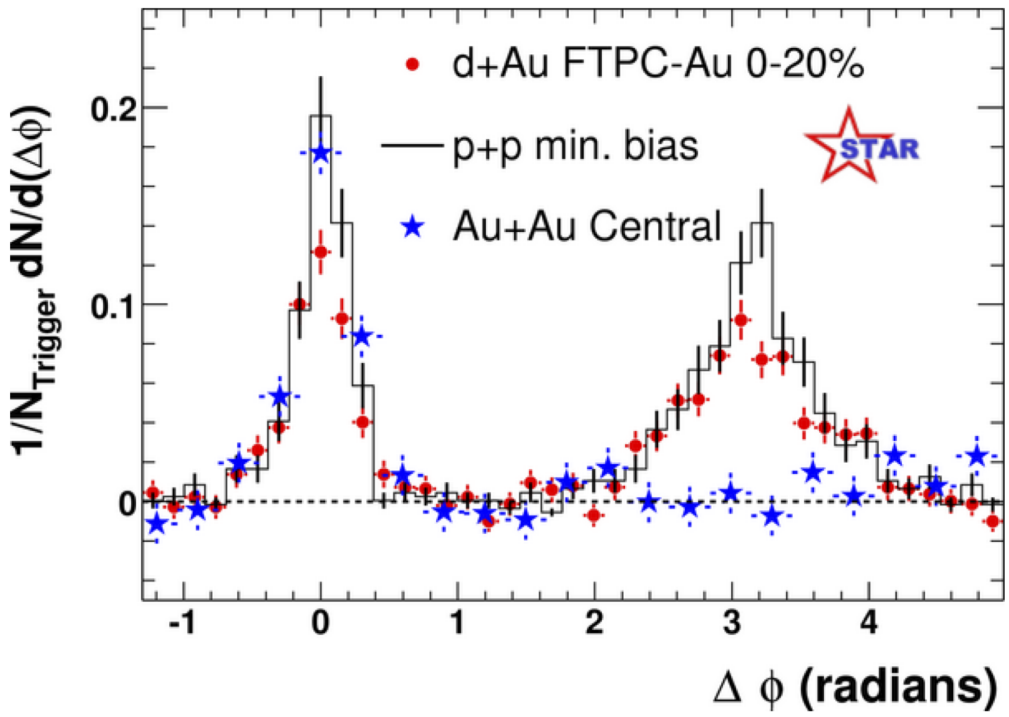

Figure 2.8: Dihadron azimuthal correlations at high p_T showing correlations for p+p, central d+Au and central Au+Au collisions (background subtracted). Indicative that higher-momentum fragments interact strongly with the medium as a final state effect. [3, 96]

seen in $p + p$, d+Au and Au+Au in the figure, with similar correlation strengths, widths and (not shown) charge-sign ordering (the correlation is stronger for oppositely charged hadron pairs [3]). A hadron pair from back-to-back dijets will have an enhanced correlation strength at $\Delta\phi \approx \pi$, as observed for $p + p$ and for d+Au with a slightly broader width than the near-side correlation peak. However, the back-to-back dihadron correlation is missing in central Au+Au collisions, while for peripheral Au+Au collisions the correlation appears quite similar to that seen in $p+p$ and d+Au. The results compared with p+p and peripheral Au+Au collisions illustrate that the momentum-balancing hadrons azimuthally opposite a high-p_T trigger particle in central Au+Au collision are greater in number, widely dispersed in azimuthal angle, and significantly softer [96].

If the correlation can be attributed to jet fragmentation then the away-side peak suppression in Au+Au collisions is due to final-state interactions of hard-scattered partons in the dense medium [2]. And, we measure preferentially the hard hadrons from the partons which

scatter outward toward the surface of the collision zone for a short duration in the dense medium. However, the dominant contribution of jet fragmentation must still be confirmed in the region with trigger particles higher than $p_{T\ \mathrm{trig}} > 6$ GeV/c where the meson and baryon yields are similar to those of jets fragmenting in vacuum in order to more accurately compare to p+p and d+Au results. Preliminary studies of the azimuthal correlation with harder trigger particles show similar results to Figure 2.8 with larger statistical uncertainties [97] and suggest that the peak structures are indeed due to jet quenching [96].

2.3 Particle Spectra

In order to have a different phase of matter, a phase transition is required where the new phase consists of free quarks and gluons. Experiments currently are determining the nature of the phase transition, attempting to answer the question of a defined order transition or a cross-over transition. Analyzing particle spectra can help build a stronger case for a phase transition and describe some of its characteristics, though are not sufficient alone. Two types of spectra can be analyzed: transverse momentum or mass, p_T or m_T, and rapidity, y, spectra. The rapidity spectra are distributions of particles in the longitudinal (beam) direction. Transverse momentum or mass spectra are distributions of particles perpendicular to the beam direction. Both types allow for a study of hadronic matter properties such as the energy density, ϵ, pressure, P, and entropy density, s, as a function of baryon chemical potential, μ_B, and temperature, T. Both are highly related to underlying collision dynamics though only transverse spectra will be explored in this thesis.

Hydrodynamics provides the model framework in which to analyze the particle spectra. This model describes collective flow, expansion and other bulk matter phenomena of a collision. The basic equations of the model begin with conservation of energy-momentum ($\partial_\mu T^{\mu\nu} = 0$) and conservation of current ($\partial_\mu N_i^\mu = 0$). The energy-momentum tensor, $T^{\mu\nu}$, contains terms to include the energy density, hydrostatic and bulk pressure, energy/heat

transfer, and the shear stress tensor. The set of conserved currents individually include a charge density and charge current for quantities like the net baryon current. In each of the conserved quantities, there are ideal terms and dissipative terms that define ideal hydrodynamics (excluding dissipative terms) and viscous hydrodynamics (including some number of dissipative terms) respectively.

In ideal hydrodynamics the energy density estimated via Björken's formula [98] (assuming no work through $P\mathrm{d}V$),

$$\epsilon_{Bj}(\tau) = \frac{\langle m_T \rangle}{\tau \pi R^2} \frac{dN}{dy} \tag{2.17}$$

where τ is the proper time, $\langle m_T \rangle$ is the average transverse mass obtained via spectra analysis, R is the effective transverse radius and $\frac{dN}{dy}$ is the number of particles per unit rapidity. One can also determine if the matter in a collision comes to some chemical equilibrium by comparing the average number of particles of a given species, $\langle N_i \rangle$, to another in order to cancel out the volume dependency of the $\langle N_i \rangle$ equation,

$$\langle N_i \rangle = V \left[n_i^{\mathrm{th}}(T, \mu) + \sum_R \Gamma_{R \to i} n_R(T, \mu) \right] \tag{2.18}$$

where V is the volume, n_i^{th} is the number density of directly emitted particle i, n_R is the number density of resonance R, and $\Gamma_{R \to i}$ is the branching ratio of resonance R to particle species i. Since the average number of particles of a given species can be determined via particle spectra, and branching ratios from Reference [39], the particle rations depend on the remaining variables T and μ. The last check of ideal hydrodynamics is whether the matter reaches kinetic equilibrium. Kinetically equilibrated matter has an isotropic momentum distribution due to a pressure gradient leading to radial expansion. With a finite velocity, though, the distribution becomes Lorentz boosted and such distortions carry information regarding kinetic equilibrium of the system. The Blastwave Model [82, 83], discussed below, utilizes this framework to obtain a kinetic freeze-out temperature and radial flow velocity from particle spectra.

2.3.1 Blastwave Model

Expansion with some velocity, β_T, correlates with a linear increase in the apparent 'temperature' (slope parameter) with increasing particle mass. A "blast wave" model includes an expansion velocity that is assumed to increase with the radius, r,

$$\beta_T = \frac{\beta_s r}{R_G} \tag{2.19}$$

where β_s is the flow velocity at the surface and R_G is the outer radius of the expanding fireball [53]. More succinctly, a blastwave model describes identified particle transverse spectra with contributions from thermal emission and radial flow [53]. Below are descriptions of a few common blastwave models.

Siemens and Rasmussen developed a blastwave model [83] to describe particle production in Ne+NaF reactions. This model is characterized by a fast hydrodynamic expansion leading to quick hadronic decoupling and a 'finalized' momentum distribution where the only further effects on particle momenta come from collective expansion. Of utmost importance in this model is the spherically symmetric expansion of the shells (blast waves) with a constant radial velocity. The language used to describe the physical picture coined the term blast wave and brought such a model to heavy ion collisions [99]. The model, despite its motivation in hydrodynamics, developed from two freeze-out conditions — $dt = \beta_T dr$ and $t = t_0 + \beta_T r$ — and the Cooper-Frye formula,

$$E\frac{dN}{d^3p} = \frac{dN}{dyd^2p_T} = \int d^3\Sigma_\mu(x) p^\mu f(x,p) \tag{2.20}$$

where E is the energy, $\Sigma_\mu(x)$ is the freeze-out hypersurface, p^μ is the four-momentum, and $f(x,p)$ is the phase-space distribution function. The model assumes the thermodynamic variables (T and μ) and the transverse velocity (β_T) to be constant. Hence the momentum

distribution takes the form [83, 99]

$$\frac{dN}{d^3p} = \frac{e^{-\gamma E/T}}{2\pi^2}\left[\left(1+\frac{T}{\gamma E}\right)\frac{\sinh a}{a} - \frac{T}{\gamma E}\cosh a\right]\int_0^1 r^2(\zeta)\frac{dr}{d\zeta}d\zeta \tag{2.21}$$

where E is the hadron energy; T is the temperature of all shells of the fireball; γ is the Lorentz gamma factor with the velocity representing the collective radial flow; a is a dimensionless parameter defined as a function of transverse velocity, momentum, and temperature, $a = \gamma\beta_T p/T$; and r is the radius parameterized in ζ, which corresponds to the freeze-out times when the hadrons in the given blast shell (at radius r) cease interacting. The parameter ζ may always be restricted to the interval $0 \leq \zeta \leq 1$. Because this model assumes the aforementioned freeze-out conditions, shells which are further out from the center of the fireball will freeze-out later in time. Additionally, the hypersurface vector is parallel to the flow vector, another result of the freeze-out conditions.

The assumptions of Siemens and Rasmussen make the model appropriate for low-energy scattering processes where the expansion of the matter from colliding nuclei is largely isotropic. For higher energies, however, the expansion is known to be anisotropic [98], namely cylidrically symmetric. The blastwave model of Schnedermann, Sollfrank, and Heinz [82] modifies the Cooper-Frye formula to include a cylindrically symmetric hypersurface and boost-invariance in the freeze-out description, and hydrodynamic and kinetic equations.

In the parameterization, $\zeta \to (t(\zeta), r(\zeta))$, again the curve ζ represents times when the cylindrical shells freeze-out and can be fully determined given one coordinate since for finite values, other freeze-out points can be obtained via Lorentz transformation. Assuming again a constant radial velocity and the freeze-out condition $dt/d\zeta = 0$, the Cooper-Frye formula simplifies to

$$\frac{dN}{dyd^2p_T} = (\text{const.})m_T K_1\left[\frac{m_T}{T}\cosh(\alpha_T)\right] I_0\left[\frac{p_T}{T}\sinh(\alpha_T)\right] \tag{2.22}$$

where m_T is the transverse mass, p_T is the transverse momentum, K_1 and I_0 are Bessel functions, T is the temperature, and α_T is the space-time transverse coordinate. This form

of blastwave model has been used to describe various analyses of transverse spectra from SPS and RHIC energies [100]. Further modification to the boost-invariant blastwave model includes resonance decays which, at high energies, contributes heavily to light particle production. Inclusion of resonances is extremely important to calculating particle abundances and is essential to the success of any thermal model. Boost-invariance also implies that the values of thermodynamic variables on one freeze-out shell is the same for any other freeze-out shell, meaning the values are the same at any rapidity.

It is important to note that rapidity distributions at RHIC energies have a Gaussian shape with a dependence of thermodynamic variables on rapidity, both indicative that the system at these high energies is not boost invariant. There exists, however, a plateau region, $|y| < 1$, that does indicate boost-invariance and blastwave calculations performed over this region can be applied to any other value of rapidity in that region.

The final two blastwave models to be briefly discussed are the single-freeze-out model [101, 102] and the non-boost-invariant single-freeze-out model [99]. The single-freeze-out model applies the assumption of a constant proper time in Minkowski space, with the transverse size of the system defined by a maximum parameter, and finally a Hubble-like velocity field at freeze-out. These assumptions lead to a velocity-dependent volume element in the Cooper-Frye formula and also easily lead to the inclusion of resonance states. The non-boost-invariant single-freeze-out model modifies the system boundaries to include a dependence of the transverse size on the longitudinal coordinate. This last model compares well with pion and Kaon spectra from BRAHMS but needs to incorporate the rapidity dependence of the baryon chemical potential to accurately model the protons [99].

2.4 Particle Ratios and the Coulomb Source

By looking at relative particle abundances of particular particles quite a bit of information regarding the environment of the expanding fireball can be determined. These aspects of

the collision are important to understanding, for example, what production mechanisms dominate in that energy range, or when the available energy for particle production is high enough to erase initial condition importance.

An antibaryon to baryon ratio as a function of center of mass energy, such as one found in Ref. [103], is indicative of the baryon chemical potential, μ_B, of the nuclear collision. The μ_B of the collision represents the amount of energy necessary to pair produce a baryon from the surrounding environment. As the available energy increases the easier and easier it becomes to pair produce, rather than transform one type of baryon to another. Higher energies allowing for pair production approach a baryon-free central region, as is expected [53].

Pion production in heavy ion collisions of nuclei where the number of neutrons is approximately equal to the number of protons ($N = Z$, up to about ^{40}Ca) is in equal proportions for π^+, π^-, and π^0 due to the isospin symmetry of the initial state. This property changes when the number of neutrons begins to overwhelm the number of protons. Once $N > Z$ there is an excess of π^- due to the increased number of neutrons at the low energies of AGS and SPS experiments. However, once the available energy in a collision becomes high enough, like RHIC energies, the disparity between charges begins to disappear. Taking a ratio of charged pions will place a particular collision energy in an isospin dominated production regime or in an energy dense environment rich with pair production.

Similarly, as energy of the collisions increases, heavier particles like Kaons become easier to produce and are found more abundantly. Kaon production, namely K and $\bar{K}$, comes from two mechanisms like pions: associated production and pair production. Associated production ($N + N \rightarrow Y + K$) leads to a higher number of K^+ mesons along with hyperons like Λ, Σ, Ξ, and Ω. Pair production ($N + N \rightarrow N + N + K + \bar{K}$) is more costly energy-wise but produces K^+ and K^- in equal proportions. The production of Kaons becomes more important as the collision energy increases due to fermi statistics, and the differences between the charged particle abundances decreases as the available energy for particle production increases.

Antiparticle-particle ratios in the context of a statistical-thermal model suggests a chemical equilibrium of the final state [53]. A statistical-thermal model consists of two parameters, temperature T and baryon chemical potential μ_B, and usually involves a ratio similar to

$$\frac{\bar{p}}{p} = \frac{e^{-(E+\mu_B)/T}}{e^{-(E-\mu_B)/T}} = e^{-2\mu_B/T} \tag{2.23}$$

where the temperature T can be obtain via particle spectra, for example. A prediction of the temperature of the environment and the baryon chemical potential of the collision system can thus be made.

Particle ratios produced by the NA49 Collaboration as a function of center of mass energy show evidence for the onset of deconfinement [9, 104–106] resulting in the structures of the "Kink", the "Horn", the "Step", and the "Dale". Each of these structures are illustrated below. These structures are predicted in the statistical model for the early stage (SMES) of nucleus-nucleus collisions based on work by Fermi [107]. This model assumes the collision is either in a thermalized hadron gas—the confined phase—or in a thermalized QGP state—the deconfined phase. The model assumes a first order phase transition between the two phases, constant entropy and strangeness during expansion, and uses Fermi-Landau initial conditions.

The Kink, in Figure 2.9, is seen in the particle ratio of the average yield of pions to the average number of wounded nucleons in the collision plotted against Fermi's measure,

$$F = \left[\frac{(\sqrt{s_{NN}} - 2m_N)^3}{\sqrt{s_{NN}}}\right]^{\frac{1}{4}} \tag{2.24}$$

where $\sqrt{s_{NN}}$ is the center of mass energy per nucleon-nucleon pair, and m_N is the nucleon rest mass. It represents the sudden change in the number of pions per participating nucleon (wounded nucleon). Nucleus-nucleus collisions are plotted in solid symbols while $p+p$ data

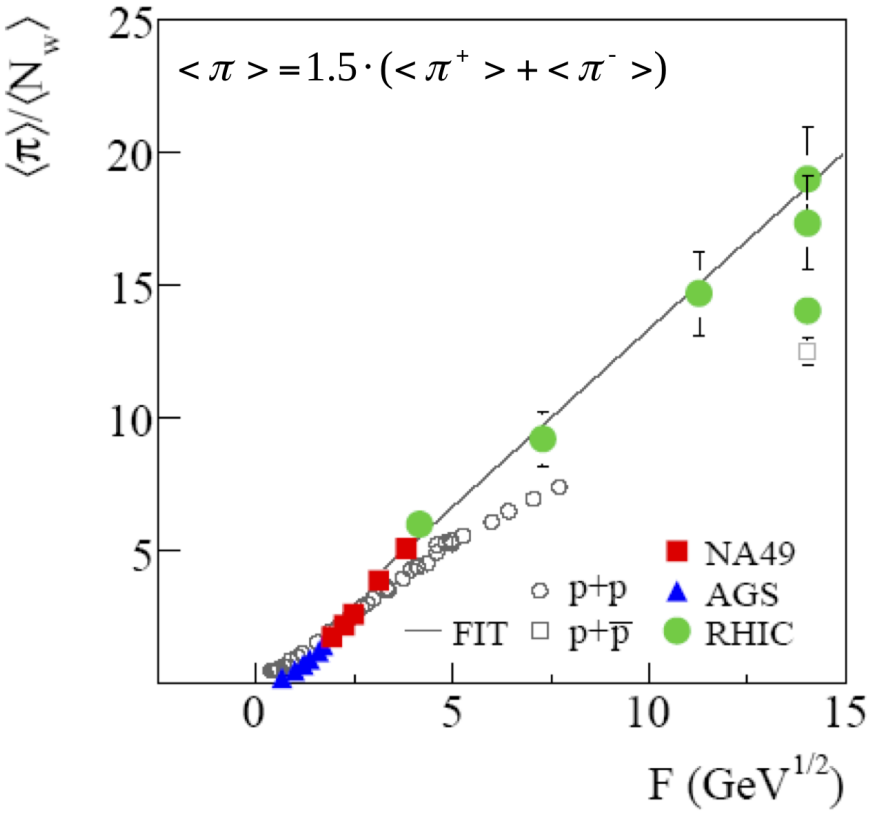

Figure 2.9: The Kink taken from Ref. [9]. Energy dependence, $\sim (s_{NN})^{\frac{1}{4}}$, of the mean pion multiplicity per wounded nucleon measured in central Pb+Pb and Au+Au collisions (full symbols), compared with the corresponding results from $p + p(\bar{p})$ reactions (open symbols).

are plotted in open symbols. The fit to the data is parameterized by the equation [9],

$$\frac{\langle \pi \rangle}{\langle N_w \rangle} = a + bF + cF^2 \tag{2.25}$$

and the results of the fit indicate an increase in the slope parameter by 1.3 for collision systems with $F > 3.5$ GeV$^{\frac{1}{2}}$ from $F < 1.85$ GeV$^{\frac{1}{2}}$ [9]. Hence, there is a 'kink' in the slope parameter indicative of the onset of deconfinement [104, 108].

The Horn is a sharp and narrow peak in strangeness production, $E_s = \frac{\langle K \rangle + \langle \Lambda \rangle}{\langle \pi \rangle}$, or in particular the approximate strangeness ratio of $\langle K^+ \rangle / \langle \pi^+ \rangle$. In Figure 2.10 the steep increase followed by a turnover in the data is evident and is followed by a plateau at higher energies. The plateau is consistent with the onset of deconfinement from the SMES model [104, 108].

The Step, in Figure 2.11, is a plateau in the energy dependence of the inverse slope

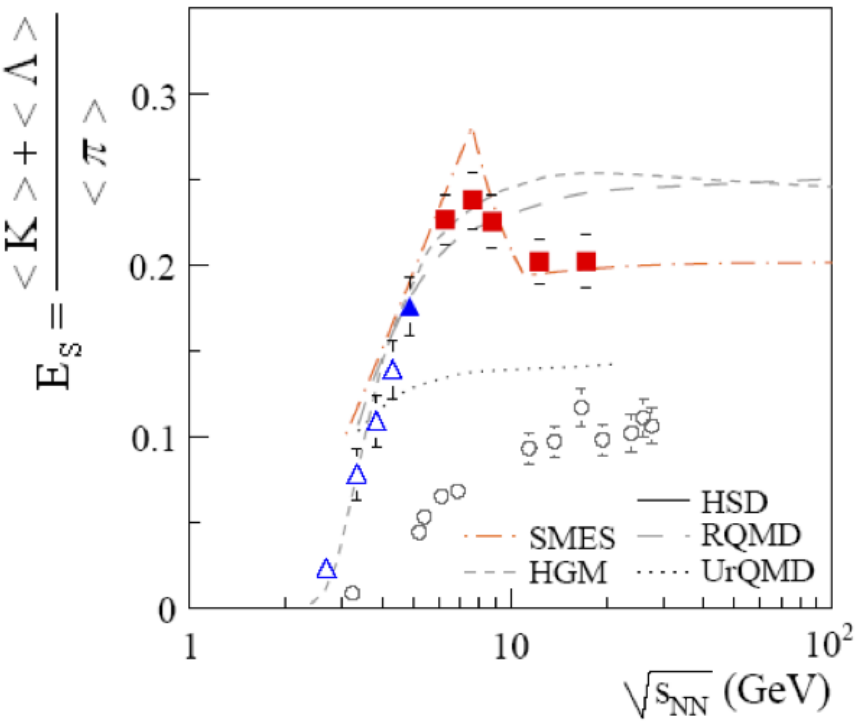

Figure 2.10: The Horn taken from Ref. [9]. Energy dependence of the $(\langle K \rangle + \langle \Lambda \rangle)/\langle \pi \rangle$ ratio, an approximation of strangeness production, measured in central Pb+Pb and Au+Au collisions (full symbols) compared with the corresponding results from $p + p(\bar{p})$ reactions (open circles).

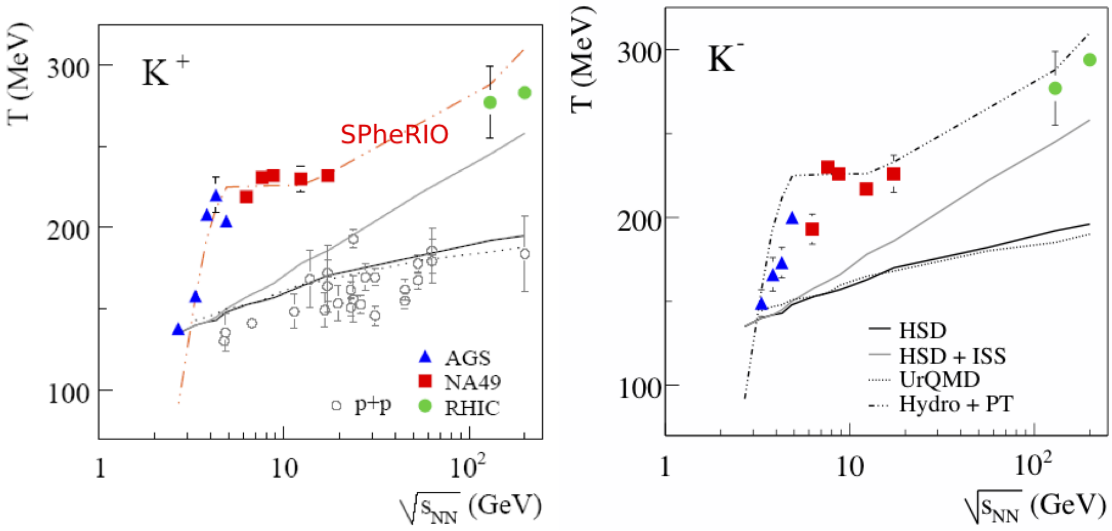

Figure 2.11: The Step taken from Ref. [9]. Energy dependence of the inverse slope parameter T of the transverse mass spectra of K^+ (left) and K^- mesons (right) measured at mid-rapidity in central Pb+Pb and Au+Au collisions. The K^+ slope parameters are compared with those from $p+p(\bar{p})$ reactions in the left-hand plot (open circles). The curves represent predictions from various models described in the text.

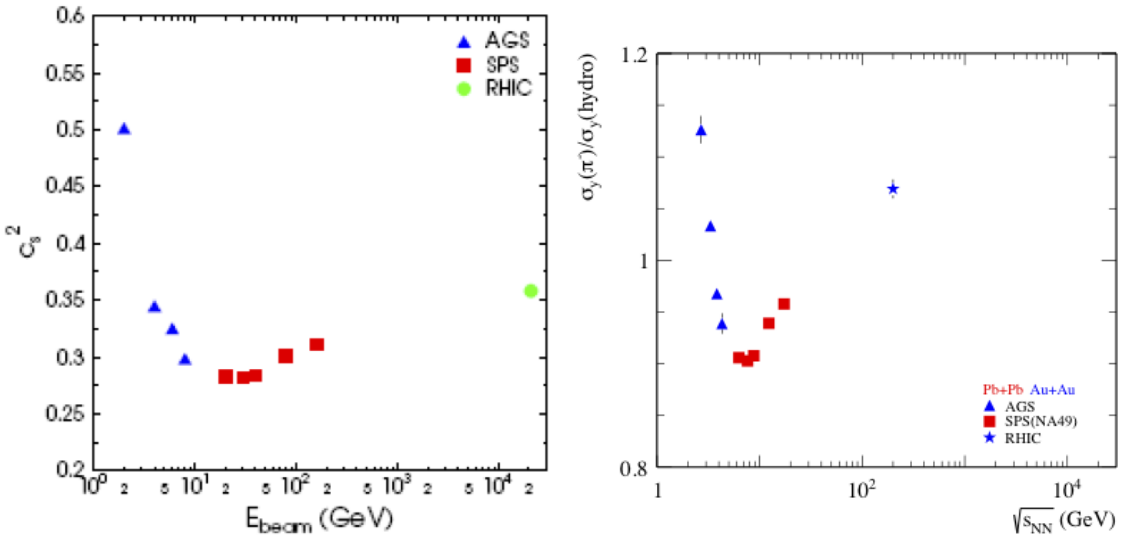

Figure 2.12: The Dale; left taken from Ref. [9], right taken from Ref. [109]. Left panel: Energy dependence of the speed of sound in the medium. Right Panel: Energy dependence of the ratio of the measured pion rapidity width to the value calculated according to Landau's hydrodynamical model, Equation 2.26.

parameter, T, of the transverse mass, m_T, spectra for charged kaons. It arises from the assumption of a first order phase transition in the SMES model. In the mixed phase, the temperature and pressure are constant so the plateau is suggested to be caused by a softening of the equation of state. In the figure, energy versus the slope parameter of K^+ mesons is on the left and while for K^- mesons is on the right. The figure clearly shows a steep rise of T measured at the AGS to a plateau at SPS energies followed by the indication of a rise in T with the RHIC data. Although the scatter of data points is large, T appears to increase smoothly in $p + p(\bar{p})$ interactions.

A softening of the equation of state would also lead to a weakening of the collective expansion in the longitudinal direction. The Dale structure arises from the energy dependence of the calculated velocity of sound in the medium and is representative of the longitudinal expansion. In Figure 2.12 the dale is illustrated in two ways. In the left-hand panel, the speed of sound is shown as a function of center-of-mass energy where blue triangles are data from AGS experiments, red squares from SPS experiments and the greed dot from a RHIC experiment. The right-hand panel illustrates the comparison of the measured pion rapidity

width to the calculated width of the pion rapidity distribution according to the Landau hydrodynamical model [110, 111] equation,

$$\sigma_y^2(\text{hydro}) = \frac{8}{3}\frac{c_s^2}{1-c_s^4}\ln\left(\frac{\sqrt{s_{NN}}}{2m_N}\right) \tag{2.26}$$

where σ_y^2(hydro) is the pion rapidity distribution width, c_s is the speed of sound in the medium, $\sqrt{s_{NN}}$ is the center of mass energy per nucleon-nucleon pair, and m_N is the nucleon mass. The plot utilizes the value of $c_s = 1/3$ [109] to make the pion rapidity distribution width prediction. Both plots indicate a softening of the equation of state by the existence of a clear minimum as a function of the center-of-mass energy coupled with the step structure as is predicted for the onset of deconfinement.

Three of these structures need some value associated with the pion or kaon spectra. Pions are extremely important for gathering information regarding the onset of deconfinement, expansion temperature and the nature of the collision environment. One important aspect of a nucleus-nucleus collision environment can be gained by studying the pion spectra and it is detailed below in Section 2.4.1.

2.4.1 The Coulomb Source Effect

The Coulomb source effect in ultrarelativistic heavy ion collisions relies on the Coulomb force from the net positive charge density of the expanding fireball on the formed pions emitted at the thermally equilibrated freeze-out volume. The effect of the Coulomb interaction is greatest on the least massive particles, hence pions. Any positively charged pion emitted will be slightly accelerated away from the positive source while any negatively charged pion will be marginally decelerated leading to modifications in the momentum distribution of the final particle spectra. A ratio made from positive versus negative pions enhances these differences in the low-momentum region of the particle spectra and allows for a calculation of the Coulomb source potential, V_C, as well as the initial pion ratio, R_i [112]. This ratio

studies the interaction region of nucleus-nucleus collisions by effectively determining the charge density of the source at freeze-out.

An enhancement in the ratio has been seen by experiments at the Bevelac [113–116] as well as the AGS [117, 118]. These results suggest the enhancement is due to the positive charge of the source. Theoretical contributions to these studies suggest that the source is a static Coulomb source, however a static source is not valid for heavy ion collisions since dominant charge-carrying protons are emitted alongside pions and expand in the fireball. Further investigation results [119–121] show that the Coulomb potential in nucleus-nucleus collisions depends on the source radius and the charge of the system. These studies clearly indicate with increasing center of mass energy (and hence more energy available for pion production) the ratio of charged pions approaches unity. In other words, as the pion ratio increases with center of mass energy, the Coulomb potential falls. Since the charge of the system is determined by the collision centrality and the potential decreases, it is the source radius that increases indicating an expanding freeze-out surface.

The modification of the pion spectra by the Coulomb potential occurs after freeze-out, on the 'initial' pion spectra, resulting in the measured, 'final', spectra. The final energy, E_f, of the pion becomes

$$E_f = E_i \pm V_C \tag{2.27}$$

where E_i is the initial energy, V_C is the Coulomb potential, and the addition or subtraction depends on the charge of the pion. Consequently, the final pion ratio, R_f, becomes energy dependent,

$$R_f(E_f) = \frac{E_f - V_C}{E_f + V_C} \frac{\sqrt{(E_f - V_C)^2 - m^2}}{\sqrt{(E_f + V_C)^2 - m^2}} \frac{n^+(E_f - V_C)}{n^-(E_f + V_C)} \tag{2.28}$$

where the first two terms are the charge appropriate proper Jacobian for a static spherical source, $J = (E_f \pm V_C)\sqrt{(E_f \pm V_C)^2 - m^2}$ [112], and $n^{\pm}(E)$ is the pion emission function of

the initial pion spectrum, typically best following a Bose-Einstein distribution:

$$n^{\pm}(E_f \mp V_C) = A^{\pm}(e^{(E_f \pm V_C)/T_\pi} - 1) \tag{2.29}$$

where T_π is the slope parameter for the initial pion distribution. Note that the initial pion ratio, R_i, is defined to be $R_i = A^+/A^-$. Remember, the Coulomb source, too, is expanding with the pions and the source potential is further modified to incorporate the reduced magnitude of the potential. The effective potential can be calculated as a function of pion momentum by integrating the proton emission function up to the maximum kinetic energy corresponding to the selected pion velocity,

$$E_{\max} = \sqrt{(m_p p_\pi / m_\pi)^2 + m_p^2} - m_p \tag{2.30}$$

to obtain,

$$V_{\text{eff}} = V_C(1 - e^{-E_{\max}/T_p}) \tag{2.31}$$

where T_p is the slope parameter for the Maxwell-Boltzmann-like proton distribution. In this analysis, the effective Coulomb potential, V_{eff}, and total yield pion ratio, R_f, are the free parameters while the rapidity window, pion slope parameter and proton slope parameter are held fixed. Further details can be found in Chapter 4.

Chapter 3

The STAR Experiment

3.1 Introduction to the STAR Experiment

STAR is an acronym for the Solenoidal Tracker At RHIC (Relativistic Heavy Ion Collider). The detector consists of several subsystems designed to track and measure the momentum, energy, velocity, and position, as well as many other observables, of thousands of particles at the top RHIC energy of 200 GeV per nucleon pair for Au+Au collisions [122–139]. At the time of construction, STAR had the largest time-projection chamber in the world [137].

Though always improving, STAR has subsystems like an electromagnetic calorimeter and shower maximum detector surrounding the barrel and one end of the cylindrical time-projection chamber, a resistance plate time-of-flight system, muon telescope detectors, beam-beam counters, a vertex position detector, time-projection chambers for the forward region and a powerful iron magnet surrounding the three-story facility, see Figure 3.1. The TPC acts like a digital camera capturing an image of a collision a few nanoseconds following a collision. The following chapter will discuss in detail some of these subsystems from theory and design to application.

3.2 The Time Projection Chamber

This subsystem identifies emitted charged particles based on ionization energy loss and measures the full track position to obtain a momentum for each of these particles. STAR's

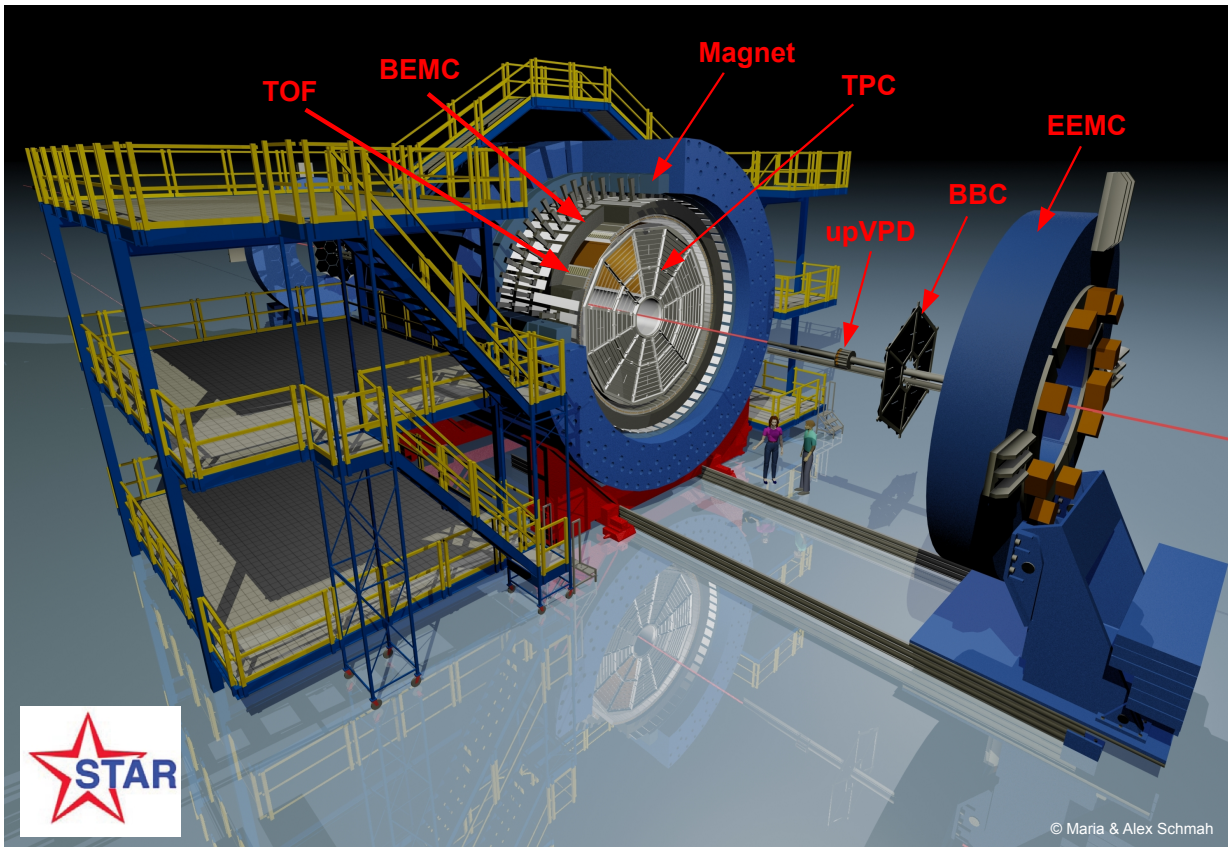

Figure 3.1: An illustration of the full STAR experiment. The two people at the bottom right near the bare electronics platforms are for scale. Most of the detector subsystems are included for the 2011 configuration of the experiment, including the: Time Projection Chamber (TPC), Barrel Electromagnetic Calorimeter (BEMC), End-cap Electromagnetic Calorimeter (EEMC), Time of Flight and Vertex Position Detector (TOF and upVPD), Beam-Beam Counter (BBC), and Magnet [140].

Time Projection Chamber, or TPC, is a cylindrical cavity filled with P-10 gas (90% Argon and 10% Methane) and has a well-known drift velocity of 5.1 cm/μs. Either end of the cylinder has high-voltage anodes in multi-wire proportional counters for read-out. At the center of the chamber is a 70 μm thin membrane cathode made of carbon loaded Kapton film. A schematic is shown in Figure 3.2 below.

The TPC has a pseudo-rapidity coverage from $|\eta| < 1.8$ with full 2π azimuthal coverage in the center-of-mass frame. It measures 2.0 m in radius and 4.2 m in length. The central membrane (CM, labeled "high voltage membrane" in the figure) cathode, held at -28 kV, separates the two main sections of gas volume, and straddles the center of one concentric field

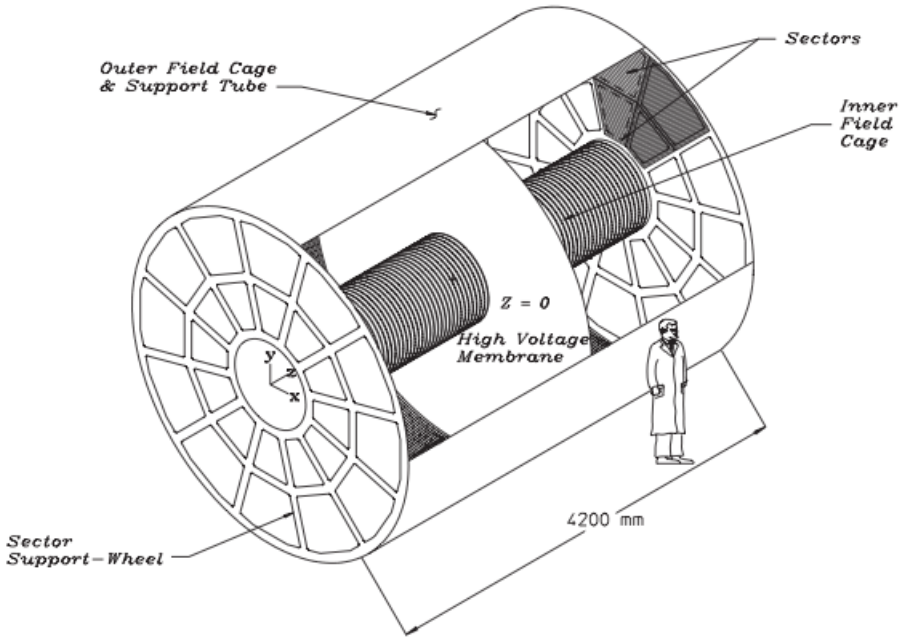

Figure 3.2: The time-projection chamber. A schematic picture of the TPC at STAR.

cage cylinder. The field cage ensures the uniformity of the electric field, a critical component to ensure a constant drift velocity, from the CM to the grounded plane of wires at the end caps. At both ends are Multi-Wire Proportional Counters (MWPCs) which consist of anode wires, each 1390 kV for outer sectors and 1170 kV for inner sectors, a plane of grounded wires and a gating grid of wires.

STAR's MWPC (see Figure 3.3) is like a typical MWPC: anode wires are protected by the gated grid of wires and are oriented to obtain the maximum resolution for higher-momentum tracks. Drifting electrons avalanche quickly near the anode wires with a uniform avalanche distance to induce an image charge on cathode pads. The pad plane is designed so that the maximum induced charge from the anode wires covers up to three pads. This allows for a three-point Gaussian fit or weighted mean and good determination of the centroid, thus a better resolution of the primary ionization position. Distances between the anode plane and pad plane are optimized to match the diffusion width of the drifting electrons in order to

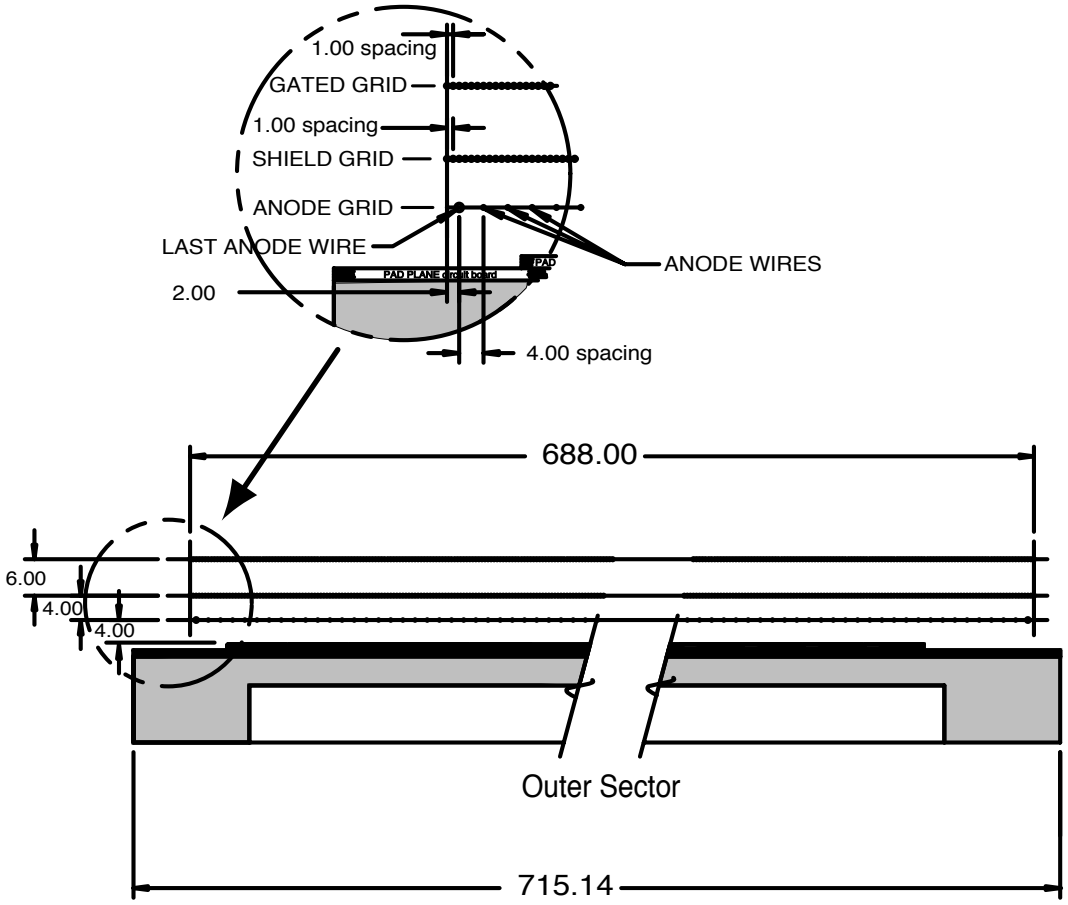

Figure 3.3: The time-projection chamber MWPC. A cutaway view of an outer sub-sector pad plane. The cut is taken along a radial line from the center of the TPC to the outer field cage so the center of the detector is towards the right hand side of the figure. The figures shows the spacing of the anode wires relative to the pad plane, the ground shield grid, and the gated grid. The bubble diagram shows additional detail about the wire spacing. The inner sub-sector pad plane has the same layout except the spacing around the anode plane is 2 mm instead of the 4 mm shown here. All dimensions are in millimeters.

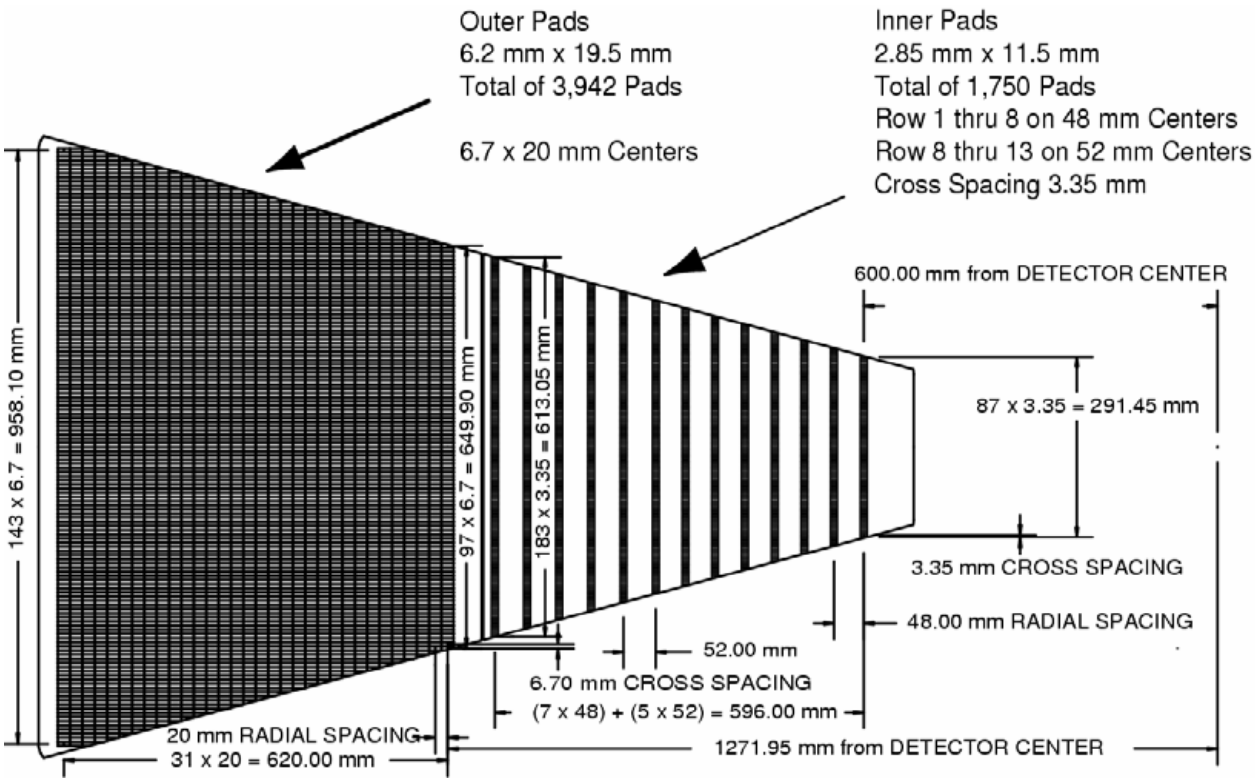

Figure 3.4: The time-projection chamber sector diagram. The anode pad plane with one full sector shown. The inner sub-sector is on the right and it has small pads arranged in widely spaced rows. The outer sub-sector is on the left and it is densely packed with larger pads.

give the best signal-to-noise ratio without compromising two-track resolution.

Inner sectors are specifically designed for the optimum two-hit determination–small pads arranged in widely spaced rows–while outer sectors are designed to best define the $\frac{dE}{dx}$ resolution–the densely packed larger pads. A full sector is illustrated in Figure 3.4 where the inner sector is the right-hand side of the figure and the outer sector is the left-hand side of the figure. All measurements are in millimeters.

Since the ionization electrons must traverse a 2.1 m drift volume, minimal diffusion is necessary for spatial precision measurements. The magnetic field plays two roles; aiding in minimal diffusion is one of them. The second role for the magnetic field is to bend charged particle tracks for momentum measurements. For a more detailed discussion of the magnet see reference [139]. Momentum measurements rely on the uniform field of a solenoid magnet to track a particle's curvature through the gas-filled chamber. At full-field, the magnetic field

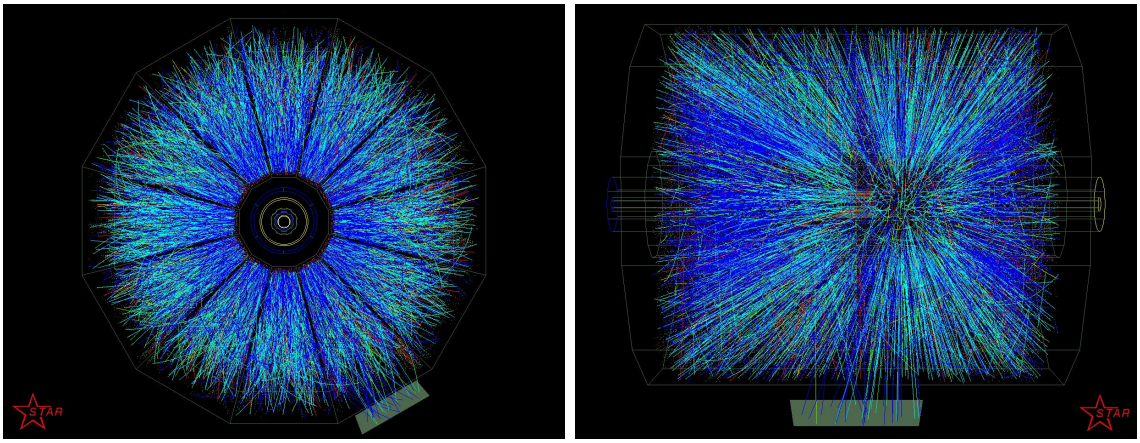

Figure 3.5: An example of event reconstruction using the STAR TPC from a central $Au + Au$ collision during the first run at RHIC. The left-hand panel illustrates a view looking down the beam line (the z-direction going into the page). One can clearly see the sectors of the TPC as well as the inner field cage dimension. The light-color shaded box is one RICH detector module installed at the time. The right-hand panel is a side view of the same event where the beam line is the horizontal. Again, the light-color shaded box is the RICH module. Track color represents the particle's energy loss with dark blue being smallest and red being largest.

measures 0.5 T and allows for measurements with transverse momentum $p_T > 100$ MeV/c.

3.2.1 Event Reconstruction

The TPC read-out system obtains electron ionization cluster information in 512 time buckets (which with a weighted average yields the z-position) and by the charge measured on adjacent pads in a single pad row (yielding the x- and y-position). In this way, measuring energy loss and tracking position, the TPC acts like a digital camera, capturing the trajectories of thousands of particles at once (up to 1,000 particles per unit of pseudorapidity at full RHIC energy of $\sqrt{s_{NN}} = 200$ GeV). At the very first stages of data acquisition after amplification, shaping and digitization, ADC and TDC values are converted to hits. From hits to global tracks, any reconstructed track that happened to be read-out in the TPC at the time of triggering, an algorithm spins over the hit information many times; first it creates tracklets (small track segments of only a few hits each) as candidates for a track and then fits again with an algorithm that keeps —or rejects — hits depending on their position with respect to the overall fitted track. At this point, a pion mass is assumed and Coulomb scattering

as well as energy loss are corrected for when creating these tracks. At the end of the tracking algorithm, all global tracks have information regarding their position and 3-momenta defined and stored. An example of event reconstruction using the STAR TPC from a central $Au + Au$ collision during the first run at RHIC can be seen in Figure 3.5. The left-hand panel illustrates a view looking down the beam line (the z-direction going into the page). One can clearly see the sectors of the TPC as well as the inner field cage dimension. The light-color shaded box is one Ring Imaging Cherenkov (RICH) module installed at the time. The right-hand panel is a side view of the same event where the beam line is the horizontal. Again, the light-color shaded box is the RICH module. Track color represents the particle's energy loss with dark blue being smallest and red being largest. At this point, tracks are used to find vertex candidates with the Vertexer, or vertexing algorithm, which nominally looks for at least five tracks within a 1.5 cm radial and 3 cm long cylinder to converge. With a ranking system in the Vertexer, the tracks are utilized to find probable collision vertices, or primary vertices.

For the BES energies, possible vertices are formed from two tracks rather than five and global tracks are associated with primary vertices when its helical trajectory distance in the z-direction is within 6 cm and its radial distance is within 6 cm of the vertex location (these values are modified from the full energy values of 3 cm and 1.5 cm respectively) which will be discussed in Section 4.2. Once a global track has been associated with a primary vertex, the track is re-fit with the additional point of the primary vertex on the helix to obtain a "new" momentum. By including the vertex position in the fit for primary tracks the resolution of the momentum is highly improved [141]. These new helices are then dubbed primary tracks and all their information is stored in the primary track collection of the event's container. As expected, the vertex resolution decreases with the number of tracks used in the calculation and the vertex resolution is 350 μm when there are at least 1,000 tracks associated with that vertex.

Often there are many primary vertices found in a given "event" and the Vertexer algo-

rithm ranks the found vertices by likelihood that that vertex is the one which satisfied the trigger requirements and caused the readout of all the detector subsystems. Additional discussion of the Vertexer and its performance during the BES data acquisition will be discussed in Section 4.2.

3.2.2 Particle Identification (PID) of the TPC via dE/dx

Particle identification (PID) in the TPC is based upon the energy that particle has lost in the active gas volume. Energy loss for particles with low momentum is highly correlated with mass, but the differentiation between particle species (mass dependence of energy loss) blurs as the particle's momentum increases to $v > 0.7c$. The energy loss of a particle traversing a medium is characterized by the Bethe-Bloch formula [39],

$$-\frac{dE}{dx} = Kz^2\frac{Z}{A}\frac{1}{\beta^2}\left[\frac{1}{2}\ln\left(\frac{2m_e c^2\beta^2\gamma^2 T_{\max}}{I}\right) - \beta^2 - \frac{\delta^2}{2}\right] \tag{3.1}$$

where K is a constant, z the intrinsic particle charge, Z the charge of the medium, A the atomic mass of the medium, $\beta\gamma = p/mc$ with p the momentum c the speed of light in vacuum and m the mass of the particle, m_e the electron mass, $T_{\max}$ the maximum kinetic energy that can be given to a free electron in an interaction, I the average ionization energy of the material, and δ is a correction based on the electron density. The energy loss of a particle as it traverses the active volume of the STAR detector is specifically characterized and parameterized with the Bichsel functions [142] [143] which are used in this analysis. Equation 3.1 illustrates the mass and momentum dependence of the energy loss as charged particles traverse any medium while the equations in references [142] and [143] are extensions of the Bethe-Bloch formula specific to the STAR detector.

With the design of the TPC sectors, a particle traversing the entire gas volume of the TPC would obtain 45 padrow hits for energy loss measurements. The mean of the measured charge clusters is highly sensitive to the fluctuations in the tail of the distribution. Thus, only

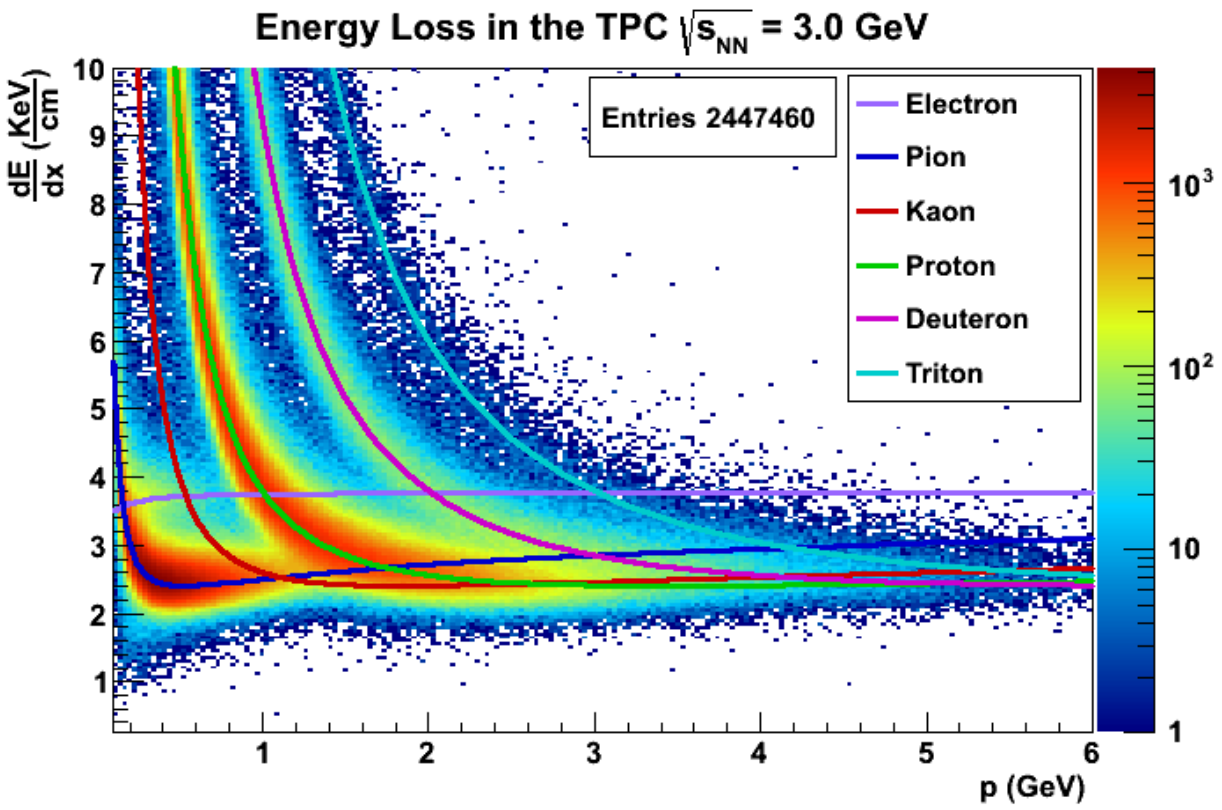

Figure 3.6: Ionization energy loss as a function of momentum. Colored lines are the theoretical predictions of the specified particle's Bichsel function while the scatterplot bands represent the actual measured dE/dx values.

70% of each track's charge distribution is used for defining the average ionization energy loss for data analysis. Particle distributions for dE/dx as a function of momentum is illustrated in Figure 3.6. Clear particle separation can be seen for pions and kaons up to approximately 750 MeV/c while protons and anti-protons can be identified up to about 1.0 GeV/c. The colored lines represent the theoretical predictions of the Bichsel functions while the scatterplot bands represent the actual measured dE/dx values. Proton and deuteron bands also have contributions from interactions with the beam pipe and other inner material of the experiment. Decays of pions and kaons contribute to the muon band. Additionally, common neutral particles also decay to contribute to the pion and/or proton bands, like the K^0_S and Λ particles.

3.3 The Time Of Flight Detector

The Time Of Flight (TOF) detector is a set of multi-gap resistive plate chambers (MRPC), and two standard scintillation detectors. Its purpose is to extend the direct particle identification capabilities of STAR out to 1.9 GeV/c for pions and 3.1 GeV/c for protons. The 120 trays of MRPCs cover the full azimuth of STAR and have a pseudorapidity coverage of $-1 < \eta < 1$.

The scintillation detectors, called pseudo-Vertex Position Detectors (pVPD) sit outside the STAR magnet on the east and west ends of the detector arrangement, as shown in Figure 3.7. These instruments are very close to the beam-pipe and serve the purpose of detecting the very high-energy, very forward emitted photons from particle collisions. The fast pulse these photons produce in the pVPD effectively serve as the "start time" of the TOF detector with an overall resolution of 24 ps (58 ps resolution for the pVPD single detector) for $p+p$ collisions and 140 ps for $Au+Au$ collisions.

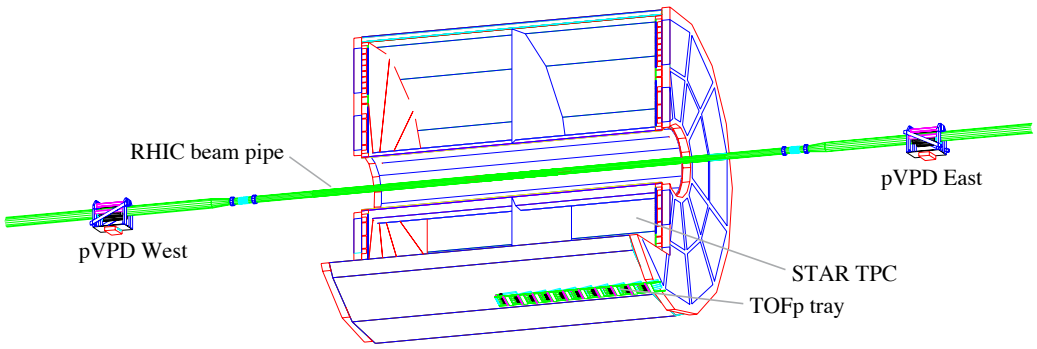

Figure 3.7: The pVPD position. A cut-out of the STAR detector identifying the position of the pVPD portion of the time-of-flight detector subsystem. Both pVPD devices are identical in construction and occupy positions near the beam pipe at approximately 5.6 meters from the interaction region.

Each of the six pVPD assemblies are constructed with a front "cap" of magnetic shield, an air gap, an approximately 1 cm-thick layer of Lead (∼1 radiation length), a 1/4"-thick layer of scintillator, a PMT, and a linear resistive base, very reminiscent of a flashlight design [144]. Figure 3.8 illustrates the assembly construction where a particle would be incident on the left and electronic read-out would occur on the right. Three of these assemblies are arranged as in

Figure 3.9 and attached very near the beam pipe at ±5.6 meters from the defined detector center. The configuration in Figure 3.9 covers approximately 19% of the pseudorapidity inverval $4.43 < \eta < 4.94$.

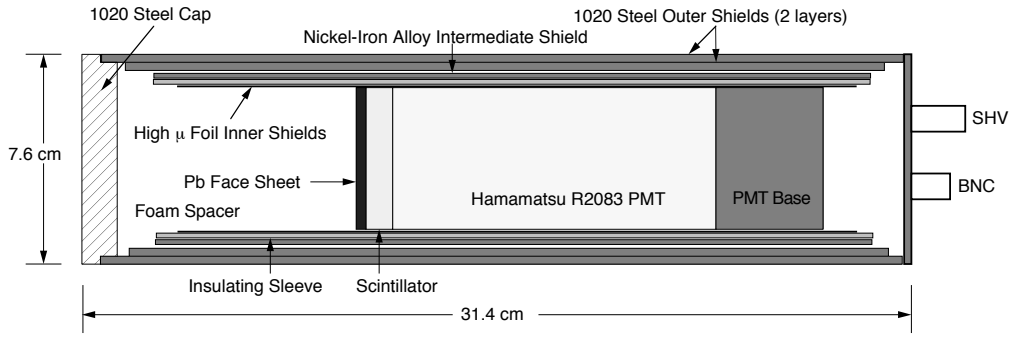

Figure 3.8: The pVPD construction. A cutaway of the detector assembly for the pVPD. This design construction was used for all six modules.

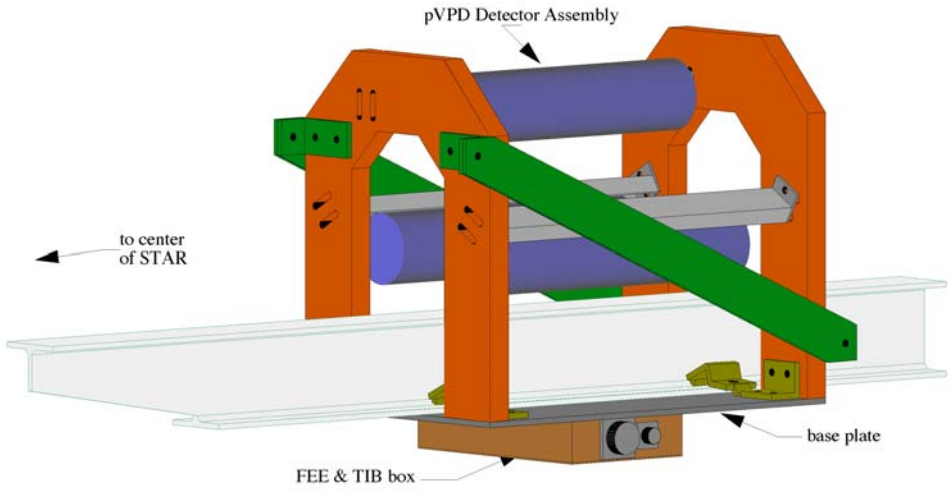

Figure 3.9: The pVPD full assembly. A schematic of the pVPD attachment to the beam pipe. This construction is identical for both pVPDs on the east and west sides.

Typical resistive plate chambers (RPC) consist of parallel plates in a gaseous mixture with resistive electrodes. The resistive electrodes serve to quench streamers (the ionized region brought about by the strong field of the avalanche electrons) so that they do not initiate a spark breakdown and thus allows RPCs to operate at much higher gains in avalanche mode. Because RPCs could first be used inexpensively for muon detection capabilities with large-area coverage, the technology was expanded to extend their application to a time-of-

flight system [145] [146]. At first, the size of the gap between plates was expanded from 2 mm, the typical gap size, to 6 or 8 mm. With the larger gap, gap tolerance is less critical; additionally a light gas can be used instead of a highly electronegative gas like freon. The advantage to using light gases is the elimination of high charges (ionic currents) produced in the gas gap allowing for an increase in the firing rate. Unfortunately, with the larger gap, there is worsening of timing resolution. The next incarnation of RPCs was a multi-gap system where the outer plates have the electrodes attached and the inner plates create small 2 to 3 mm gaps. In this way, we obtain all the advantages given by the wide-gap RPC with the timing resolution of the small gap RPC.

A through-going particle produces individual and separate clusters of primary ionization; each of these clusters will start an avalanche and the final signal will be the sum of all the avalanches. In the MRPC there is a strong feedback mechanism that forces the gas gain to be equal in all subgaps. The sheets of resistive material, electrically floating and transparent to the fast signals generated by the avalanches, allow the simultaneous readout of many subgaps, and then the signal is truly the sum of independent avalanches (the charge spectrum has a Γ shape, similar to a Landau distribution). The avalanches occur in independent subgaps. Then each avalanche — at least one per subgap, depending on the gas mixture — accumulates the same charge.

At STAR, the MRPC, or TOFr, consists of a stack of resistive glass plates arranged in parallel with the uppermost and lowermost plates extending further in width than the intermediate plates, see the lower schematic in Figure 3.10. Attached to the outer plates are electrodes which, when a high voltage is applied, produce a strong electric field between all the intermediate plates. The intermediate plates create a series of gas gaps by initially obtaining the voltage as defined by electrostatics, but are kept at the correct voltage by the flow of electrons and ions produced in the gas via avalanches. We operate these devices in avalanche mode, with a non-flammable gas mixture which contains 90% of tetra-fluoro-ethane ($C_2H_2F_4$); 5% of iso-Butane and 5% of SF_6 [147].

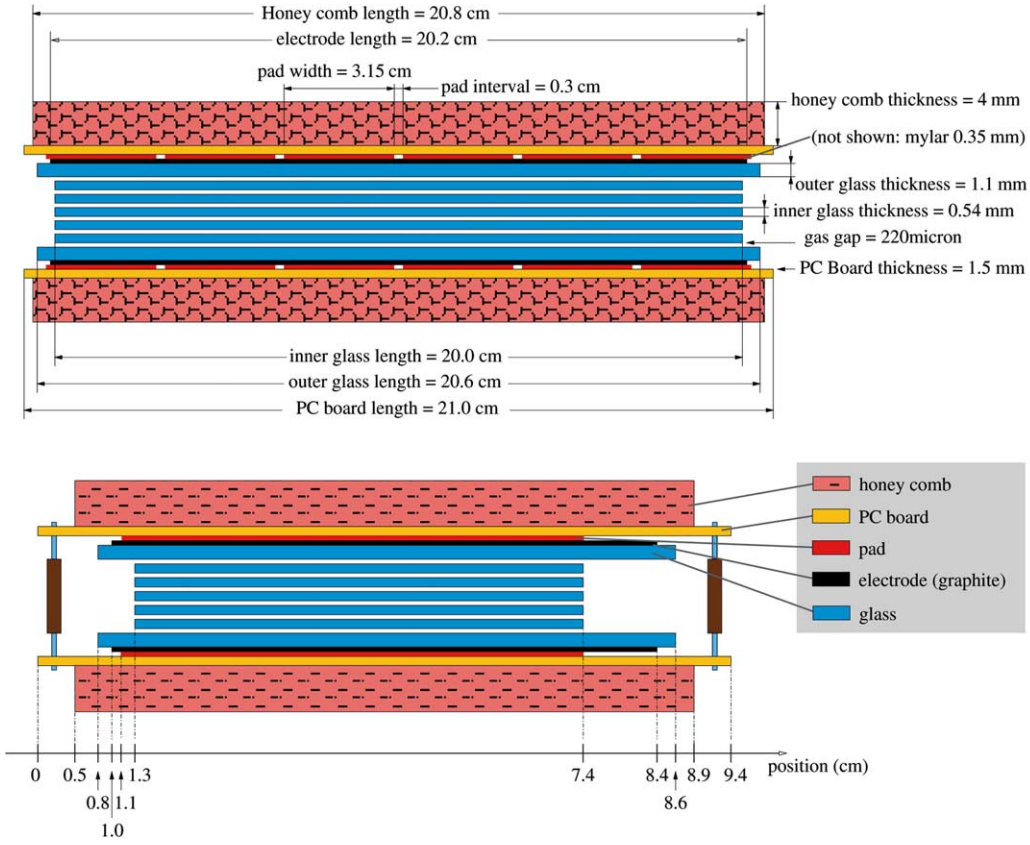

Figure 3.10: Detailed cut-out of TOFr trays. A schematic picture of the TOFr tray assembly where the upper picture depicts the length of the tray and the lower picture depicts the width of the tray. These pictures are not of the same scale.

3.3.1 Particle Identification (PID) of the TOF via $1/\beta$

Timing information from the pVPD (the "Start" time) and the TOFr trays (the "Stop" time) in addition to information about the track length from the TPC allows for the calculation of the velocity of the particles.

$$\beta = \frac{L}{tc}$$

With this velocity and the momentum measurement, also from the TPC, a calculation of the square of the mass, m^2, of each particle can be made.

$$m^2 = p^2(\frac{1}{\beta^2} - 1)$$

This method is the direct identification of hadrons via a calculation of the mass that the TOF detector allows us to do. Figure 3.11 shows the $1/\beta$ distribution from TOFr measurements as a function of momentum, p, as calculated by the TPC tracking algorithm. The small plot in the upper right indicates the Gaussian-like distribution of particles in m^2 in a given transverse momentum region, $1.2 < p_T < 1.4$ GeV/c. Raw yields of identified hadrons are obtained from Gaussian fits to these distributions in $1/\beta$ for each p_T bin. Calibration of each MRPC's timing is completed first by correcting for differing cable lengths for different read-out channels and then using a pure pion sample selected from a well-separated region of energy loss, $dE/dx < 0.028 \times 10^{-4}$ GeV/cm in the momentum range $0.3 < p < 0.6$ GeV/c in order to shift the mean value of the overall distribution to zero, channel by channel, assuming that every particle was a pion. Following this, a slewing correction is made to correct for a correlation between the timing and signal amplitude of the electronics and finally a z-position correction is made since there is a transmission timing dependence on the position of hits on the read-out strip [148].

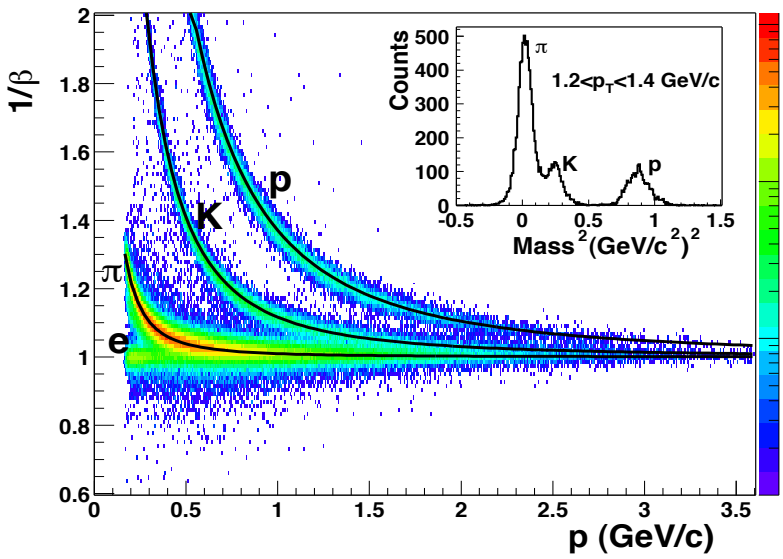

Figure 3.11: Particle Identification using TOF. The $1/\beta$ distribution from TOFr measurements as a function of momentum, p, as calculated by the TPC tracking algorithm. The small plot in the upper right indicates the Gaussian-like distribution of particles in m^2 in a given transverse momentum region, $1.2 < p_T < 1.4$ GeV/c.

3.4 The Trigger Detectors

3.4.1 Beam–Beam Counters

The BBCs were designed to be the triggering system for $p + p$ collisions but also have use in other areas. Specifically, they can reject beam gas events, measure absolute luminosity with 15% precision, and measure relative luminosities of different proton spin orientations with high precision. The timing difference between the east BBC and west BBC can also be used to measure the primary vertex position. Additionally, the small tiles in the array illustrated in Figure 3.12 and described below are used to reconstruct the first-order event plane for directed-flow analysis.

The BBCs are scintillator annuli mounted around the beam pipe outside the pole tips of the STAR magnet, about 3.75 meters from the center of the detector. The BBCs consist of small and large scintillator tiles arranged as in Figure 3.12. The array of small hexagonal tiles complete a ring around the beam pipe with a 9.6 cm inner- and 48 cm outer-diameter, covering a pseudorapidity range of $3.4 < |\eta| < 5.0$. In the center of this ring, marked B

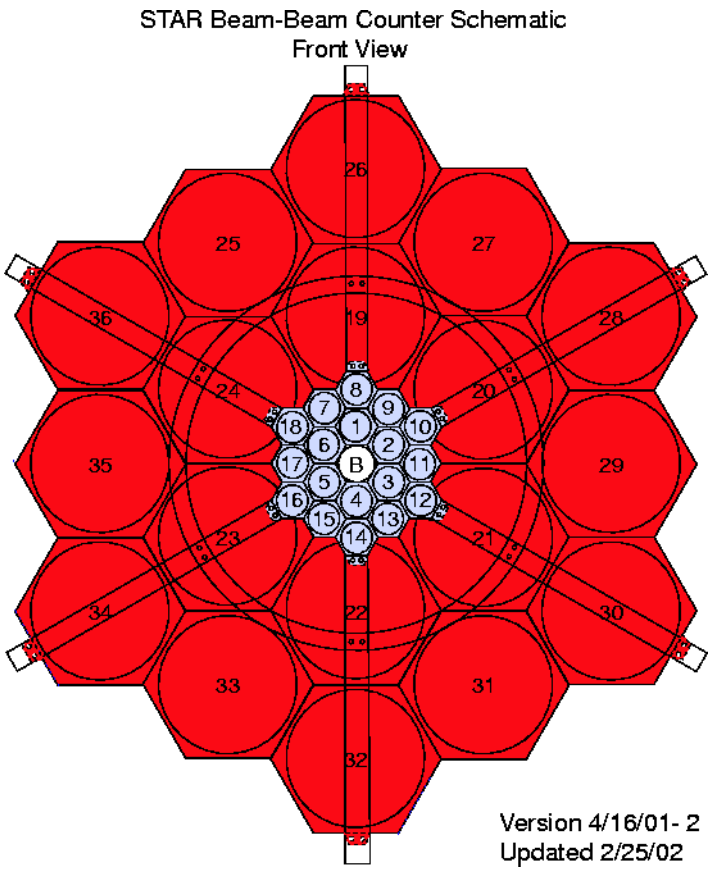

Figure 3.12: The BBC scintillator array. Diagram of the BBC scintillator array.

in Figure 3.12 is the beam pipe. Completing a ring around the small tile array is an array of large hexagonal tiles with an inner-diameter of 38 cm and an outer-diameter of 193 cm covering a pseudorapidity range of $2.1 < |\eta| < 3.6$. Each scintillator tile has four wavelength shifting optical fibers inside of grooves which were inscribed onto the hexagonal scintillator. Charged particles traversing through the BBCs produce light in the tiles and these fibers collect the scintillation light. Both BBCs were required to fire to trigger minimum bias $p+p$ collisions.

3.4.2 Zero Degree Calorimeter

Placed far to the east and west of the main STAR detector assembly, at ± 18 meters from the detector center and at 2 milliradians relative to the beam axis, are the Zero Degree

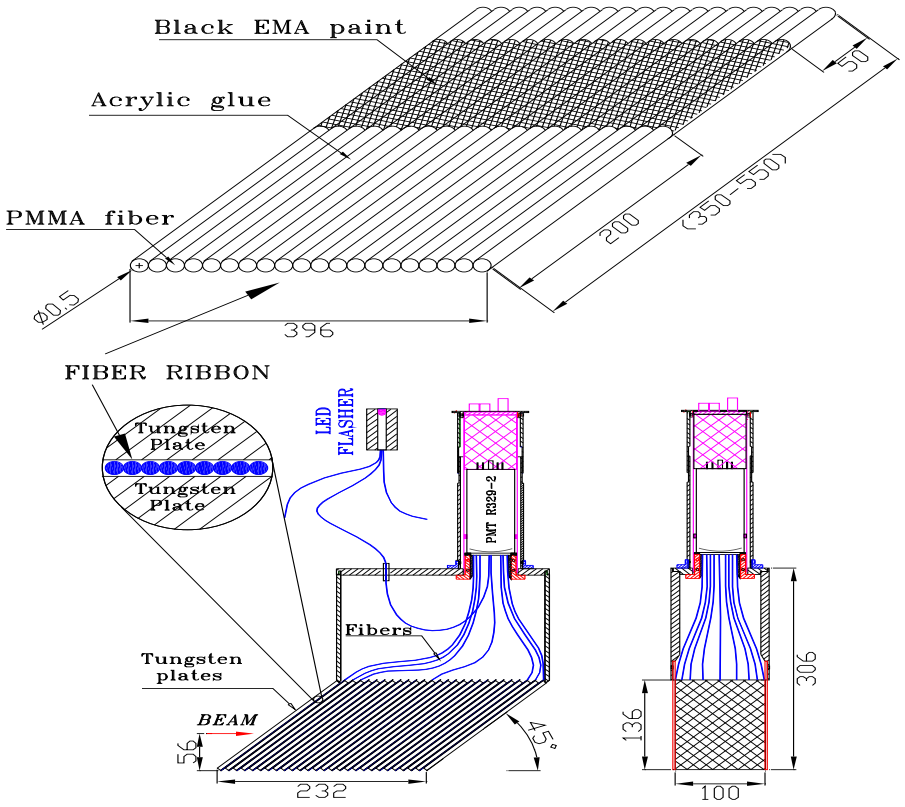

Figure 3.13: ZDC module construction. Mechanical design of the production Tungsten Modules. All dimensions are in mm.

Calorimeters (ZDCs). The purpose of the ZDCs is to detect neutrons emitted within this cone along both beam directions and measure their total energy (from which we can calculate multiplicity) [149]. These detectors are hadronic calorimeters designed to measure very far forward neutrons that did not participate in the nuclear collision, also called spectator particles. Since the dipole magnets of RHIC, just upstream along the beam line, will bend the charged spectator fragments away from the ZDCs, the neutral fragments are what the detectors measure; these are neutrons.

Both ZDCs are comprised of three identical 50 χ_0 long hadronic calorimeter modules, see Figure 3.13. Each module consists of a series of tungsten plates alternating with layers of wavelength shifting fibers which are connected to a PMT. Additionally each module has a Shower Maximum Detector (SMD) consisting of two layers of scintillator planes, one in the horizontal direction and the other in the vertical direction. The SMD mainly identifies the

position of the neutral particles that initiate hadronic showers. These ZDC modules were designed to minimize the loss in energy resolution due to shower leakage [149].

The ZDCs provide centrality determination as well as triggering. The ZDC coincidence of the two beam directions is a minimal bias selection of heavy ion collisions. This makes it useful as an event trigger and a luminosity monitor [150] and for this reason identical detectors were built for all four RHIC experiments. The neutron multiplicity is also known to be correlated with event geometry [151] and will be used to measure collision centrality in mutual beam interactions [149].

3.5 Software and Detector Acceptance and Efficiency

3.5.1 TPC Tracking Efficiency

The tracking efficiency is highly dependent on the acceptance of the TPC since tracking is completed with information from the TPC alone. Spatial gaps in the active region — creating dead zones — as well as electronic efficiency and two-hit resolution all contribute to the inefficiency of measuring tracks in the detector. Additionally, any software cuts implemented also reduce the efficiency of detecting tracks in the active zones. The dead zones of the TPC, like gaps between sectors where wires must pass or isolation gaps between pads to distinguish them, are necessary features for data collection, and its accuracy in some cases. These physical gaps contribute ∼4% to the overall inefficiency of the TPC tracking. Software cuts that neglect the leading edge of an induced charge on the outer-most two pad rows as well as dead channels and number of hit requirements on tracks contribute to the inefficiency. Since a leading edge falling on either of the two outer-most pad rows would not have the symmetry of additional pad rows to complete a three-point Gaussian weighted fit, they are only used for constructing hits when the symmetry is present; this contributes ∼2% loss in tracking efficiency. Software cuts on hit number prevent broken tracks from being included in the track count but sacrifice tracks with a small angle with respect to the beam

axis as well as low-momentum tracks that spatially curl too much inside the TPC, due to the strong magnetic field, to obtain more than a few hits.

Dead channels may arise during data collection that cannot be reconfigured, mended or replaced until after the full run time of the RHIC accelerator. These issues may be caused by bad hardware, a blown soldering joint, loose cables, software loss of communication or a number of other issues that do not allow experts to easily bring sections of a detector back online. The number of dead channels is a dynamic aspect of the detector but usually contributes no more than $\sim$1% loss to the tracking efficiency.

Analyses attempt to correct for these inefficiencies by the embedding process. By taking simulated tracks and embedding them in real events and then sending these events through the reconstruction software we quantify a tracking efficiency based on the qualities of a real event. The qualities that may affect this efficiency include ionization, the inner material budget, track density, electron drift, gas gain, signal collection, dead channels, electronic amplification and noise. Specific energy and centrality efficiencies for this analysis will be discussed in Sections 4.3 and 4.4.

3.5.2 TOF Matching Efficiency

A key aspect of utilizing the TOF information is to ensure that a hit in the TOFr trays matches with a track in the outer edges of the TPC active volume. Making this match allows for the momentum of the particle to be associated with a flight time, and thus to obtain $1/\beta$ or the particle mass. Without matching a TOFr tray hit to a track in the TPC, these track variables cannot be determined. Each of the trays has a series of pick-up pads, approximately six per tray see Figure 3.14, to which a track may be associated. Three types of associations are possible: one TPC track to one TOFr hit, multiple TPC tracks to one TOFr hit, and one TPC track to multiple TOFr hits. Only TPC tracks with associations of the first and last type are considered in this analysis. This selection leads to additional efficiency losses since not only are we including the efficiency of finding a track in the TPC,

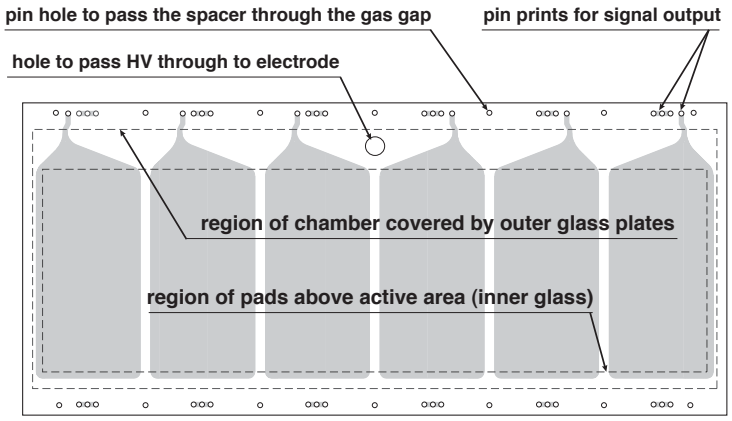

Figure 3.14: TOFr tray pick-up pad layout. Note the shape of each of the six read-out strips, or pick-up pads, for each MRPC.

but also if that track falls in the acceptance of the TOF as well as if it can be substantially associated with the proper tray hit. There are differences in matching efficiency as a function of momentum and particle species, but the overall peak efficiency is around ∼60%. Further discussion of TOF matching efficiency for specific particle species, centrality and energy will be in Sections 4.3 and 4.4.

Chapter 4

Analysis Methods

4.1 Introduction

Utilizing the RHIC ring during the Beam Energy Scan (BES) pushed the accelerator into energy regimes for which it was not designed. Many modifications to run-time operations as well as data processing were made to allow for the accurate recording of data. One importnat change to a major component of data processing—vertex analysis and the algorithm to find vertices in recorded events—is discussed in this chapter followed by the unique interpretation of the STAR detector geometry and collision geometry for fixed target analysis. Lastly, methods for analyzing traditional Au+Au events at $\sqrt{s_{NN}} = 19.6$ GeV are presented.

4.2 Modifications to the STAR Vertexing Algorithm

An accurate primary vertex location is necessary for the determination of many physics variables in collisions of any species. It is important to reconstruct a vertex in a given event which corresponds to the collision(s) that caused the read-out of all detectors (fire the trigger) associated with that event, in order both to properly analyze the results and to determine the integrated luminosity for the triggers. The challenge is with a high luminosity environment in addition to a long detector read-out time (between bunch crossings) will cause many pile-up vertices to be recorded in each event.

There are three different types of pile-up that may occur with a long detector read-out

time. First is within bucket pile-up, or any collision which occurs during the same bunch crossing as the event that fired the trigger. Second and third are pre-crossing pile-up and post crossing pile-up where the collisions that are recorded with the collision that fired the trigger are either some bunch crossing(s) before or some bunch crossing(s) after the collision. A cartoon illustration can be seen in Figure 4.1. In each case, the vertex in blue is constructed from the collision that fired the trigger, while the vertex in red is a pile-up vertex. The pile-up collision for 4.1 left-hand panel occurred after the triggered collision (post-crossing), meaning that the tracks associated with the triggered collision had already drifted away from the TPC Central Membrane. When this event is reconstructed, these tracks are connected properly, but the tracks from the post crossing vertex have discontinuities at the Central Membrane. In 4.1 right-hand panel the pile-up collision happened before the triggered collision, so the tracks from that collision had already started to drift down the TPC when the trigger was fired [152].

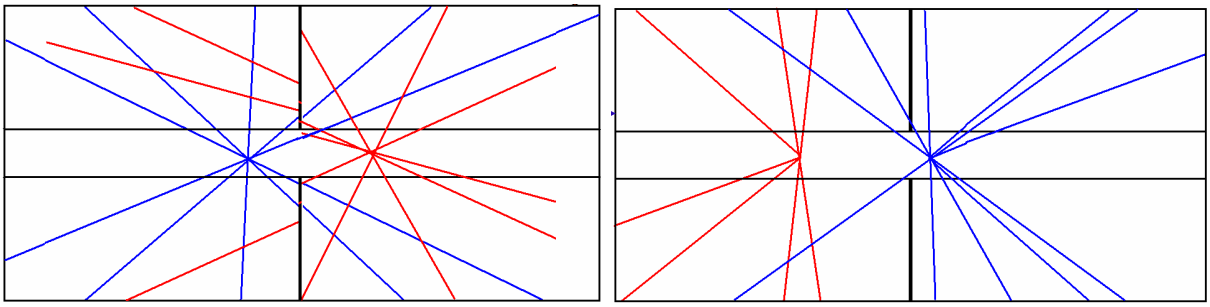

Figure 4.1: Cartoon events showing the way the two different types of pile-up will be reconstructed for a particular event. In each case, the vertex in blue is constructed from the collision that fired the trigger, while the vertex in red is a pile-up vertex. The pile-up collision for the left-hand panel occurred after the triggered collision (post-crossing), which means that the tracks associated with the triggered collision had already drifted away from the TPC Central Membrane. When this event is reconstructed, these tracks are connected properly, but the tracks from the post crossing vertex have discontinuities at the Central Membrane. In the right-hand panel the pile-up collision happened before the triggered collision, so the tracks from that collision had already started to drift down the TPC when the trigger was fired [152].

The STAR vertexing algorithm for ion collisions uses the Minuit minimization technique to find the most probable vertex that fired the trigger. Tracks are used to find vertex candidates with the Vertexer which nominally looks for at least five tracks within a 1.5 cm

radial and 3 cm long cylinder to converge. It then calculates a z-position of this vertex and runs in a loop to find additional tracks within a new cylinder centered around this vertex position. When a track has a DCA (distance of closest approach) within the cylinder, the vertexer associates this new track with this vertex, removes outlier tracks, and re-calculates the z-position to go through the loop again. The algorithm uses several variables to rank vertices: the number of tracks crossing the central membrane, number of track matches to the Barrel Calorimeter (BEMC), and a comparison to an estimation of the average dip angle for vertices with a similar z-location. The dip angle of a track is the angle between that track and the z axis. A collision that is near the edge of the detector will have a number of out-going particles that do not have reconstructed tracks in the TPC because the tracks will not leave enough hits in the TPC. The vertices constructed from these collisions will have an average dip angle that is skewed when compared to a vertex constructed for a similar collision in the center of the detector. The primary vertex is the vertex with the highest rank. All other vertices are saved in order of their vertex rank [152].

For the BES energies, however, the detector systems were bombarded with stray particles from collisions of gold ions upstream with different parts of the accelerator: the beam pipe, gas, bending magnets, flanges, etc. Random coincidences (random pile-up) of these stray particles would sometimes satisfy trigger requirements and cause the read-out of all detectors. The beam halo was large enough and populated enough to have collisions at a measurably high rate, see Figure 4.2. The top plots are vertex distributions far zoomed out, while the bottom set is the same but zoomed in the x- and y-dimensions.

With such a high pile-up environment, it became necessary to study the performance of the traditional vertexer in these even more demanding conditions. Noted during fast offline production — a sneak peak using the last year's calibrations into the data being taken during the current run — were some strange features in well-known distributions like multiplicity and average dip angle. From the studies of the vertexer, we were able to discover that with the tight cuts of the full energy minimization some tracks from the halo collisions

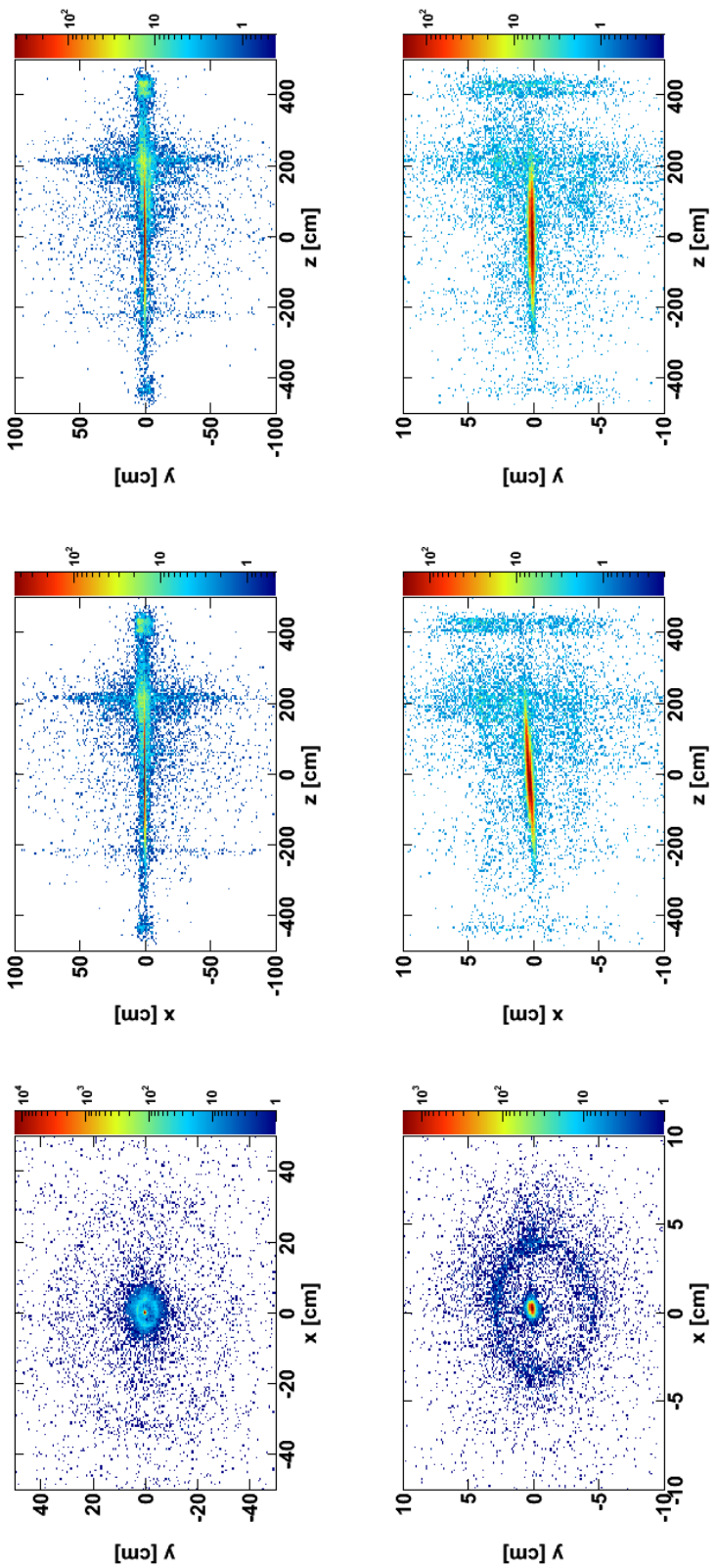

Figure 4.2: Reconstructed Vertex Locations for (R, Z, N) = (6, 6, 2). The left-hand column/top plots are vertex distributions far zoomed out ($|x| < 100$ cm), while the bottom set is the same but zoomed in the $x-$ and $y-$dimensions.

with the aluminum beam pipe were being pulled into good $Au + Au$ vertices, see Figure 4.3. This pulling of tracks and displacing of the beam-on-beam-pipe vertex, or shadow vertex, was skewing the multiplicity, lowering the vertex rank (for having incorrect values of BEMC matches, and CM crossers) and displacing the vertex location causing incorrect recalculations of track momentum.

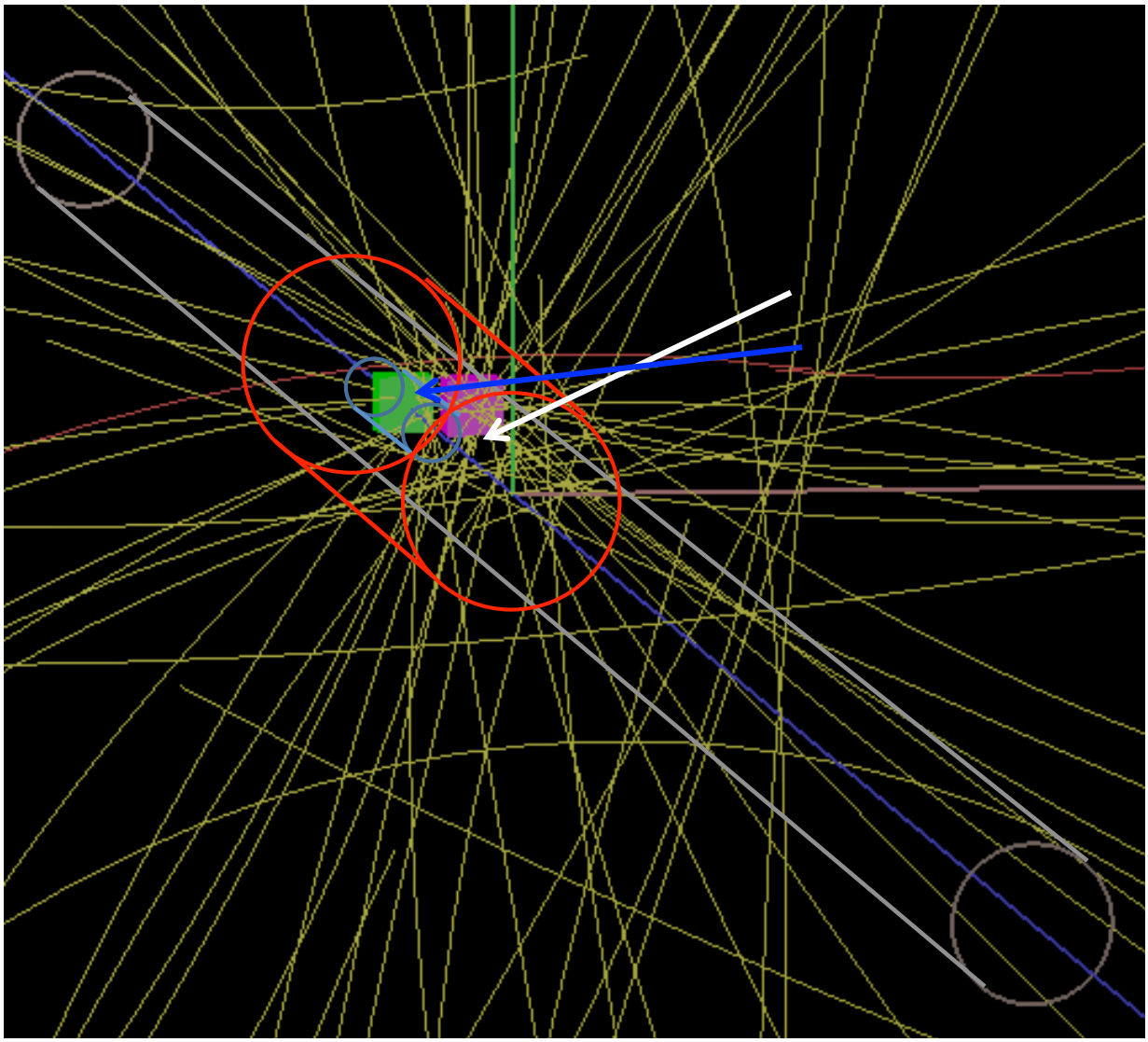

Figure 4.3: A reconstructed event with two vertices. The Blue arrow points to the good $Au + Au$ event. The White arrow points to the $Au + Al$, beam on beam pipe, vertex which has been pulled close to the beamline by the default vertexer parameters: a shadow vertex. Grey illustrates the beam pipe, sea-green the central membrane, the red cylinder the expanded (R, Z, N) = (6, 6, 2) parameter cuts and the smaller light-blue cylinder the default parameters and the indigo line represents the beamline. All deep yellow lines are reconstructed tracks.

(R, Z, N) cm	Number of Vertices	Number of Good Vertices	Index 0	Index 1	Index 2	Index 3	Index 4
1.5, 3, 5	198/3841	75	75	0	0	0	0
6, 6, 5	909/3841	103	88	4	7	2	1
6, 6, 2	1417/3841	139	96	15	17	7	8

Table 4.1: Comparing the three vertexing parameter sets investigated for data production. The radial parameter is indicated first describing the maximum radial distance away from the beam line the vertexer will loop over tracks; then the z-parameter describing how far along the beam line in the positive and negative direction the vertexer will look for tracks; and finally the N parameter describing the minimum number of tracks required to make a vertex. The total number of events analyzed for vertices was 3841 and a "good" vertex is defined as having a radial position within 2 cm of the nominal beam line and a z-position within 30 cm of the center of the detector.

Specifically, the default vertexer loops over tracks within ±3cm from the estimated z-vertex position and within a radius of 1.5 cm. Additionally a minimum of 5 tracks must be present in order for a vertex to be formed. We studied at first, six separate parameter changes to these cuts by expanding the cylinder up to the geometrical location of the beam pipe and reducing the number of tracks necessary to create a vertex. Labels for each of the studies were by their parameters: R — radial distance (1.5 for default, 3 or 6 cm), Z — beam line distance (3 for default or 6 cm), N — number of tracks needed to create a vertex (5 for default or 2). After a preliminary study, only two settings made a significant difference to the default parameters: (R, Z, N) of (6, 6, 5) and (R, Z, N) of (6, 6, 2).

By including the beam pipe in the cylinder to find vertices, the extra tracks that the default vertexer was assigning to good $Au + Au$ collisions could be properly placed with vertices located on the beam pipe. Additionally, the lower track requirement allowed the vertexer to find additional vertices along the beam line that the default would not.

A summary of vertex finding efficiency is found in table 4.1 where the total number of

events analyzed for vertices was 3841 and a "good" vertex is defined as having a radial position within 2 cm of the nominal beam line and a z-position within 30 cm of the center of the detector. The "wide open" cuts (R, Z, N) of (6, 6, 2) are more efficient at finding good $Au + Au$ vertices and placing knock-out events on the beam pipe. Thus for production of the Beam Energy Scan (BES) data all global tracks are associated with primary vertices when the helical trajectory's distance of closest approach (DCA/dca) is within 6 cm of the vertex location in the $\pm z$-direction and out to a radial distance of 6 cm from the nominal beam line.

4.3 Fixed Target Interactions

With the vertexing parameters expanded to place vertices on the beam pipe, data analysis of these collisions — of the Au-like ion beam on the Al beam pipe — could be performed. Ultimately being able to use STAR as a fixed target experiment as well as a colliding beam experiment has allowed the Beam Energy Scan (BES) to reach further into the high baryon chemical potential and low temperature region of the nuclear matter phase diagram.

4.3.1 A Fixed Target Geometry

STAR was built to measure symmetric collisions of separate particle beams, but never intended to measure collisions with fixed targets. By analyzing the data from the ion beam with the beam pipe material, Al, we are pushing the absolute limits of STAR's capability. An example of a reconstructed fixed target collision is illustrated in Figure 4.4. The black rings denote the endcaps of the TPC, the yellow horizontal line represents the beam line, the red vertical line illustrates the position of the central membrane and all the blue and cyan lines are reconstructed tracks where the darker shade represents the part of the track which is extrapolated from the helical fit to the hit points (the lighter shade). As you can see, all of the tracks are directed asymmetrically to one side of the detector, not distributed

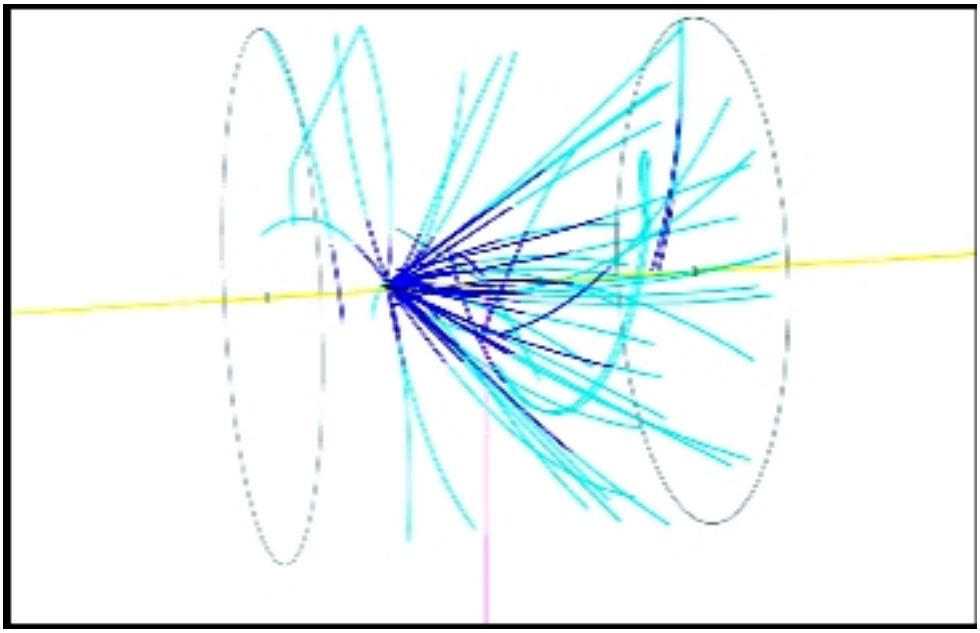

Figure 4.4: An example of a fixed target collision as measured in the STAR detector. The black rings denote the endcaps of the TPC, the yellow horizontal line represents the beam line, the red vertical line illustrates the position of the central membrane and all the blue and cyan lines are reconstructed tracks where the darker shade represents the part of the track which is extrapolated from the helical fit to the hit points (the lighter shade).

in the forward and backward regions as one would expect for a colliding beam event.

In order to ensure that tracks are long and obtain plenty of hit points for decent resolution and dE/dx measurements we need to look at a z-vertex position, V_z, displaced from the center of the detector, and in fact look at the region from 150 cm $< |V_z| <$ 200 cm. When we select for events with this displaced vertex position we have a different geometry for detector acceptance. This geometry is illustrated in Figure 4.5. All detector subsystems are labeled in the diagram, as well as the Al portions of the beam pipe in green and the Be portion in blue. Also in green are sample tracks that illustrate the pseudorapidity acceptance of the TPC and TOF for an event with a vertex at the very edge of the detector.

For the BES energies that we can analyze a significant number of events to obtain particle spectra the highest mid-rapidity we have is $y_{\text{mid}} = 1.5$ for the $\sqrt{s_{NN}} = 4.5$ GeV energy. This data was collected during the $\sqrt{s_{NN}} = 19.6$ GeV energy beams. It is important to note that for the highest energy, we begin losing acceptance in the forward region but have full

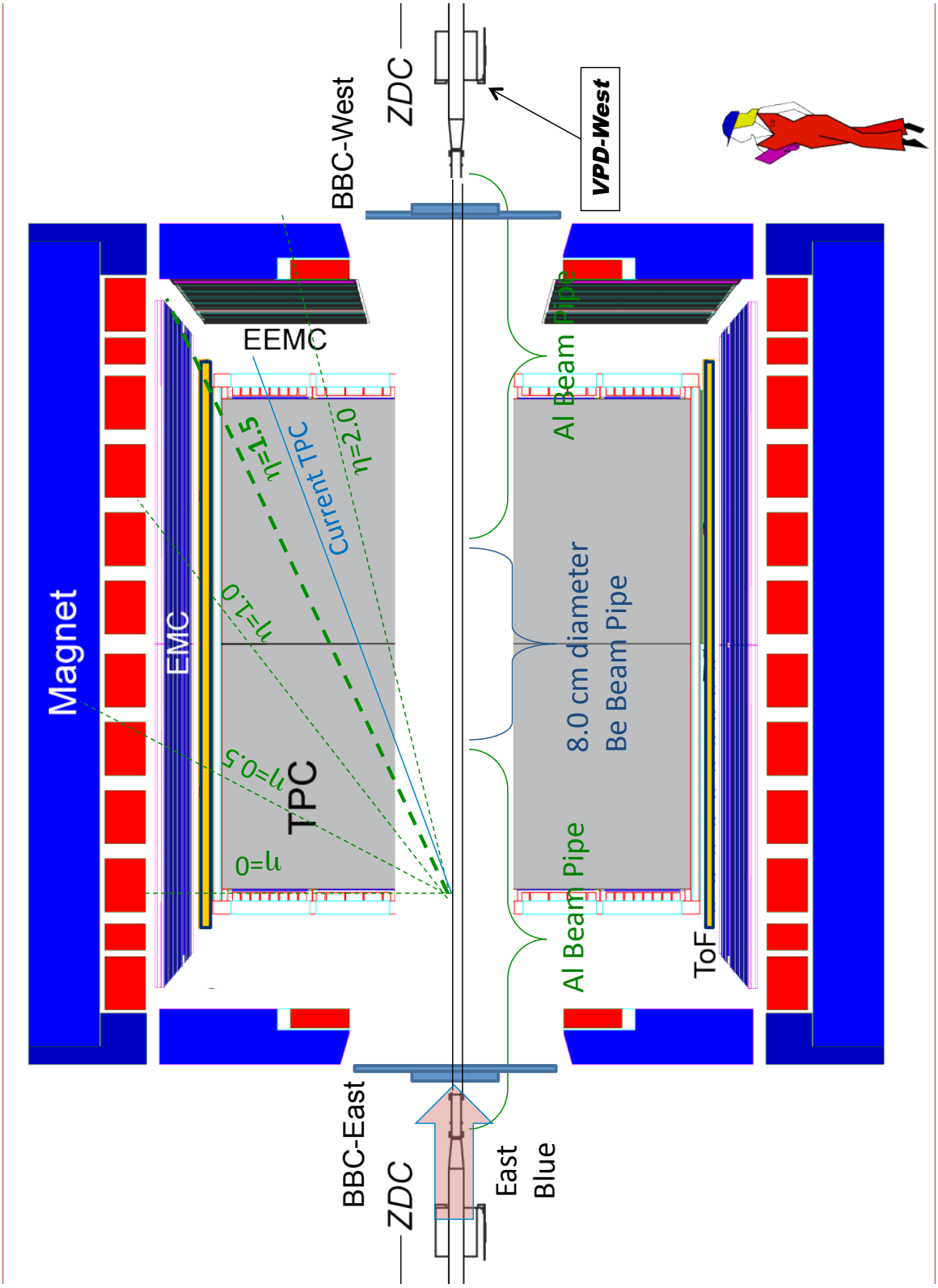

Figure 4.5: The STAR fixed target geometry where all detector subsystems are labeled appropriately, as well as the *Al* portions of the beam pipe in green and the *Be* portion in blue. Also in green are sample tracks that illustrate the pseudorapidity acceptance of the TPC and TOF for an event with a vertex at the very edge of the detector

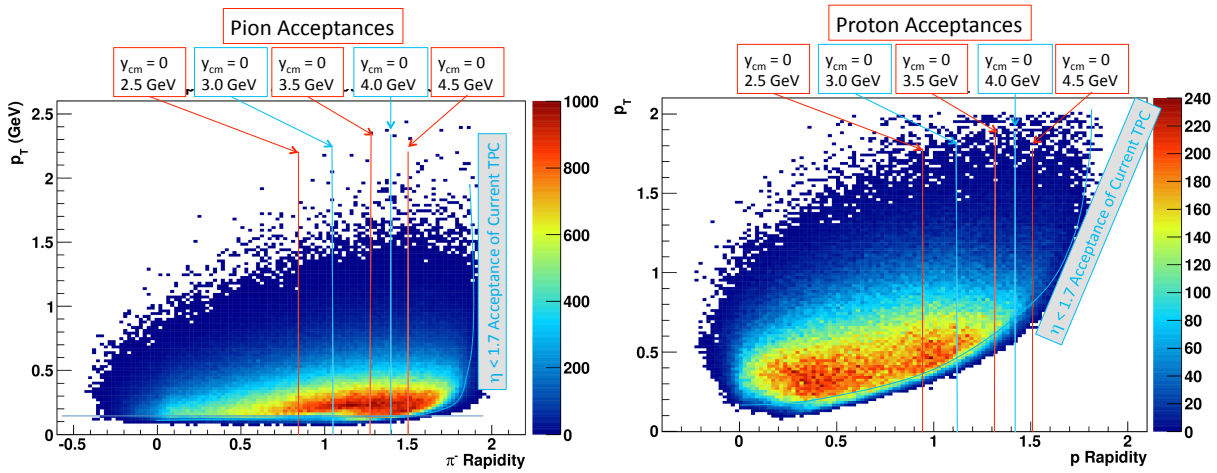

Figure 4.6: Pion (left) and proton (right) acceptance for the STAR fixed target geometry. Note that as the energy of the beam changes, so does mid-rapidity and thus the acceptance of the detector. Pions have relatively uniform acceptance in this geometry. However, protons have a high cut-in that depends on the beam energy. This efficiency loss will affect the ability to obtain a spectrum in the low momentum region.

acceptance from beam rapidity back to target rapidity. For the other energies, we have some acceptance in the forward region, but full acceptance from beam rapidity back to target rapidity.

When changing beam energy in the accelerator, the acceptance of the detector changes as well. This is a feature of a fixed target experiment. Particle acceptances can be seen in Figure 4.6 with pions on the left and protons on the right. Note that as the energy of the beam changes, so does mid-rapidity and thus the acceptance of the detector. Pions have relatively uniform acceptance in this geometry. However, protons have a high cut-in that depends on the beam energy. This efficiency loss will affect the ability to obtain a spectrum in the low momentum region.

4.3.2 Understanding Centrality and Event Selection

Another challenge of the fixed target collisions appears when attempting to determine centrality of $Au + Al$ to compare to other spectra. Recall that Al has 27 nucleons while Au has 197. As we recall, the nucleon density of the nucleus is uniform [153], and we can estimate

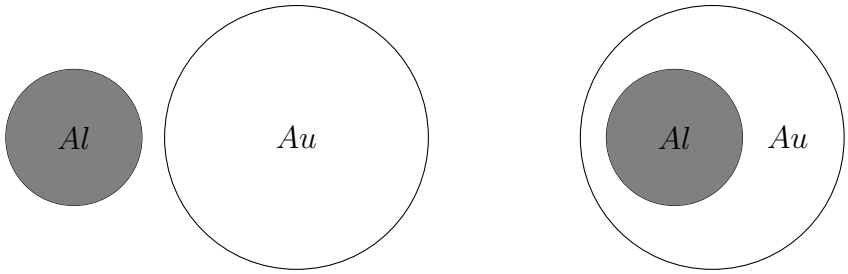

(a) (b)

Figure 4.7: For comparative size, in (a) the Au nucleus on the right has a diameter which is approximately twice as large as the Al nucleus on the left. When the Au collides with the Al nucleus, there is a range of impact parameters where the Al is completely absorbed, as in (b).

the radius of the nucleus from it's volume and the number of nucleons:

$$R = R_0 A^{1/3}$$

where $R_0 \simeq 1.2$ fm and A is of course the number of nucleons. Au has a radius of 6.97 fm and Al has a radius of 3.6 fm, see Figure 4.7. This leads to a range of impact parameters where the Al nucleus is completely absorbed by the Au ion. We had to determine what "most central" would mean for this type of collision, and it largely depended on the number of participating Au nucleons. Since Au is nearly spherical and relativistically flattened, the number of nucleons toward the center is higher than the edges, see Figure 4.8. It shows Woods-Saxon populated nuclei for Au (blue) and Al (red). The dark blue nucleons have participated in the collision — are participants — while the light blue have not — are spectators. The impact parameter here is small enough that all the Al nucleons are participants.

We also needed a variable in which to approximate the impact parameter and define centrality. By utilizing simulations from UrQMD [154] [155] we looked for highly correlated variables, similar to the use of reference multiplicity for nominal $Au + Au$ collisions, with impact parameters for the $Au + Al$ $\sqrt{s_{NN}} = 3.0$ GeV collision system. Total multiplicity

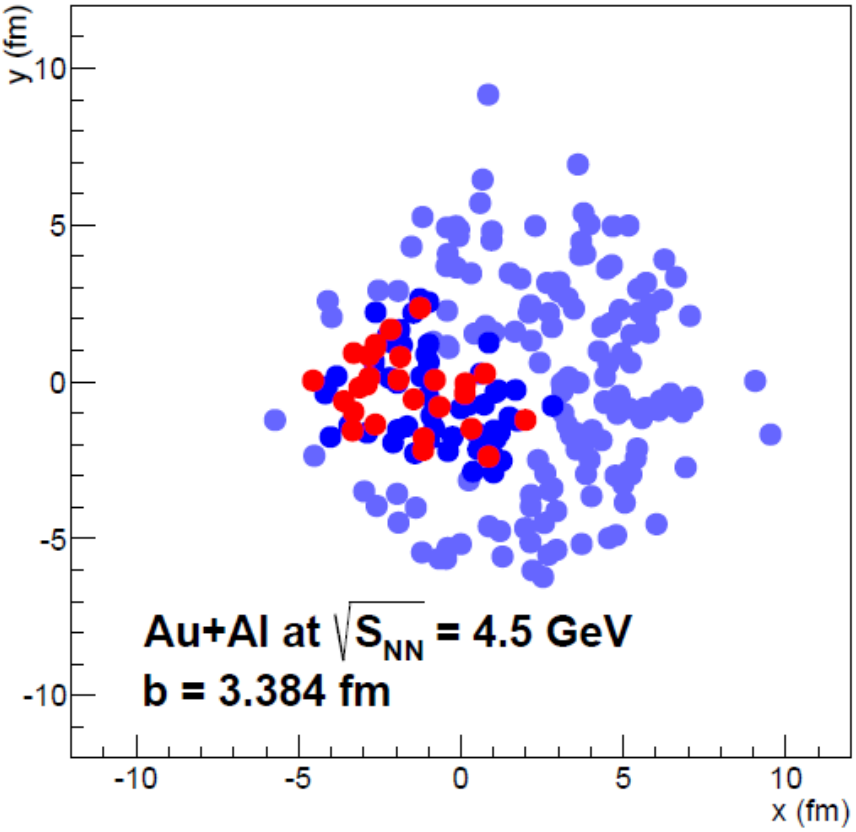

Figure 4.8: An illustration of Woods-Saxon populated nuclei for *Au* (blue) and *Al* (red). The dark blue nucleons have participated in the collision — are participants — while the light blue have not — are spectators. The impact parameter here is small enough that all the *Al* nucleons are participants.

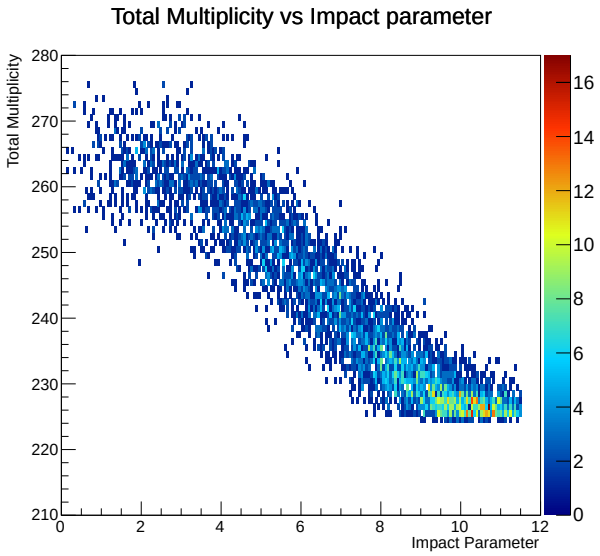

Figure 4.9: This plot illustrates the strong correlation between the total multiplicity of an event, including all spectators and produced particles over the entire rapidity range versus impact parameter.

versus impact parameter can be seen in Figure 4.9. Total multiplicity is defined as all spectators and produced particles over the entire rapidity range. This type of strong correlation is what we want to reproduce using the measurable variables (of which total multiplicity is not experimentally observable) available with the STAR detector. Pion multiplicity versus impact parameter and a crude detector model for the TPC acceptance — called TPC multiplicity — versus impact parameter can be seen in Figure 4.10. The pion multiplicity in the figure comes from counting charged pions produced in the simulated collision that fall within a crude detector model of the TPC acceptance: $-0.5 < \eta < 1.96$. The correlation between these two variables — pion multiplicity and impact parameter — is good, and with the crude detector model the shape of the correlation is very similar despite the inclusion of protons in the total multiplicity of Figure 4.9. This is indicative that the majority of particles in the TPC acceptance are charged pions. Proton multiplicity and mid-rapidity proton multiplicity are shown in Figure 4.11. Recall that for the $Au + Al$ $\sqrt{s_{NN}} = 3.0$ GeV collision system mid-rapidity is $y_{\text{mid}} = 1.05$ and mid-rapidity protons are more reference-multiplicity like in that they fall within $0.55 < y_{\text{proton}} < 1.55$ and cover a full unit of rapidity. Unfortunately,

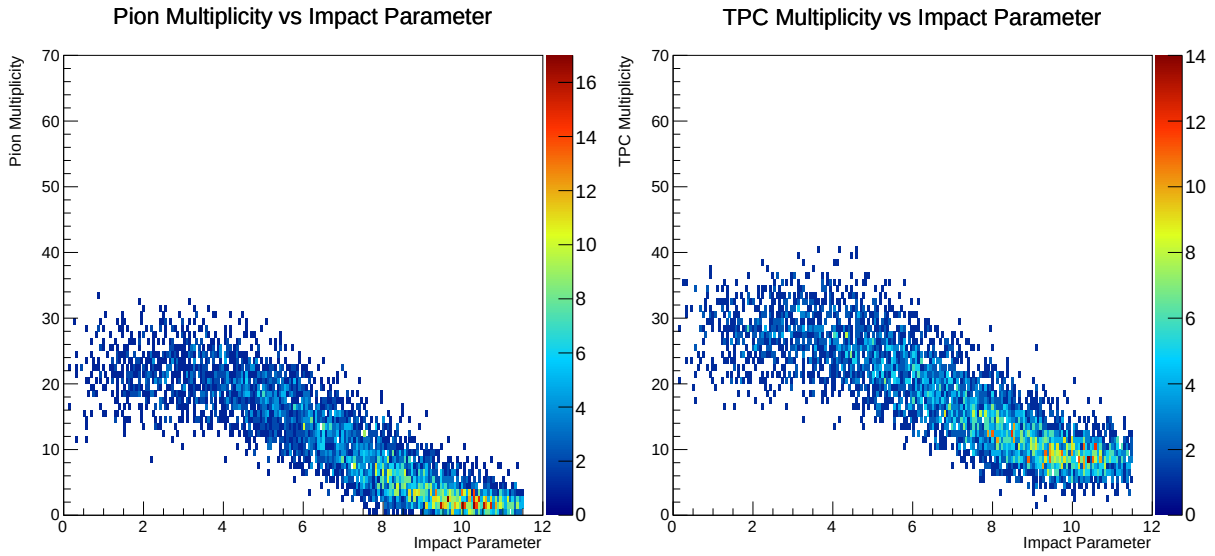

Figure 4.10: On the left-hand panel is the pion multiplicity versus impact parameter. The correlation between the two variables can clearly be seen. On the right-hand panel is the charged particle multiplicity found in the pseudorapidity of the TPC range for the adjusted fixed target geometry.

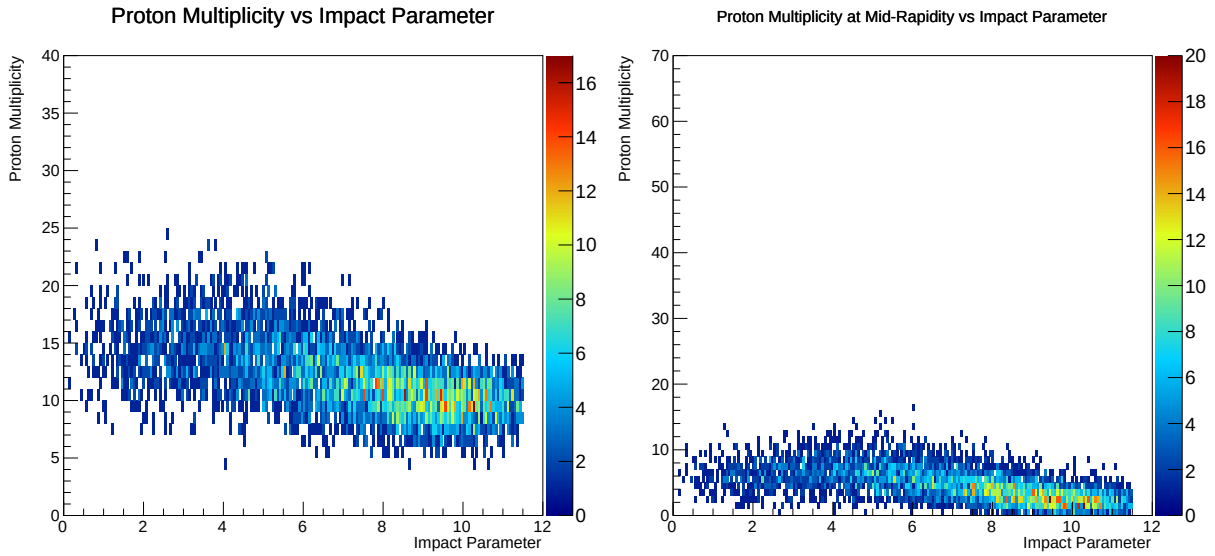

Figure 4.11: On the left-hand panel is the total proton multiplicity versus impact parameter. The proton multiplicity distribution is found in a similar way to the pion distribution. Because the event is simulated, as long as the identified proton falls within the crude TPC model, it is counted in the multiplicity. On the right-hand panel is the proton multiplicity around mid-rapidity versus impact parameter. In neither case is a clear and strong correlation between the variables seen.

protons do not present a strong correlation with impact parameter. Even attempting to ensure that the protons we count are coming from the collision of nuclei, the mid-rapidity

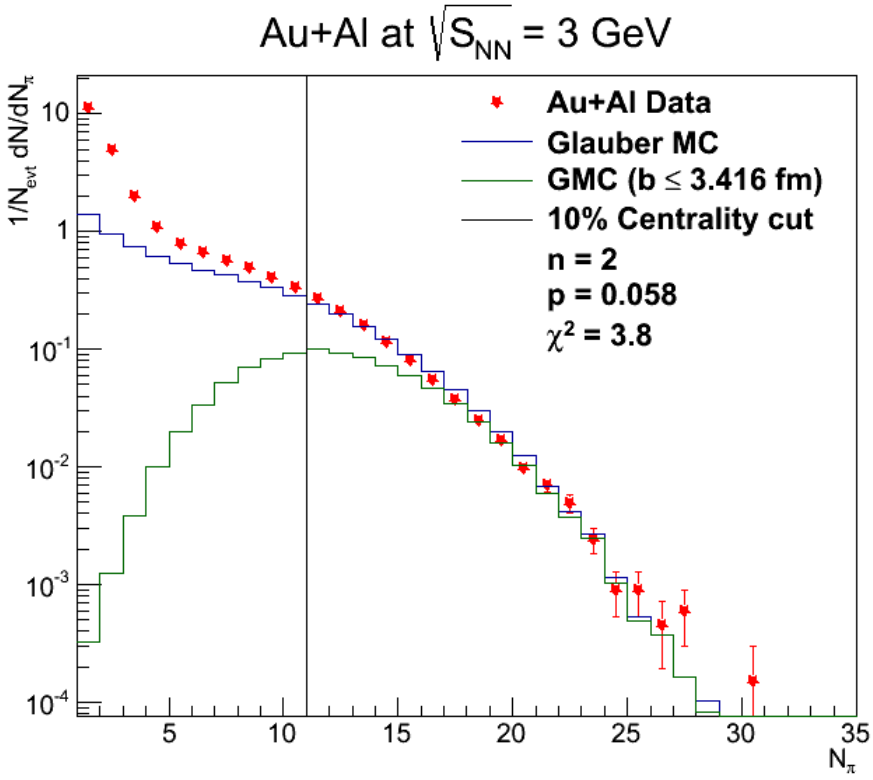

Figure 4.12: This figure shows the experimental pion multiplicity (red stars) fit with a Glauber Monte Carlo (blue histogram) for pion multiplicity; the fit parameters and goodness of fit are stated on the plot. The green histogram is the same Glauber Monte Carlo for collisions with an impact parameter $b \leq 3.416$ fm only. This allowed us to determine the number of pions which would give us the top 10% of centrality.

proton plot in the figure, the correlation becomes even weaker. Protons, in this case, prove themselves incapable of representing collision centrality.

Since pion multiplicity is shown to be indicative of the collision impact parameter, a fit to this distribution with a Glauber Monte Carlo to define centrality classes is next. In the model, nucleons are randomly scattered according to a Woods-Saxon distribution for each nucleus, again as in Figure 4.8. Then, an impact parameter is arbitrarily selected for the collision and the transverse position with respect to the impact parameter of each of the nucleons is computed. Any nucleons within the overlap region are counted as participants, N_{part}, while the number of binary collisions, (N_{coll}), is counted by any nucleon overlapping the two dimensional area (cross-section) of a nucleon from the opposing nucleus. For each Au+Al

collision, a Negative Binomial Distribution is utilized N_{part} times to determine the number of pions produced for that event. The parameters for the Negative Binomial Distribution, n and p, are determined by performing a grid search of various combinations and determining the suitability of the parameters by a χ^2 test to the data. The pion multiplicity is found by selecting measured events with some preliminary cuts in the z- and radial vertex position as well as ensuring the collisions sprayed particles into the TPC rather than out of it. The number of pions is determined by making a mass assumption and comparing the energy loss of the particle to the STAR adapted Bethe-Bloch function in the Bichsel class [142]. If the particle's energy loss fell within 2σ of the gaussian-like distribution around the pion Bichsel line, that particle was counted as a pion. No cuts to eliminate the anomalous low multiplicity are made, but is understood to include collisions of fragments like α particles on the Al bream pipe. The pion multiplicity distribution is plotted in Figure 4.12. The red stars are data fit with the Glauber Monte Carlo (blue histogram); the fit parameters with the best goodness of fit, $\chi^2 = 3.8$, are $n = 2.0$ and $p = 0.058$. The green histogram is the same Glauber Monte Carlo for collisions with an impact parameter $b \leq 3.416$ fm only. This distribution was integrated to find the pion multiplicity corresponding to the top 10% of centrality. For $Au + Al$ $\sqrt{s_{NN}} = 3.0$ GeV the number of pions indicative of the top 10% central events is $M_\pi = 11$.

Event selection for fixed target spectra analysis requires few cuts, four in total: two geometric vertex requirements, one dynamic requirement, and one centrality requirement. These are summarized in table 4.2. Since these collisions were preferentially selected against being recorded, no trigger requirements are needed. Distributions in the z-vertex position and the x-y-vertex position before any cuts are applied are shown in Figure 4.13. The left-hand panel, the number of events versus the z-vertex position, allows us to see the inner material budget by the peaks at the faces of the FTPC detectors located at approximately ± 150 cm in the STAR coordinate system and additional peaks at approximately ± 50 cm which are the remainders of the old Silicon Vertex Tracker (SVT) detector supports. The

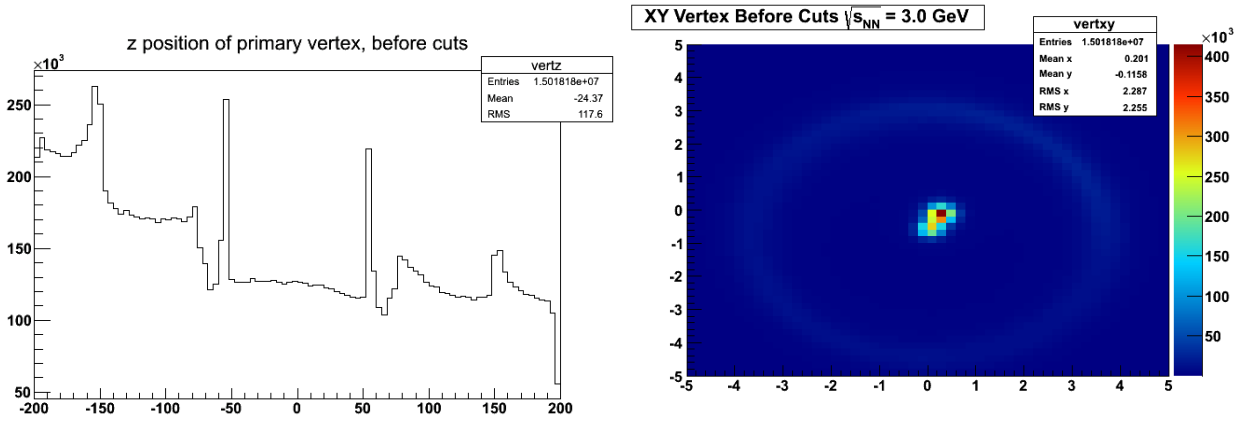

Figure 4.13: On the left-hand panel is the number of events versus the z-vertex position, allows us to see the inner material budget by the peaks at the faces of the FTPC detectors located at approximately ± 150 cm in the STAR coordinate system and additional peaks at approximately ± 50 cm which are the remainders of the old Silicon Vertex Tracker (SVT) detector supports. The feature at approximately ± 75 cm is the switch from an Al beam pipe material to a Be beam pipe material. On the right-hand panel is the x-y-vertex position for all vertices, with most collisions occurring in the beam spot in the approximate center.

feature at approximately ± 75 cm is the switch from an Al beam pipe material to a Be beam pipe material. The right-hand panel of 4.13 illustrates the x-y-vertex position for all vertices, with most collisions occurring in the beam spot in the approximate center. The two geometric cuts applied are a z-vertex position at the edge of the TPC, -200 cm $< V_z < -150$ cm, and radial vertex position on the beam pipe, 2 cm $< V_r <$ 5 cm. The upper limit on the radial position is to eliminate any events recorded as a result of a collision with the face of the FTPC detectors.

Additionally, to ensure that the collisions sprayed particles into the TPC rather than out of it, the dynamic requirement relies on the total momentum of the collision multiplied by the z-vertex position to be less than zero: $(p_{\mathrm{Tot}} \times V_z) < 0$. To get a better idea of this, take a fixed target collision at the center of the detector and suppose all of the particles spray in the $+z$-direction. In order to measure long tracks, we really want this vertex to be displaced in the $-z$-direction and as close to the edge of the TPC as possible. Thus, for collisions that spray into the detector, the total momentum will point in the direction opposite the sign of the z-vertex position and the product of the two values will always be negative. Lastly, only

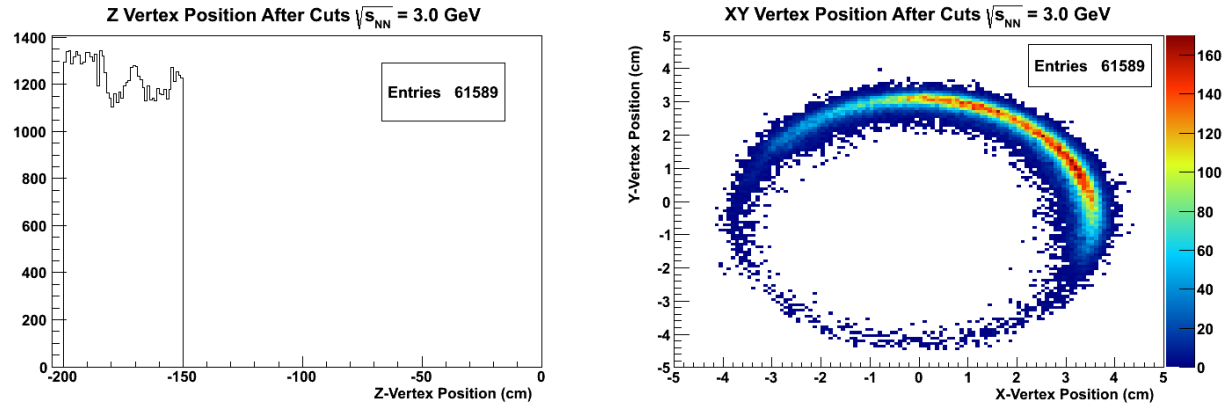

Figure 4.14: On the left-hand panel is the number of events versus the z-vertex position after all geometric, dynamic and centrality cuts are applied. Only events from the West side of the detector (spraying to the East) are analyzed. On the right-hand panel is the x-y-vertex position after all geometric, dynamic and centrality cuts are applied. These cuts select the shape of the beam pipe very well.

Z-Vertex Position	XY-Vertex Position	Total Momentum	Centrality	Spray Direction
-200 cm $< V_z < -150$ cm	2 cm $< V_r <$ 5 cm	$p_{\mathrm{Tot}} > 0$	$\mathrm{M}_\pi = 11$	$(p_{\mathrm{Tot}} \times V_z) < 0$

Table 4.2: A summary of the analysis event cuts for the fixed target data.

the top 10%, the most central, events are analyzed and are selected using the number of pions in the event, $\mathrm{M}_\pi = 11$. Figure 4.14 illustrates the z-vertex position and the x-y-vertex position after all cuts are applied. On the left-hand panel of 4.14 is the number of events versus the z-vertex position after all geometric, dynamic and centrality cuts are applied. Only events from the West side of the detector (spraying to the East) are analyzed. On the right-hand panel of 4.14 is the x-y-vertex position after all geometric, dynamic and centrality cuts are applied. These cuts select the shape of the beam pipe very well.

4.3.3 Fitting Methods

Event information and track information for events satisfying the cuts detailed in Table 4.2 are collected from the full dataset. From the curvature of a particle's track inside the

solenoidal magnetic field, B, the transverse momentum, p_T, is calculated knowing that it is perpendicular to the magnetic field, $p_T \perp B_z$, and assuming the magnitude of the particle's charge is 1 C. To extract the pion yield in a particular region of transverse mass, $m_T - m_0$, and rapidity, y, both of which have a mass dependence, a pion mass assumption, m_π, is made for every track and used with p_T to obtain $m_T - m_\pi$ and y. Recall,

$$m_T = \sqrt{E_{\mathrm{TOT}}^2 - p_z^2} = \sqrt{m_0^2 + p_T^2} \tag{4.1}$$

and

$$y = \frac{1}{2} \ln \left(\frac{E_{\mathrm{TOT}} + p_z}{E_{\mathrm{TOT}} - p_z} \right) \tag{4.2}$$

where E_{TOT} is the total energy of a particle, and p_z is the longitudinal or z-component of the momentum — along the direction of the beam line and magnetic field. The analysis identified particles by the energy loss of each track in the active gas volume, or dE/dx. The energy loss of each track as it traverses the TPC (dE/dx) is plotted as a function of the track momentum is plotted in Figure 4.15. The colored lines are the Bichsel functions for a given particle species as indicated in the legend. It is clear from the dE/dx distributions that PID is relatively clean and possible in the fixed target configuration using the TPC.

The $n\sigma$ variable is defined as the distance between the dE/dx of a track and the Bichsel Curve of the particle of interest in units of σ,

$$n\sigma_X = \frac{\log(dE/dx) - \log(B_X)}{\sigma_X} \tag{4.3}$$

where X is the particle of interest, B_X the expected mean value from the Bichsel parameterization, and σ_X the dE/dx resolution of the TPC — a function of the track length. The mean of the $n\sigma$ distribution is zero for the particle of interest. Because energy loss in the TPC is a random process we expect to see Gaussian distributions for each particle species in $n\sigma$ space.

The tracks are divided into 25 MeV transverse mass bins and their $n\sigma$'s are histogrammed.

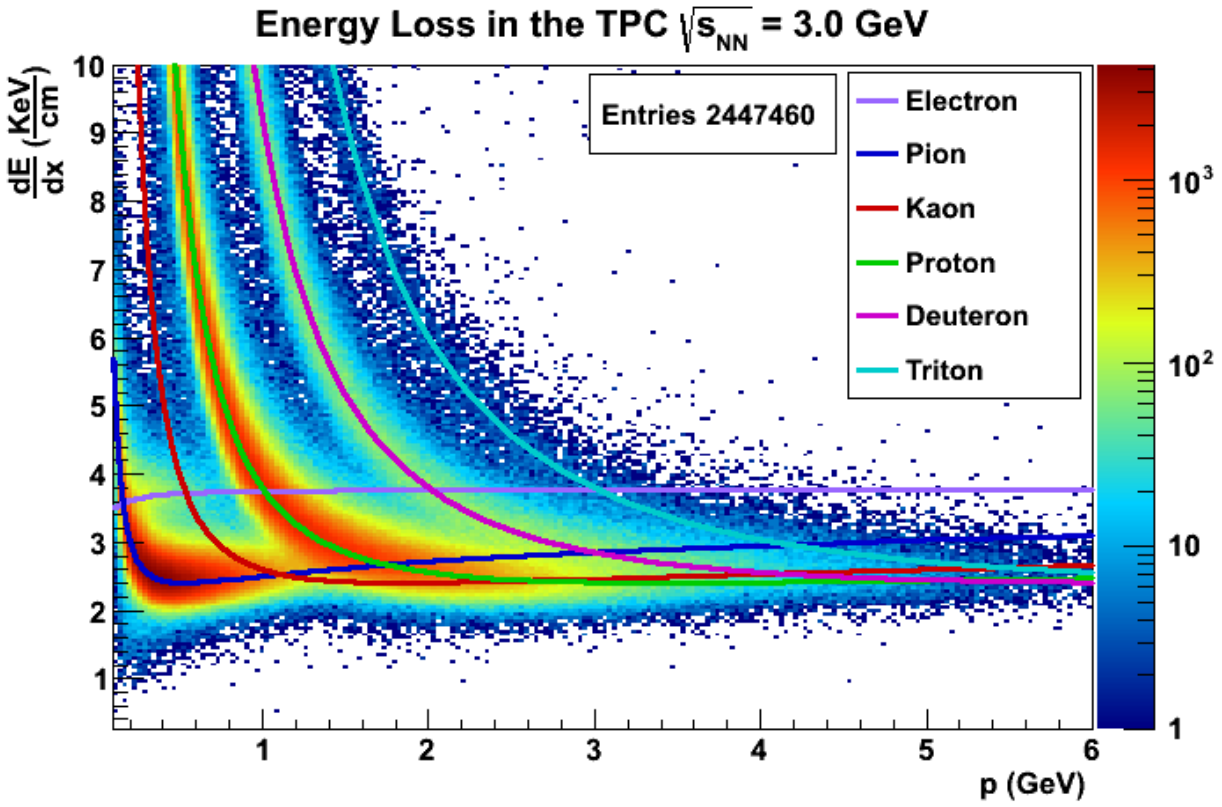

Figure 4.15: The energy loss of each track as it traverses the TPC (dE/dx) is plotted as a function of the track momentum. The colored lines are the Bichsel functions for a given particle species as indicated in the legend. It is clear from the dE/dx distributions that PID is possible in the fixed target configuration using the TPC.

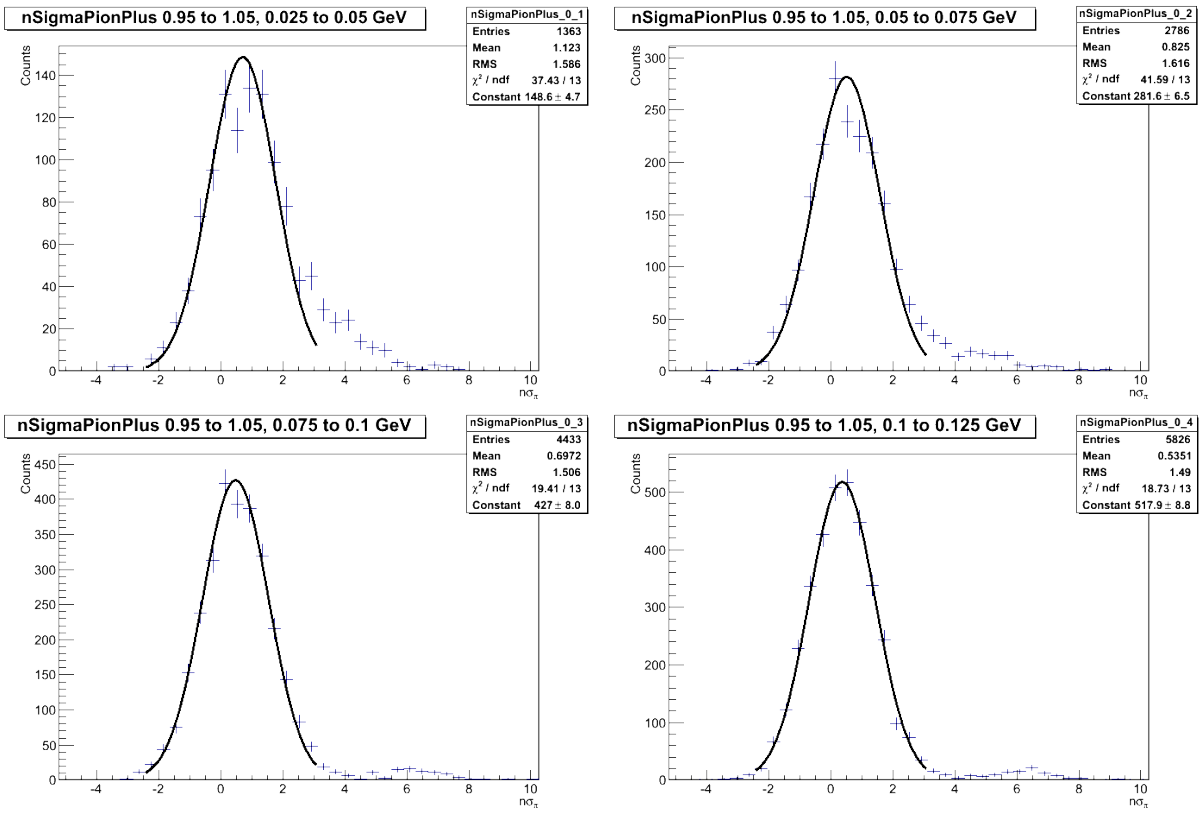

Figure 4.16: Positive pion fits for $Au + Al$ $\sqrt{s_{NN}} = 3.0$ GeV. These are organized in 25 MeV bins in $m_T - m_0$ in a rapidity window of 0.1 units from $0.95 < y < 1.05$. The Gaussian fits, drawn in black, are in $n\sigma_\pi$ and are of the $m_T - m_0 = 0$ to 0.125 GeV/c^2 range. The track data are the blue crosses.

Only tracks within ± 0.05 units of rapidity from mid-rapidity are considered. The histograms are then fit with a single Gaussian,

$$N = A \exp\left[-\frac{1}{2}\left(\frac{f(dE/dx) - \mu)}{\sigma}\right)\right] \tag{4.4}$$

where N is the yield, A the amplitude, μ the centroid, and σ the width parameters. The mean, width, and fit range are fixed with the amplitude (labeled as constant in the figures) as the only permitted floating parameter. The mean, width, and fit range are fixed to values which result in the best χ^2/NDF value. The Gaussians are then integrated to find the raw yields of the particles of interest.

Positive and negative pion fits for $Au + Al$ $\sqrt{s_{NN}} = 3.0$ GeV are illustrated in Figures

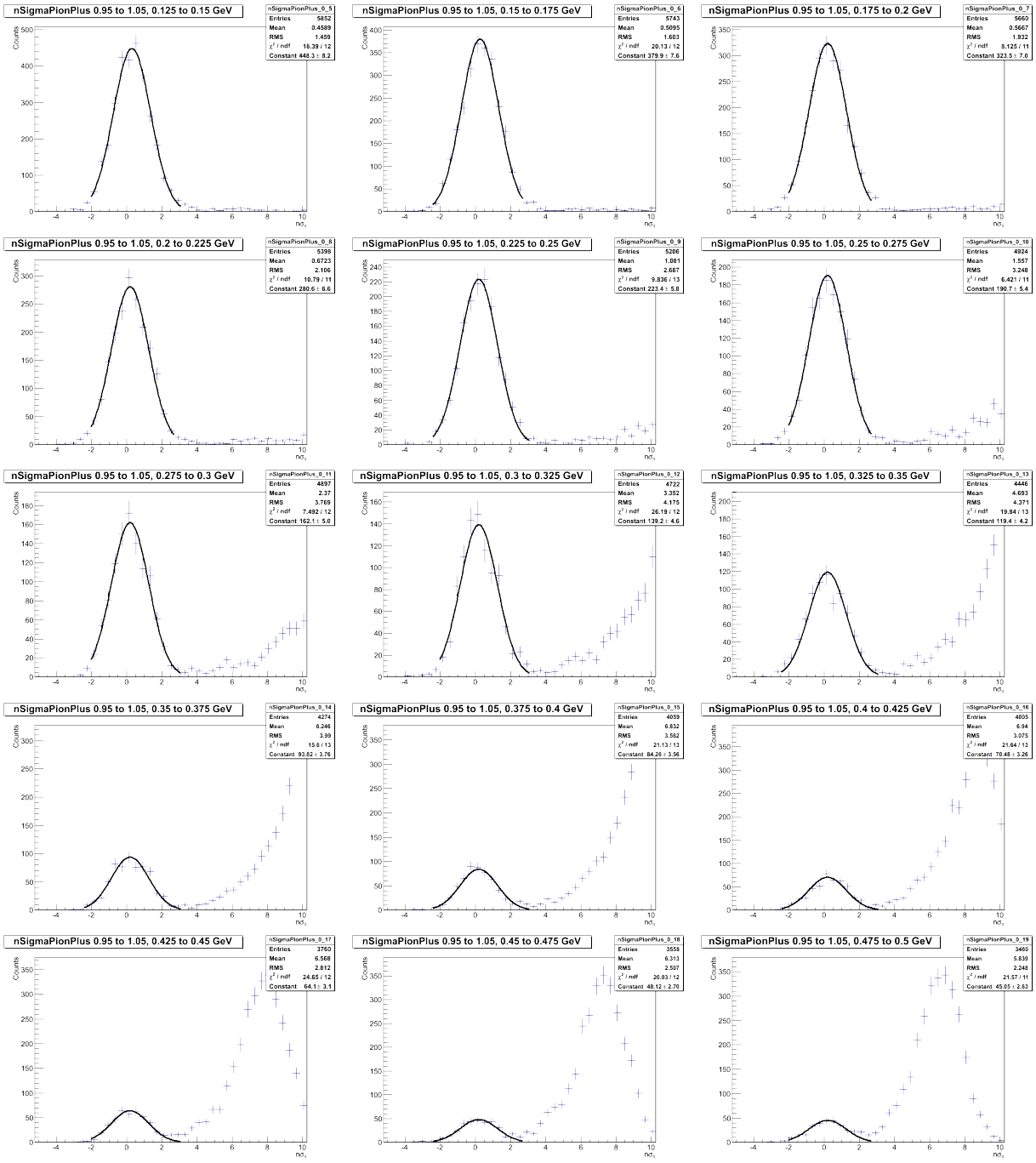

Figure 4.17: Positive pion fits for $Au + Al$ $\sqrt{s_{NN}} = 3.0$ GeV. These are organized in 25 MeV bins in $m_T - m_0$ in a rapidity window of 0.1 units from $0.95 < y < 1.05$. The Gaussian fits, drawn in black, are in $n\sigma_\pi$ and are of the $m_T - m_0 = 0.125$ to 0.500 GeV/c^2 range. The track data are the blue crosses.

4.16, 4.17, 4.18, and 4.19. These are organized in 25 MeV bins in $m_T - m_0$ in a rapidity window of 0.1 units from $0.95 < y < 1.05$. The Gaussian fits are in $n\sigma_\pi$, drawn in black,

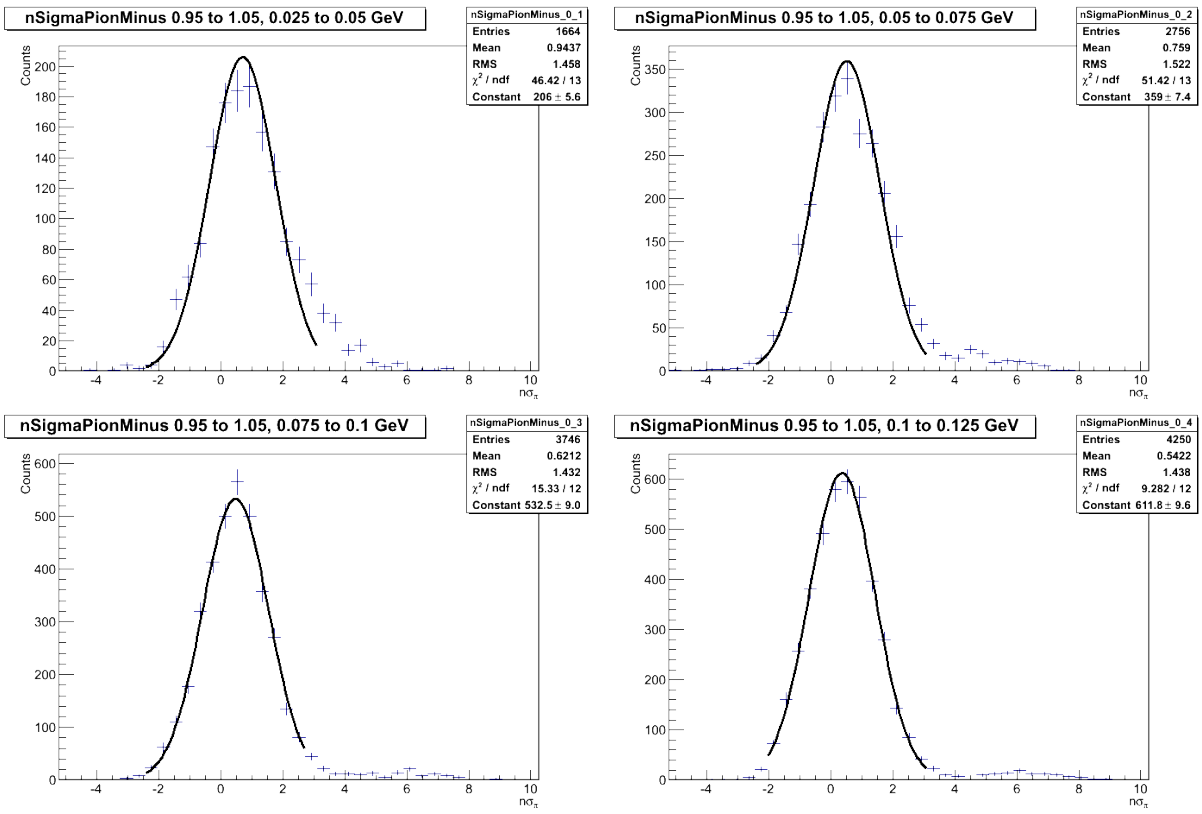

Figure 4.18: Negative pion fits for $Au+Al$ $\sqrt{s_{NN}} = 3.0$ GeV. These are organized in 25 MeV bins in $m_T - m_0$ in a rapidity window of 0.1 units from $0.95 < y < 1.05$. The Gaussian fits, drawn in black, are in $n\sigma_\pi$ and are of the $m_T - m_0 = 0$ to 0.125 GeV/c^2 range. The track data are the blue crosses.

and are of the $m_T - m_0 = 0$ to 0.500 GeV/c^2 range of histograms. The track data are the blue crosses.

4.3.4 Corrections, Systematics and Errors

For fixed target collisions, the normal correction methods utilized by STAR end users had to be modified to take into account the differing geometry and symmetries in the events of interest. Normally, an analysis would request for embedding. Embedding is the process of creating simulated Monte Carlo tracks of a given momentum range, species set and rapidity/pseudo-rapidity range, embedding these tracks into real raw data events, and simulating response of the subsystems utilizing the GEANT model of the STAR detector, called STARSim. Embedding allows the end user to calculate efficiencies of particle detection and

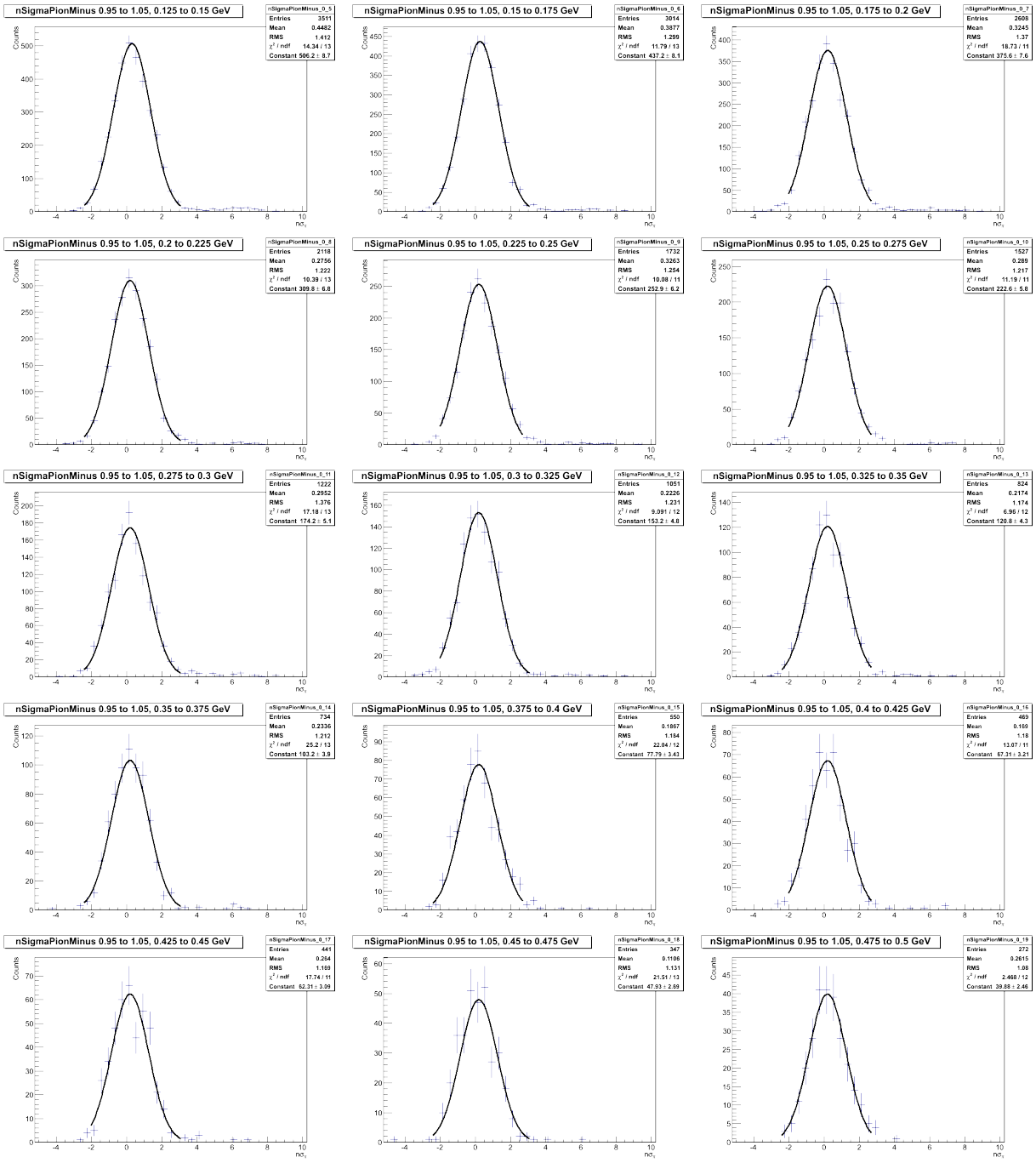

Figure 4.19: Negative pion fits for $Au+Al$ $\sqrt{s_{NN}} = 3.0$ GeV. These are organized in 25 MeV bins in $m_T - m_0$ in a rapidity window of 0.1 units from $0.95 < y < 1.05$. The Gaussian fits, drawn in black, are in $n\sigma_\pi$ and are of the $m_T - m_0 = 0.125$ to 0.500 GeV/c^2 range. The track data are the blue crosses.

account for detector acceptance, the two major correction factors for any particle spectra. With the special circumstances of the fixed target interactions, and the small number of

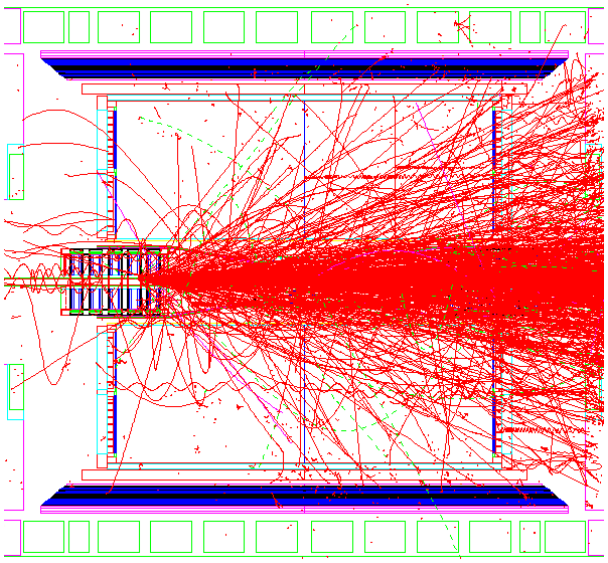

Figure 4.20: An example of a completely simulated (UrQMD) $Au + Al$ event processed through STARSim — offline software that uses GEANT to simulate a detector response.

overall tracks in the TPC from these interactions, fully simulated events from UrQMD [155] are in the process of running through STARSim. An example of a completely simulated (UrQMD) $Au + Al$ event processed through STARSim is illustrated in Figure 4.20. The key with embedding is to determine if a simulated particle is the reconstructed with the correct values of all its track information: momentum, rapidity, energy, mass, etc. When the track is detected at all, the spectra can be corrected for detector acceptance. When the track values are correct, then the spectra can be corrected for efficiency. Since all efficiency studies for fixed target are underway, the remaining analysis will not be efficiency corrected.

Additionally, despite our best efforts, a conclusive determination of the projectile species cannot be made. All physics results indicate a Au or very nearly Au-like projectile, but without calculations that demonstrate a relatively large and finite probability of a beam-halo Au nucleus straying from the beam line and colliding with the beam pipe material, evidence that the projectile is Au is incomplete.

4.4 Beam–Beam Collisions

Beam-beam collision measurements are the traditional collision type measured at STAR. As part of the Beam Energy Scan (BES) program at RHIC, the $\sqrt{s_{NN}} = 19.6$ GeV $Au + Au$ collision system ran during 2011, completing the first set of collision energies in the program. This is the type of collision that STAR was designed to record: symmetric particle production with full azimuthal angle coverage in the TPC and TOF (see Sections 3.2 and 3.3 for more details). The only specialty in this collision system (compared to $\sqrt{s_{NN}} = 200$ GeV $Au+Au$) is that the beams are not accelerated in the RHIC rings, but rather 'stored' until brought into collision.

4.4.1 Trigger Requirements

The trigger at STAR is divided into three aptly named levels: level 0 (L0), level 1 (L1), and level 3 (L3). The L0 system receives digitized data from the fast "trigger" detectors (like the BEMC or TOF) for every bunch crossing (every $\sim$107 ns) to indicate if the event at the very basic level (i.e. multiplicity) is interesting. The subsequent levels perform some amount of data processing to determine just how interesting an event is up to L1 when the TPC is finally read out. The L3 pool performs fast tracking and event reconstruction with a dedicated CPU farm which allows the online display to draw events during run time for quality assurance and detector performance.

The trigger supplies a unique identification number, or token, consisting of 12 bits attached to detector information to the DAQ buffer system while the logic determines if an event is interesting. The token is, and must be, unique since any combination of detectors may be live at any given time and cause detector read-out for a given bunch crossing. Thus all data from each detector per event is associated with the unique 12 bit token until all the data is recorded for that event, at which time the token is recycled and able to be used again [156].

Z-Vertex Position	XY-Vertex Position	Trigger ID Number	DCA Radial	DCA Longitudinal
$\|V_z\| < 30.0$ cm	$\|Vr\| < 2.0$ cm	340001, 340011, 340021	$\|\mathrm{DCA_R}\| < 2.0$ cm	$\|\mathrm{DCA_L}\| < 2.0$ cm
Fit Points Fraction	Total Hit Number	Track Flag	Track Momentum	Rapidity Window
Fit/Poss > 0.52	NHits > 25	$0 <$ Flag < 1000	$p > 0.1$ GeV	$\|y\| < 0.05$

Table 4.3: A summary of the analysis event (first three cells of the top row) and track (last two cells of the top row and all cells of the bottom row) cuts for the beam-beam collision data.

The trigger requirements for this analysis were those of the minimum bias selection. Traditionally, minimum bias in higher energy $Au+Au$ collisions means a coincidence between the east and west BBC detectors as well as a requirement on the pVPD vertex position measurement. However, this particular minimum bias requirement, for the BES program as a whole, differed from traditional minimum bias in that the logic required to record an event was an 'OR' between the ZDC coincidence, pVPD coincidence, and BBC coincidence. This title trigger attempts to include as little bias as possible into the dataset while still recording data. The logic labels a minimum bias event as interesting by determining that a collision did occur.

4.4.2 Event and Track Selection

Standard STAR event selection criteria for this analysis were used. The trigger detectors are optimized to preferentially select events which occur closest to the center of the detector. So, most of the events cuts used are to ensure uniform coverage in the forward and backward directions and to have a symmetry around mid-rapidity, $y = 0$. The number of cuts to select on good events and then within that event to select high quality tracks are many. A summary of the basic event and track cuts are summarized in Table 4.3.

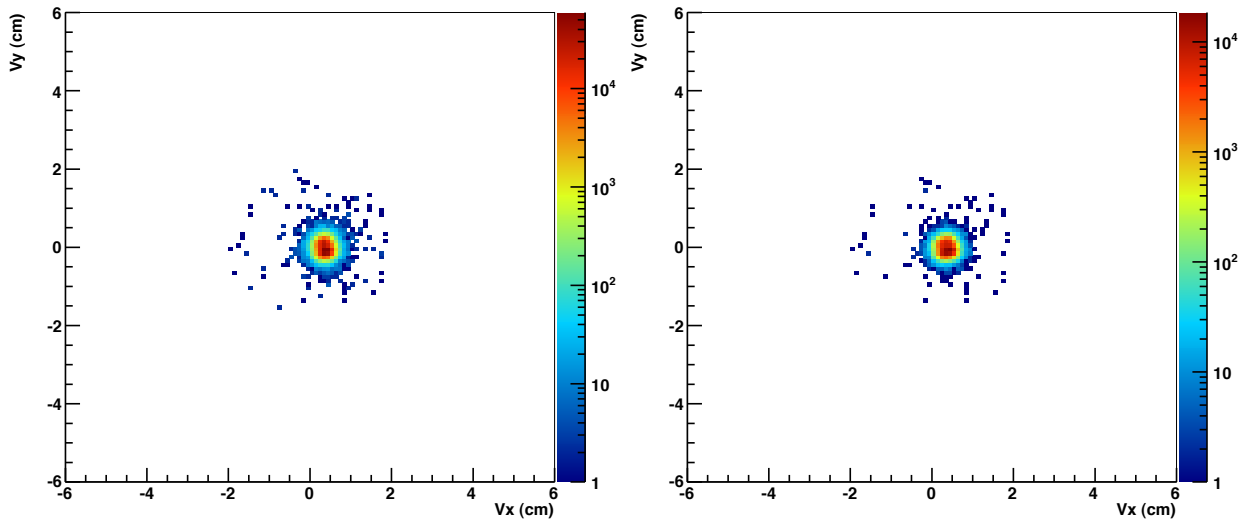

Figure 4.21: On the left-hand panel is the x-y-vertex position before all event geometric cuts are applied. On the right-hand panel is the x-y-vertex position after all event geometric cuts are applied. These cuts select the shape of the beam spot and illustrate the beam profile very well.

Since the data set, unlike the fixed target set, had a specified trigger defining minimum bias events, the trigger identification numbers (explicitly stated in the top row's third column) we utilized to select events that came from the minimum bias set. To ensure uniform coverage with the TPC and TOF detectors (as well as the BEMC and others not used in this analysis), a vertex position cut in the longitudinal direct of $|V_z| < 30.0$ cm was used. Additionally, to exclude many beam-gas or beam-beam pipe collisions, a radial vertex cut of $|V_r| < 2.0$ cm is also enforced. Because the beam profile for the 19.6 GeV data set is slightly larger, the nominal radial cut of $|V_r| < 1.5$ cm was too strict and removed good $Au + Au$ events from the data set (see Section 4.2 for more details). These cuts all apply to the event on the whole. The remaining cuts in the table refer to individual tracks in an event and are further discussed below.

The distance of closest approach (DCA), detailed in Section 4.2, was further restricted from the nominal value used in the vertexer algorithm. The purpose of the vertexer method of associating a track with a larger DCA window ensured that tracks were associated to the proper vertex, be that vertex in the beam line or on the beam pipe. But to ensure that an

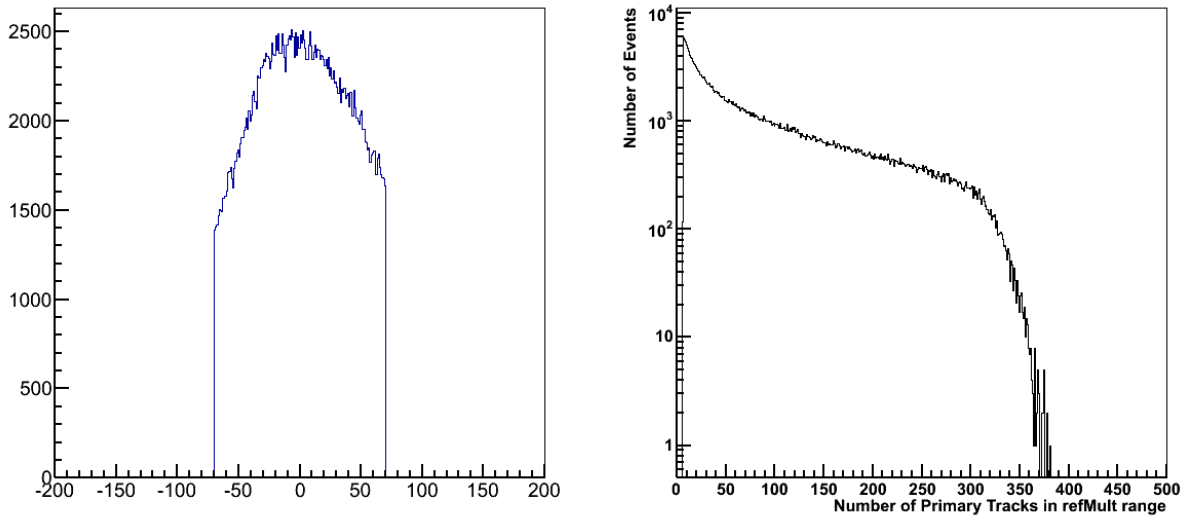

Figure 4.22: On the left-hand panel is the z-vertex position after all event geometric cuts are applied. On the right-hand panel is the reference multiplicty distribution: the number of events given the number of particles with $|\eta| < 0.5$)

individual track is a good track, it should closely approach the vertex position both radially, $\mathrm{DCA_R} < 2.0$ cm, as well as longitudinally, $\mathrm{DCA_L} < 2.0$ cm.

A feature of the strength of the magnetic field when the data was taken means that any track with a momentum below a certain value will not traverse into the TPC detector. Additionally, it would be near impossible to tell if the track could be firmly associated with the vertex of the collision of interest. So, a cut on the momentum of $p > 0.1$ GeV is made to ensure the track travels into the TPC.

The geometry of a track in the TPC allows for a different number of TPC pad row hits to be available per track. The maximum number of hits possible for a given track is 45. To ensure that a track was not accidentally split in it's reconstruction, a ratio of the number of pad row hits that were used to fit the track's trajectory (as well as calculate its momentum) versus the possible number of hits the track could have had if that track cleanly traversed the available length of the TPC. Tracks with ratios with less than 50% were cut out to exclude split tracks. Meaning, included tracks all have a ratio, Fit/Poss > 0.52.

Additionally, long tracks are better for such an analysis since the calculation of the

momentum is more precise and accurate. The number of hits that are associated with a track correlates to how long the track is in the TPC. A cut on the number of hits, NHits > 25, was made to ensure long tracks in the analysis. Long tracks typically also coincide with a good track flag, or coded number indicating the likelihood that a track was recorded at the proper time (indicating if it is a pile-up track, or an in-time track) along with which detectors have data on that track and the quality of the fit. Any negative track flag indicates that the fit of that track was bad in some way (too many fit iterations, not enough points to fit or outlier removal eliminated too many points, for example). A track with a flag number in the 1000's indicated that the track is a pile-up track, out-of time. So, a track flag cut of $0 <$ Flag < 1000 is included to select well-fit, in-time tracks. Finally, a cut on the rapidity is made to analyze mid-rapidity tracks since this is a mid-rapidity analysis.

4.4.3 Fitting Methods

Event information and track information for events satisfying the cuts detailed in Table 4.3 are collected from the full dataset. It is important to note that more stringent track requirements are made for the beam–beam collision analysis than the fixed target analysis. With more energy, a copious number of particles for each species is produced and tracks of good quality can be selected without the risk of increasing statistical error. Additionally, a larger number of events of this particular type are recorded again to support more stringent requirements on track quality.

In the same process as fixed target, the transverse momentum, p_T, is calculated from the curvature of a particle's track inside the solenoidal magnetic field, B, knowing that it is perpendicular to the magnetic field, $p_T \perp B_z$, and assuming the magnitude of the particle's charge is the same as the electron, $e = 1.602 \times 10^{-19}$ C, or 1 in the detector's system units. To extract the particle yield in a particular region of transverse mass, $m_T - m_0$, and rapidity, y, both of which have a mass dependence, a mass assumption, m_0, is made for every track and used with p_T to obtain $m_T - m_0$ and y. Recall Equations 4.1 and 4.2 for transverse

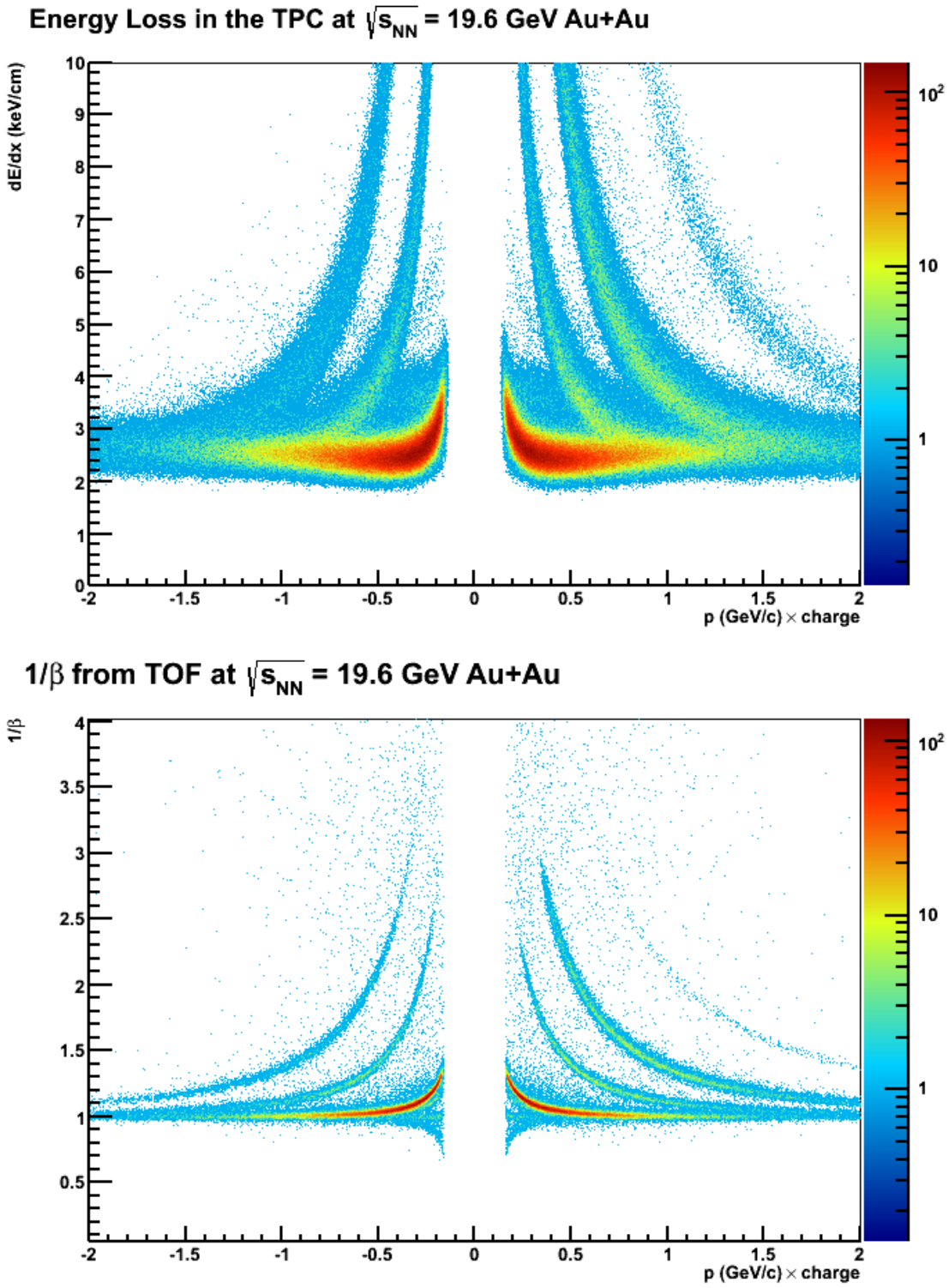

Figure 4.23: The energy loss of each track as it traverses the TPC (dE/dx) is plotted in the top panel as a function of the rigidity: track momentum × charge. $1/\beta$ as measured with the TOF is plotted as a function of the rigidity in the bottom panel.

mass and rapidity. Since the particles of interest are pions, Kaons, protons and antiprotons, their respective masses are used in each of the equations for their respective particle yield extractions.

For a given m_0, only the yield of the particle with that mass is extracted. First, the range in $m_T - m_0$ between 0 and 1.0 GeV/c^2 is divided evenly into 40 bins, resulting in bins of size $\Delta(m_T - m_0) = 0.025$ GeV/c^2. Next, the rapidity range between $|y| < 0.05$, or 0.1 units around midrapidity, $y_{\mathrm{CM}} = 0$ is selected. The analysis identified particles by the energy loss of each track in the active gas volume, or dE/dx, as well as by the $1/\beta$ measurement from the TOF. The energy loss of each track as it traverses the TPC (dE/dx) is plotted as a function of the track rigidity (momentum $\times$ charge) in the top panel of Figure 4.23. In the bottom panel of Figure 4.23, $1/\beta$ is plotted as a function of rigidity. Clear particle separation can be seen in the TPC for low momentum: pions can be cleanly identified up to ~0.8 GeV/c, Kaons can be identified to about ~0.7 GeV/c and protons can be identified up to ~1.0 GeV/c. When particle species begin to overlap, the TOF continues to have clear particle separation. The combination of the two detectors' information allows for an extensive range in momentum to be analyzed.

Each bin in centrality, particle species, rapidity window and $m_T - m_0$ is then fit with a quadruple-Gaussian,

$$N = A_1 \exp\left[-\frac{1}{2}\left(\frac{f_1(dE/dx) - \mu_1)}{\sigma}\right)\right] + A_2 \exp\left[-\frac{1}{2}\left(\frac{f_2(dE/dx) - \mu_2)}{\sigma}\right)\right] + A_3 \exp\left[-\frac{1}{2}\left(\frac{f_3(dE/dx) - \mu_3)}{\sigma}\right)\right] + A_4 \exp\left[-\frac{1}{2}\left(\frac{f_4(dE/dx) - \mu_4)}{\sigma}\right)\right] \quad (4.5)$$

where the mean μ_n comes from the Bichsel parameterization [142] of energy loss in the TPC with modifications due to detector calibration, and width σ_n is related to the resolution of the TPC and is a function of track length. Means, widths, and fit ranges are fixed when fitting and only the amplitudes are permitted to float. The Gaussian corresponding to the

particle of interest in the particular bin is then integrated to find the raw yield of the particle. As there are significantly more particle species and centrality bins in this analysis, all fits are shown in Appendix A.

Electrons present the most common contamination as their particle band in dE/dx passes under each particle species. When the electrons are completely engulfed by a particular particle, the electron amplitudes are estimated and fixed by a fit function to the regions where the electrons are clearly separated from the other particle distributions. This happens most notably with fitting the Kaons. The Kaon band obscures the electron band from 0.175 GeV/c to 0.65 GeV/c; this region has fixed electron amplitudes in the fit. The mean, width, and fit range are fixed to values which result in the best χ^2/NDF value.

4.4.4 Corrections, Systematics and Errors

Recall from Section 4.3 that the two important correction factors that need to be implemented are for detector acceptance and efficiency; these factors are calculated via the embedding process where simulated Monte Carlo tracks of a given momentum range, species set and rapidity/pseudo-rapidity range are embedded into real raw data events and STARSim simulates the detector response. The key with embedding is to determine if a simulated particle is reconstructed with the correct values of all its track information: momentum, rapidity, energy, mass, etc. A match in the distributions of reconstructed embedded tracks and real data tracks for quantities reflecting track quality and used in track selection allows for an accurate calculation of the overall efficiency and acceptance.

The ratio of the distribution of reconstructed and simulated Monte Carlo tracks as a function of $m_T - m_0$ gives the acceptance $\times$ efficiency correction factor for the rapidity window studied. Specific values for the acceptance $\times$ efficiency correction factors for 0-5% central collisions for $\pi^{\pm}$, $K^{\pm}$, p, and $\bar{p}$ are illustrated in Figures 4.24, 4.25, and 4.26, respectively.

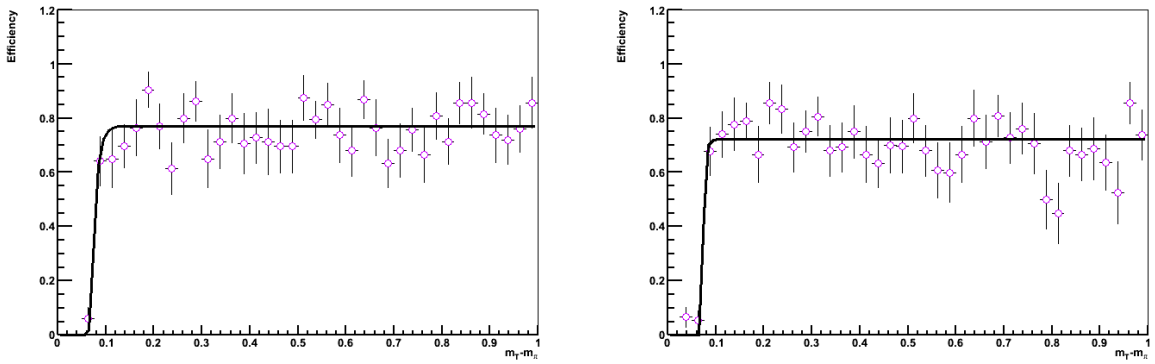

Figure 4.24: Efficiency for $\pi^{\pm}$ in $Au+Au$ $\sqrt{s_{NN}} = 19.6$ GeV as measured by a GEANT simulation of particle tracks through the STAR detector compared to the original Monte Carlo generated tracks.

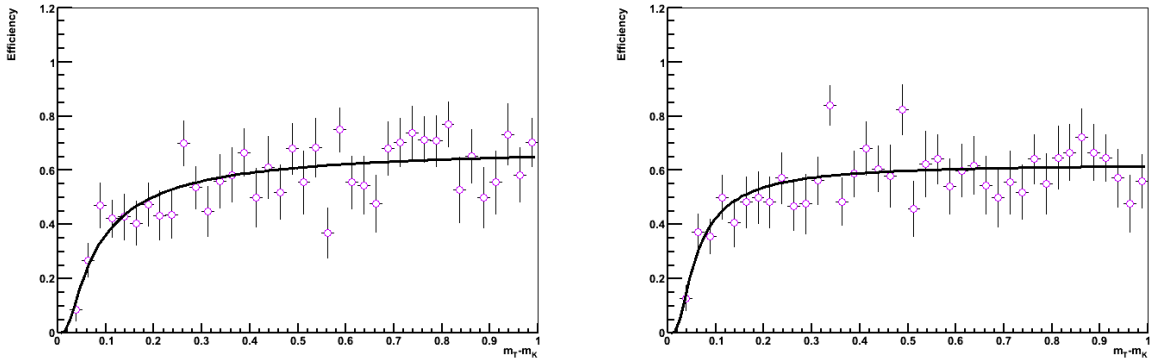

Figure 4.25: Efficiency for $K^{\pm}$ in $Au+Au$ $\sqrt{s_{NN}} = 19.6$ GeV as measured by a GEANT simulation of particle tracks through the STAR detector compared to the original Monte Carlo generated tracks.

Each of these histograms are fit with an exponential of the form,

$$\text{Efficiency} = Ae^{(-B/(m_T-m_0))^C} \tag{4.6}$$

where the fit parameters do not have particular physical meaning, but allow for a good parameterization. The efficiency depends on a particles mass and transverse momentum as well as the event centrality. Particles with shorter lifetimes will be harder to detect. Particles produced in a more central collision are in an environment of densely packed tracks, lowering the tracking efficiency. The efficiency drops sharply below $m_T - m_0 \approx 0.3$ GeV/c due to

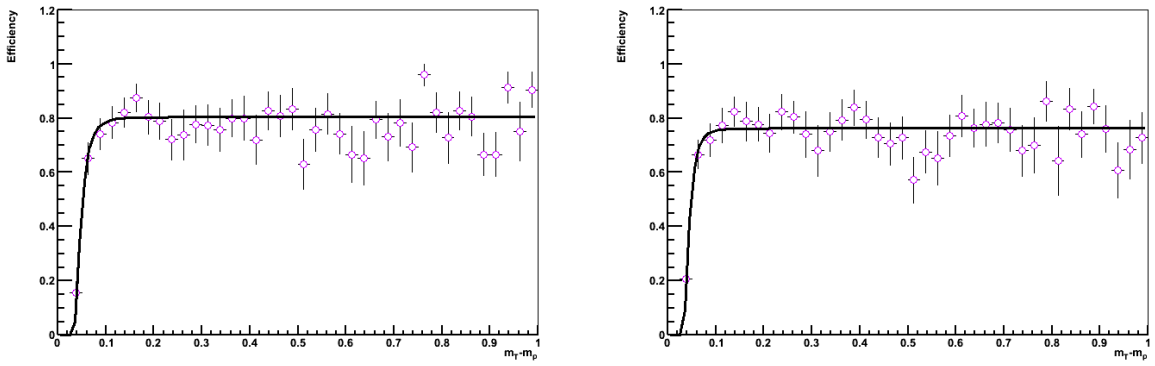

Figure 4.26: Efficiency for p on the left and $\bar{p}$ on the right in $Au + Au$ $\sqrt{s_{NN}}$ = 19.6 GeV as measured by a GEANT simulation of particle tracks through the STAR detector compared to the original Monte Carlo generated tracks.

the tight curl of low-momentum particles in the magnetic field, greatly influencing the TPC acceptance.

The efficiency also depends on the analysis cuts applied. For example, reducing the number of fit points required for a track to be included in the analysis would increase the efficiency. The embedding study was done for all six particle species ($\pi^{\pm}$, $K^{\pm}$, p, and $\bar{p}$) and the function extracted from the fit utilized to correct the spectra. Overall, the systematic error for the efficiency is estimated to be 8%.

As particles traverse the detector material they will lose energy, and a correction is made for Coulomb scattering and energy loss at reconstruction assuming all particles are pions. However, not all produced particles are pions and further corrections must be made for the heavier particles ($K^{\pm}$, p, and $\bar{p}$). The momentum bins in $m_T - m_0$ must be shifted by subtracting (Daniel: based on the figure, I feel that the correction value should be added) the shift correction value from the bin center value. These shift corrections come from the embedding process, described at the beginning of this section, where the difference in $m_T - m_0$ between a reconstructed track and its corresponding simulated track is plotted as a function of $m_T - m_0$ of the simulated (embedded) track. Figure 4.27 illustrates the energy loss as function of p_T for Kaons and protons respectively. The distribution is fit with

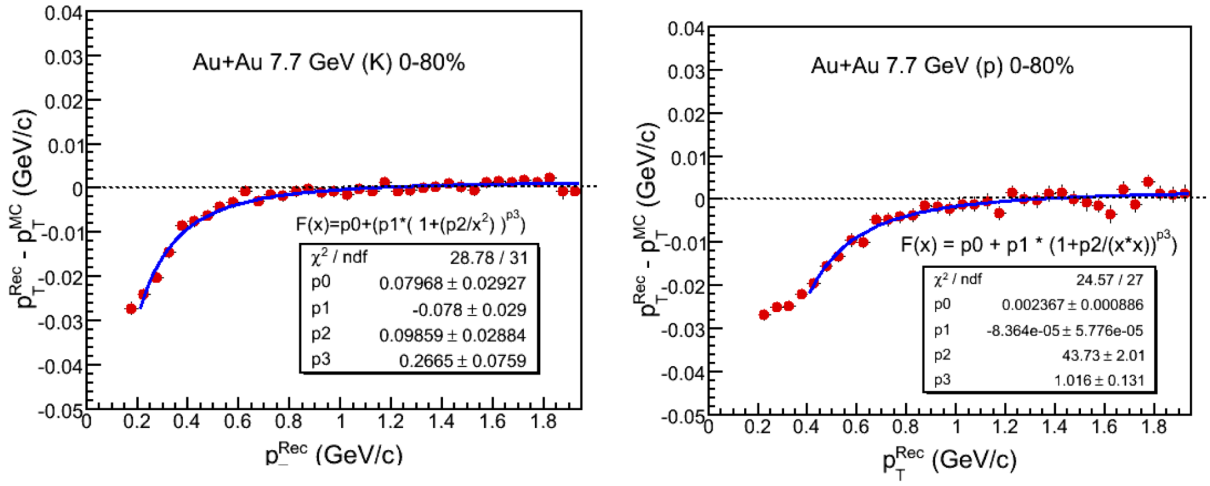

Figure 4.27: The difference between the reconstructed momentum and simulated momentum plotted as a function of the simulated momentum. The function is a parameterization of the difference and the value is utilized for the energy loss correction of Kaons (on the left) and protons (on the right).

a function of the form,

$$f(p_T) = A + B\left(1 + \frac{C}{p_T^2}\right)^D \tag{4.7}$$

shown in blue where A, B, C, and D are the fit parameters $p0$, $p1$, $p2$, and $p3$ in the figure's legend, respectively. The energy loss also effects the bin width in $m_T - m_0$, and is a multiplicative correction with a stronger effect on lower momentum.

The track matching efficiency of the TOF software is determined by comparing the number of tracks found in the TPC with the number of matched hits in the TOF detector as a function of momentum $(m_T - m_0)$. Identified particle plots of these ratios are shown in Figure 4.28. The tracks are identified through dE/dx in the TPC when the energy loss is within 1σ of the predicted Bichsel [142] parameterization. These represent a pure particle sample and each track is then tested for a match in the TOF detector. In the figure, black markers indicate the positive particles, while magenta markers indicate negative particles. This distribution is fit with a function of the form,

$$\text{MatchingEfficiency} = Ae^{(-B/(m_T - m_0))^C} \tag{4.8}$$

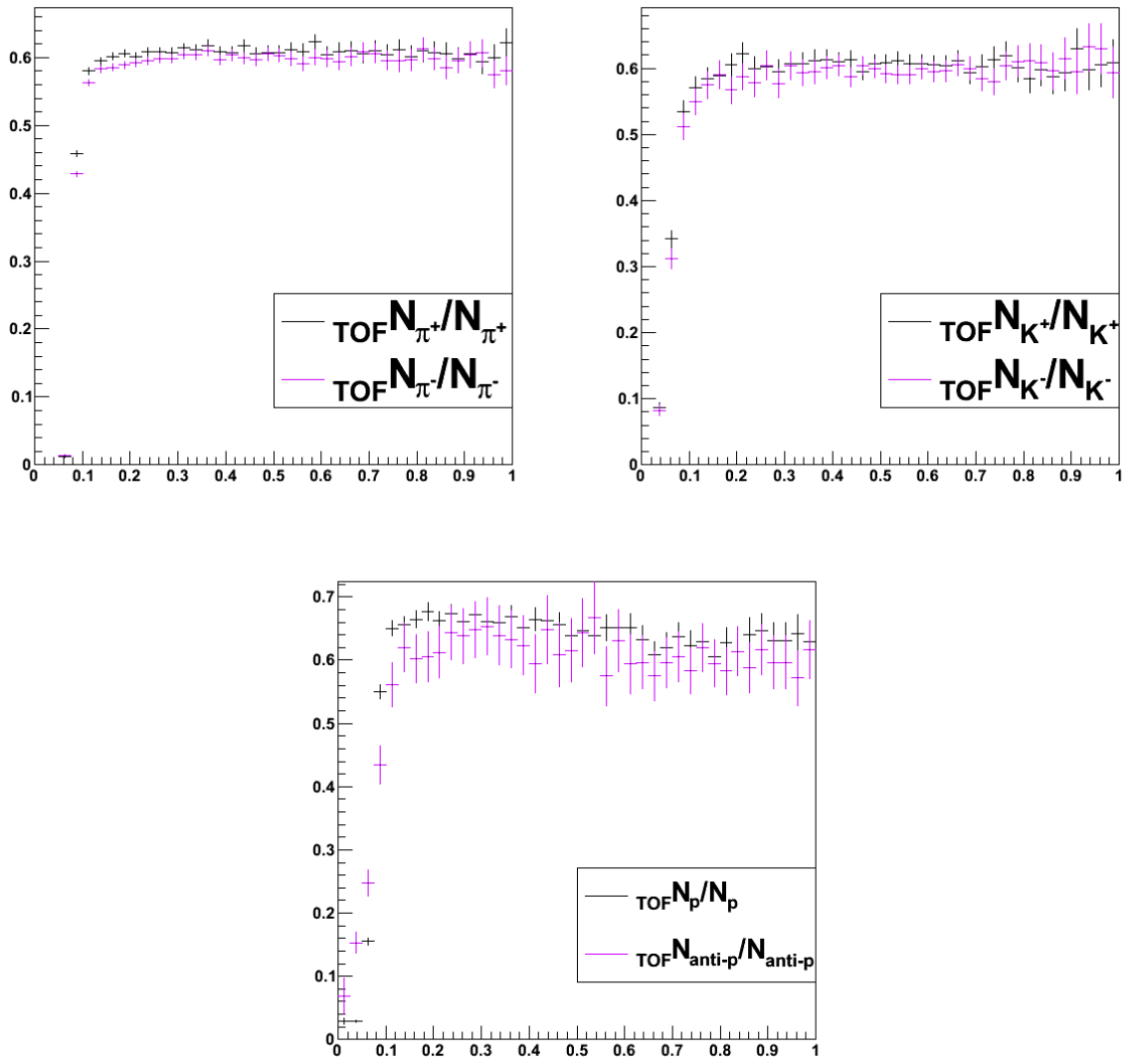

Figure 4.28: The track matching efficiency between the TPC and TOF detectors. Black markers indicate the positive particles, while magenta markers indicate negative particles.

where A, B, and C are fit parameters. Yields from the TOF detector are corrected by the function evaluated at the value of $m_T - m_0$.

Systematic uncertainties for the spectra are estimated in two ways. First, varying the analysis cuts found in Table 4.3 and then assessing the purity of the identified hadron samples in dE/dx measurements provides a rough estimate of the systematic error. Second, varying the values of Gaussian fit parameters and fit ranges make the final estimate for the systematic uncertainty. Utilizing these techniques, the systematic error sources are summarized in

Hadron	V_Z	Track Cuts	Energy Loss Correction	Fit Parameters
π	3%	3.2%	5%	5%
K	3%	6.2%	5%	10%
p	3%	5.4%	5%	4%

Table 4.4: A summary of the systematic errors on produced particle yields for the beam-beam collision data.

Table 4.4.

Chapter 5

Results and Discussion

First, fixed target results are presented followed by beam-beam results where all results shown include errors discussed in Sections 4.3 and 4.4, respectively. Comparisons to STAR data as well as world data are made in the respective results sections.

5.1 Fixed Target Interactions

Utilizing the analysis methods of the previous chapter, Chapter 4, $\pi^{\pm}$ and $p/\bar{p}$ spectra have been extracted and are presented below along with Coulomb results and comparisons to world experiments.

Pion spectra for the top 10% of central events for three energies, $Au-$like$+Al$ at $\sqrt{s_{\rm NN}} =$ 3.0 GeV, $\sqrt{s_{\rm NN}} = 3.5$ GeV and $\sqrt{s_{\rm NN}} = 4.5$ GeV, are shown in Figure 5.1. Plotted as a function of $m_T - m_\pi$, open stars represent π^- while solid stars represent π^+. In green symbols are $\pi^{\pm}$ from $\sqrt{s_{\rm NN}} = 3.0$ GeV, in blue symbols are $\pi^{\pm}$ from $\sqrt{s_{\rm NN}} = 3.5$ GeV, and in red symbols are $\pi^{\pm}$ from $\sqrt{s_{\rm NN}} = 4.5$ GeV. The drop-off at low $m_T - m_\pi$ is due to the efficiency and acceptance of the STAR detector as a fixed target experiment. Further studies with GEANT may prove useful to correct these spectra and describe what portion of these low-momentum pions can actually be measured with the detector. The limited reach in momentum is due to the detector acceptance discussed in Section 4.3.1. The spectra from each energy is fit with a linear function to guide the eye rather than to imply physics.

Proton spectra plotted as a function of $m_T - m_p$ in solid stars for three energies, $Au-$like$+$

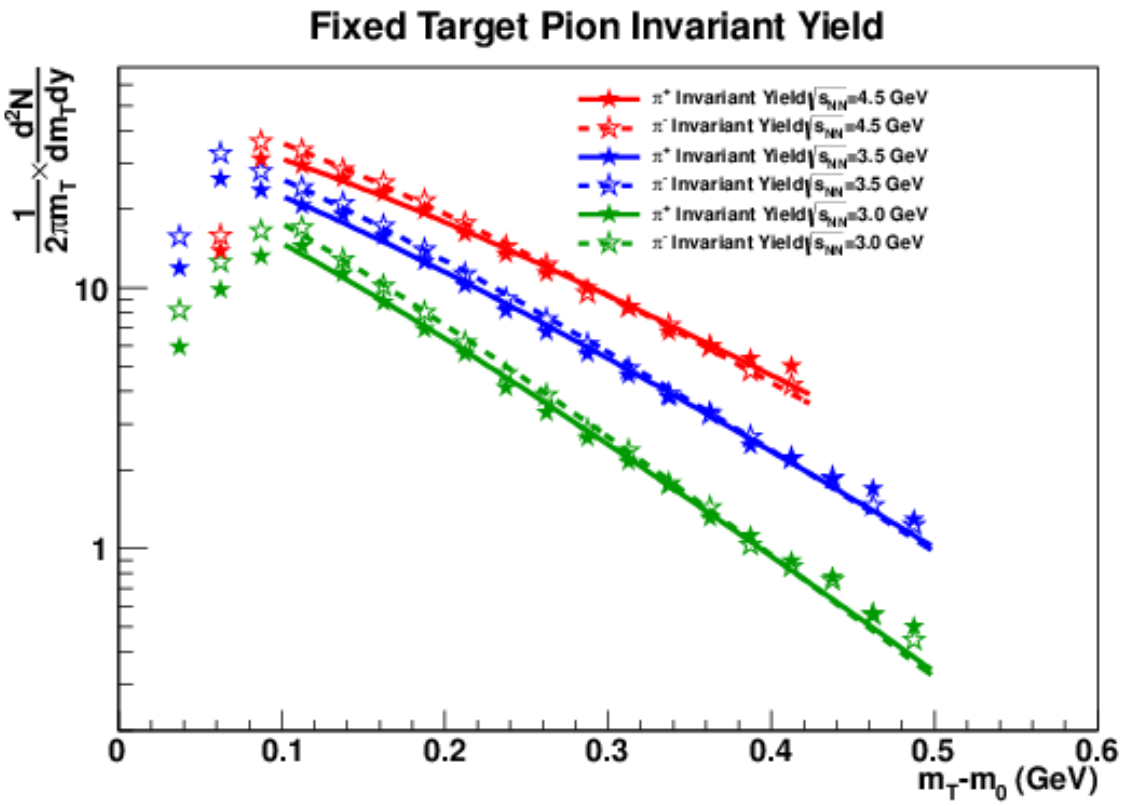

Figure 5.1: Pion spectra are plotted as a function of $m_T - m_\pi$. Open stars represent π^- while solid stars represent π^+. The fixed target energy of $\sqrt{s_{\rm NN}} = 3.0$ GeV in green is compared with the fixed target $Au-$like $+ Al$ energies of $\sqrt{s_{\rm NN}} = 3.5$ GeV in blue and $\sqrt{s_{\rm NN}} = 4.5$ GeV in red.

Al at $\sqrt{s_{\rm NN}} = 3.0$ GeV, $\sqrt{s_{\rm NN}} = 3.5$ GeV and $\sqrt{s_{\rm NN}} = 4.5$ GeV, in Figure 5.2. In green are p from $\sqrt{s_{\rm NN}} = 3.0$ GeV, in blue are p from $\sqrt{s_{\rm NN}} = 3.5$ GeV, and in red are p from $\sqrt{s_{\rm NN}} = 4.5$ GeV. The drop-off at low $m_T - m_p$ is due to the efficiency and acceptance of the STAR detector as a fixed target experiment discussed in Section 4.3.1. Again, studies with GEANT may prove useful to correct these spectra at low-momentum. Each of the spectra are fit with a linear function to guide the eye rather than to imply physics. At these energies, $\bar{p}$ production is limited if not energetically impossible.

Figure 5.3 shows the π^+/π^- ratios as a function of $m_T - m_\pi$ for three fixed-target data sets from STAR for $Au-$like $+ Al$ collisions at $\sqrt{s_{\rm NN}} = 3.0$, 3.5, and 4.5 GeV all utilizing the top 10% of central events. These pion ratio data are fit with the Coulomb model described in Section 2.4.1, which assumes similar initial spectra that are then modified by the Coulomb

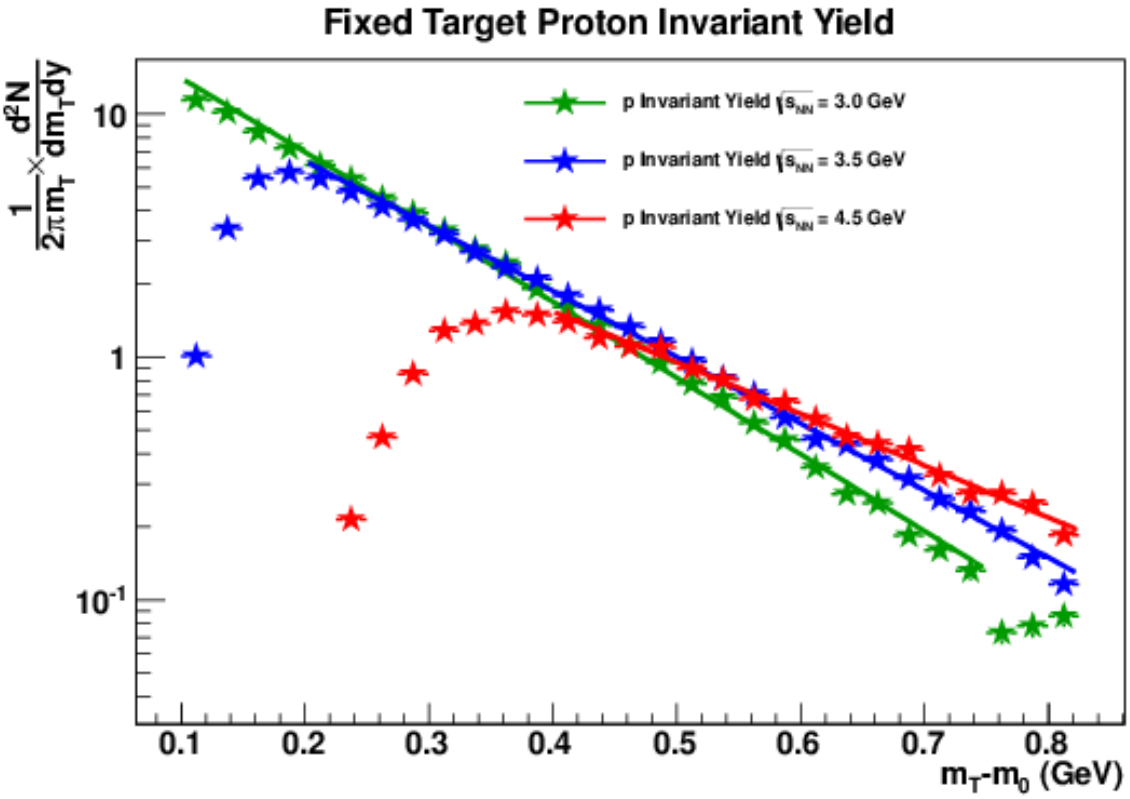

Figure 5.2: Proton spectra are plotted as a function of $m_T - m_p$. The fixed target energy of $\sqrt{s_{\rm NN}} = 3.0$ GeV in green is compared with the fixed target $Au-$like $+$ Al energies of $\sqrt{s_{\rm NN}} = 3.5$ GeV in blue and $\sqrt{s_{\rm NN}} = 4.5$ GeV in red.

potential after emission from the nuclear source. The energy $\sqrt{s_{\rm NN}} = 3.0$ GeV in green is compared with the fixed target $Au-$like $+$ Al energies of $\sqrt{s_{\rm NN}} = 3.5$ GeV in blue and $\sqrt{s_{\rm NN}} = 4.5$ GeV in red. Comparisons are also made to other world experiments and a collision energy from the BES measured with STAR.

The Coulomb potential and $p(\bar{p})$ yield are shown in Figure 5.4 in red with the right-hand red y-axis and $p(\bar{p})$ yield in magenta(cyan) utilizing the left-hand y-axis (respectively) as a function of center of mass energy. Comparisons to other world data and some collision energies from the BES measured with STAR also appear in the figure. Fixed target data from the current measurement are in solid red stars. Displaying these two sets of data together highlight their similarity in shape with collision energy, which is not unexpected as the Coulomb potential is related to the net charge of the source and the bulk of that net

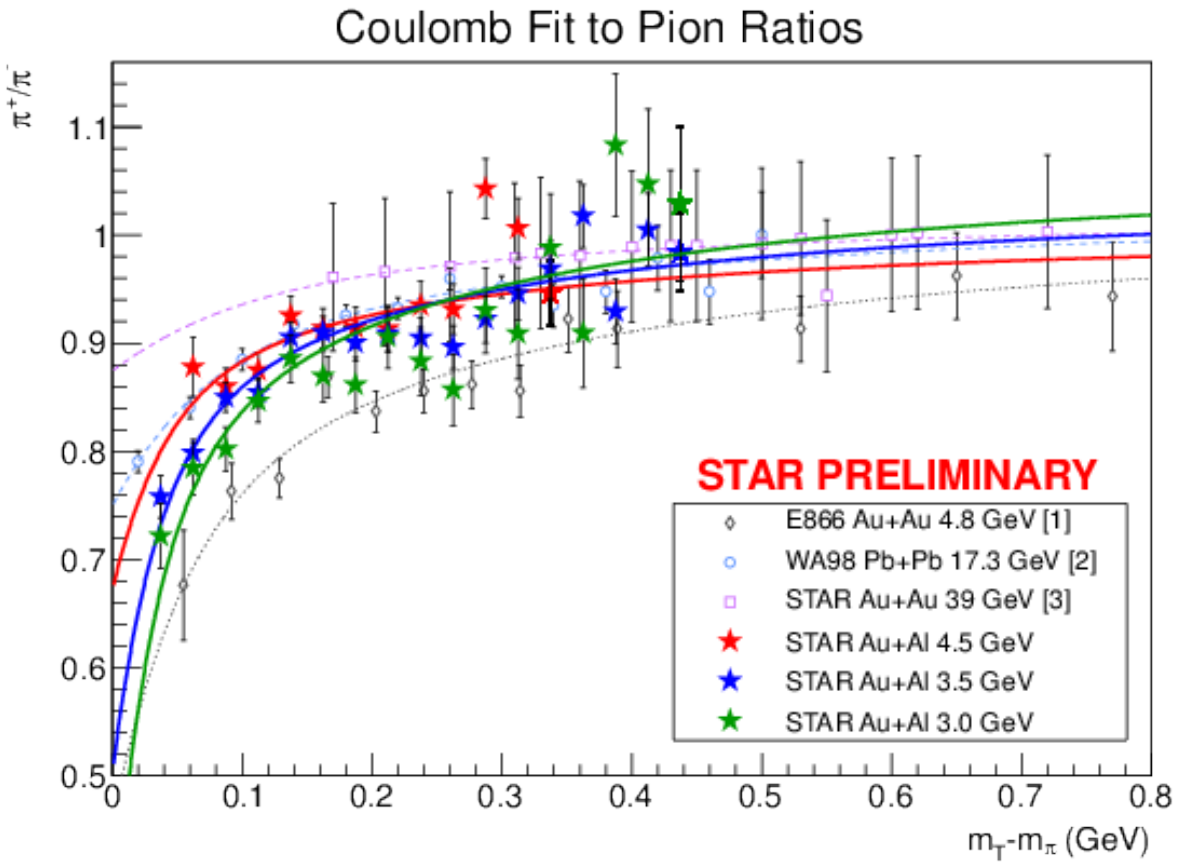

Figure 5.3: Pion ratios, π^+/π^-, are plotted as a function of $m_T - m_\pi$ and fit with the Coulomb Source Potential described in Chapter 2. The fixed target energy of $\sqrt{s_{\rm NN}} = 3.0\ GeV$ in green is compared with the fixed target $Au-$like$+\,Al$ energies of $\sqrt{s_{\rm NN}} = 3.5$ GeV in blue and $\sqrt{s_{\rm NN}} = 4.5$ GeV in red. Comparisons are also made to other world experiments and a collision energy from the BES measured with STAR.

charge is due to stopped protons.

Naively, one would expect that $V_C = Q/4\pi\epsilon_0 r$, where Q is the net charge of the source and r is the pion emission radius. From this equation, the emission radius can be estimated to be 3.06 $\pm$ 0.47, 3.39 $\pm$ 0.23, and 3.06 $\pm$ 0.28 fm for the 4.5, 3.5, and 3.0 GeV systems respectively. For comparison, the radius of the overlap region is estimated to be 3.4 fm from the Glauber Monte Carlo for the top ten percent of centrality. That fact that the estimated emission radius is similar in size to the overlap radius suggests that there is not much expansion, implying a short lifetime of the source.

Figure 5.5 shows the mid-rapidity charged pion dN/dy values scaled by the number

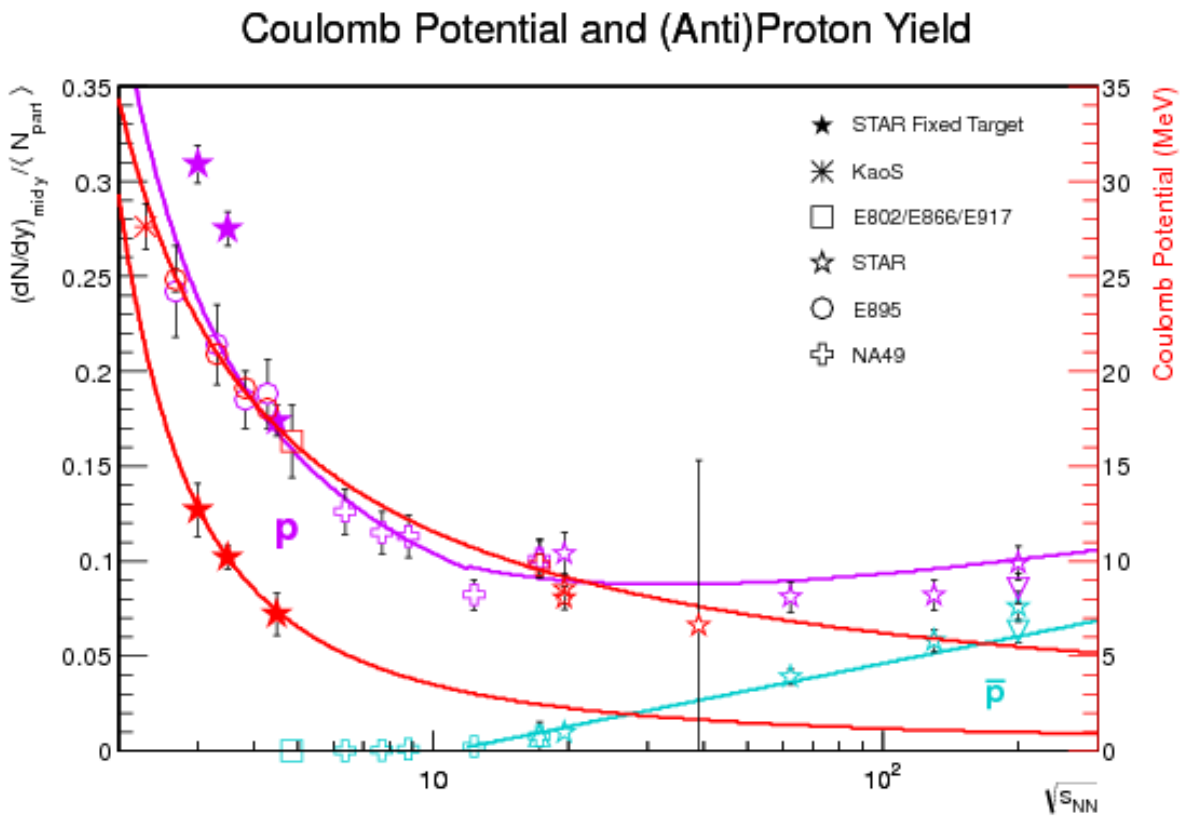

Figure 5.4: The Coulomb potential (V_C) in solid red stars with the right-hand red y-axis and mid-rapidity dN/dy (anti)proton yield in solid (cyan)magenta stars utilizing the left-hand y-axis are plotted as a function of center of mass energy. Comparisons are also made to other world experiments and some collision energies from the BES measured with STAR. Fixed target data are in solid stars. For comparison, scaled mid-rapidity proton yields (open magenta symbols) and Coulomb potentials (open red symbols) are also shown for $Au + Au$ collisions at 1.0 AGeV (KaoS [157]), at 2, 4, 6, and 8 AGeV (E895 [158,159]), and at 2, 4, 6, 8, and 10.8 AGeV (E866 [119,160]). Yields and potentials also are shown for central Pb+Pb collisions at 20, 30, 40, 60, 80, and 158 AGeV (NA44 [161,162], and NA49 [9,163]). Additional data from references [30,120,164–169] are also included. The proton yields are fit with a falling exponential function to guide the eye.

of participants for the $Au-$like $+$ Al data at the three energies studied. The yields are determined by integrating the Bose-Einstein fit functions for all $m_T - m_0$. The average number of participants comes from a Monte Carlo Glauber model estimated for the top 10% centrality for $Au-$like $+$ Al. This method yields an estimate of 88 participating nucleons for each of the three energies. For comparison, the mid-rapidity scaled dN/dy values are also shown for central $Au + Au$ and $Pb + Pb$ data from several other experiments across a broad range of collisions energies. For these comparison data, the estimated number of participants

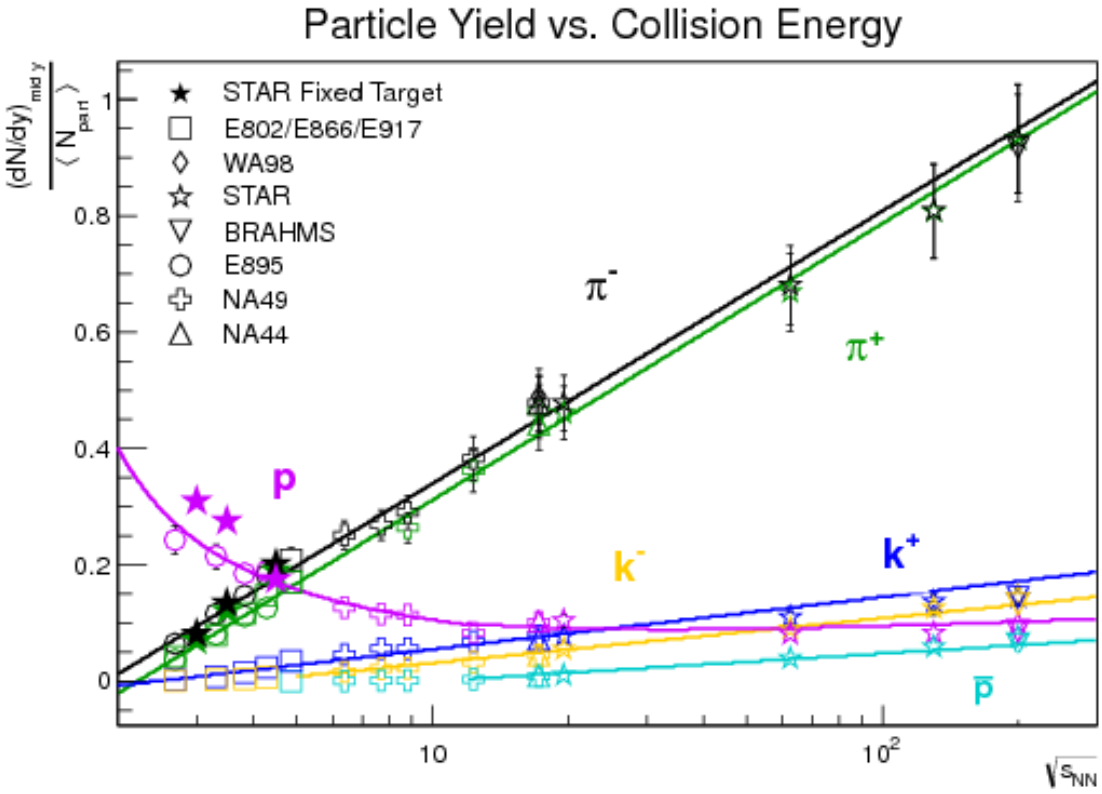

Figure 5.5: The mid-rapidity ($|y - y_{CM}| < 0.1$) dN/dy yields scaled by the average number of participants are shown for negative (solid stars) and positive (open stars) pions from central (top 10%) $Au-$like $+ Al$ collisions at the three collision energies ($\sqrt{s_{NN}}$ = 3.0, 3.5, 4.5 GeV). For comparison, scaled mid-rapidity pion yields are also shown for $Au+Au$ collisions at 1.0 AGeV (KaoS [157]), at 2, 4, 6, and 8 AGeV (E895 [158,159]), and at 2, 4, 6, 8, and 10.8 AGeV (E866 [119,160]). Yields and potentials also are shown for central Pb+Pb collisions at 20, 30, 40, 60, 80, and 158 AGeV (NA44 [161,162], and NA49 [9,163]). Additional data from references [30,120,164–169] are also included. The pion yields are fit with a linear function to guide the eye.

is determined using either the values stated by the collaborations, or from Glauber model estimates using the centrality selection of the collaborations. The published data are fit with a simple linear function which is meant to guide the eye rather than to imply physics. Note that the extracted scaled pion yields from the new $Au-$like $+ Al$ data are consistent with trends previously seen in central data from heavy symmetric systems. Of additional import is the enhancement of the π^- yields with respect to that of the π^+ in the $Au-$like $+ Al$ data as has been seen in $Au + Au$ data at similar energies. This enhancement is expected as the neutron-to-proton ratio is closer to unity in aluminum than in either gold or lead.

5.2 Beam–Beam Collisions

With the analysis methods described in the previous chapter, Chapter 4, identified particle spectra have been extracted and are presented below along with the Coulomb potential and some signs of the onset of deconfinement. In Figure 5.6, particle spectra are plotted as a

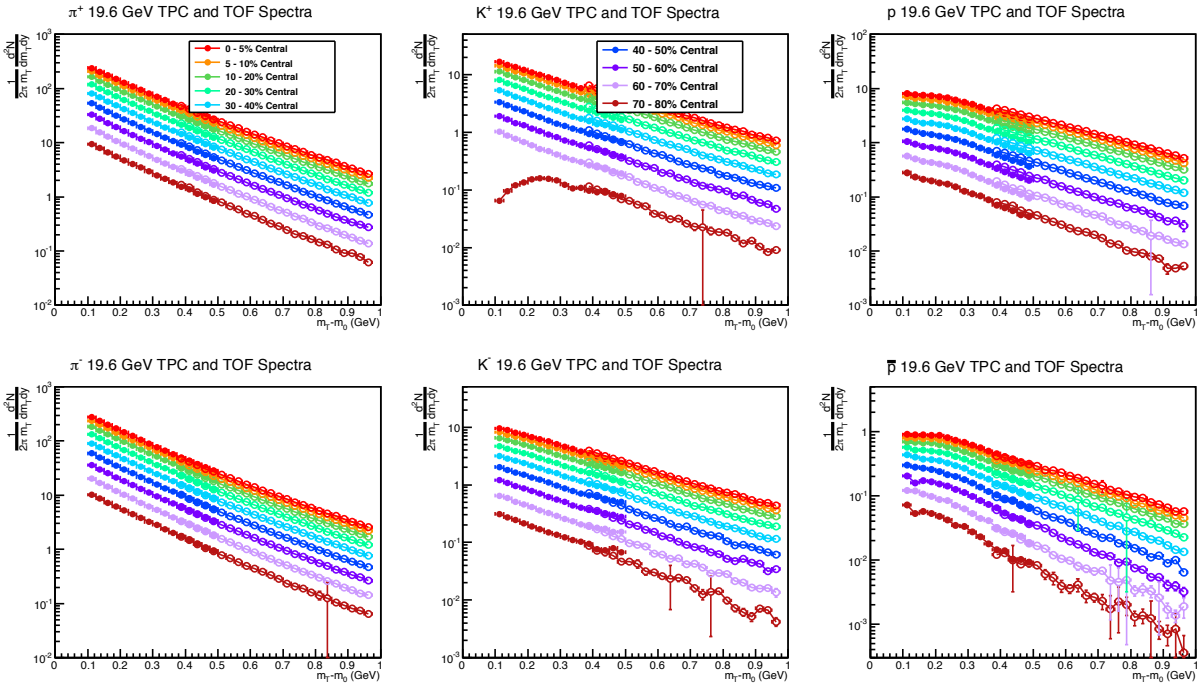

Figure 5.6: Particle spectra are plotted as a function of $m_T - m_0$. Open symbols represent identified particles with the TOF detector while solid symbols represent particles identified with the TPC detector at the energy of $\sqrt{s_{\rm NN}} = 19.6$ GeV. Each color represents a different centrality with the most central on top an the most peripheral on bottom. Statistical and systematic errors are included. Pions are on the left, kaons in the center and protons are on the right. All positive particles are in the top row and negative particles are in the bottom row.

function of $m_T - m_0$. Open symbols represent particles identified with the TOF detector while solid symbols represent particles identified with the TPC detector at the energy of $\sqrt{s_{\rm NN}} = 19.6$ GeV for $Au+Au$ collisions. Each color represents a different collision centrality with the most central on top an the most peripheral on bottom. Statistical and systematic errors are included. Pions are on the left, kaons in the center and protons are on the right. All positively charged particles are in the top row, while negatively charged particles are in the bottom row. The main corrections applied to these spectra are acceptance, efficiency,

momenta, matching efficiency (in the case for the TOF identified particles), and energy loss.

As expected, pions contribute the majority to produced particles since they are lightest of the hadrons and also have the largest interaction cross-section. Positively charged Kaons are next most numerous, which is expected due to their light mass and contribution from weak decays of strange baryons produced in the collision. Protons and negatively charged Kaons follow next and the least contribution to produced particles is from anti-protons.

The number of (anti-)protons produced per unit of rapidity normalized to the number of participating nucleons versus the center of mass energy is shown in Figure 5.7. Results for $Au + Au$ at $\sqrt{s_{NN}} = 19.6$ GeV are displayed in solid red stars. Scaled comparisons to other world data are also shown for references [9, 30, 119, 120, 157–169] and are in additional figures to follow. The proton yields are fit with a falling exponential function of the form $\frac{dN}{dy}/N_{\text{part}} = A \exp\left(- \log(\sqrt{s})/B \right)$ and anti-protons are fit with a function of the form $\frac{dN}{dy}/N_{\text{part}} = \frac{A \exp\left(-\log(\sqrt{s}/B)\right)+C}{A \exp\left(-\log(\sqrt{s}/B)\right)+1}$ to guide the eye only.

Proton dN/dy is calculated using a fitted Fermi-Dirac distribution giving a value of $dN/dy_p = 35.0211 \pm 0.3883$ while the anti-proton dN/dy uses an exponential in p_T [2] to fit resulting in the value $dN/dy_{\bar{p}} = 3.8936 \pm 0.1412$. The average number of participants in $Au + Au$ at $\sqrt{s_{NN}} = 19.6$ GeV is $N_{\text{part}} = 353$. Thus, the values in Figure 5.7 are $dN/dy_p = 0.09921 \pm 0.0011$ for protons and $dN/dy_{\bar{p}} = 0.1103 \pm 0.0004$ for anti-protons.

In Figure 5.8, the Coulomb potential (V_C) in open red stars with the right-hand red y-axis and mid-rapidity dN/dy (anti)proton yield in solid (cyan)magenta stars utilizing the left-hand y-axis are plotted as a function of center of mass energy. Displaying these two sets of data together highlight their similarity in shape with collision energy, which is not unexpected as the Coulomb potential is related to the net charge of the source and the bulk of that net charge is due to stopped protons. Also highlighted in the figure are the fixed target data in open black stars. The Coulomb potential for $\sqrt{s_{\text{NN}}} = 19.6$ GeV is $V_C = 8.07 \pm 0.61$ V with an initial pion ratio of $R_i = \frac{\pi^+}{\pi^-} = 0.953 \pm 0.002$ utilizing the Coulomb fit discussed in Section 2.4 on the Coulomb Potential. This calculated Coulomb potential follows the world

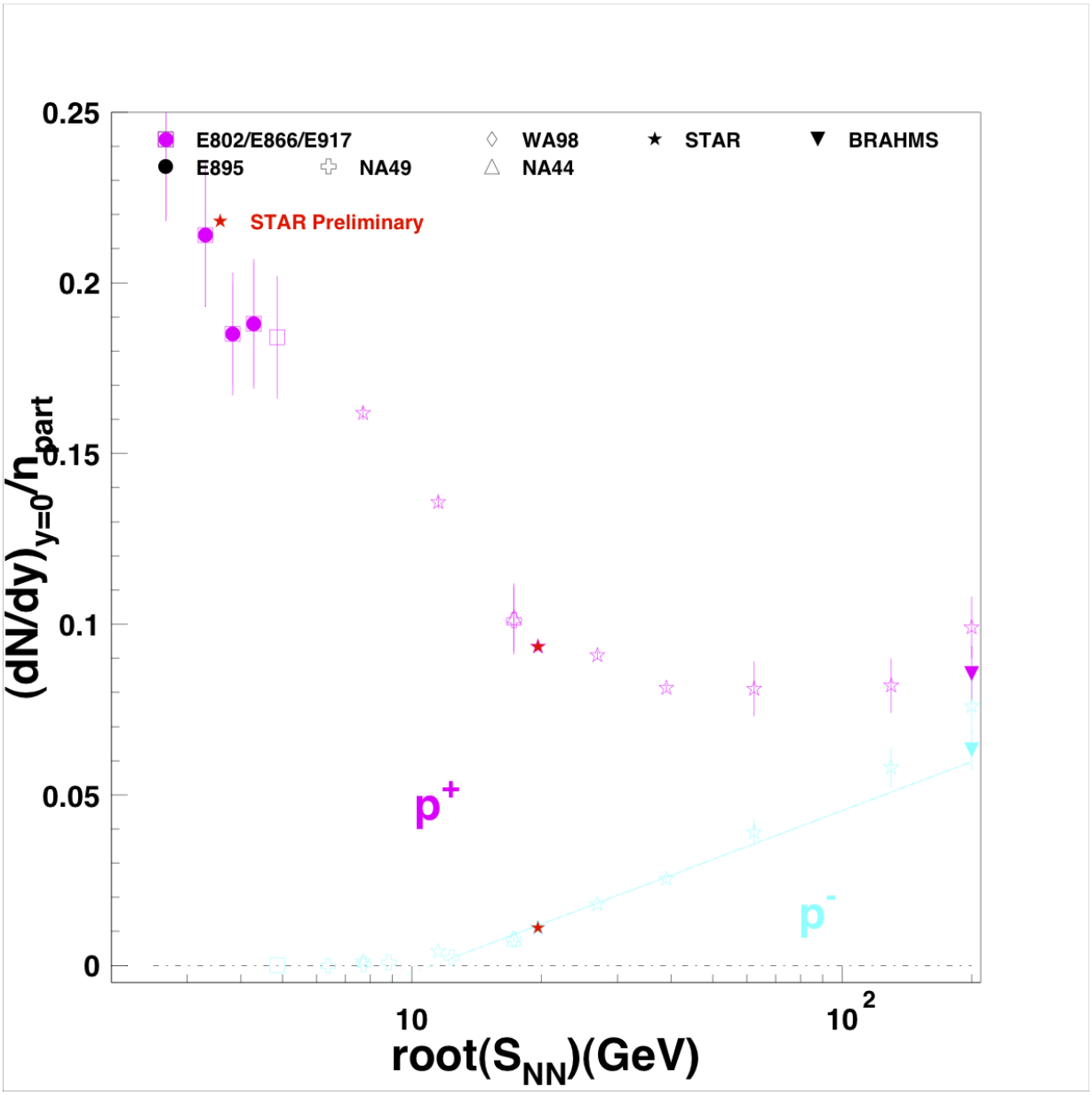

Figure 5.7: The number of (anti-)protons produced per unit of rapidity normalized to the number of participating nucleons versus the center of mass energy. Results for $Au + Au$ at $\sqrt{s_{NN}} = 19.6$ GeV are shown in solid red stars. Scaled comparisons to other world data are also shown for $Au + Au$ collisions at 1.0 AGeV (KaoS [157]), at 2, 4, 6, and 8 AGeV (E895 [158, 159]), and at 2, 4, 6, 8, and 10.8 AGeV (E866 [119, 160]). Yields and potentials also are shown for central Pb+Pb collisions at 20, 30, 40, 60, 80, and 158 AGeV (NA44 [161, 162], and NA49 [9, 163]). Additional data from references [30, 120, 164–169] are also included. The proton yields are fit with a falling exponential function to guide the eye.

trend while the pion ratio falls well within world data and is comparable to similar SPS energies.

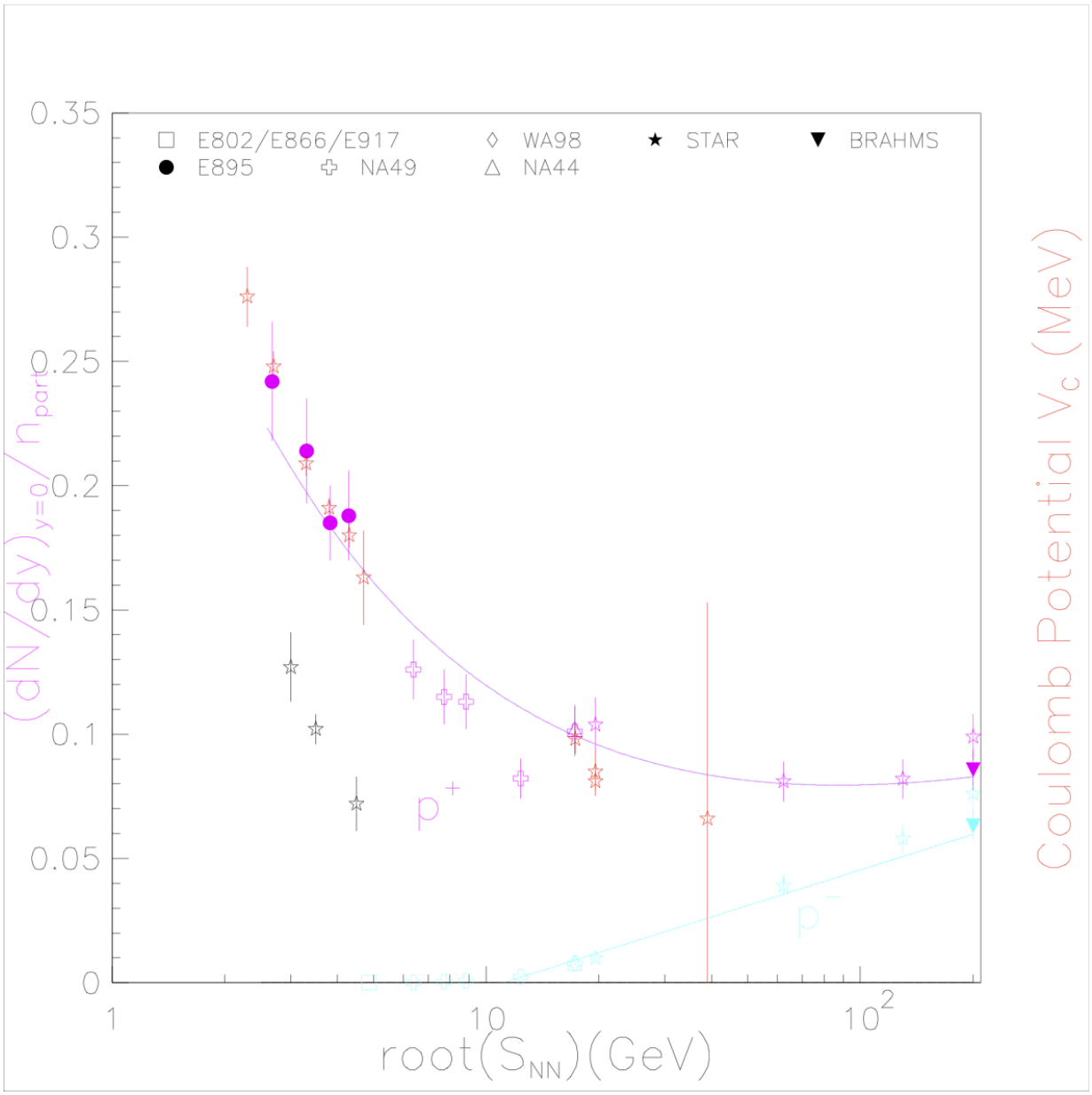

Figure 5.8: The Coulomb potential (V_C) in open red stars with the right-hand red y-axis and mid-rapidity dN/dy (anti)proton yield in solid (cyan)magenta stars utilizing the left-hand y-axis are plotted as a function of center of mass energy. Comparisons are also made to other world experiments and some collision energies from the BES measured with STAR. Fixed target data are in open black stars. For comparison, scaled mid-rapidity proton yields (open magenta symbols) and Coulomb potentials (open red symbols) are also shown for $Au + Au$ collisions at 1.0 AGeV (KaoS [157]), at 2, 4, 6, and 8 AGeV (E895 [158,159]), and at 2, 4, 6, 8, and 10.8 AGeV (E866 [119,160]). Yields and potentials also are shown for central Pb+Pb collisions at 20, 30, 40, 60, 80, and 158 AGeV (NA44 [161,162], and NA49 [9,163]). Additional data from references [30,120,164–169] are also included. Note the proton yields are fit with a falling exponential function to guide the eye.

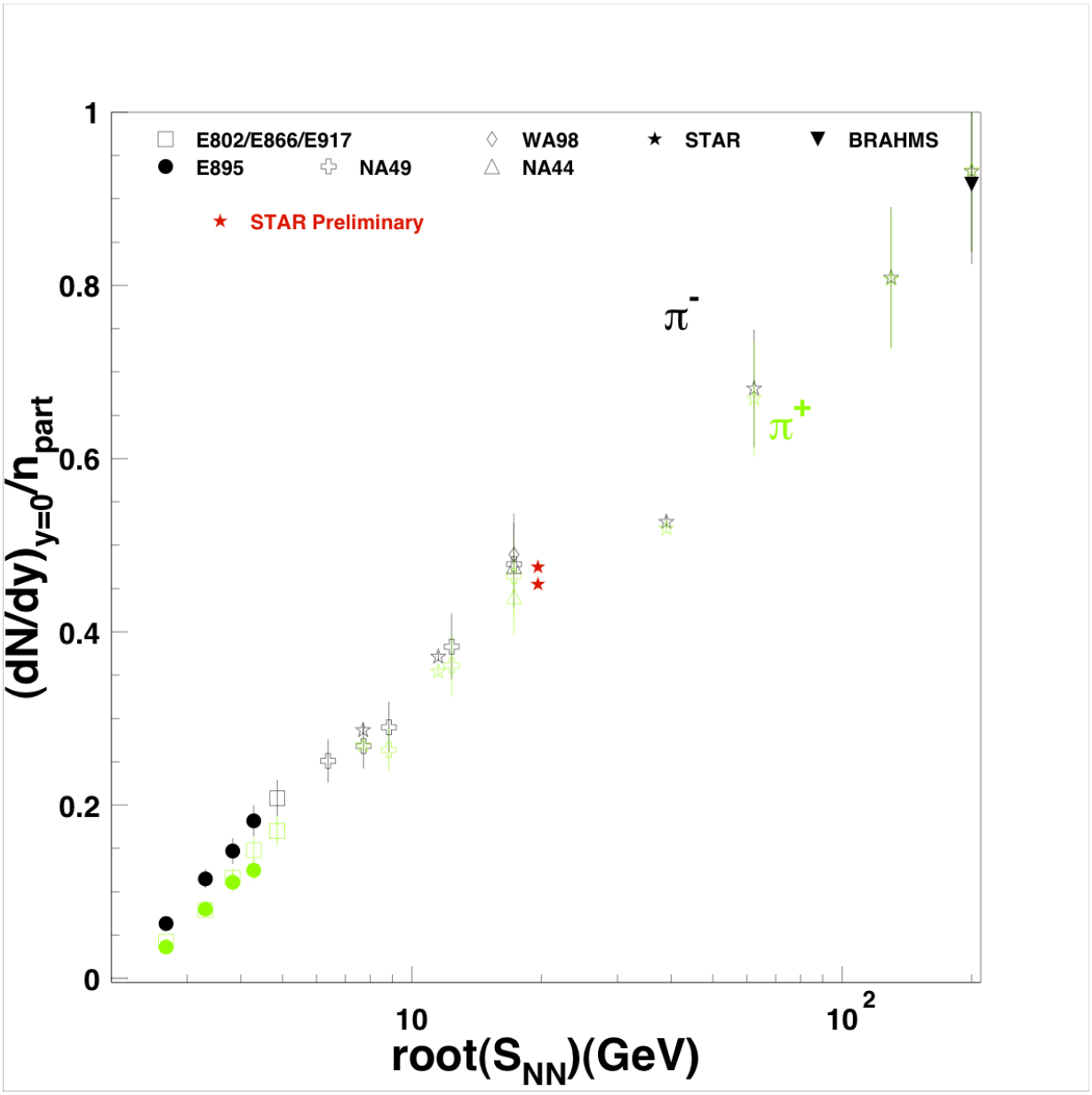

Figure 5.9: The number of pions produced per unit of rapidity normalized to the number of participating nucleons versus center of mass energy. Results for $Au+Au$ at $\sqrt{s_{NN}} = 19.6$ GeV are displayed in solid red stars. Scaled comparisons to other world data are also shown for $Au+Au$ collisions at 1.0 AGeV (KaoS [157]), at 2, 4, 6, and 8 AGeV (E895 [158,159]), and at 2, 4, 6, 8, and 10.8 AGeV (E866 [119, 160]). Yields and potentials also are shown for central Pb+Pb collisions at 20, 30, 40, 60, 80, and 158 AGeV (NA44 [161, 162], and NA49 [9, 163]). Additional data from references [30, 120, 164–169] are also included.

Figure 5.9 illustrates the number of pions produced per unit of rapidity normalized to the number of participating nucleons versus center of mass energy. Results for $Au + Au$ at $\sqrt{s_{NN}} = 19.6$ GeV are displayed in solid red stars. Pion distributions were fit with a

Bose-Einstein exponential for values $dN/dy_{\pi^+} = 160.615 \pm 1.765$ for π^+ and for π^- the fit obtains $dN/dy_{\pi^-} = 167.675 \pm 1.765$. Normalizing to the number of participants, we obtain the values $dN/dy_{\pi^+} = 0.455 \pm 0.005$ and $dN/dy_{\pi^-} = 0.475 \pm 0.005$, respectively, for the values in the figure.

Figure 5.10 illustrates the Kink discussed in Section 2.4 where the number of pions produced per unit of rapidity normalized to the number of participating nucleons is plotted against Fermi's measure, $F = \left[\frac{(\sqrt{s_{NN}}-2m_N)^3}{\sqrt{s_{NN}}}\right]^{\frac{1}{4}}$. Results for $Au + Au$ at $\sqrt{s_{NN}} = 19.6$ GeV are displayed in open red squares. Pion dN/dy is calculated as above, using a Bose-Einstein exponential and Fermi's measure for the 19.6 GeV data is $F = 4.1077$. Again, the pion values fall within world trends and further display the "kink" in the fitted slope and adds to the indication for the onset of deconfinement.

Figure 5.11 illustrates the Horn discussed in Section 2.4 where the number of kaons produced per unit of rapidity normalized to the number of participating nucleons is plotted as a function of center-of-mass energy. Results for Au+Au at $\sqrt{s_{NN}} = 19.6$ GeV are displayed in solid red stars. Kaon distributions were fit with a Bose-Einstein exponential for values $dN/dy_{K^+} = 28.2047 \pm 0.6707$ for K^+ and for K^- the fit obtains $dN/dy_{K^-} = 18.3207 \pm 0.6001$. Normalizing to the average number of participants, we obtain $dN/dy_{K^+} = 0.0799 \pm 0.0019$ and $dN/dy_{K^-} = 0.0519 \pm 0.0017$, respectively, which are the values plotted in the figure. These results are in line with world data and contribute to the pronouncement of the "horn" feature.

The Step discussed in Section 2.4 where the positively charged kaon temperature is plotted against center-of-mass energy Figure 5.12 displays is further cemented with the addition of STAR data in solid red stars. Data from collision energies of $Au + Au$ at $\sqrt{s_{NN}} = 7.7, 11.5, 19.6$ and 39 GeV are in the figure. All temperatures are obtained from a Bose-Einstein fit to the spectra. Particularly, the temperature for $\sqrt{s_{NN}} = 19.6$ GeV positively charged kaons is $T_{K^+} = 190.2 \pm 1.1$ MeV. This value for the temperature falls along trends of world data and further solidifies the idea of a softening of the equation of

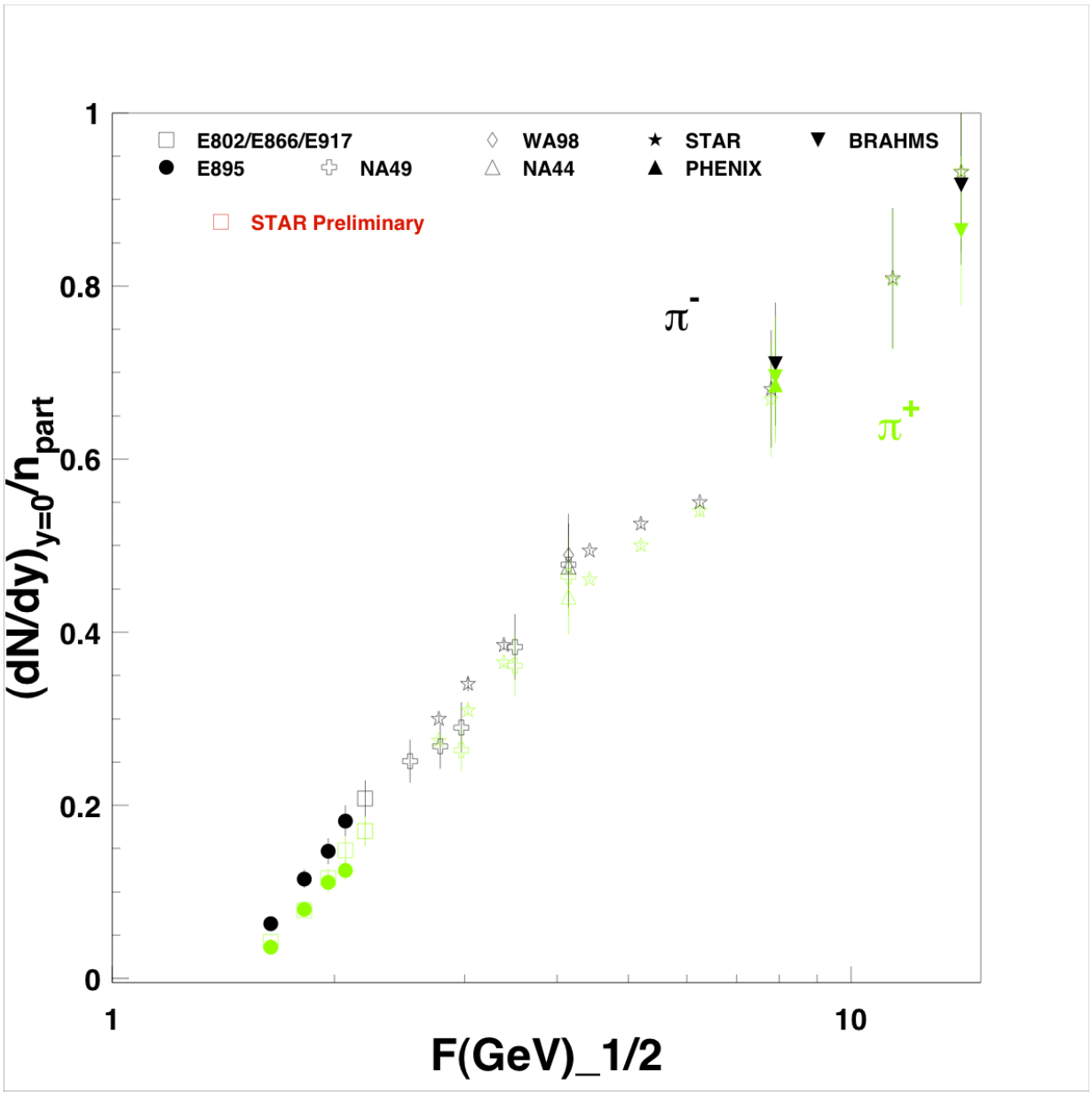

Figure 5.10: The Kink: the number of pions produced per unit of rapidity normalized to the number of participating nucleons versus Fermi's measure. Results for $Au + Au$ at $\sqrt{s_{NN}} = 19.6$ GeV are displayed in open red squares. Scaled comparisons to other world data are also shown for $Au + Au$ collisions at 1.0 AGeV (KaoS [157]), at 2, 4, 6, and 8 AGeV (E895 [158, 159]), and at 2, 4, 6, 8, and 10.8 AGeV (E866 [119, 160]). Yields and potentials also are shown for central Pb+Pb collisions at 20, 30, 40, 60, 80, and 158 AGeV (NA44 [161, 162], and NA49 [9, 163]). Additional data from references [30, 120, 164–169] are also included.

state, or the "step" structure of the plot.

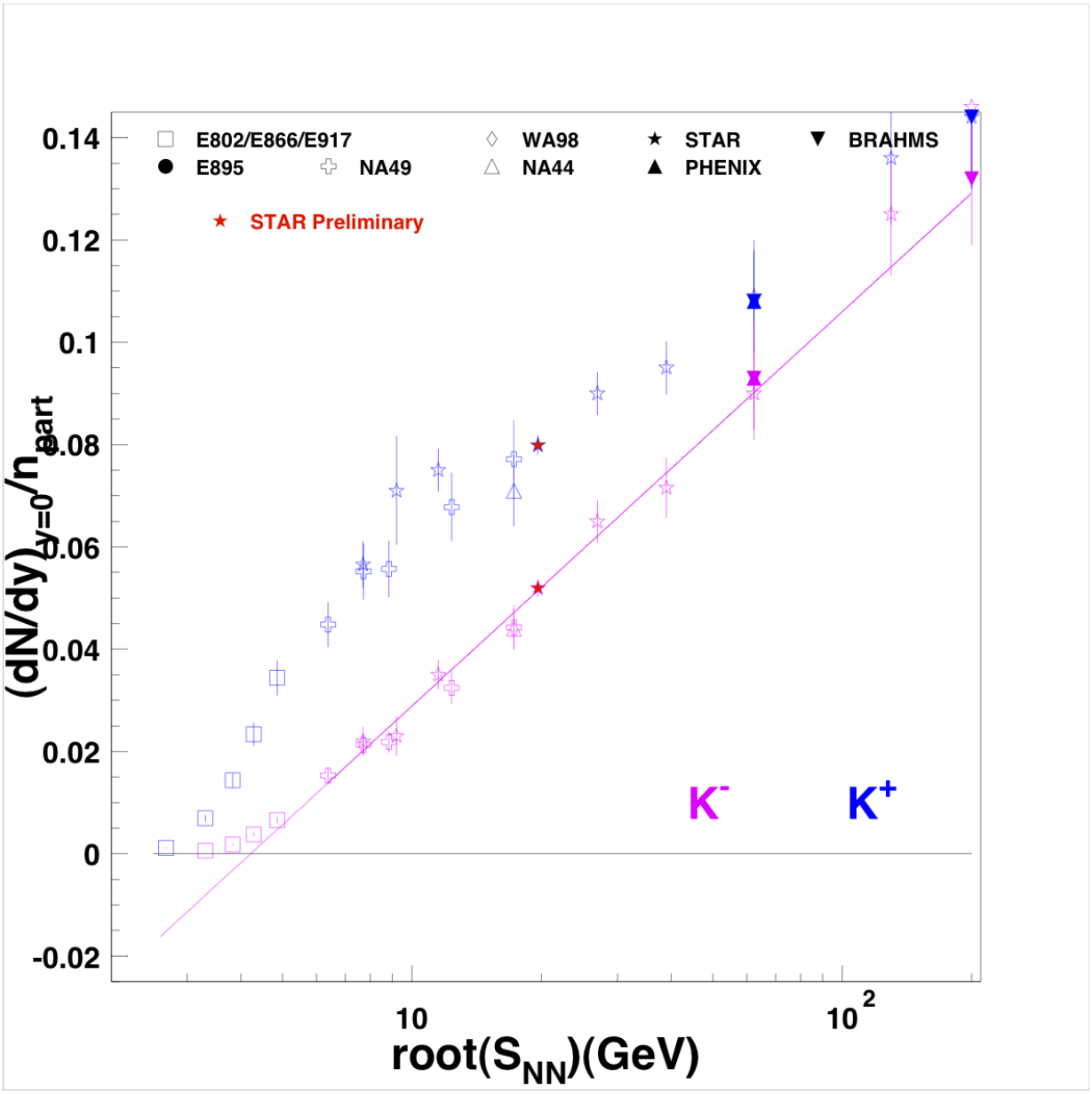

Figure 5.11: The Horn: the number of kaons produced per unit of rapidity normalized to the number of participating nucleons versus center-of-mass energy. Results for Au+Au at $\sqrt{s_{NN}} = 19.6$ GeV are displayed in solid red stars. Scaled comparisons to other world data are also shown for $Au + Au$ collisions at 1.0 AGeV (KaoS [157]), at 2, 4, 6, and 8 AGeV (E895 [158, 159]), and at 2, 4, 6, 8, and 10.8 AGeV (E866 [119, 160]). Yields and potentials also are shown for central Pb+Pb collisions at 20, 30, 40, 60, 80, and 158 AGeV (NA44 [161, 162], and NA49 [9, 163]). Additional data from references [30, 120, 164–169] are also included.

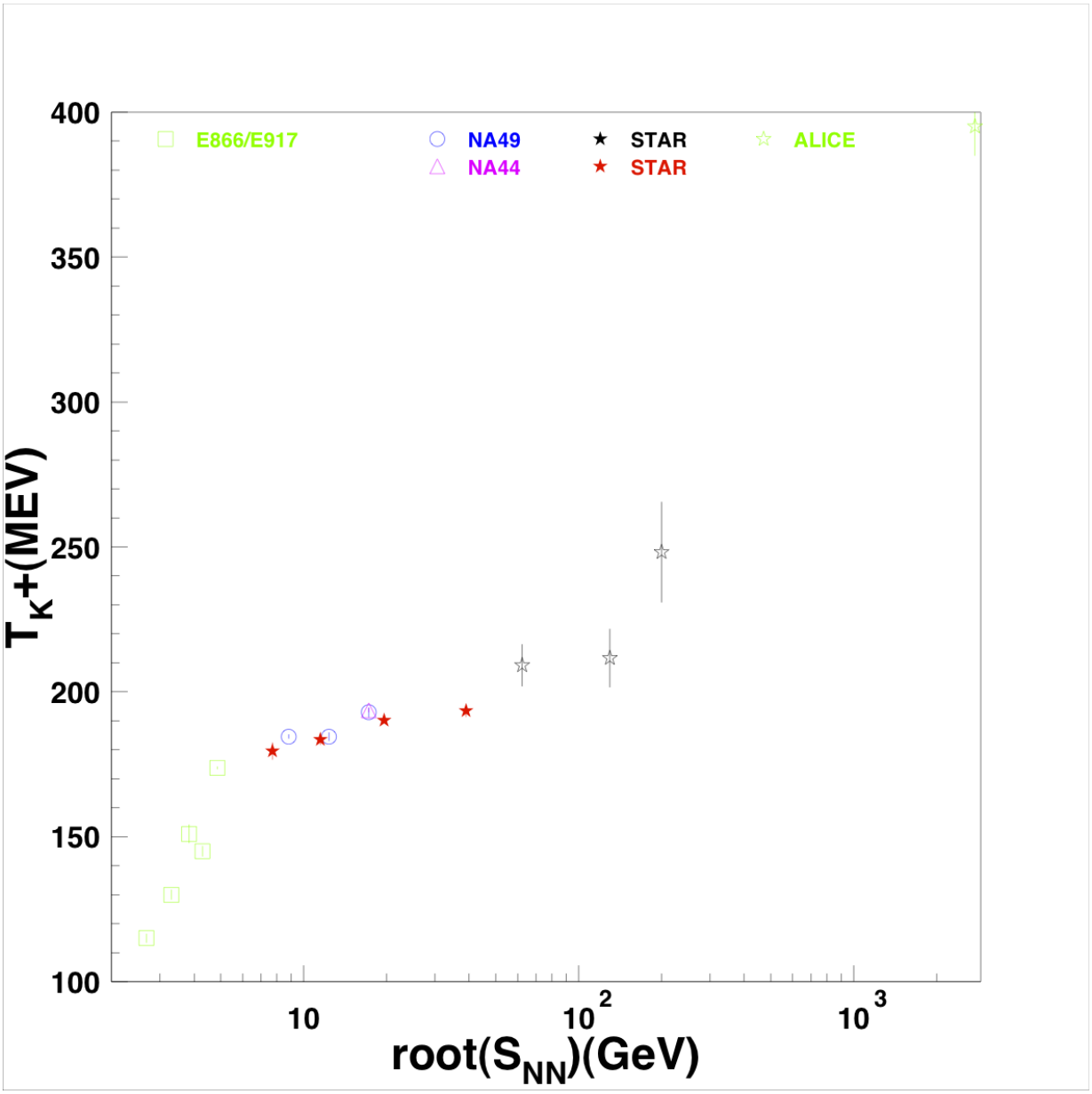

Figure 5.12: The Step discussed in Section 2.4 where the positively charged kaon temperature is plotted against center-of-mass energy. Results for $Au + Au$ at $\sqrt{s_{NN}} = 19.6$ GeV are displayed in solid red stars. Scaled comparisons to other world data are also shown for $Au + Au$ collisions at 1.0 AGeV (KaoS [157]), at 2, 4, 6, and 8 AGeV (E895 [158, 159]), and at 2, 4, 6, 8, and 10.8 AGeV (E866 [119, 160]). Yields and potentials also are shown for central Pb+Pb collisions at 20, 30, 40, 60, 80, and 158 AGeV (NA44 [161, 162], and NA49 [9, 163]). Additional data from references [30, 120, 164–169] are also included.

Chapter 6

Conclusion

Although the RHIC is a collider facility, it is possible to study fixed-target collisions using ions from the halo of the injected beam as the projectile and aluminum nuclei in the beam pipe as the target. The beam halo is likely comprised of heavy forward projectile fragments resulting from $Au + H$ beam-gas interactions in the warm bore between the D0 and DX dipole magnets or from ^{+78}Au ions resulting from electron capture off of He atoms in the cold bore of the main arc dipole magnets of RHIC.

Using the beam energies developed for the RHIC beam energy scan, STAR is able to study Au-like $+Al$ collisions at center-of-mass energies of 3.0, 3.5 and 4.5 GeV per nucleon pair. The STAR detector has been demonstrated to have good acceptance and particle identification capabilities at mid-rapidity for fixed-target collisions at these energies. The mid-rapidity pion and proton spectra have been measured and the slope parameters have been compared to previously published data for similar energies.

The shape of the ratios of positive to negative pions at low transverse mass has used to extract the Coulomb potential of the emission source. This Coulomb potential is created by the participating protons from the projectile and target which are transported to mid-rapidity during the collision. Comparisons of the Coulomb potential and the proton dN/dy can shed light of the emission radius and the lifetime of the source. Details of the pion ratios at low transverse mass allow for a better integration of the total emission ratio. This ratio helps clarify the production process which is expected to be dominated by the Delta

resonance at the lowest collisions energies and by pion pair production at higher energies.

For nominal $Au+Au$ collisions at the center-of-mass energy of 19.6 GeV per nucleon pair, pion, kaon and proton spectra have been measured and utilized to compare dN/dy's with previously published data at center-of-mass energies ranging from 1 GeV to 200 GeV per nucleon pair. Detailed comparisons of spectra, rapidity densities, particles ratios, and slope parameters have been made to the previously published data. The recent STAR analysis is consistent with previous results at the SPS. The rapidity densities are consistent with world trends for all species studied. Most species increase with collision energy; the exception is the protons, which decrease with collision energy as stopping is reduced in this energy range. The slope parameter of the positive kaons is seen to flatten across the energy range from 7 to 40 GeV. This has previously been interpreted as evidence of the onset of deconfinement. The recent STAR recent further refine this measurement.

In conclusion, it has been demonstrated that the STAR detector has good capabilities for fixed-target collisions. Data from these collisions can be used to extend the search for the critical point and the onset of deconfinement at STAR to energies below 7.7 GeV.

Appendices

Appendix A

$\sqrt{s_{\mathrm{NN}}} = 19.6$ GeV $Au+Au$ Gaussian Fits

The following pages are filled with the Gaussian fits ordered first by centrality bin, then particle type, then charge and finally the detector type which is making the identification. Pions will always come first in each section, followed by Kaons then protons.

A.1 The 70%-80% Centrality Class

This is the most peripheral bin of all centrality classes. All figures have a legend which tells of the fit parameters in the upper left corner. Axes are explained in the figure captions.

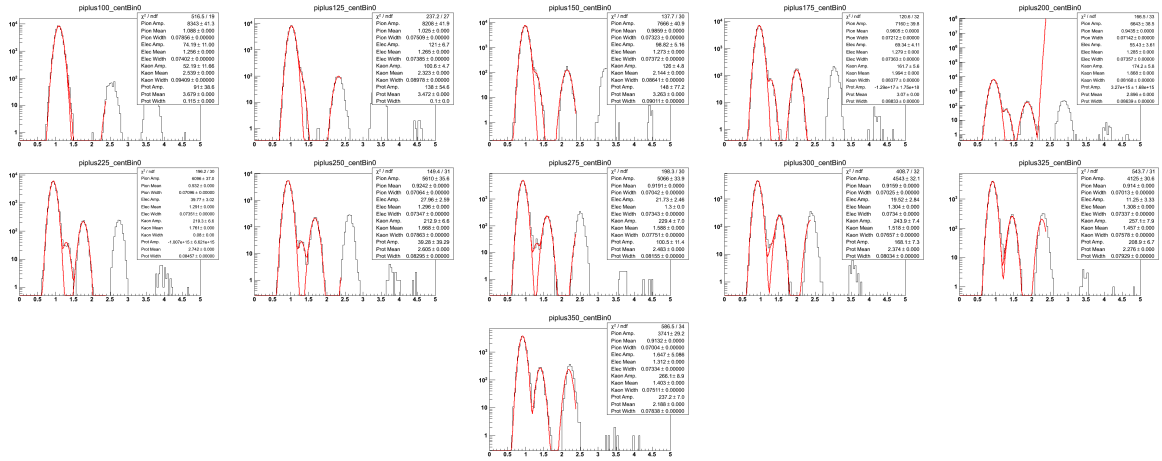

Figure A.1: Positive pion TPC fits for 70%-80% central events $Au+Au\sqrt{s_{NN}} = 19.6$ GeV. These are organized in 25 MeV bins in $m_T - m_\pi$ in a rapidity window of 0.1 units around mid-rapidity, $|y| < 0.05$. The Gaussian fits, drawn in red, are in $\log(10^6 \times dE/dx)$ and are of the $m_T - m_\pi =$ 0.100 to 0.500 GeV/c^2 range. The track data are represented in the black histogram.

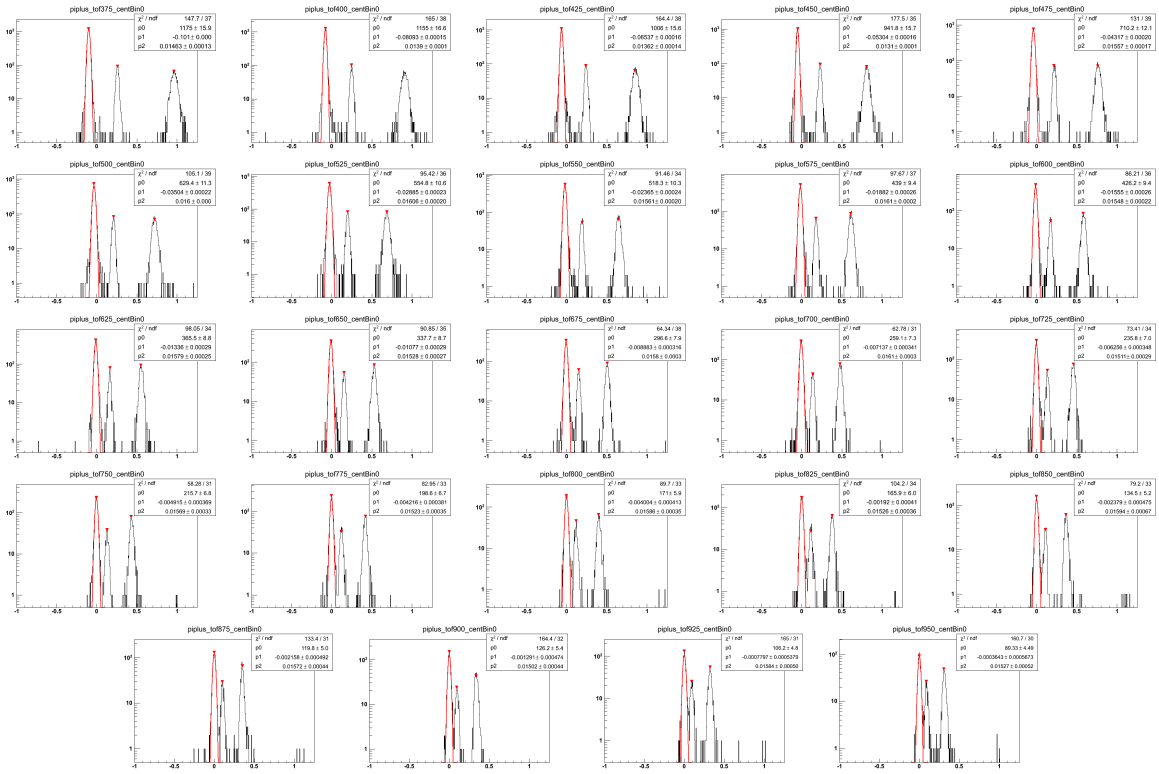

Figure A.2: Positive pion TOF fits for 70%-80% central events $Au+Au\sqrt{s_{NN}} = 19.6$ GeV. These are organized in 25 MeV bins in $m_T - m_\pi$ in a rapidity window of 0.1 units around mid-rapidity, $|y| < 0.05$. The Gaussian fits, drawn in red, are in $\beta^{-1}_{\text{expected}} - \beta^{-1}_{\text{measured}}$ and are of the $m_T - m_\pi =$ 0.350 to 1.0 GeV/c^2 range. The track data are represented in the black histogram.

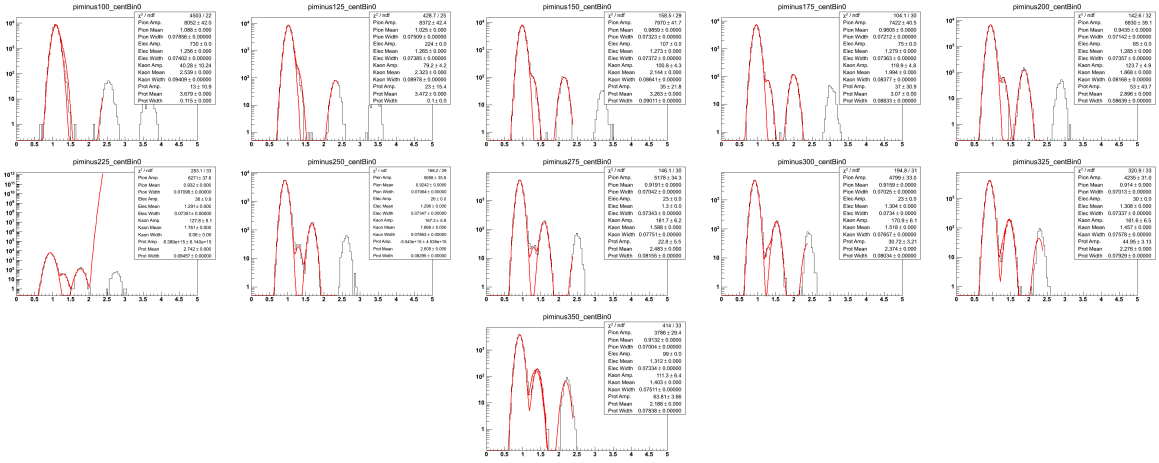

Figure A.3: Negative pion TPC fits for 70%-80% central events $Au+Au\sqrt{s_{NN}} = 19.6$ GeV. These are organized in 25 MeV bins in $m_T - m_\pi$ in a rapidity window of 0.1 units around mid-rapidity, $|y| < 0.05$. The Gaussian fits, drawn in red, are in $\log(10^6 \times dE/dx)$ and are of the $m_T - m_\pi =$ 0.100 to 0.500 GeV/c^2 range. The track data are represented in the black histogram.

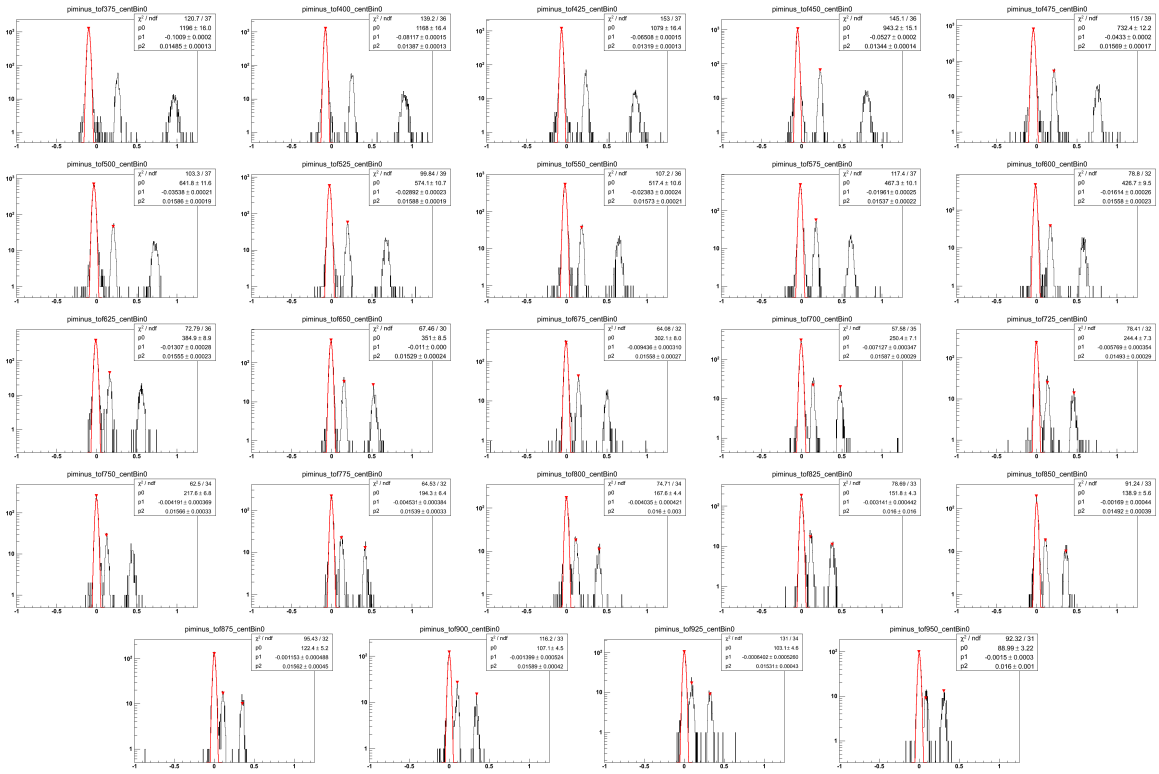

Figure A.4: Negative pion TOF fits for 70%-80% central events $Au+Au\sqrt{s_{NN}} = 19.6$ GeV. These are organized in 25 MeV bins in $m_T - m_\pi$ in a rapidity window of 0.1 units around mid-rapidity, $|y| < 0.05$. The Gaussian fits, drawn in red, are in $\beta^{-1}_{\text{expected}} - \beta^{-1}_{\text{measured}}$ and are of the $m_T - m_\pi =$ 0.350 to 1.0 GeV/c^2 range. The track data are represented in the black histogram.

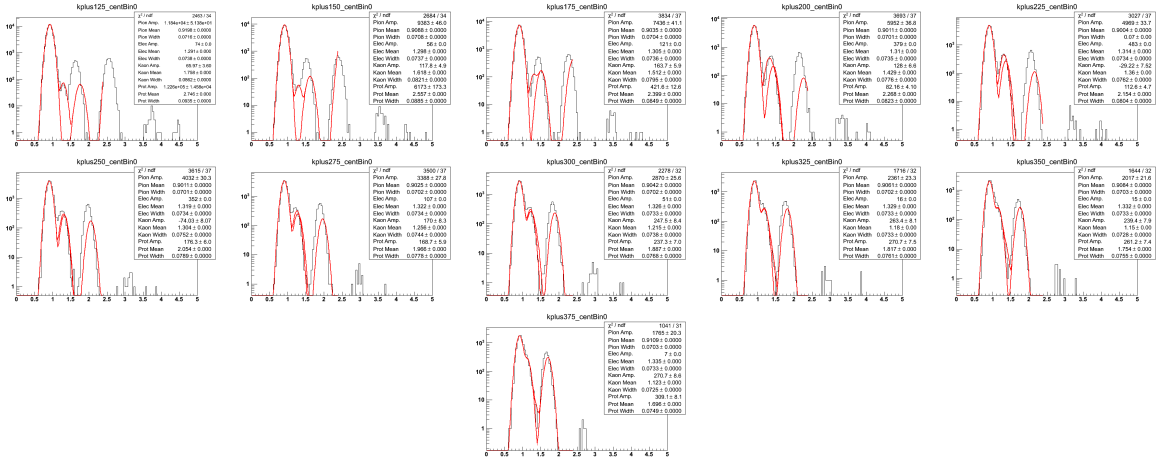

Figure A.5: Positive kaon TPC fits for 70%-80% central events $Au+Au\sqrt{s_{NN}} = 19.6$ GeV. These are organized in 25 MeV bins in $m_T - m_K$ in a rapidity window of 0.1 units around mid-rapidity, $|y| < 0.05$. The Gaussian fits, drawn in red, are in $\log(10^6 \times dE/dx)$ and are of the $m_T - m_K =$ 0.100 to 0.500 GeV/c^2 range. The track data are represented in the black histogram.

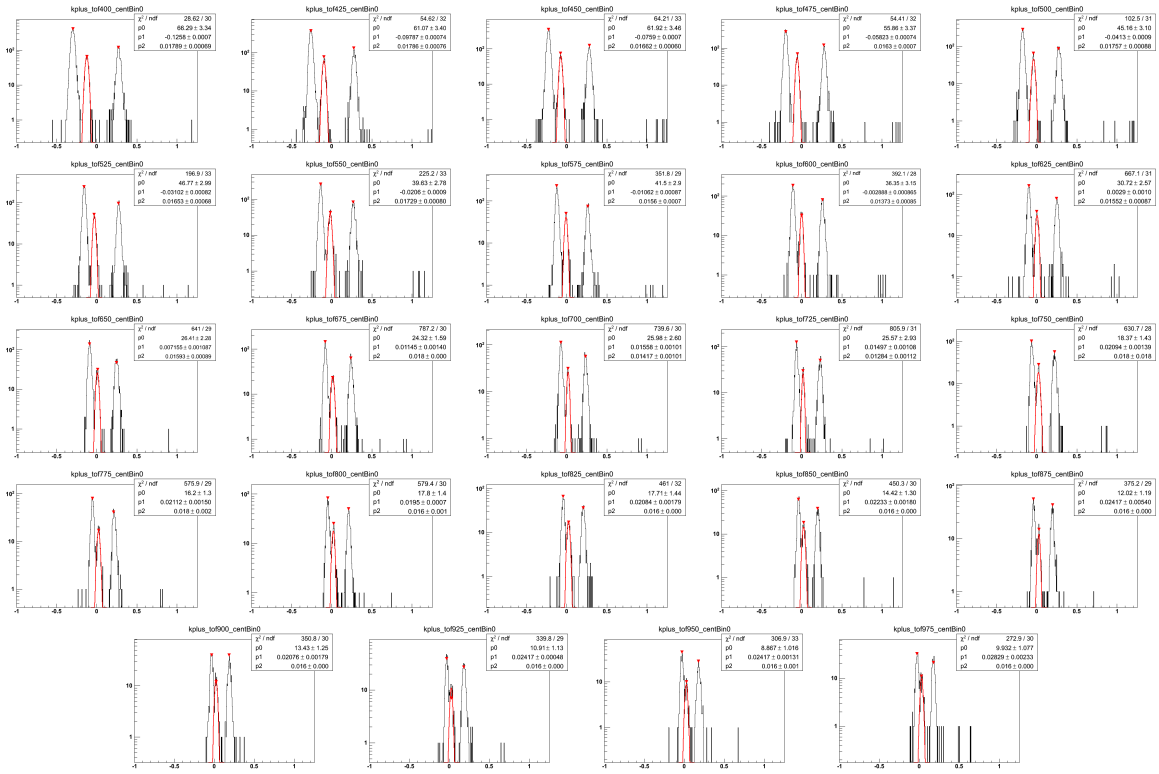

Figure A.6: Positive kaon TOF fits for 70%-80% central events $Au+Au\sqrt{s_{NN}} = 19.6$ GeV. These are organized in 25 MeV bins in $m_T - m_K$ in a rapidity window of 0.1 units around mid-rapidity, $|y| < 0.05$. The Gaussian fits, drawn in red, are in $\beta^{-1}_{\text{expected}} - \beta^{-1}_{\text{measured}}$ and are of the $m_T - m_K =$ 0.350 to 1.0 GeV/c^2 range. The track data are represented in the black histogram.

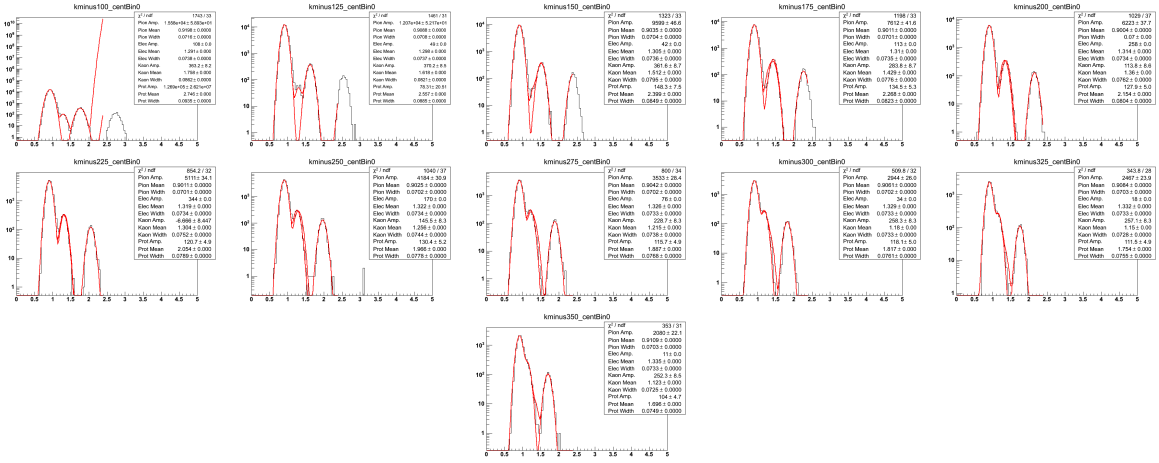

Figure A.7: Negative kaon TPC fits for 70%-80% central events $Au+Au\sqrt{s_{NN}} = 19.6$ GeV. These are organized in 25 MeV bins in $m_T - m_K$ in a rapidity window of 0.1 units around mid-rapidity, $|y| < 0.05$. The Gaussian fits, drawn in red, are in $\log(10^6 \times dE/dx)$ and are of the $m_T - m_K =$ 0.100 to 0.500 GeV/c^2 range. The track data are represented in the black histogram.

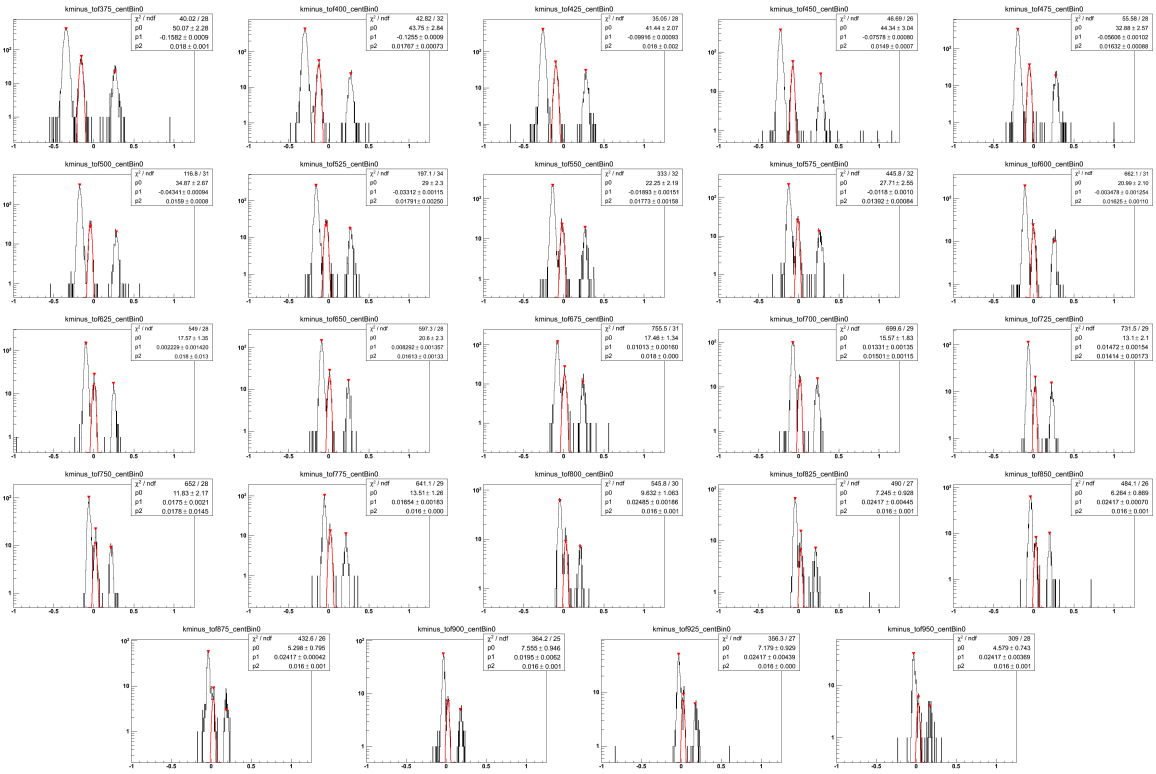

Figure A.8: Negative kaon TOF fits for 70%-80% central events $Au+Au\sqrt{s_{NN}} = 19.6$ GeV. These are organized in 25 MeV bins in $m_T - m_K$ in a rapidity window of 0.1 units around mid-rapidity, $|y| < 0.05$. The Gaussian fits, drawn in red, are in $\beta^{-1}_{\text{expected}} - \beta^{-1}_{\text{measured}}$ and are of the $m_T - m_K =$ 0.350 to 1.0 GeV/c^2 range. The track data are represented in the black histogram.

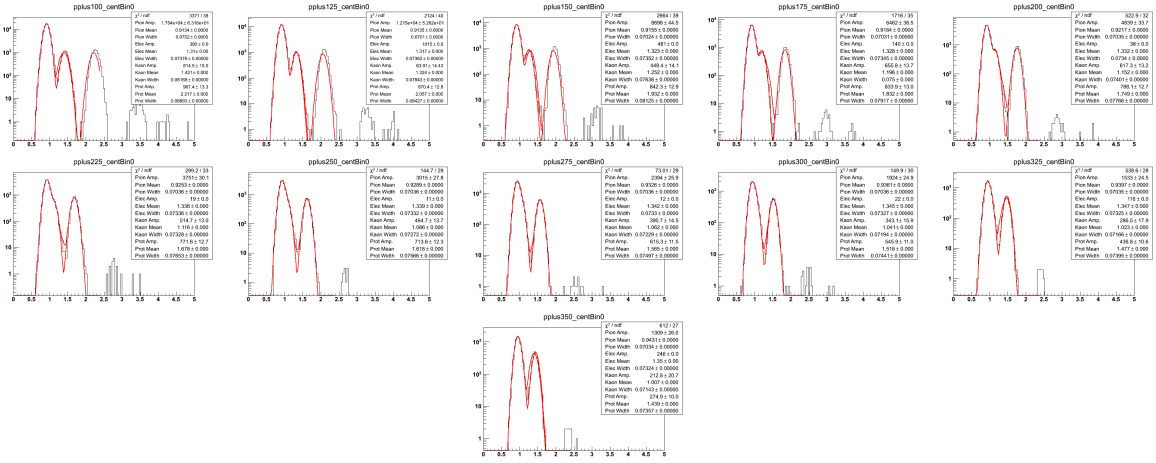

Figure A.9: Positive proton TPC fits for 70%-80% central events $Au+Au\sqrt{s_{NN}} = 19.6$ GeV. These are organized in 25 MeV bins in $m_T - m_p$ in a rapidity window of 0.1 units around mid-rapidity, $|y| < 0.05$. The Gaussian fits, drawn in red, are in $\log(10^6 \times dE/dx)$ and are of the $m_T - m_p =$ 0.100 to 0.500 GeV/c^2 range. The track data are represented in the black histogram.

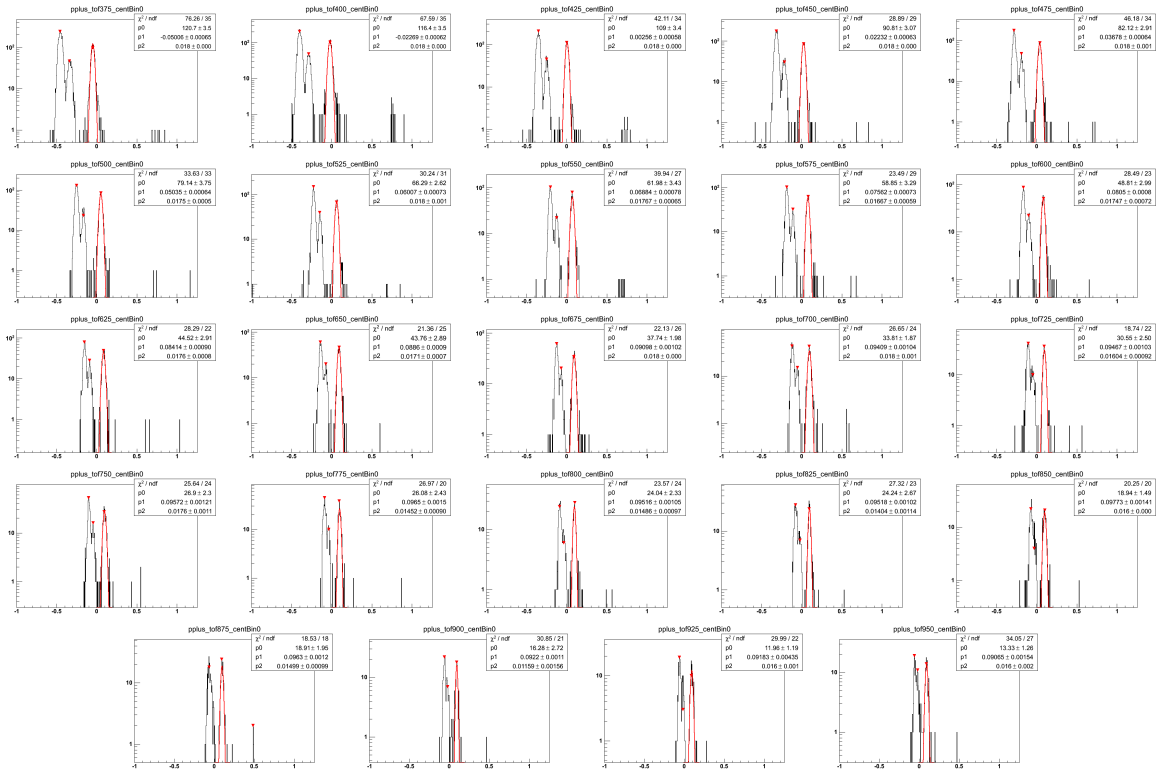

Figure A.10: Positive proton TOF fits for 70%-80% central events $Au + Au\sqrt{s_{NN}} = 19.6$ GeV. These are organized in 25 MeV bins in $m_T - m_p$ in a rapidity window of 0.1 units around mid-rapidity, $|y| < 0.05$. The Gaussian fits, drawn in red, are in $\beta^{-1}_{\text{expected}} - \beta^{-1}_{\text{measured}}$ and are of the $m_T - m_p = 0.350$ to 1.0 GeV/c^2 range. The track data are represented in the black histogram.

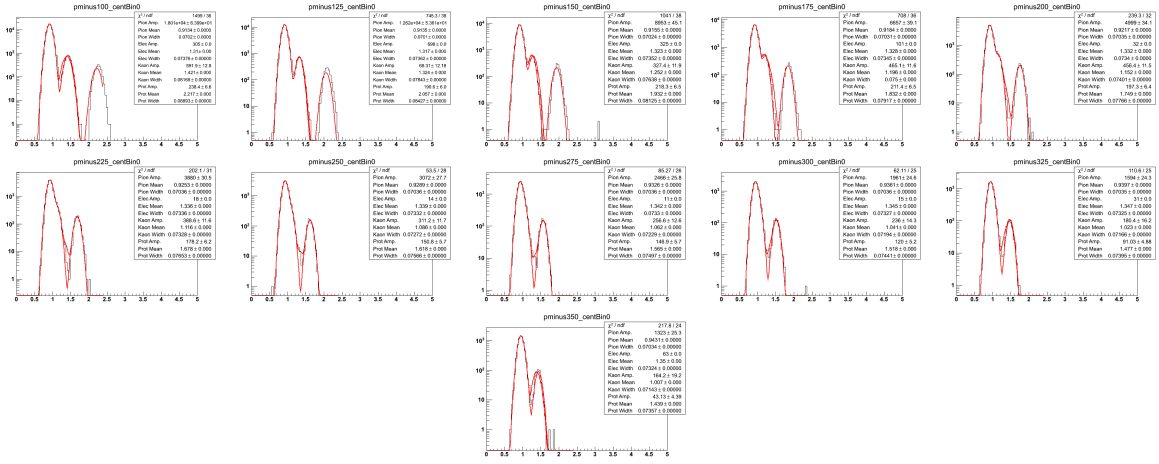

Figure A.11: Negative proton TPC fits for 70%-80% central events $Au + Au\sqrt{s_{NN}} = 19.6$ GeV. These are organized in 25 MeV bins in $m_T - m_p$ in a rapidity window of 0.1 units around mid-rapidity, $|y| < 0.05$. The Gaussian fits, drawn in red, are in $\log(10^6 \times dE/dx)$ and are of the $m_T - m_p = 0.100$ to 0.500 GeV/c^2 range. The track data are represented in the black histogram.

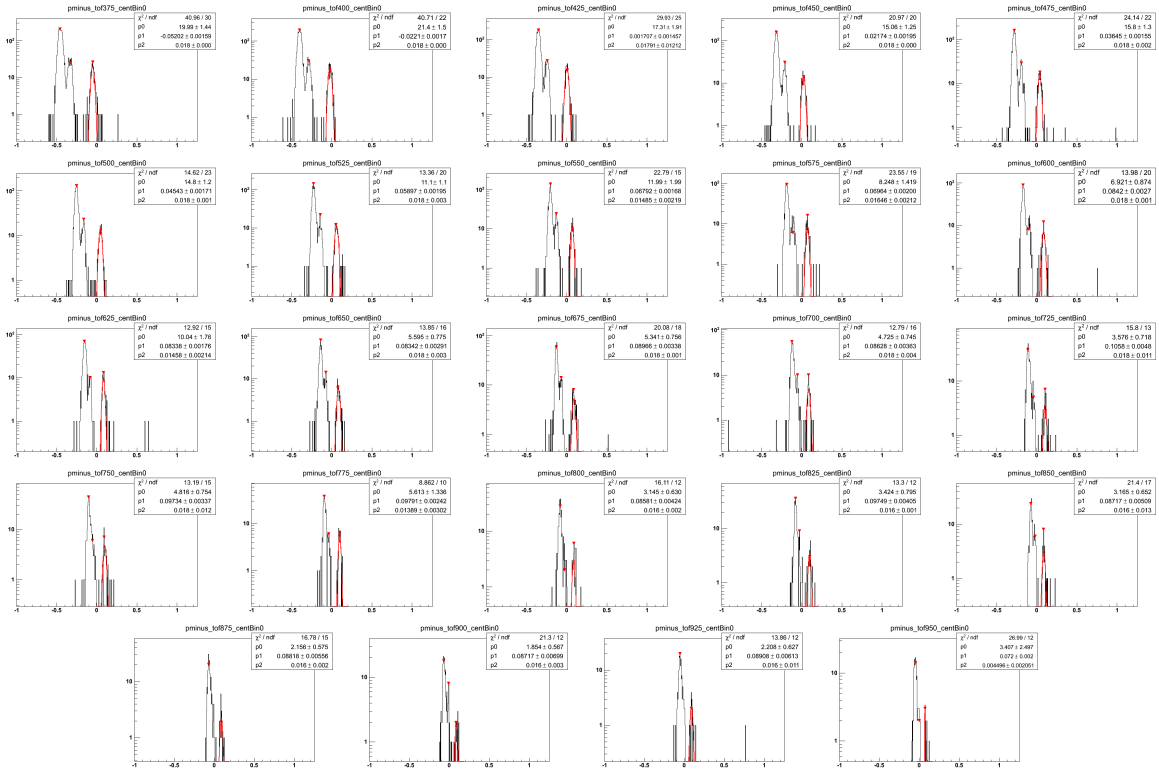

Figure A.12: Negative proton TOF fits for 70%-80% central events $Au + Au\sqrt{s_{NN}} = 19.6$ GeV. These are organized in 25 MeV bins in $m_T - m_p$ in a rapidity window of 0.1 units around mid-rapidity, $|y| < 0.05$. The Gaussian fits, drawn in red, are in $\beta^{-1}_{\text{expected}} - \beta^{-1}_{\text{measured}}$ and are of the $m_T - m_p = 0.350$ to 1.0 GeV/c^2 range. The track data are represented in the black histogram.

A.2 The 60%-70% Centrality Class

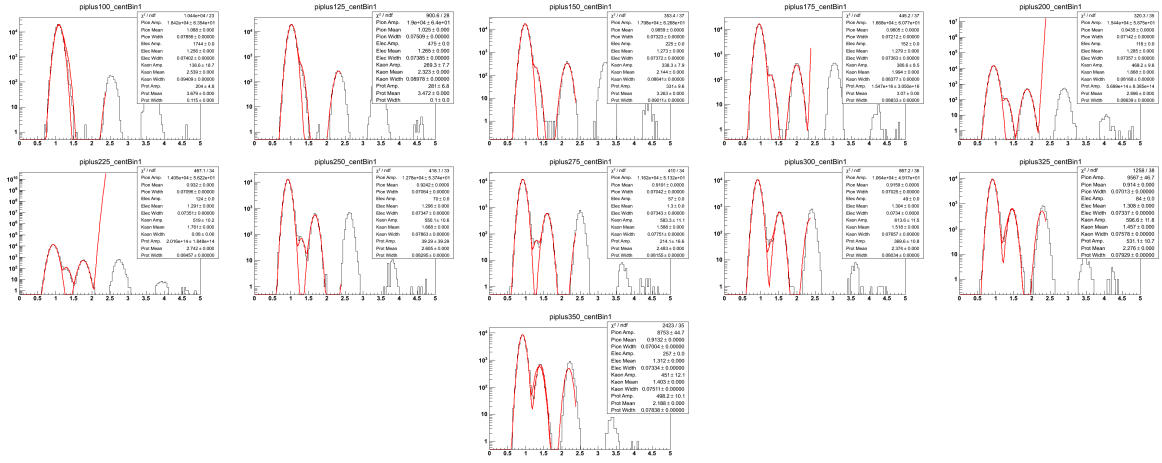

Figure A.13: Positive pion TPC fits for 60%-70% central events $Au+Au\sqrt{s_{NN}} = 19.6$ GeV. These are organized in 25 MeV bins in $m_T - m_\pi$ in a rapidity window of 0.1 units around mid-rapidity, $|y| < 0.05$. The Gaussian fits, drawn in red, are in $\log(10^6 \times dE/dx)$ and are of the $m_T - m_\pi =$ 0.100 to 0.500 GeV/c^2 range. The track data are represented in the black histogram.

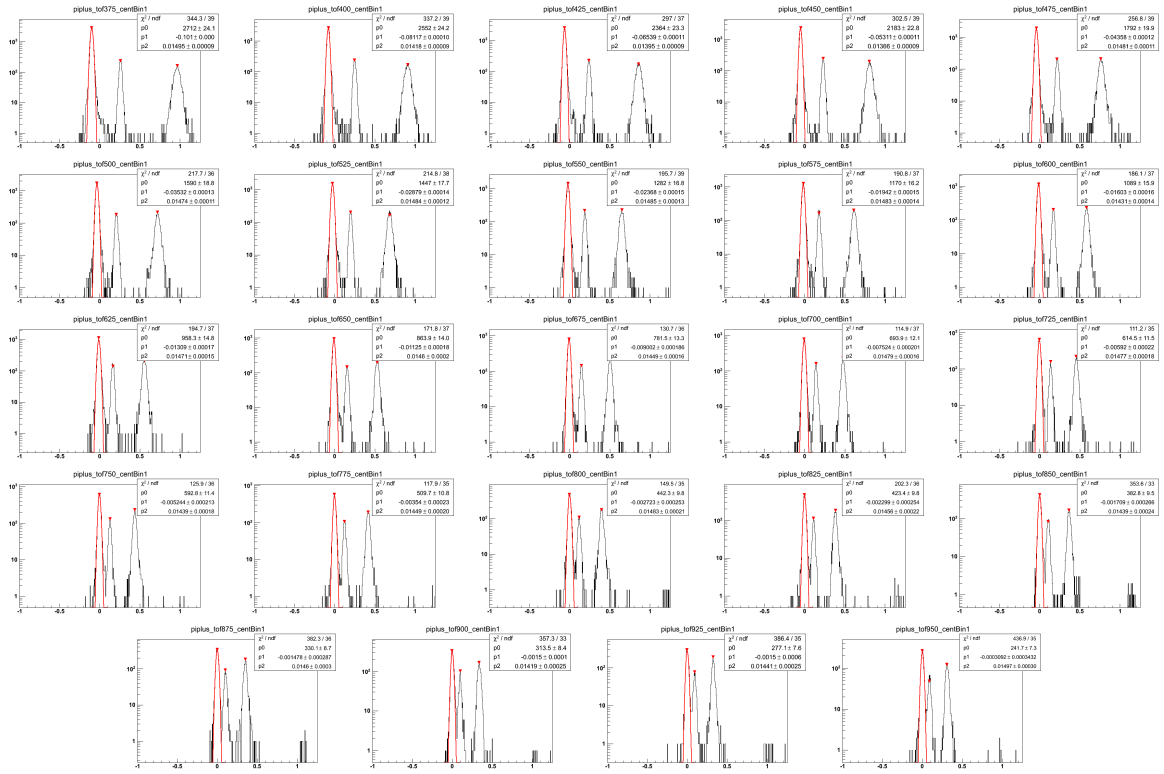

Figure A.14: Positive pion TOF fits for 60%-70% central events $Au+Au\sqrt{s_{NN}} = 19.6$ GeV. These are organized in 25 MeV bins in $m_T - m_\pi$ in a rapidity window of 0.1 units around mid-rapidity, $|y| < 0.05$. The Gaussian fits, drawn in red, are in $\beta^{-1}_{\text{expected}} - \beta^{-1}_{\text{measured}}$ and are of the $m_T - m_\pi = 0.350$ to 1.0 GeV/c^2 range. The track data are represented in the black histogram.

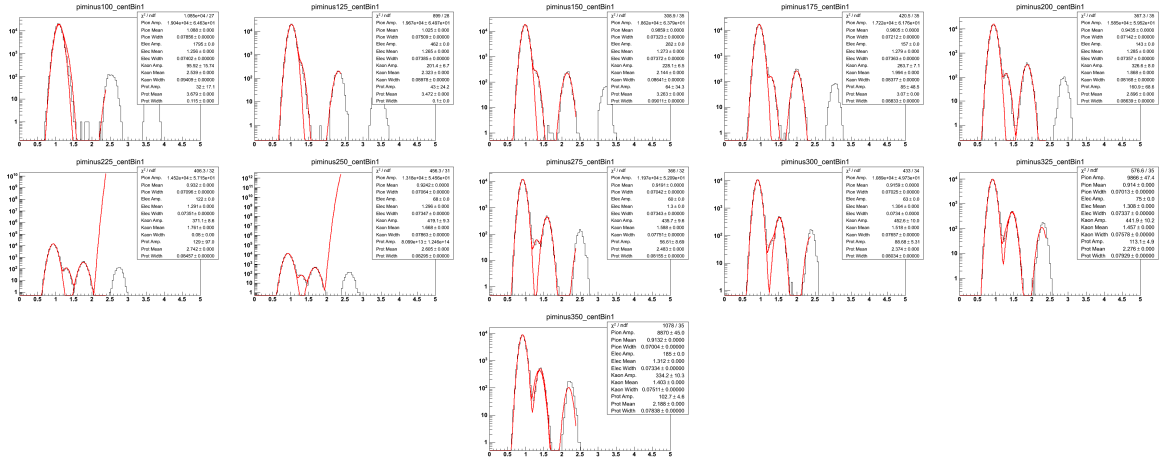

Figure A.15: Negative pion TPC fits for 60%-70% central events $Au+Au\sqrt{s_{NN}} = 19.6$ GeV. These are organized in 25 MeV bins in $m_T - m_\pi$ in a rapidity window of 0.1 units around mid-rapidity, $|y| < 0.05$. The Gaussian fits, drawn in red, are in $\log(10^6 \times dE/dx)$ and are of the $m_T - m_\pi = 0.100$ to 0.500 GeV/c^2 range. The track data are represented in the black histogram.

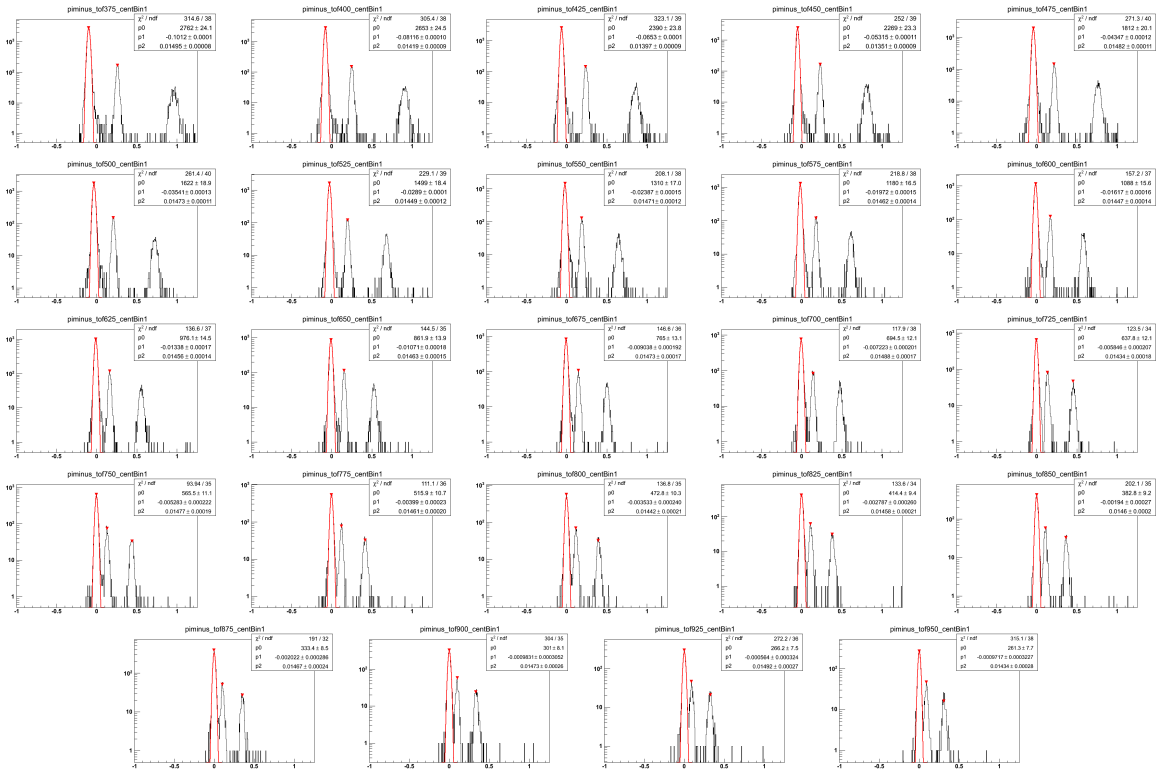

Figure A.16: Negative pion TOF fits for 60%-70% central events $Au+Au\sqrt{s_{NN}} = 19.6$ GeV. These are organized in 25 MeV bins in $m_T - m_\pi$ in a rapidity window of 0.1 units around mid-rapidity, $|y| < 0.05$. The Gaussian fits, drawn in red, are in $\beta^{-1}_{\text{expected}} - \beta^{-1}_{\text{measured}}$ and are of the $m_T - m_\pi = 0.350$ to 1.0 GeV/c^2 range. The track data are represented in the black histogram.

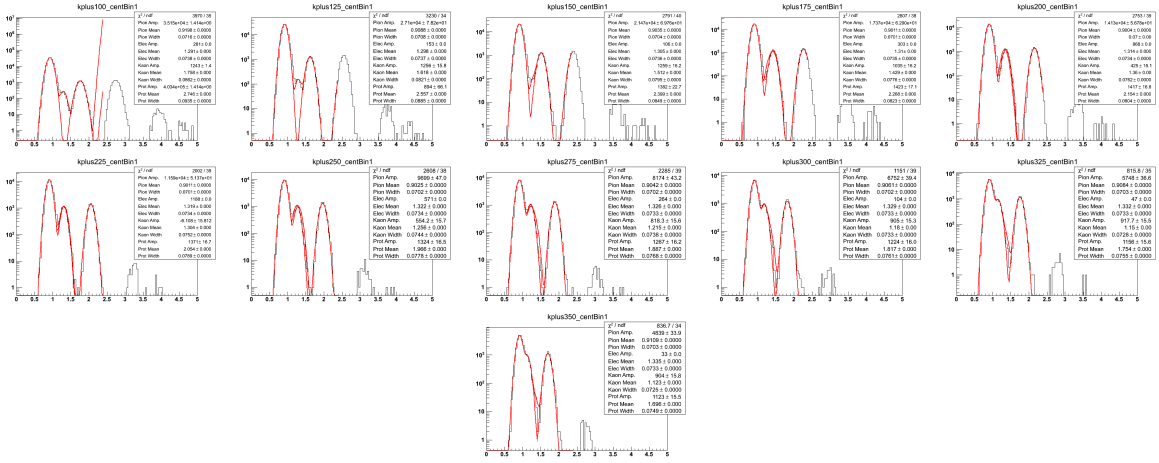

Figure A.17: Positive kaon TPC fits for 60%-70% central events $Au+Au\sqrt{s_{NN}} = 19.6$ GeV. These are organized in 25 MeV bins in $m_T - m_K$ in a rapidity window of 0.1 units around mid-rapidity, $|y| < 0.05$. The Gaussian fits, drawn in red, are in $\log(10^6 \times dE/dx)$ and are of the $m_T - m_K = 0.100$ to 0.500 GeV/c^2 range. The track data are represented in the black histogram.

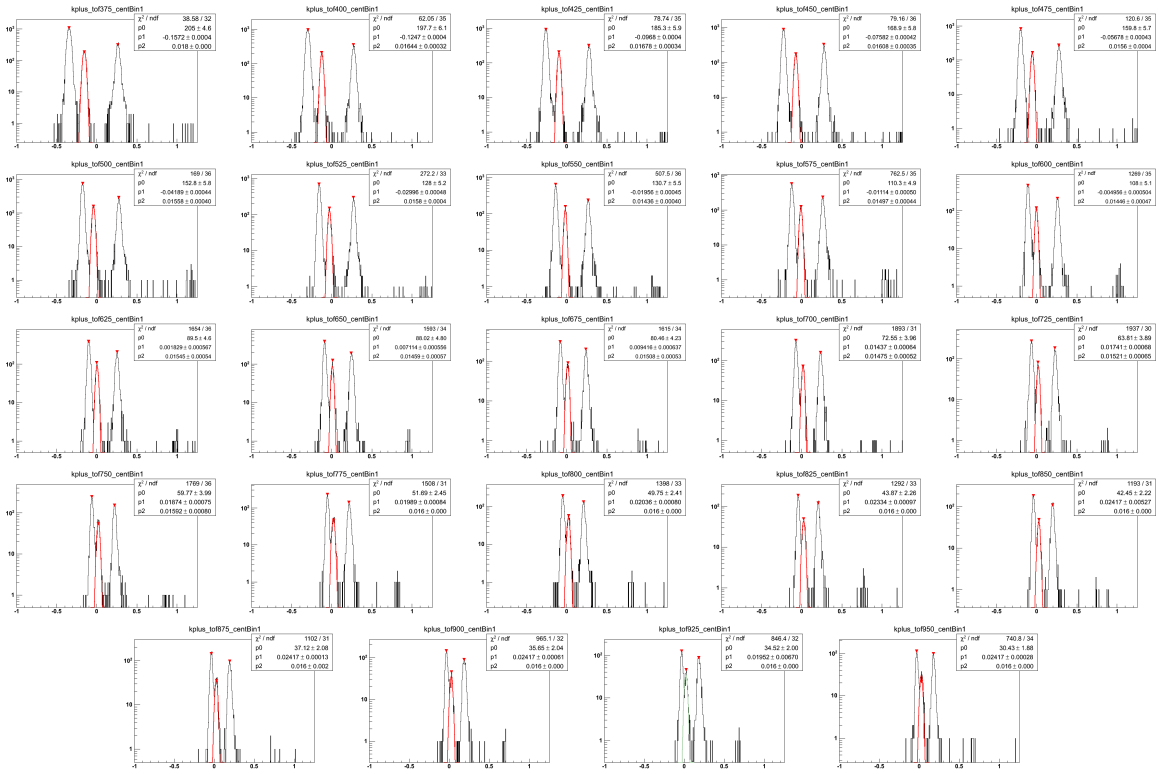

Figure A.18: Positive kaon TOF fits for 60%-70% central events $Au+Au\sqrt{s_{NN}} = 19.6$ GeV. These are organized in 25 MeV bins in $m_T - m_K$ in a rapidity window of 0.1 units around mid-rapidity, $|y| < 0.05$. The Gaussian fits, drawn in red, are in $\beta^{-1}_{\text{expected}} - \beta^{-1}_{\text{measured}}$ and are of the $m_T - m_K =$ 0.350 to 1.0 GeV/c^2 range. The track data are represented in the black histogram.

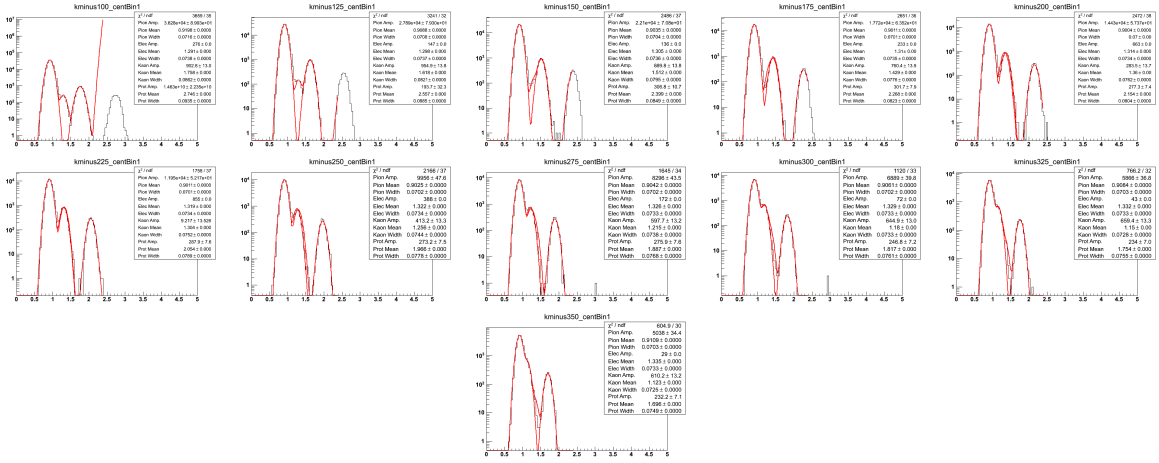

Figure A.19: Negative kaon TPC fits for 60%-70% central events $Au+Au\sqrt{s_{NN}} = 19.6$ GeV. These are organized in 25 MeV bins in $m_T - m_K$ in a rapidity window of 0.1 units around mid-rapidity, $|y| < 0.05$. The Gaussian fits, drawn in red, are in $\log(10^6 \times dE/dx)$ and are of the $m_T - m_K =$ 0.100 to 0.500 GeV/c^2 range. The track data are represented in the black histogram.

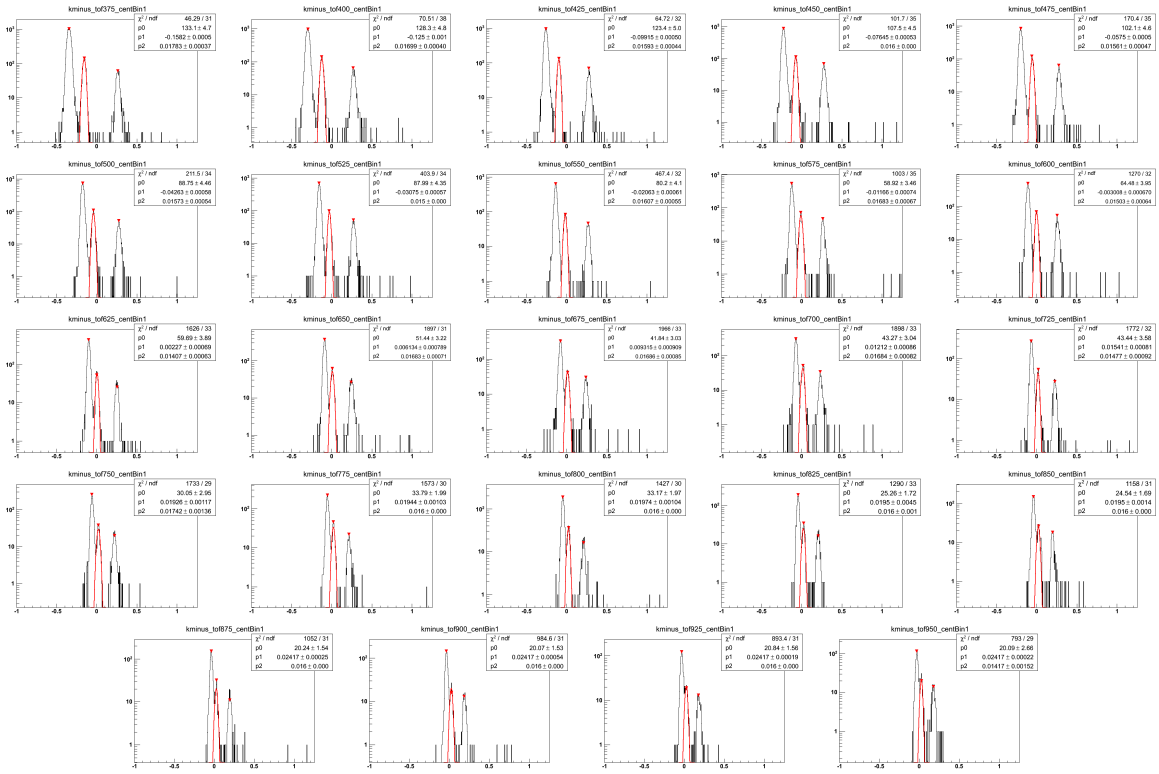

Figure A.20: Negative kaon TOF fits for 60%-70% central events $Au + Au\sqrt{s_{NN}} = 19.6$ GeV. These are organized in 25 MeV bins in $m_T - m_K$ in a rapidity window of 0.1 units around mid-rapidity, $|y| < 0.05$. The Gaussian fits, drawn in red, are in $\beta^{-1}_{\text{expected}} - \beta^{-1}_{\text{measured}}$ and are of the $m_T - m_K = 0.350$ to 1.0 GeV/c^2 range. The track data are represented in the black histogram.

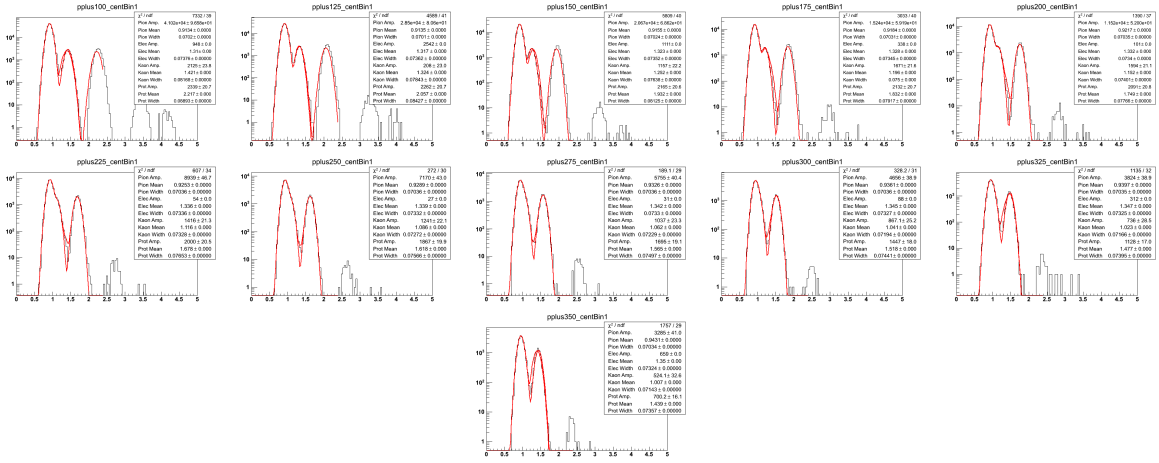

Figure A.21: Positive proton TPC fits for 60%-70% central events $Au + Au\sqrt{s_{NN}} = 19.6$ GeV. These are organized in 25 MeV bins in $m_T - m_p$ in a rapidity window of 0.1 units around mid-rapidity, $|y| < 0.05$. The Gaussian fits, drawn in red, are in $\log(10^6 \times dE/dx)$ and are of the $m_T - m_p = 0.100$ to 0.500 GeV/c^2 range. The track data are represented in the black histogram.

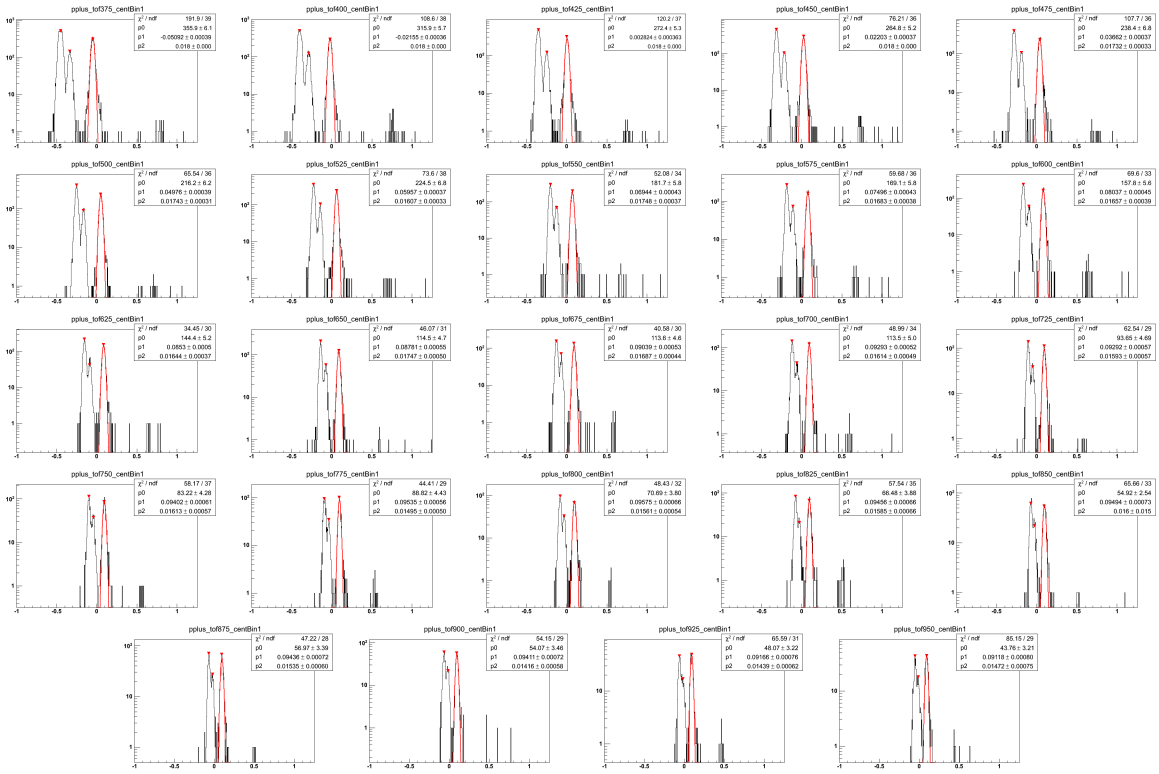

Figure A.22: Positive proton TOF fits for 60%-70% central events $Au + Au\sqrt{s_{NN}} = 19.6$ GeV. These are organized in 25 MeV bins in $m_T - m_p$ in a rapidity window of 0.1 units around mid-rapidity, $|y| < 0.05$. The Gaussian fits, drawn in red, are in $\beta^{-1}_{\text{expected}} - \beta^{-1}_{\text{measured}}$ and are of the $m_T - m_p = 0.350$ to 1.0 GeV/c^2 range. The track data are represented in the black histogram.

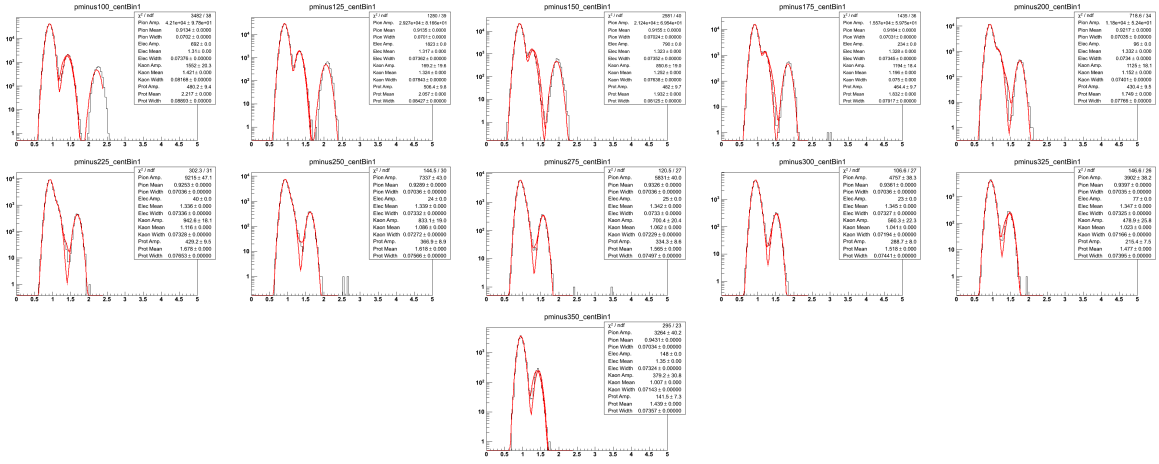

Figure A.23: Negative proton TPC fits for 60%-70% central events $Au + Au\sqrt{s_{NN}} = 19.6$ GeV. These are organized in 25 MeV bins in $m_T - m_p$ in a rapidity window of 0.1 units around mid-rapidity, $|y| < 0.05$. The Gaussian fits, drawn in red, are in $\log(10^6 \times dE/dx)$ and are of the $m_T - m_p = 0.100$ to 0.500 GeV/c^2 range. The track data are represented in the black histogram.

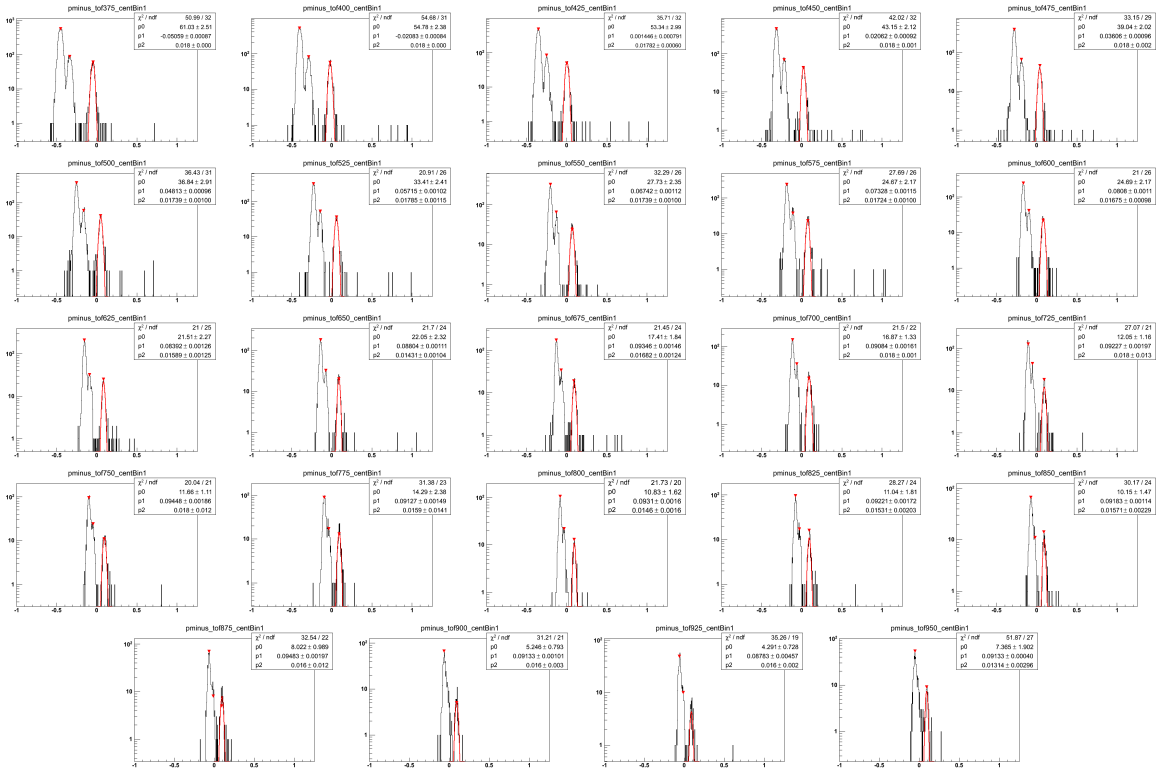

Figure A.24: Negative proton TOF fits for 60%-70% central events $Au + Au\sqrt{s_{NN}} = 19.6$ GeV. These are organized in 25 MeV bins in $m_T - m_p$ in a rapidity window of 0.1 units around mid-rapidity, $|y| < 0.05$. The Gaussian fits, drawn in red, are in $\beta^{-1}_{\text{expected}} - \beta^{-1}_{\text{measured}}$ and are of the $m_T - m_p = 0.350$ to 1.0 GeV/c^2 range. The track data are represented in the black histogram.

A.3 The 50%-60% Centrality Class

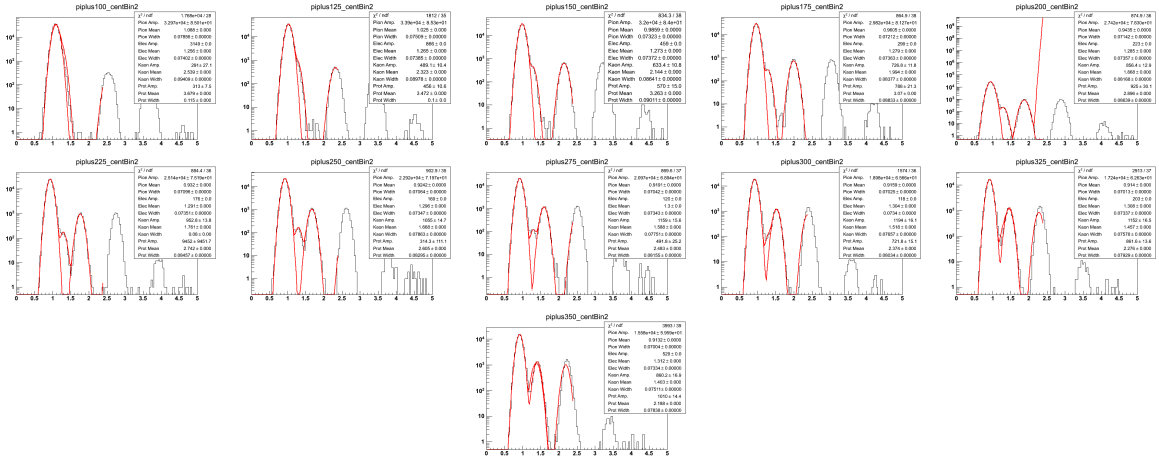

Figure A.25: Positive pion TPC fits for 50%-60% central events $Au+Au\sqrt{s_{NN}} = 19.6$ GeV. These are organized in 25 MeV bins in $m_T - m_\pi$ in a rapidity window of 0.1 units around mid-rapidity, $|y| < 0.05$. The Gaussian fits, drawn in red, are in $\log(10^6 \times dE/dx)$ and are of the $m_T - m_\pi =$ 0.100 to 0.500 GeV/c^2 range. The track data are represented in the black histogram.

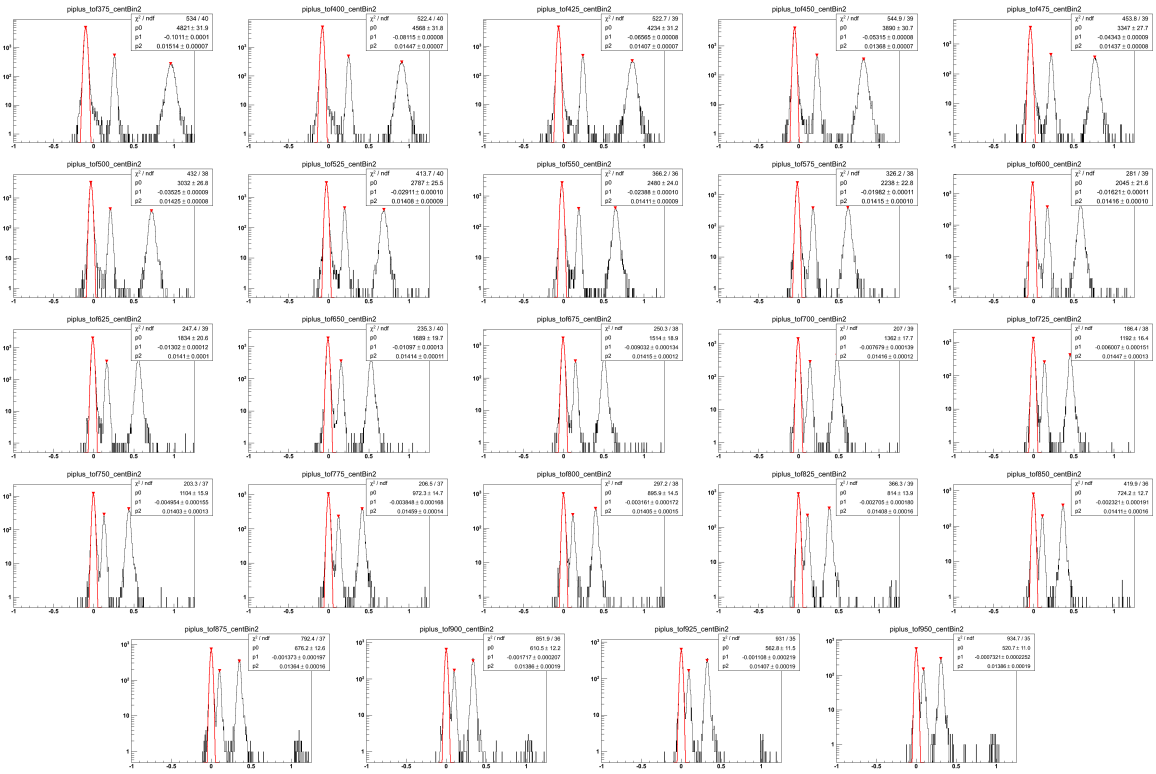

Figure A.26: Positive pion TOF fits for 50%-60% central events $Au+Au\sqrt{s_{NN}} = 19.6$ GeV. These are organized in 25 MeV bins in $m_T - m_\pi$ in a rapidity window of 0.1 units around mid-rapidity, $|y| < 0.05$. The Gaussian fits, drawn in red, are in $\beta^{-1}_{\text{expected}} - \beta^{-1}_{\text{measured}}$ and are of the $m_T - m_\pi = 0.350$ to 1.0 GeV/c^2 range. The track data are represented in the black histogram.

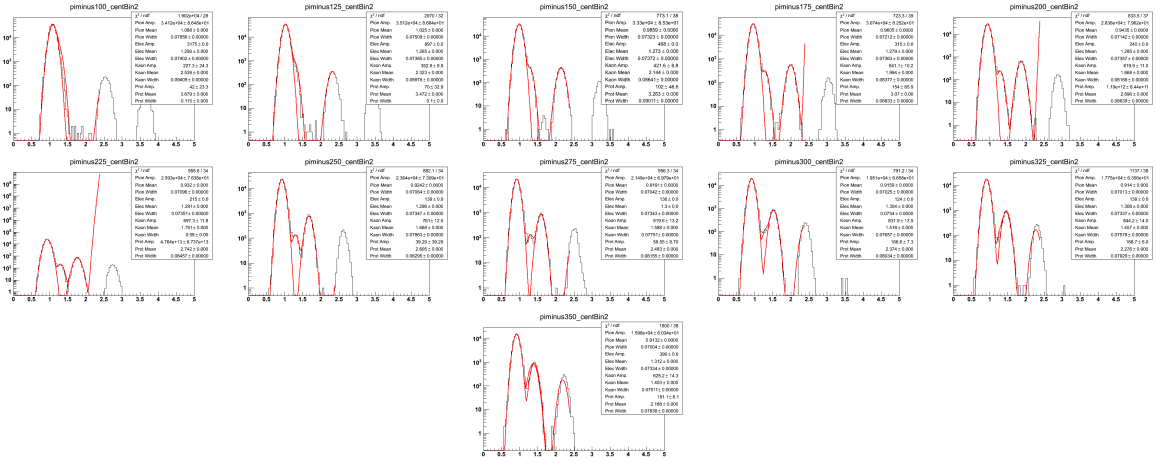

Figure A.27: Negative pion TPC fits for 50%-60% central events $Au+Au\sqrt{s_{NN}} = 19.6$ GeV. These are organized in 25 MeV bins in $m_T - m_\pi$ in a rapidity window of 0.1 units around mid-rapidity, $|y| < 0.05$. The Gaussian fits, drawn in red, are in $\log(10^6 \times dE/dx)$ and are of the $m_T - m_\pi = 0.100$ to 0.500 GeV/c^2 range. The track data are represented in the black histogram.

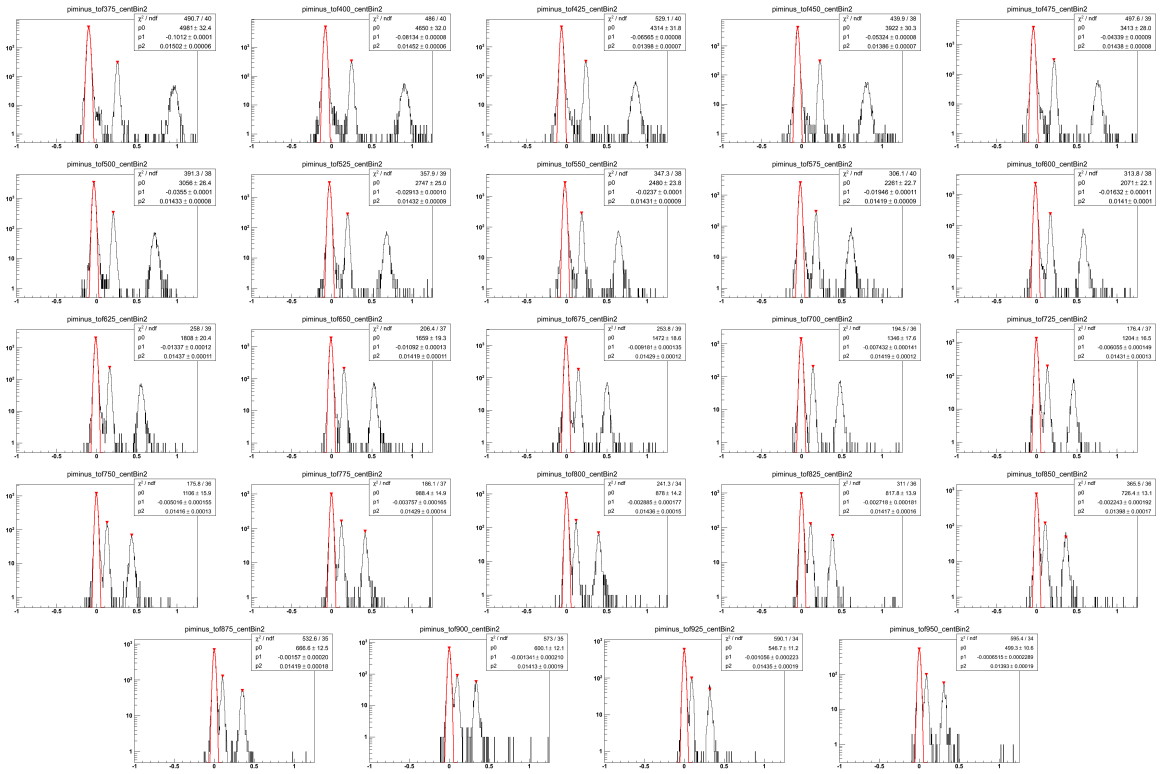

Figure A.28: Negative pion TOF fits for 50%-60% central events $Au+Au\sqrt{s_{NN}} = 19.6$ GeV. These are organized in 25 MeV bins in $m_T - m_\pi$ in a rapidity window of 0.1 units around mid-rapidity, $|y| < 0.05$. The Gaussian fits, drawn in red, are in $\beta^{-1}_{\text{expected}} - \beta^{-1}_{\text{measured}}$ and are of the $m_T - m_\pi = 0.350$ to 1.0 GeV/c^2 range. The track data are represented in the black histogram.

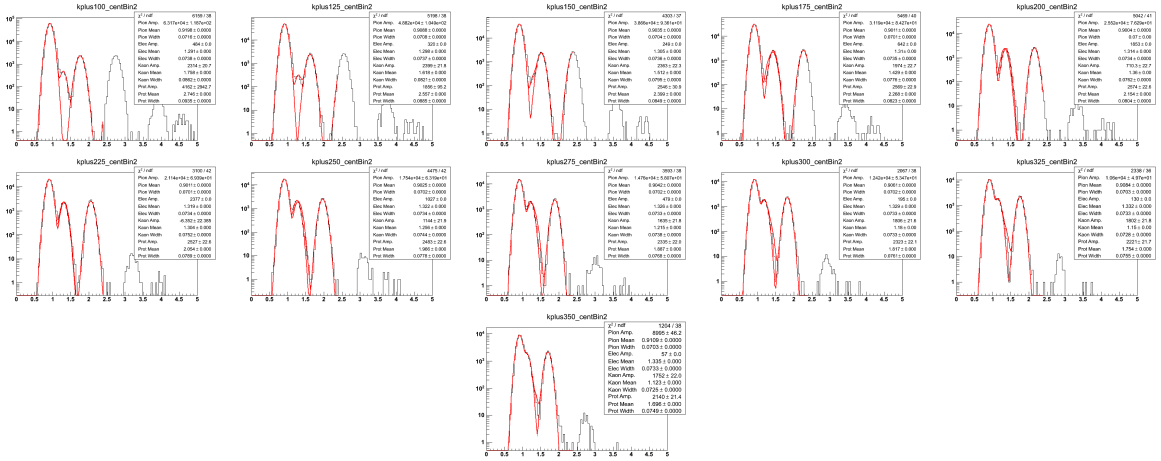

Figure A.29: Positive kaon TPC fits for 50%-60% central events $Au+Au\sqrt{s_{NN}} = 19.6$ GeV. These are organized in 25 MeV bins in $m_T - m_K$ in a rapidity window of 0.1 units around mid-rapidity, $|y| < 0.05$. The Gaussian fits, drawn in red, are in $\log(10^6 \times dE/dx)$ and are of the $m_T - m_K = 0.100$ to 0.500 GeV/c^2 range. The track data are represented in the black histogram.

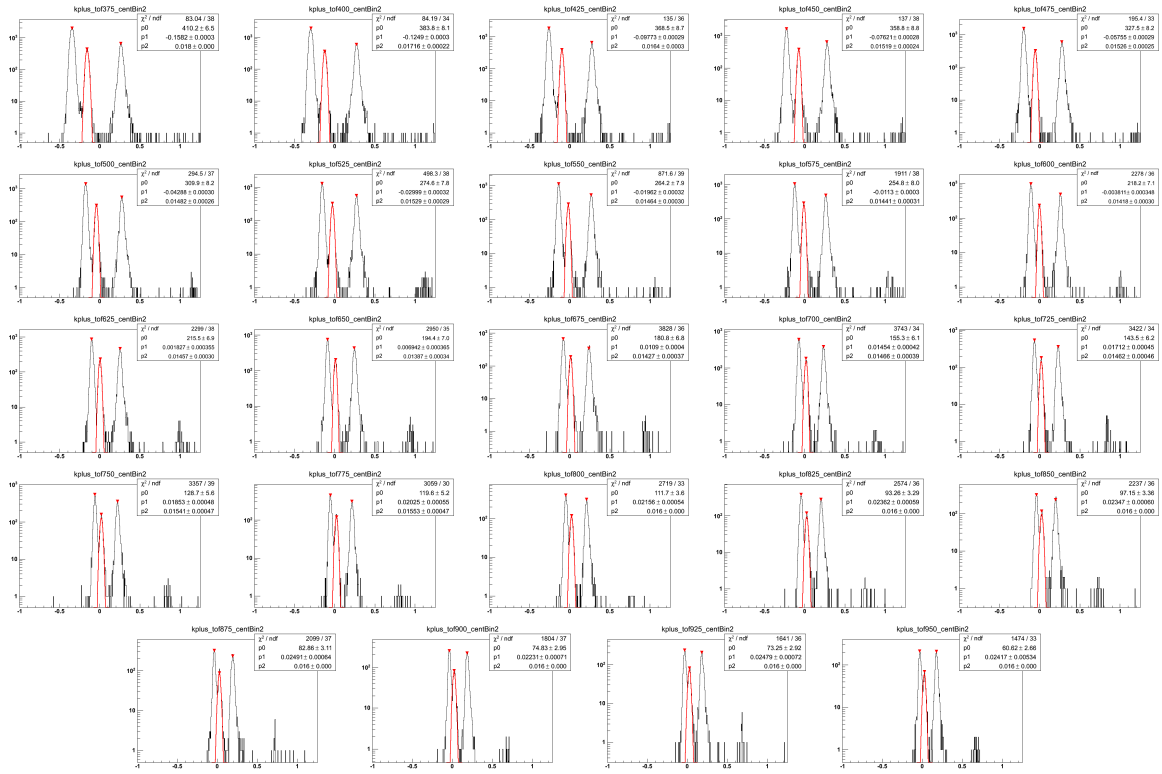

Figure A.30: Positive kaon TOF fits for 50%-60% central events $Au+Au\sqrt{s_{NN}} = 19.6$ GeV. These are organized in 25 MeV bins in $m_T - m_K$ in a rapidity window of 0.1 units around mid-rapidity, $|y| < 0.05$. The Gaussian fits, drawn in red, are in $\beta^{-1}_{\text{expected}} - \beta^{-1}_{\text{measured}}$ and are of the $m_T - m_K =$ 0.350 to 1.0 GeV/c^2 range. The track data are represented in the black histogram.

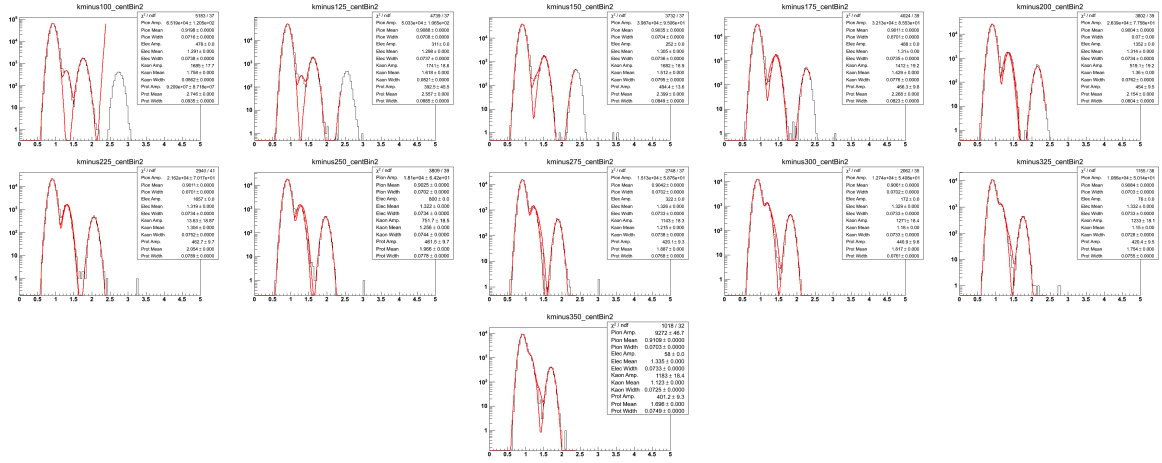

Figure A.31: Negative kaon TPC fits for 50%-60% central events $Au+Au\sqrt{s_{NN}} = 19.6$ GeV. These are organized in 25 MeV bins in $m_T - m_K$ in a rapidity window of 0.1 units around mid-rapidity, $|y| < 0.05$. The Gaussian fits, drawn in red, are in $\log(10^6 \times dE/dx)$ and are of the $m_T - m_K =$ 0.100 to 0.500 GeV/c^2 range. The track data are represented in the black histogram.

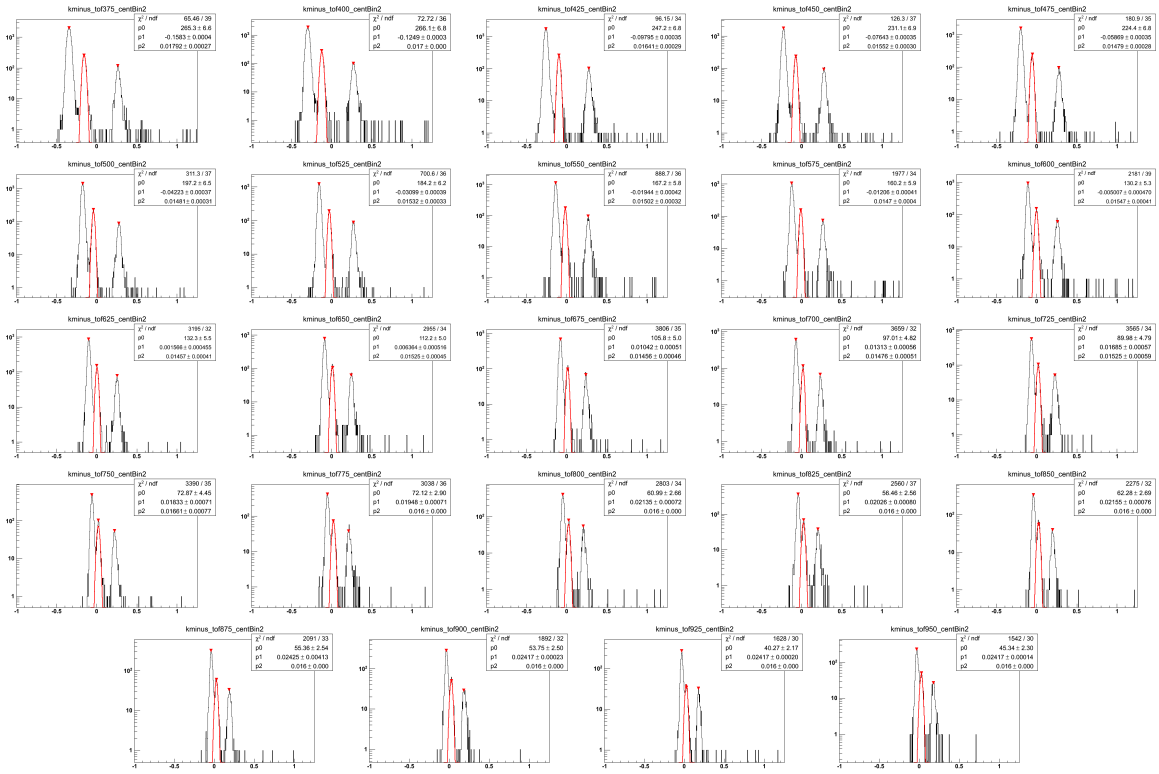

Figure A.32: Negative kaon TOF fits for 50%-60% central events $Au + Au\sqrt{s_{NN}} = 19.6$ GeV. These are organized in 25 MeV bins in $m_T - m_K$ in a rapidity window of 0.1 units around mid-rapidity, $|y| < 0.05$. The Gaussian fits, drawn in red, are in $\beta^{-1}_{\text{expected}} - \beta^{-1}_{\text{measured}}$ and are of the $m_T - m_K = 0.350$ to 1.0 GeV/c^2 range. The track data are represented in the black histogram.

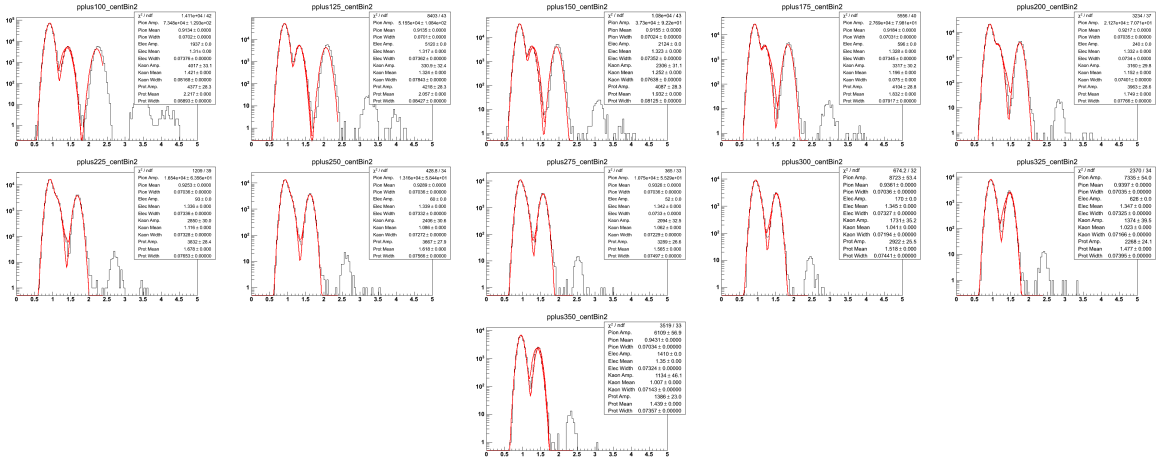

Figure A.33: Positive proton TPC fits for 50%-60% central events $Au + Au\sqrt{s_{NN}} = 19.6$ GeV. These are organized in 25 MeV bins in $m_T - m_p$ in a rapidity window of 0.1 units around mid-rapidity, $|y| < 0.05$. The Gaussian fits, drawn in red, are in $\log(10^6 \times dE/dx)$ and are of the $m_T - m_p = 0.100$ to 0.500 GeV/c^2 range. The track data are represented in the black histogram.

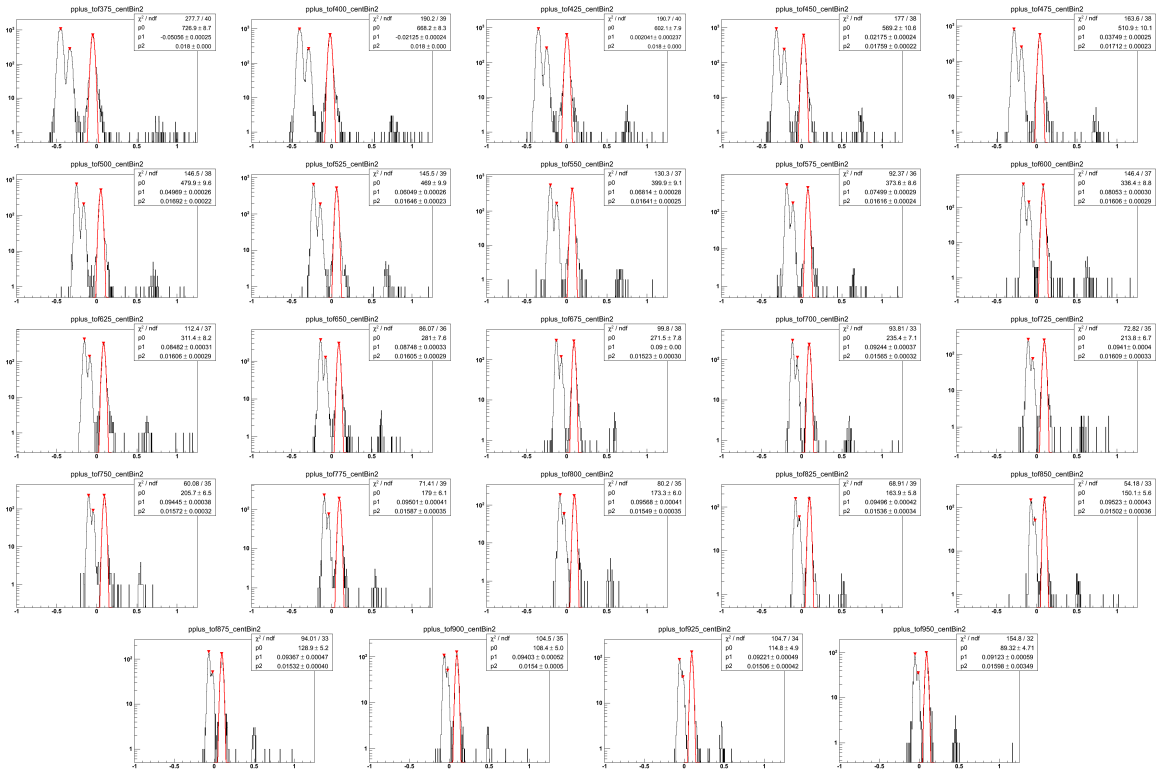

Figure A.34: Positive proton TOF fits for 50%-60% central events $Au + Au\sqrt{s_{NN}} = 19.6$ GeV. These are organized in 25 MeV bins in $m_T - m_p$ in a rapidity window of 0.1 units around mid-rapidity, $|y| < 0.05$. The Gaussian fits, drawn in red, are in $\beta^{-1}_{\text{expected}} - \beta^{-1}_{\text{measured}}$ and are of the $m_T - m_p = 0.350$ to 1.0 GeV/c^2 range. The track data are represented in the black histogram.

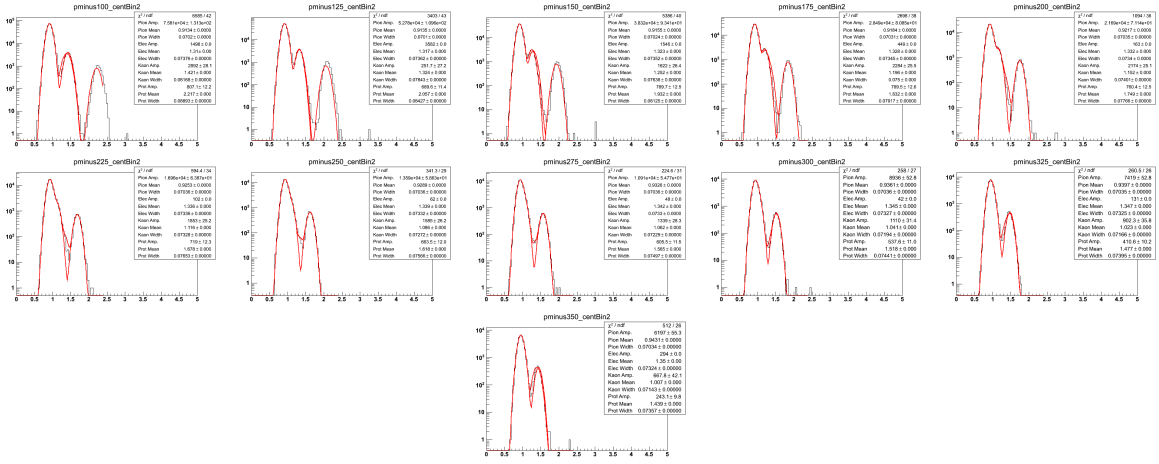

Figure A.35: Negative proton TPC fits for 50%-60% central events $Au + Au\sqrt{s_{NN}} = 19.6$ GeV. These are organized in 25 MeV bins in $m_T - m_p$ in a rapidity window of 0.1 units around mid-rapidity, $|y| < 0.05$. The Gaussian fits, drawn in red, are in $\log(10^6 \times dE/dx)$ and are of the $m_T - m_p = 0.100$ to 0.500 GeV/c^2 range. The track data are represented in the black histogram.

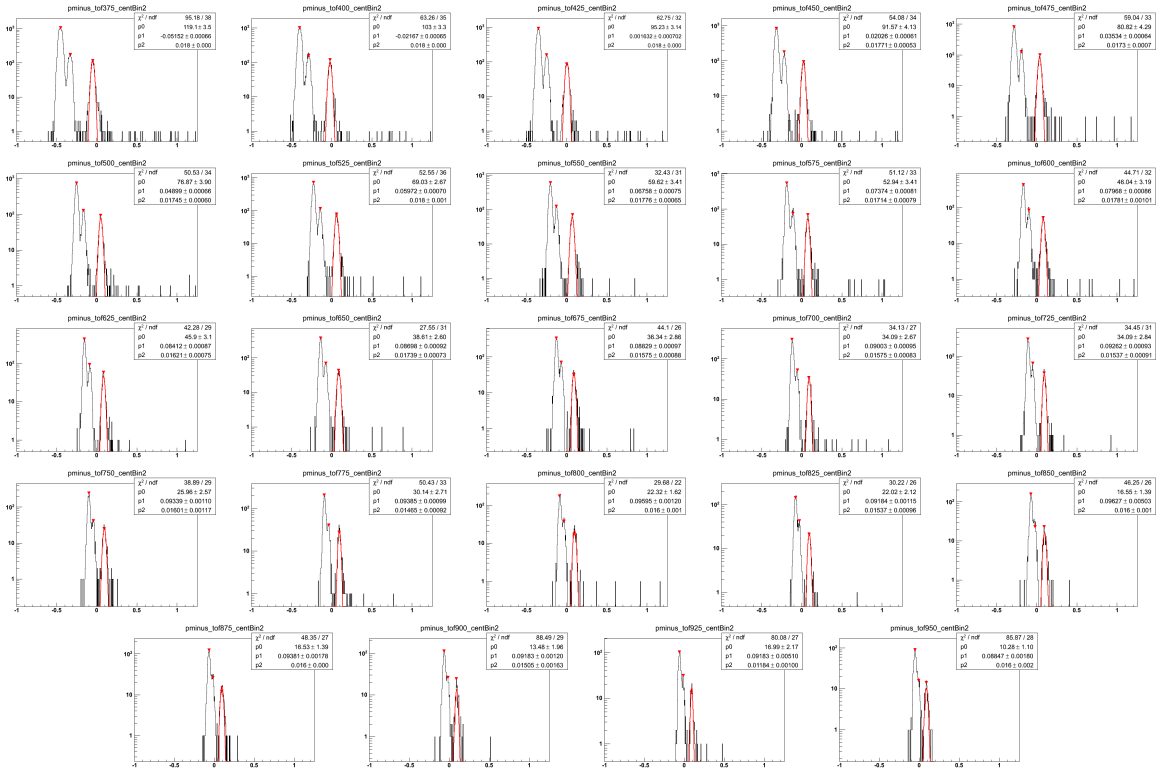

Figure A.36: Negative proton TOF fits for 50%-60% central events $Au + Au\sqrt{s_{NN}} = 19.6$ GeV. These are organized in 25 MeV bins in $m_T - m_p$ in a rapidity window of 0.1 units around mid-rapidity, $|y| < 0.05$. The Gaussian fits, drawn in red, are in $\beta^{-1}_{\text{expected}} - \beta^{-1}_{\text{measured}}$ and are of the $m_T - m_p = 0.350$ to 1.0 GeV/c^2 range. The track data are represented in the black histogram.

A.4 The 40%-50% Centrality Class

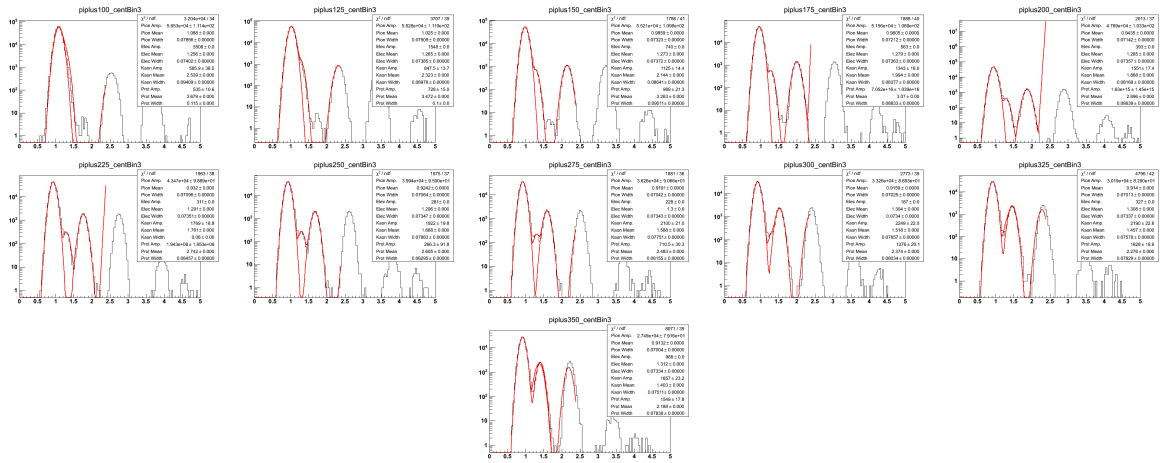

Figure A.37: Positive pion TPC fits for 40%-50% central events $Au+Au\sqrt{s_{NN}} = 19.6$ GeV. These are organized in 25 MeV bins in $m_T - m_\pi$ in a rapidity window of 0.1 units around mid-rapidity, $|y| < 0.05$. The Gaussian fits, drawn in red, are in $\log(10^6 \times dE/dx)$ and are of the $m_T - m_\pi =$ 0.100 to 0.500 GeV/c^2 range. The track data are represented in the black histogram.

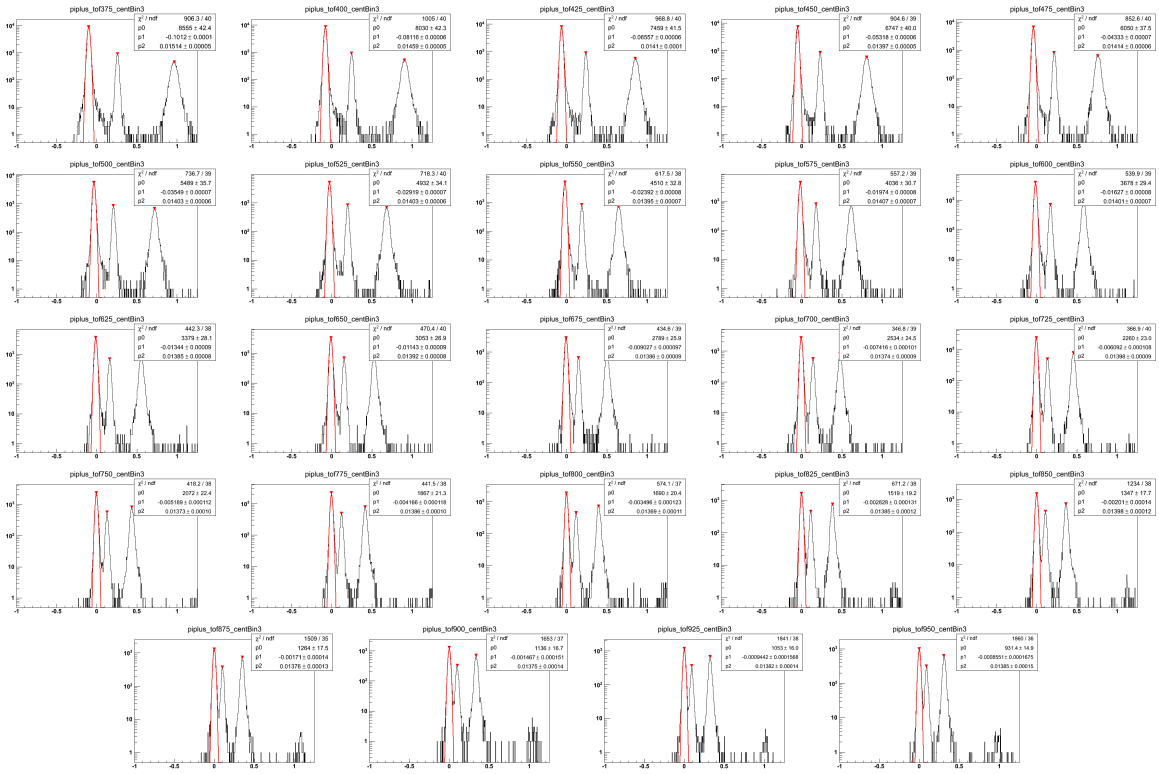

Figure A.38: Positive pion TOF fits for 40%-50% central events $Au+Au\sqrt{s_{NN}} = 19.6$ GeV. These are organized in 25 MeV bins in $m_T - m_\pi$ in a rapidity window of 0.1 units around mid-rapidity, $|y| < 0.05$. The Gaussian fits, drawn in red, are in $\beta^{-1}_{\text{expected}} - \beta^{-1}_{\text{measured}}$ and are of the $m_T - m_\pi =$ 0.350 to 1.0 GeV/c^2 range. The track data are represented in the black histogram.

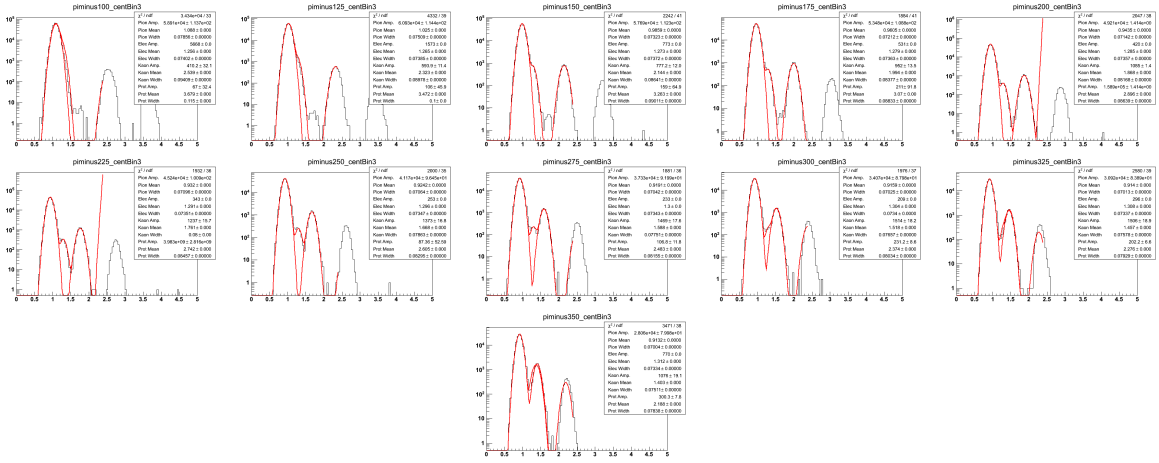

Figure A.39: Negative pion TPC fits for 40%-50% central events $Au+Au\sqrt{s_{NN}} = 19.6$ GeV. These are organized in 25 MeV bins in $m_T - m_\pi$ in a rapidity window of 0.1 units around mid-rapidity, $|y| < 0.05$. The Gaussian fits, drawn in red, are in $\log(10^6 \times dE/dx)$ and are of the $m_T - m_\pi =$ 0.100 to 0.500 GeV/c^2 range. The track data are represented in the black histogram.

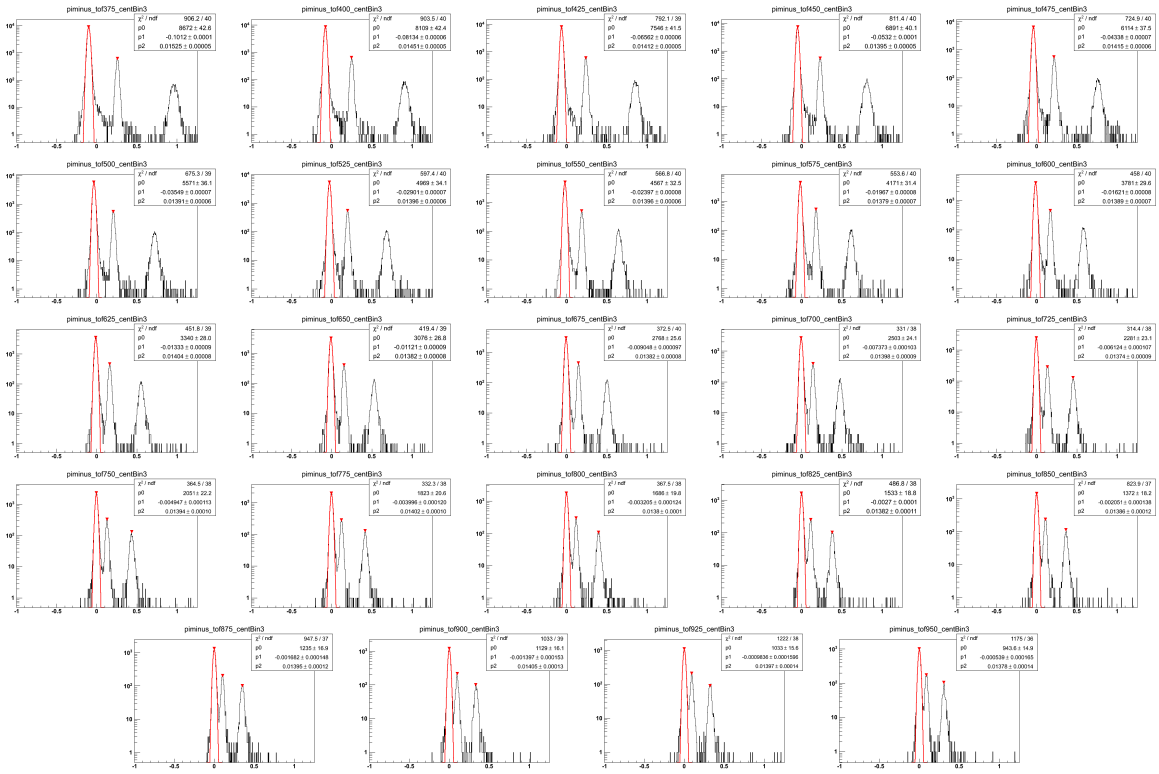

Figure A.40: Negative pion TOF fits for 40%-50% central events $Au+Au\sqrt{s_{NN}} = 19.6$ GeV. These are organized in 25 MeV bins in $m_T - m_\pi$ in a rapidity window of 0.1 units around mid-rapidity, $|y| < 0.05$. The Gaussian fits, drawn in red, are in $\beta^{-1}_{\text{expected}} - \beta^{-1}_{\text{measured}}$ and are of the $m_T - m_\pi = 0.350$ to 1.0 GeV/c^2 range. The track data are represented in the black histogram.

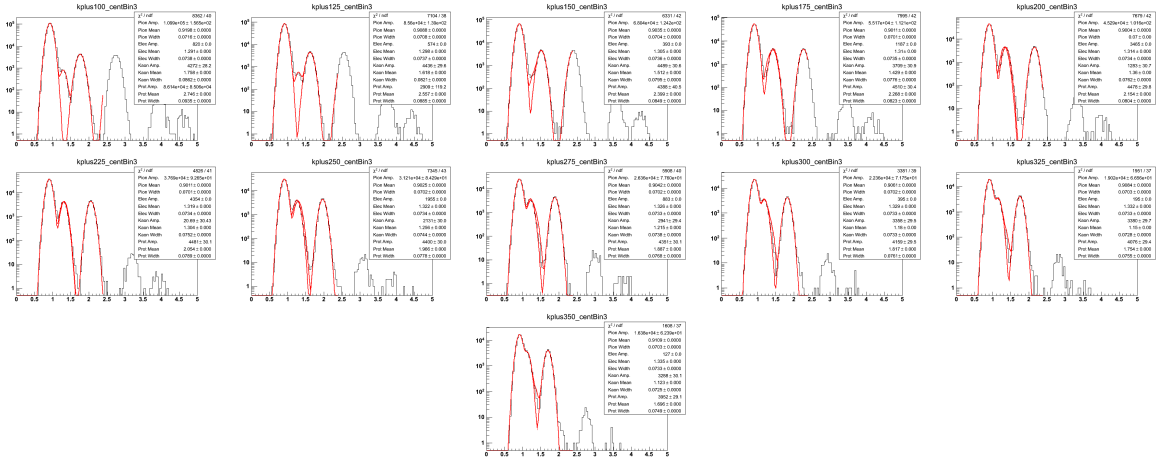

Figure A.41: Positive kaon TPC fits for 40%-50% central events $Au+Au\sqrt{s_{NN}} = 19.6$ GeV. These are organized in 25 MeV bins in $m_T - m_K$ in a rapidity window of 0.1 units around mid-rapidity, $|y| < 0.05$. The Gaussian fits, drawn in red, are in $\log(10^6 \times dE/dx)$ and are of the $m_T - m_K = 0.100$ to 0.500 GeV/c^2 range. The track data are represented in the black histogram.

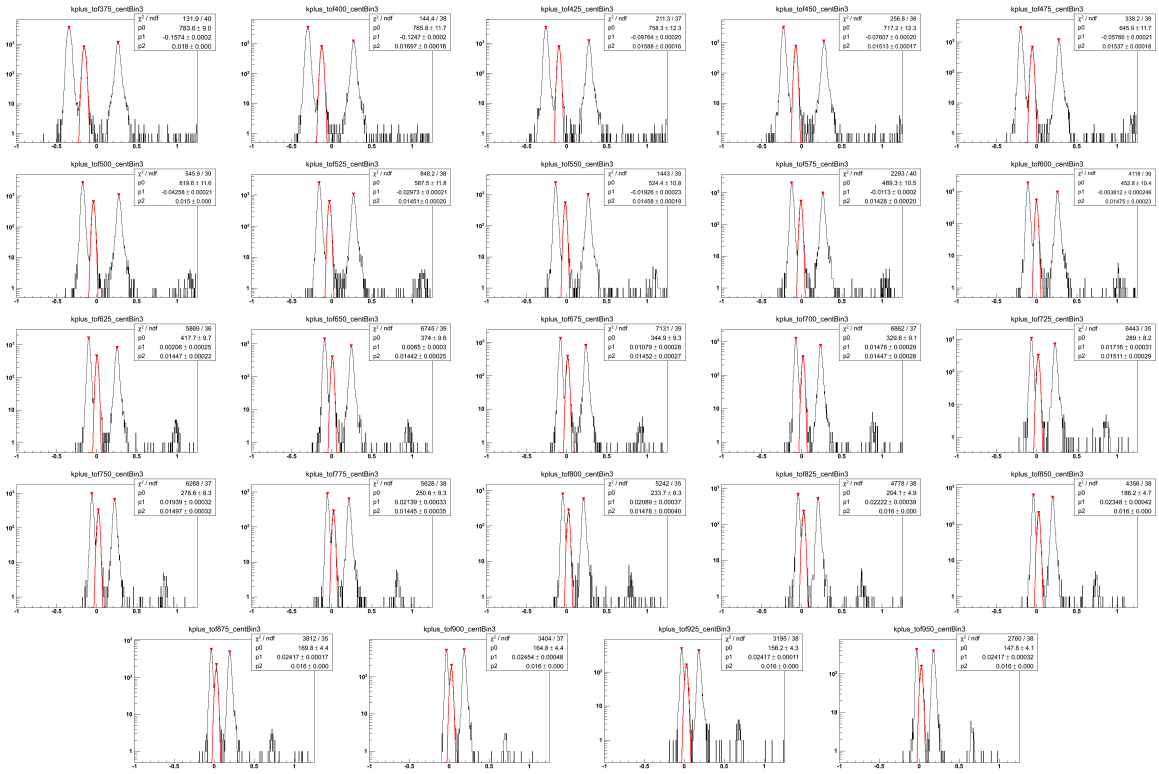

Figure A.42: Positive kaon TOF fits for 40%-50% central events $Au+Au\sqrt{s_{NN}} = 19.6$ GeV. These are organized in 25 MeV bins in $m_T - m_K$ in a rapidity window of 0.1 units around mid-rapidity, $|y| < 0.05$. The Gaussian fits, drawn in red, are in $\beta^{-1}_{\text{expected}} - \beta^{-1}_{\text{measured}}$ and are of the $m_T - m_K =$ 0.350 to 1.0 GeV/c^2 range. The track data are represented in the black histogram.

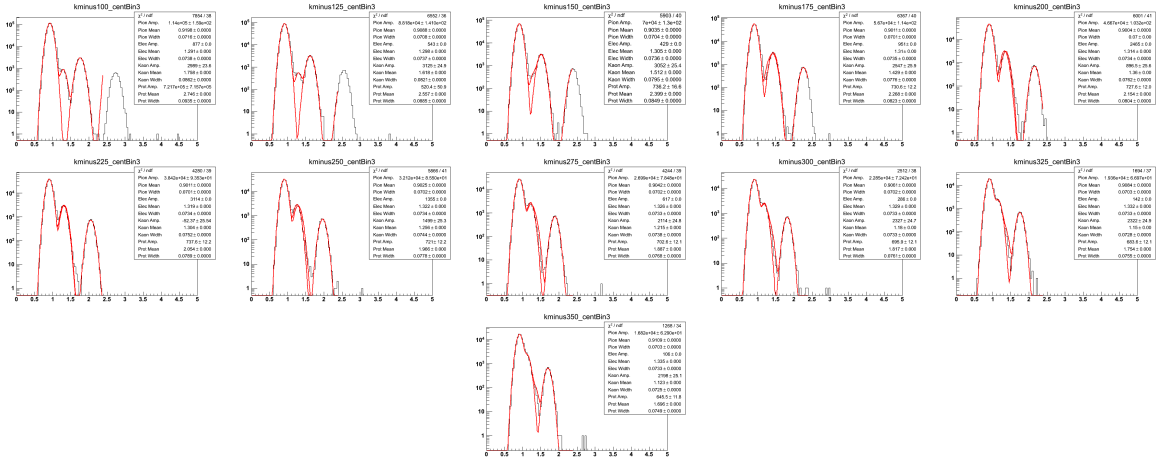

Figure A.43: Negative kaon TPC fits for 40%-50% central events $Au+Au\sqrt{s_{NN}} = 19.6$ GeV. These are organized in 25 MeV bins in $m_T - m_K$ in a rapidity window of 0.1 units around mid-rapidity, $|y| < 0.05$. The Gaussian fits, drawn in red, are in $\log(10^6 \times dE/dx)$ and are of the $m_T - m_K =$ 0.100 to 0.500 GeV/c^2 range. The track data are represented in the black histogram.

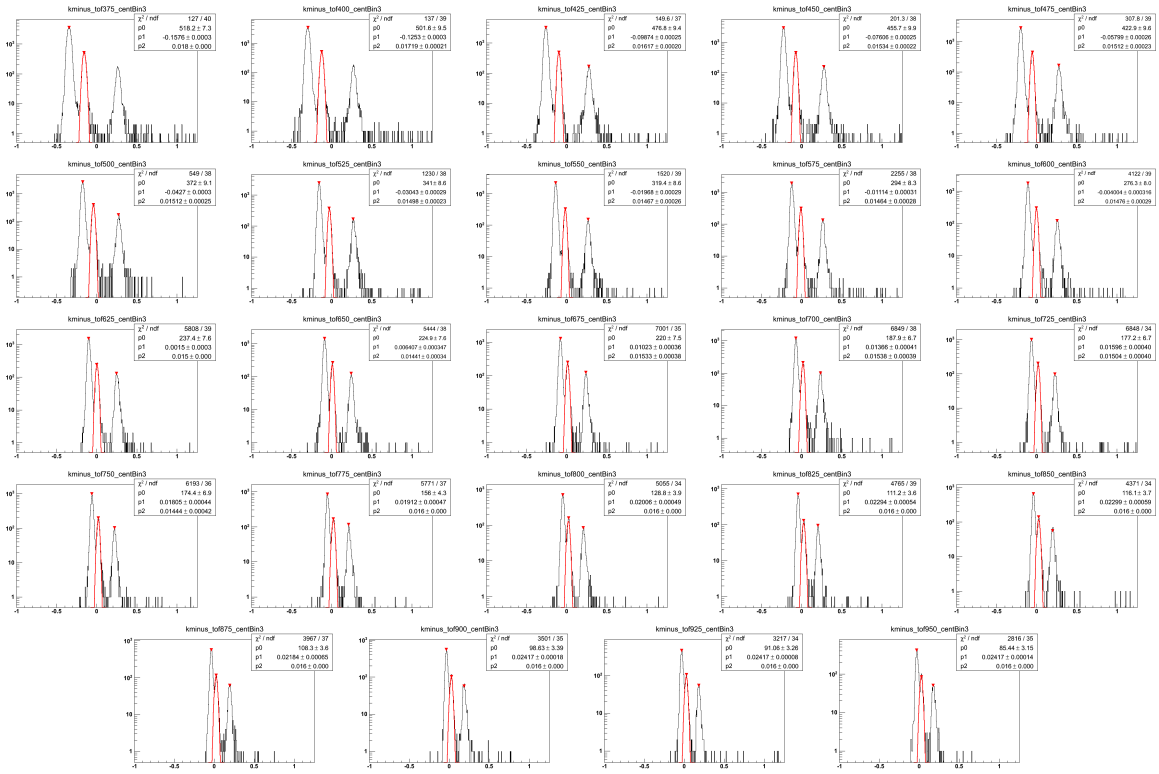

Figure A.44: Negative kaon TOF fits for 40%-50% central events $Au + Au\sqrt{s_{NN}} = 19.6$ GeV. These are organized in 25 MeV bins in $m_T - m_K$ in a rapidity window of 0.1 units around mid-rapidity, $|y| < 0.05$. The Gaussian fits, drawn in red, are in $\beta^{-1}_{\text{expected}} - \beta^{-1}_{\text{measured}}$ and are of the $m_T - m_K = 0.350$ to 1.0 GeV/c^2 range. The track data are represented in the black histogram.

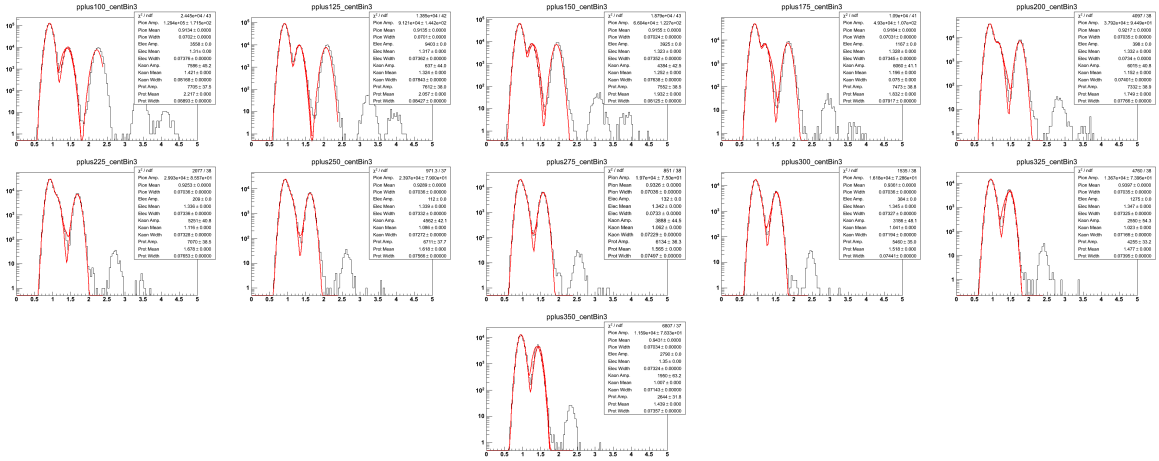

Figure A.45: Positive proton TPC fits for 40%-50% central events $Au + Au\sqrt{s_{NN}} = 19.6$ GeV. These are organized in 25 MeV bins in $m_T - m_p$ in a rapidity window of 0.1 units around mid-rapidity, $|y| < 0.05$. The Gaussian fits, drawn in red, are in $\log(10^6 \times dE/dx)$ and are of the $m_T - m_p = 0.100$ to 0.500 GeV/c^2 range. The track data are represented in the black histogram.

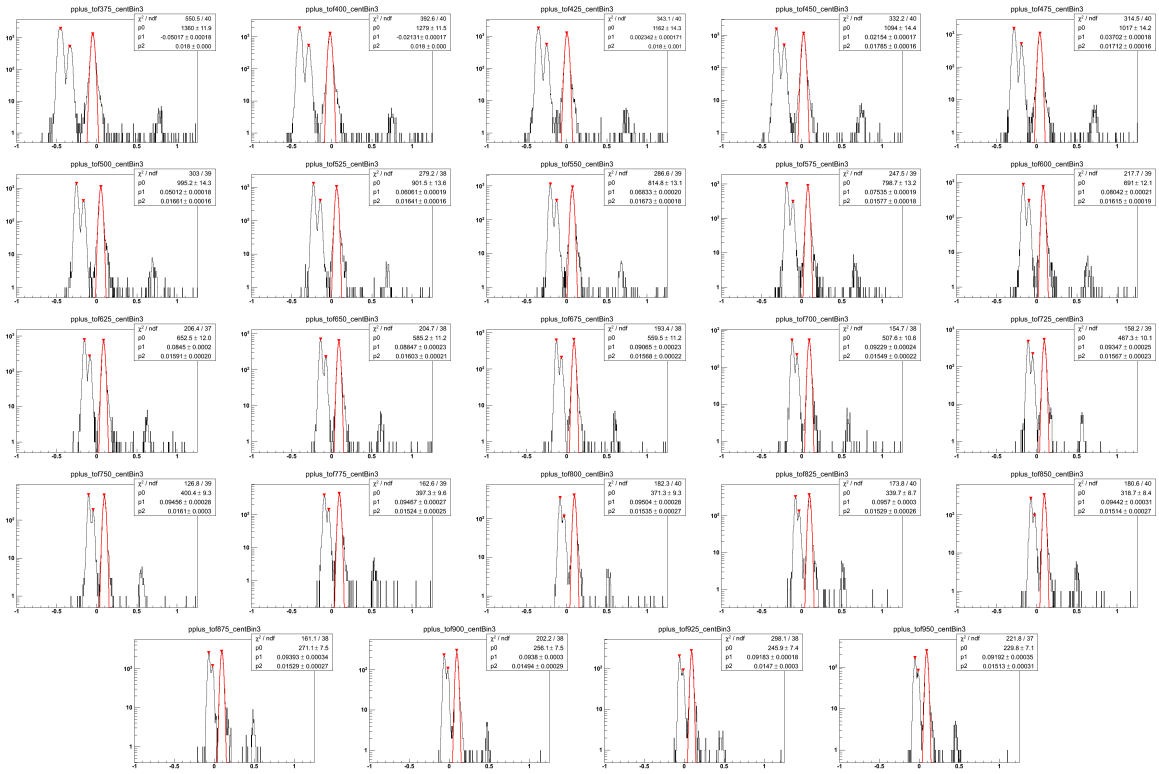

Figure A.46: Positive proton TOF fits for 40%-50% central events $Au + Au\sqrt{s_{NN}} = 19.6$ GeV. These are organized in 25 MeV bins in $m_T - m_p$ in a rapidity window of 0.1 units around mid-rapidity, $|y| < 0.05$. The Gaussian fits, drawn in red, are in $\beta^{-1}_{\text{expected}} - \beta^{-1}_{\text{measured}}$ and are of the $m_T - m_p = 0.350$ to 1.0 GeV/c^2 range. The track data are represented in the black histogram.

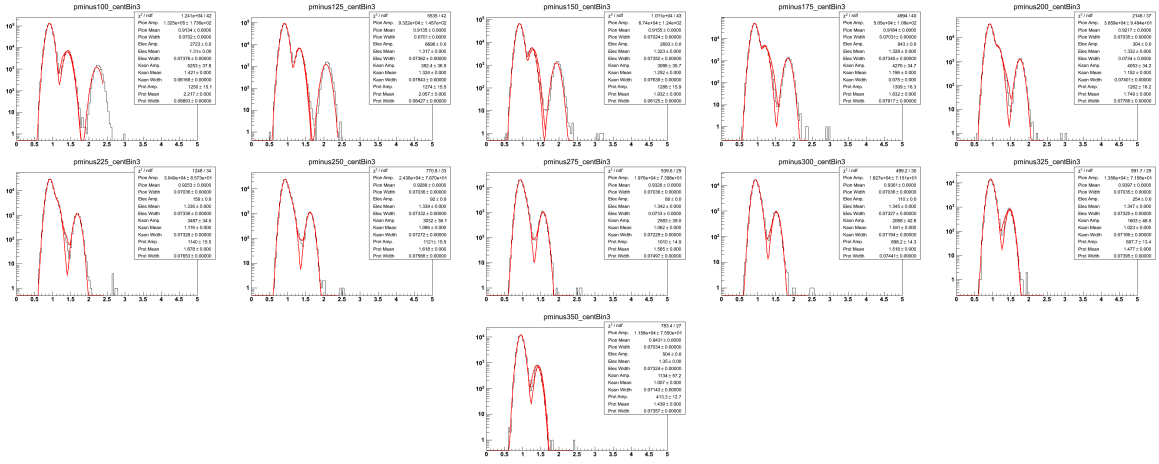

Figure A.47: Negative proton TPC fits for 40%-50% central events $Au + Au\sqrt{s_{NN}} = 19.6$ GeV. These are organized in 25 MeV bins in $m_T - m_p$ in a rapidity window of 0.1 units around mid-rapidity, $|y| < 0.05$. The Gaussian fits, drawn in red, are in $\log(10^6 \times dE/dx)$ and are of the $m_T - m_p = 0.100$ to 0.500 GeV/c^2 range. The track data are represented in the black histogram.

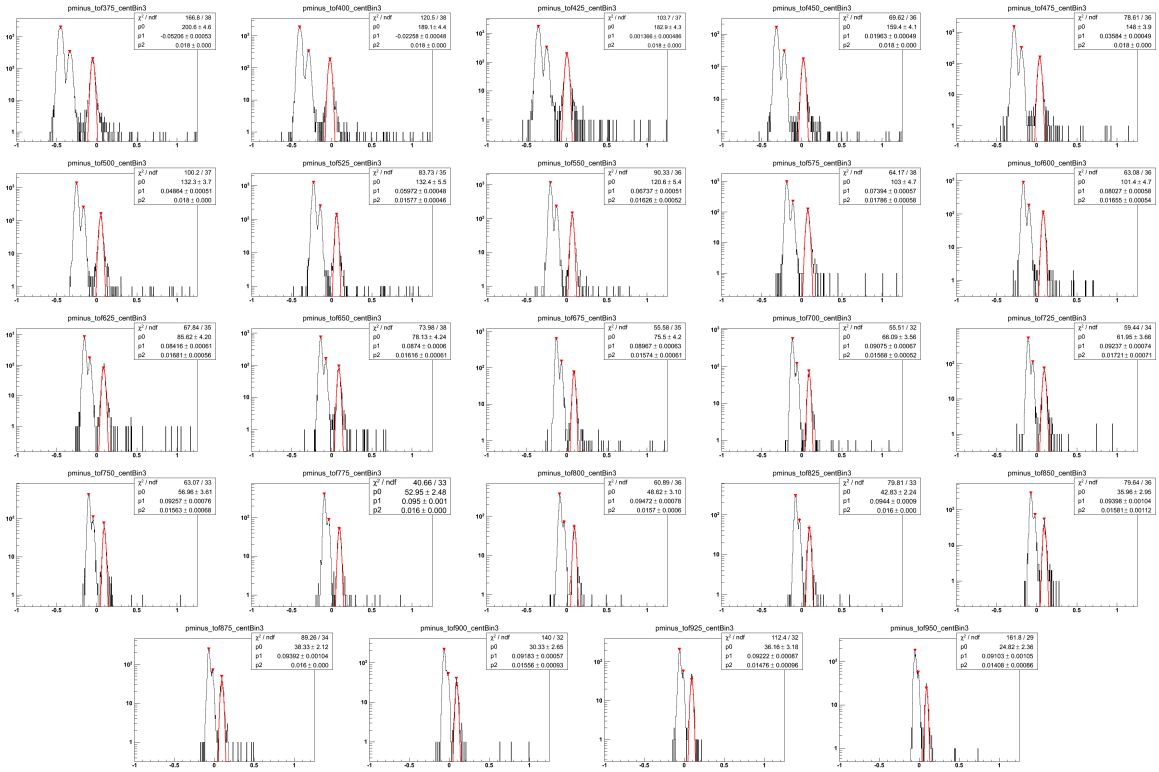

Figure A.48: Negative proton TOF fits for 40%-50% central events $Au + Au\sqrt{s_{NN}} = 19.6$ GeV. These are organized in 25 MeV bins in $m_T - m_p$ in a rapidity window of 0.1 units around mid-rapidity, $|y| < 0.05$. The Gaussian fits, drawn in red, are in $\beta^{-1}_{\text{expected}} - \beta^{-1}_{\text{measured}}$ and are of the $m_T - m_p = 0.350$ to 1.0 GeV/c^2 range. The track data are represented in the black histogram.

A.5 The 30%-40% Centrality Class

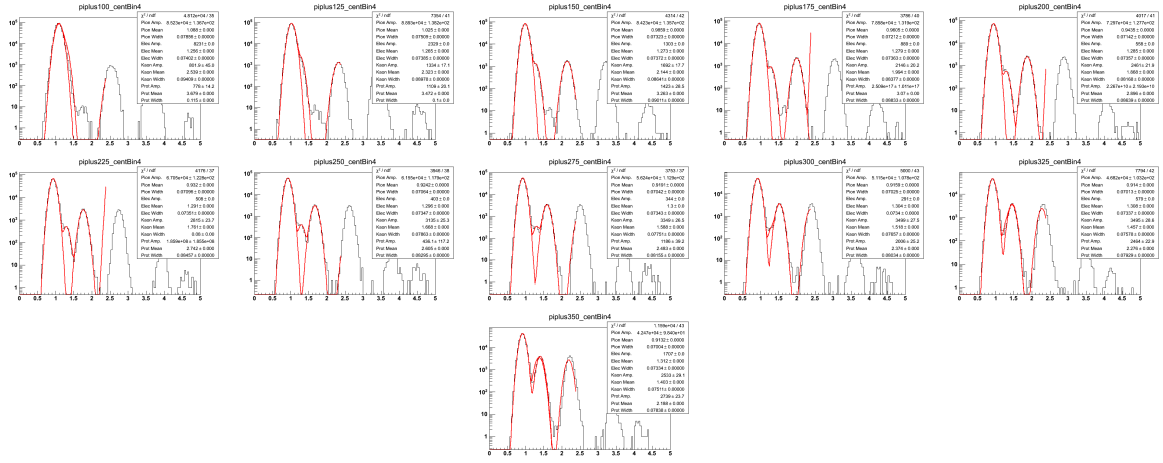

Figure A.49: Positive pion TPC fits for 30%-40% central events $Au+Au\sqrt{s_{NN}} = 19.6$ GeV. These are organized in 25 MeV bins in $m_T - m_\pi$ in a rapidity window of 0.1 units around mid-rapidity, $|y| < 0.05$. The Gaussian fits, drawn in red, are in $\log(10^6 \times dE/dx)$ and are of the $m_T - m_\pi =$ 0.100 to 0.500 GeV/c^2 range. The track data are represented in the black histogram.

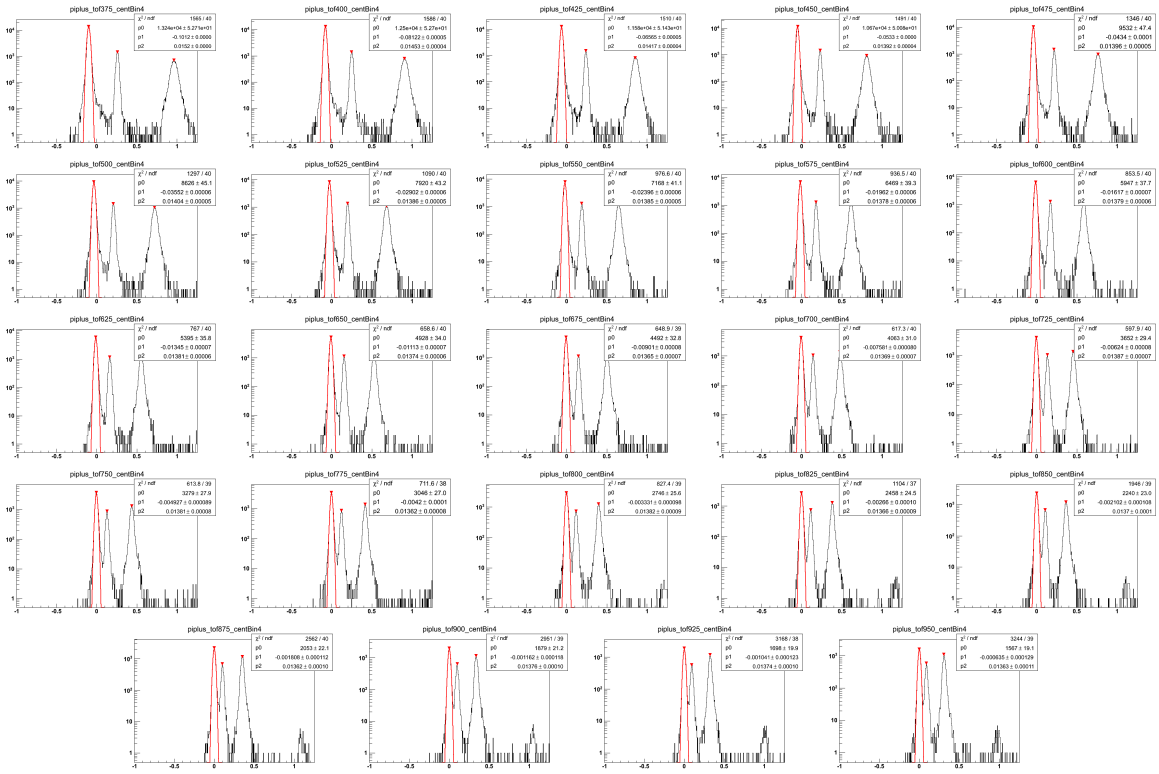

Figure A.50: Positive pion TOF fits for 30%-40% central events $Au+Au\sqrt{s_{NN}} = 19.6$ GeV. These are organized in 25 MeV bins in $m_T - m_\pi$ in a rapidity window of 0.1 units around mid-rapidity, $|y| < 0.05$. The Gaussian fits, drawn in red, are in $\beta^{-1}_{\text{expected}} - \beta^{-1}_{\text{measured}}$ and are of the $m_T - m_\pi = 0.350$ to 1.0 GeV/c^2 range. The track data are represented in the black histogram.

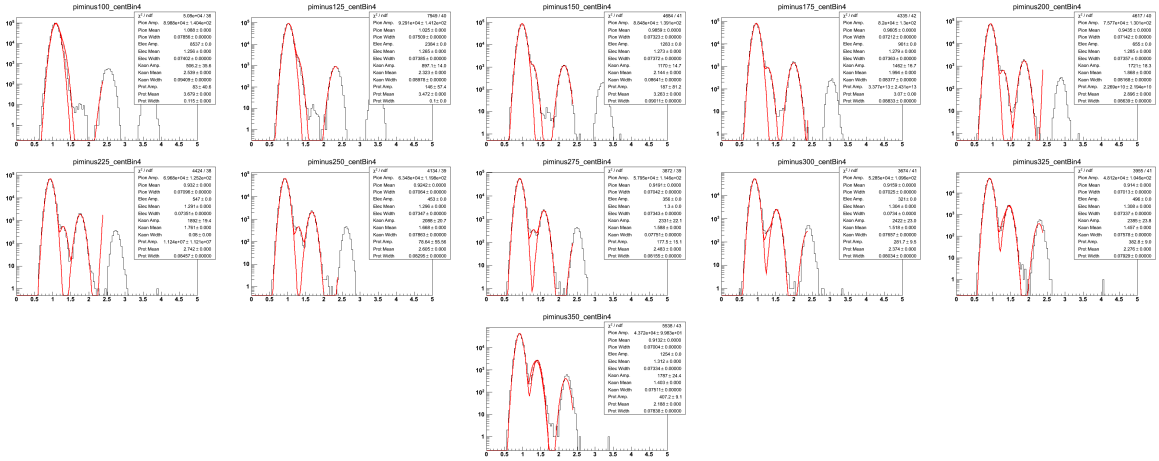

Figure A.51: Negative pion TPC fits for 30%-40% central events $Au+Au\sqrt{s_{NN}} = 19.6$ GeV. These are organized in 25 MeV bins in $m_T - m_\pi$ in a rapidity window of 0.1 units around mid-rapidity, $|y| < 0.05$. The Gaussian fits, drawn in red, are in $\log(10^6 \times dE/dx)$ and are of the $m_T - m_\pi = 0.100$ to 0.500 GeV/c^2 range. The track data are represented in the black histogram.

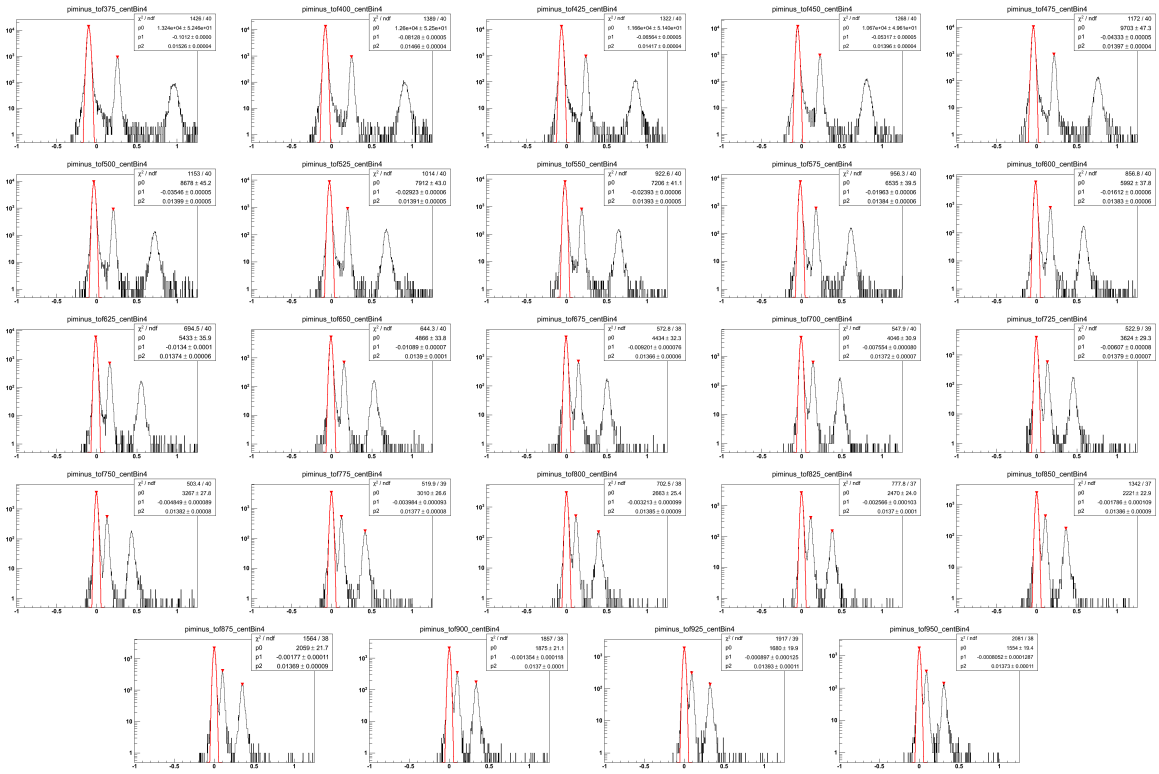

Figure A.52: Negative pion TOF fits for 30%-40% central events $Au+Au\sqrt{s_{NN}} = 19.6$ GeV. These are organized in 25 MeV bins in $m_T - m_\pi$ in a rapidity window of 0.1 units around mid-rapidity, $|y| < 0.05$. The Gaussian fits, drawn in red, are in $\beta^{-1}_{\text{expected}} - \beta^{-1}_{\text{measured}}$ and are of the $m_T - m_\pi =$ 0.350 to 1.0 GeV/c^2 range. The track data are represented in the black histogram.

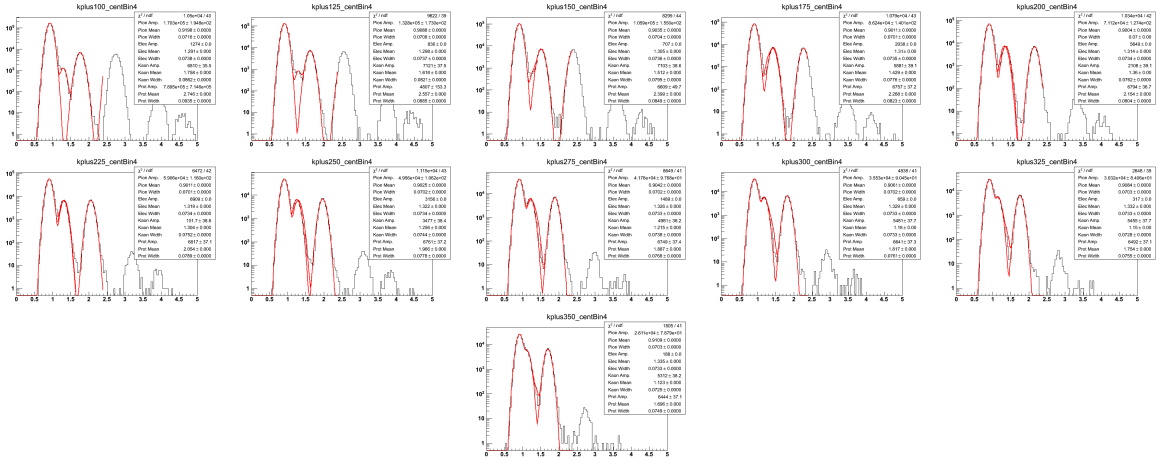

Figure A.53: Positive kaon TPC fits for 30%-40% central events $Au+Au\sqrt{s_{NN}} = 19.6$ GeV. These are organized in 25 MeV bins in $m_T - m_K$ in a rapidity window of 0.1 units around mid-rapidity, $|y| < 0.05$. The Gaussian fits, drawn in red, are in $\log(10^6 \times dE/dx)$ and are of the $m_T - m_K =$ 0.100 to 0.500 GeV/c^2 range. The track data are represented in the black histogram.

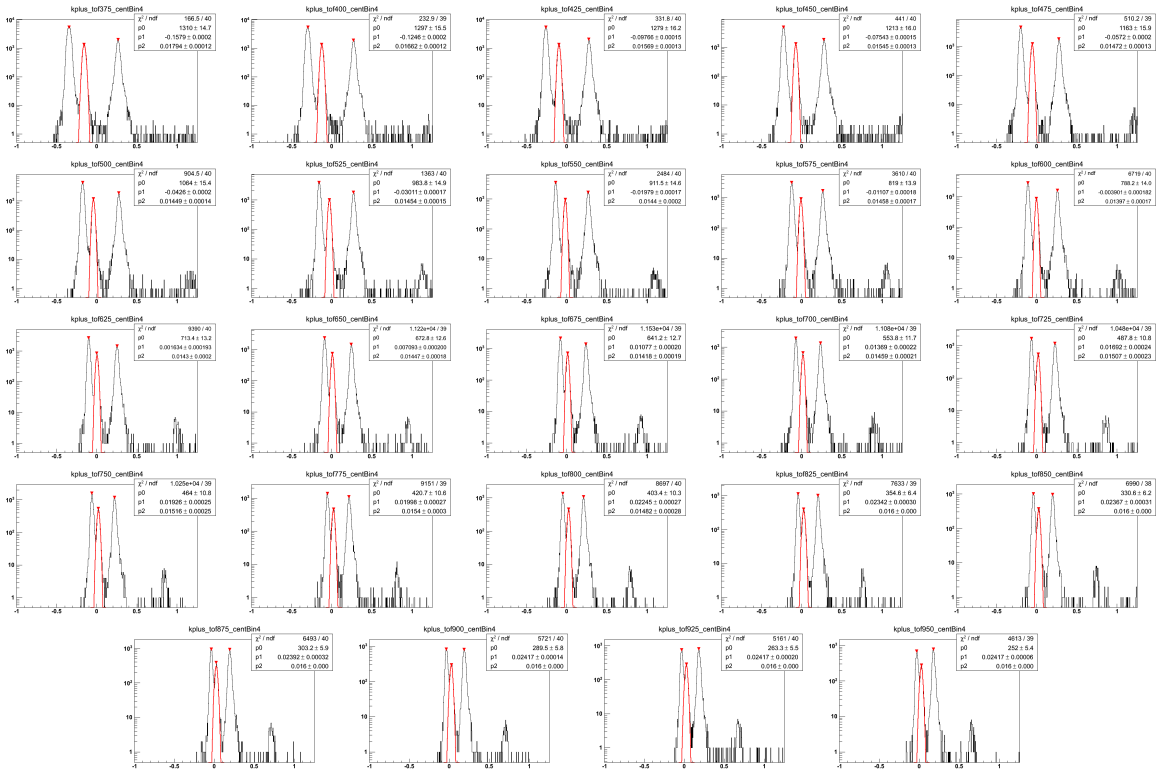

Figure A.54: Positive kaon TOF fits for 30%-40% central events $Au+Au\sqrt{s_{NN}} = 19.6$ GeV. These are organized in 25 MeV bins in $m_T - m_K$ in a rapidity window of 0.1 units around mid-rapidity, $|y| < 0.05$. The Gaussian fits, drawn in red, are in $\beta^{-1}_{\text{expected}} - \beta^{-1}_{\text{measured}}$ and are of the $m_T - m_K =$ 0.350 to 1.0 GeV/c^2 range. The track data are represented in the black histogram.

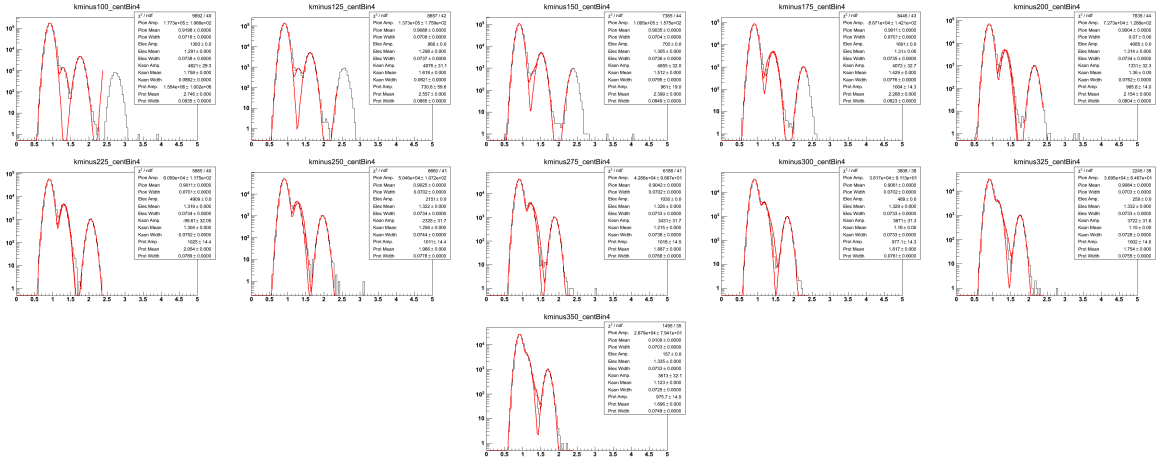

Figure A.55: Negative kaon TPC fits for 30%-40% central events $Au+Au\sqrt{s_{NN}} = 19.6$ GeV. These are organized in 25 MeV bins in $m_T - m_K$ in a rapidity window of 0.1 units around mid-rapidity, $|y| < 0.05$. The Gaussian fits, drawn in red, are in $\log(10^6 \times dE/dx)$ and are of the $m_T - m_K =$ 0.100 to 0.500 GeV/c^2 range. The track data are represented in the black histogram.

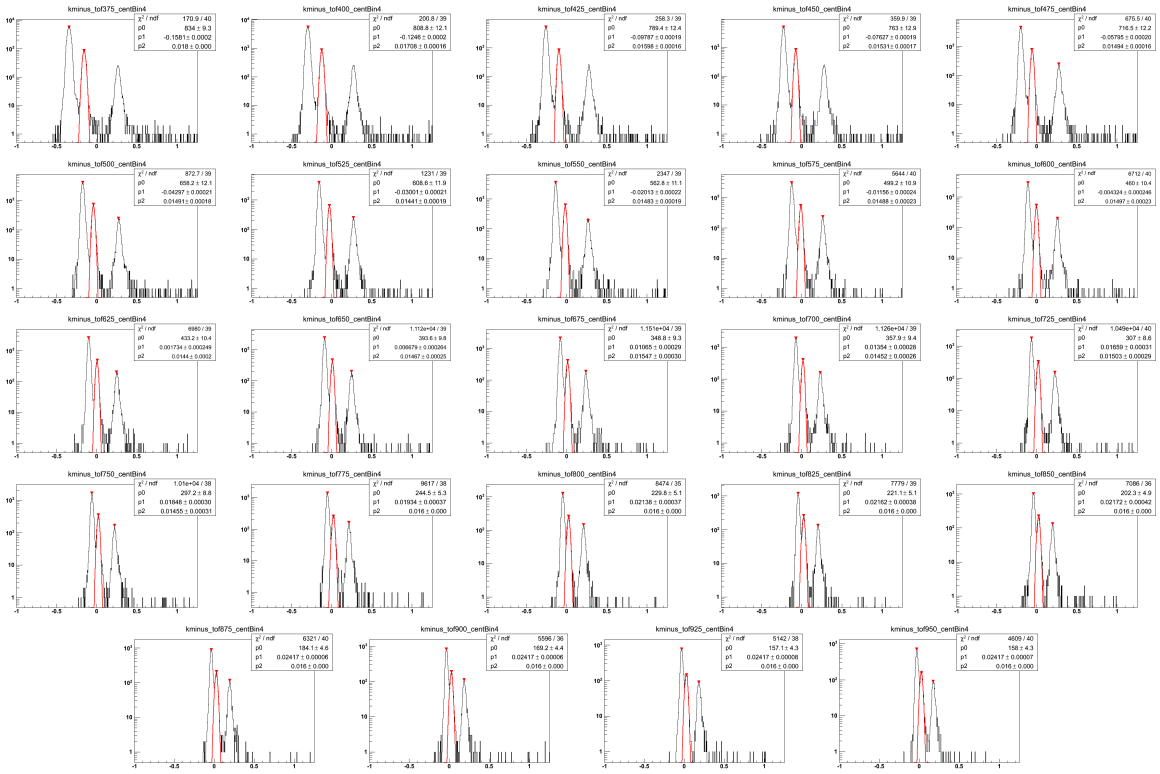

Figure A.56: Negative kaon TOF fits for 30%-40% central events $Au + Au\sqrt{s_{NN}} = 19.6$ GeV. These are organized in 25 MeV bins in $m_T - m_K$ in a rapidity window of 0.1 units around mid-rapidity, $|y| < 0.05$. The Gaussian fits, drawn in red, are in $\beta^{-1}_{\text{expected}} - \beta^{-1}_{\text{measured}}$ and are of the $m_T - m_K = 0.350$ to 1.0 GeV/c^2 range. The track data are represented in the black histogram.

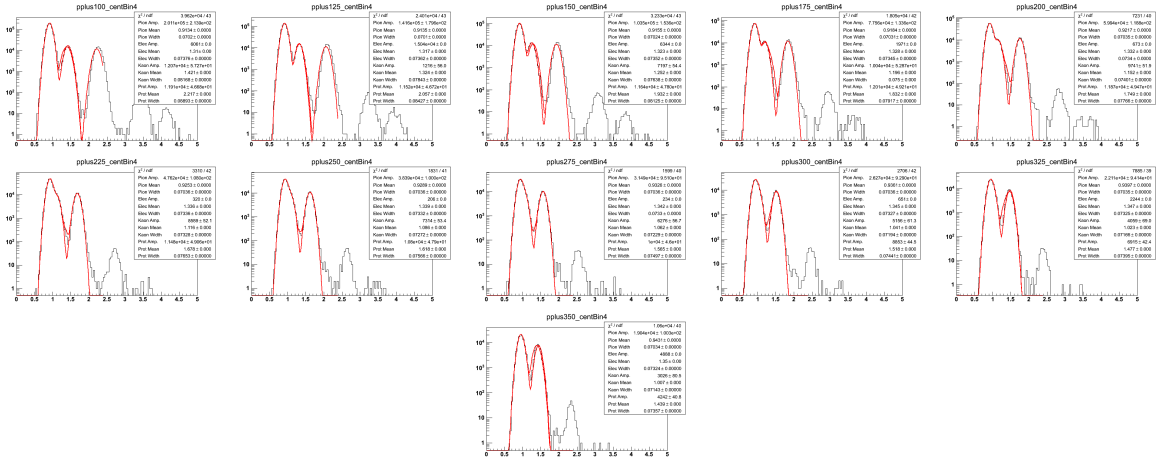

Figure A.57: Positive proton TPC fits for 30%-40% central events $Au + Au\sqrt{s_{NN}} = 19.6$ GeV. These are organized in 25 MeV bins in $m_T - m_p$ in a rapidity window of 0.1 units around mid-rapidity, $|y| < 0.05$. The Gaussian fits, drawn in red, are in $\log(10^6 \times dE/dx)$ and are of the $m_T - m_p = 0.100$ to 0.500 GeV/c^2 range. The track data are represented in the black histogram.

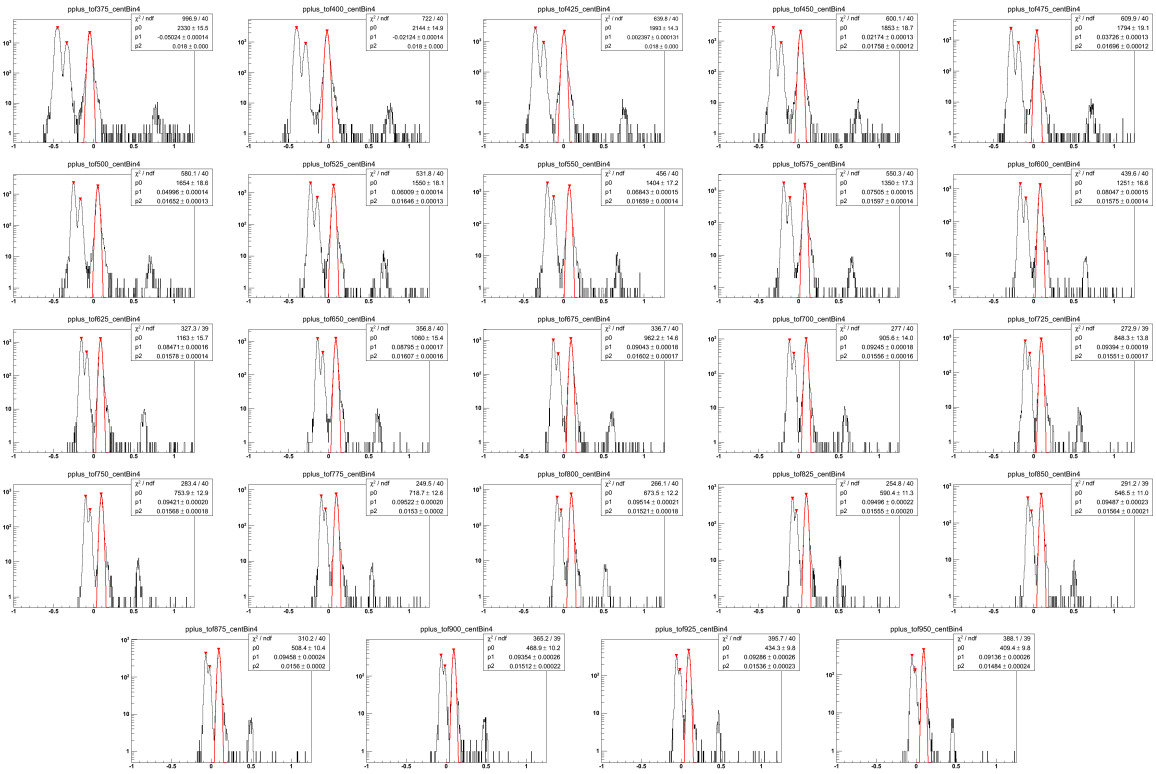

Figure A.58: Positive proton TOF fits for 30%-40% central events $Au + Au\sqrt{s_{NN}} = 19.6$ GeV. These are organized in 25 MeV bins in $m_T - m_p$ in a rapidity window of 0.1 units around mid-rapidity, $|y| < 0.05$. The Gaussian fits, drawn in red, are in $\beta^{-1}_{\text{expected}} - \beta^{-1}_{\text{measured}}$ and are of the $m_T - m_p = 0.350$ to 1.0 GeV/c^2 range. The track data are represented in the black histogram.

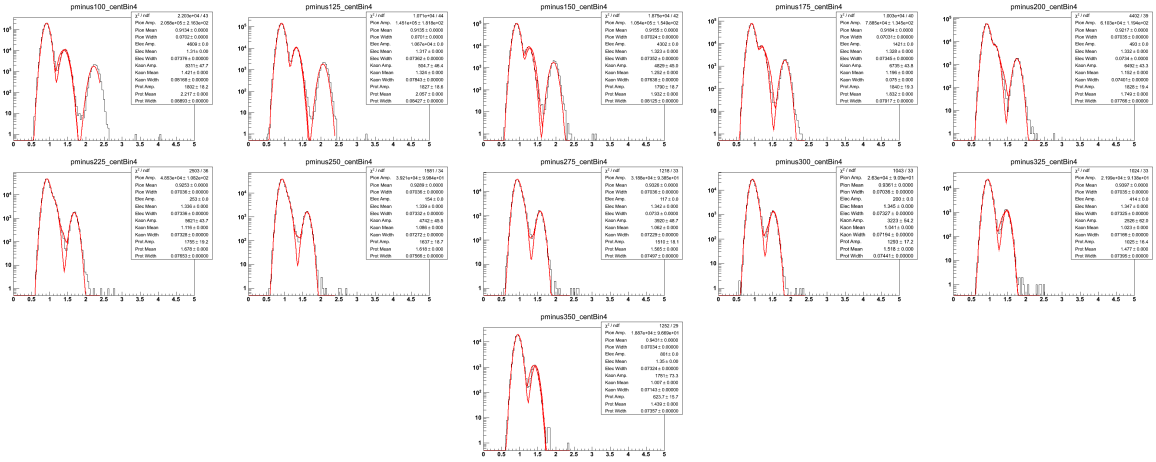

Figure A.59: Negative proton TPC fits for 30%-40% central events $Au + Au\sqrt{s_{NN}} = 19.6$ GeV. These are organized in 25 MeV bins in $m_T - m_p$ in a rapidity window of 0.1 units around mid-rapidity, $|y| < 0.05$. The Gaussian fits, drawn in red, are in $\log(10^6 \times dE/dx)$ and are of the $m_T - m_p = 0.100$ to 0.500 GeV/c^2 range. The track data are represented in the black histogram.

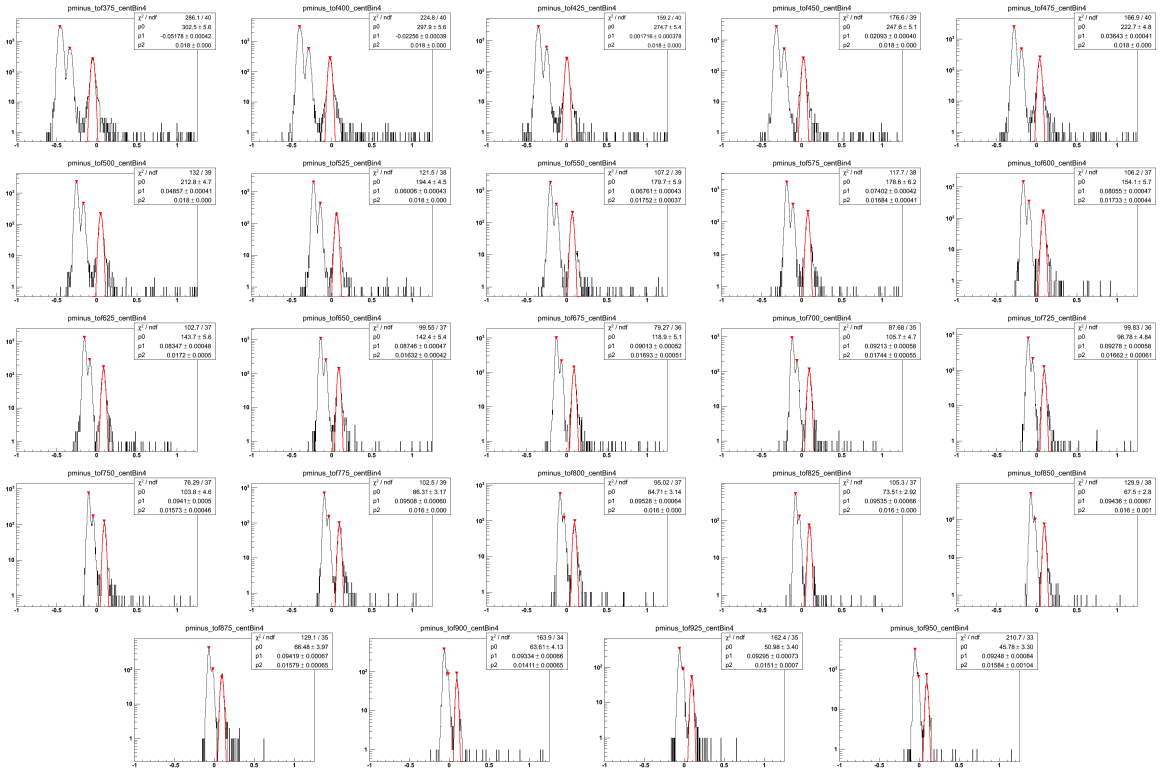

Figure A.60: Negative proton TOF fits for 30%-40% central events $Au + Au\sqrt{s_{NN}} = 19.6$ GeV. These are organized in 25 MeV bins in $m_T - m_p$ in a rapidity window of 0.1 units around mid-rapidity, $|y| < 0.05$. The Gaussian fits, drawn in red, are in $\beta^{-1}_{\text{expected}} - \beta^{-1}_{\text{measured}}$ and are of the $m_T - m_p = 0.350$ to 1.0 GeV/c^2 range. The track data are represented in the black histogram.

A.6 The 20%-30% Centrality Class

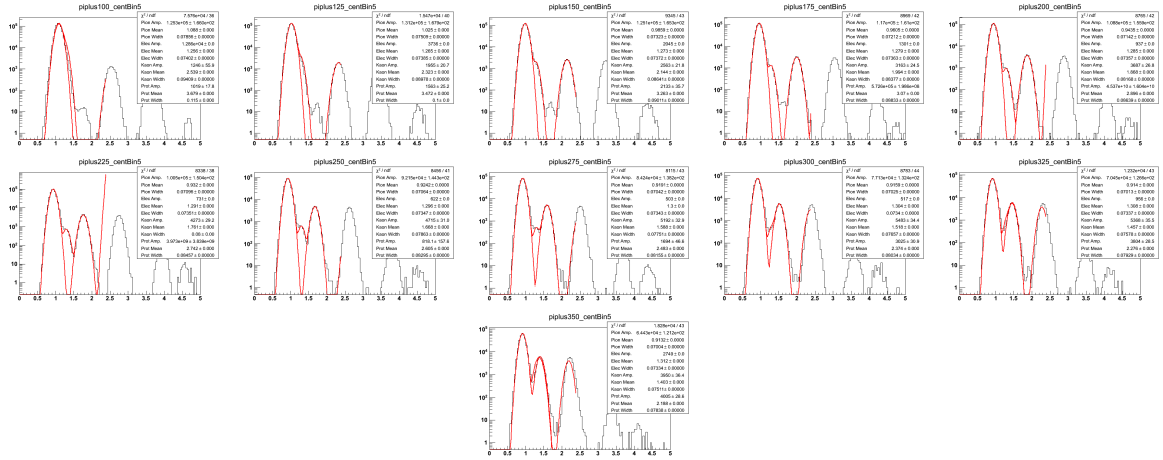

Figure A.61: Positive pion TPC fits for 20%-30% central events $Au+Au\sqrt{s_{NN}} = 19.6$ GeV. These are organized in 25 MeV bins in $m_T - m_\pi$ in a rapidity window of 0.1 units around mid-rapidity, $|y| < 0.05$. The Gaussian fits, drawn in red, are in $\log(10^6 \times dE/dx)$ and are of the $m_T - m_\pi =$ 0.100 to 0.500 GeV/c^2 range. The track data are represented in the black histogram.

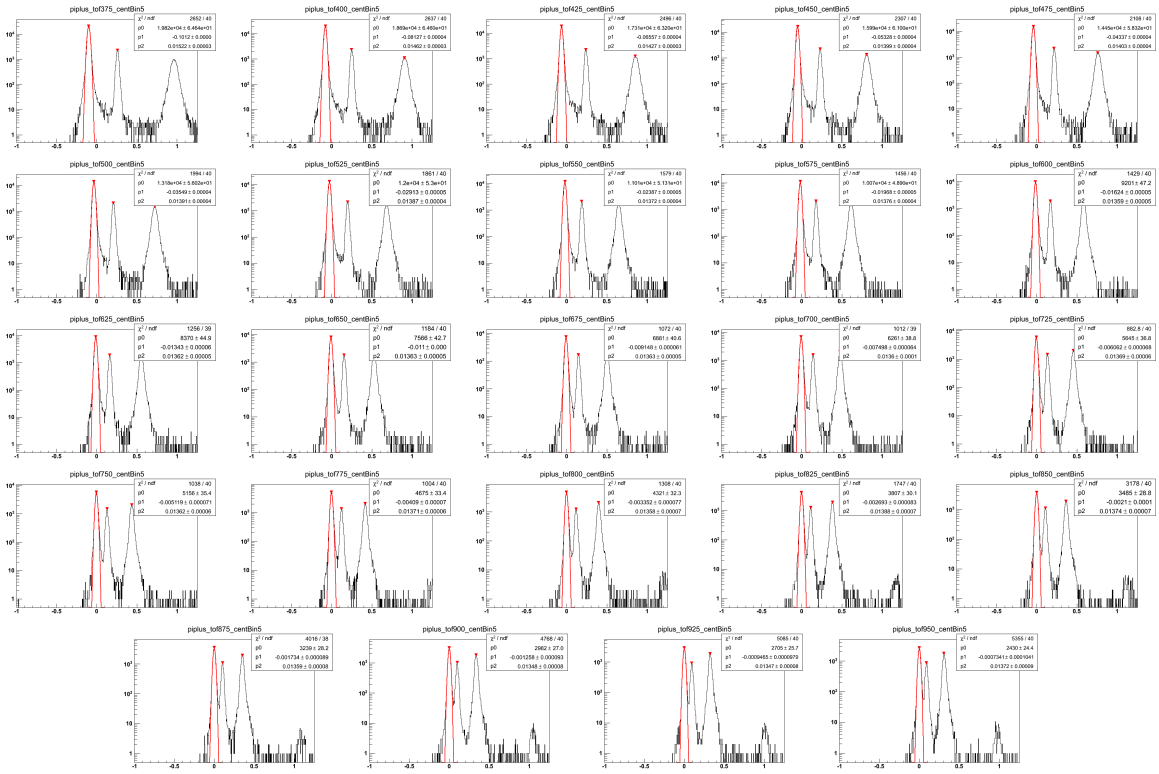

Figure A.62: Positive pion TOF fits for 20%-30% central events $Au+Au\sqrt{s_{NN}} = 19.6$ GeV. These are organized in 25 MeV bins in $m_T - m_\pi$ in a rapidity window of 0.1 units around mid-rapidity, $|y| < 0.05$. The Gaussian fits, drawn in red, are in $\beta^{-1}_{\text{expected}} - \beta^{-1}_{\text{measured}}$ and are of the $m_T - m_\pi = 0.350$ to 1.0 GeV/c^2 range. The track data are represented in the black histogram.

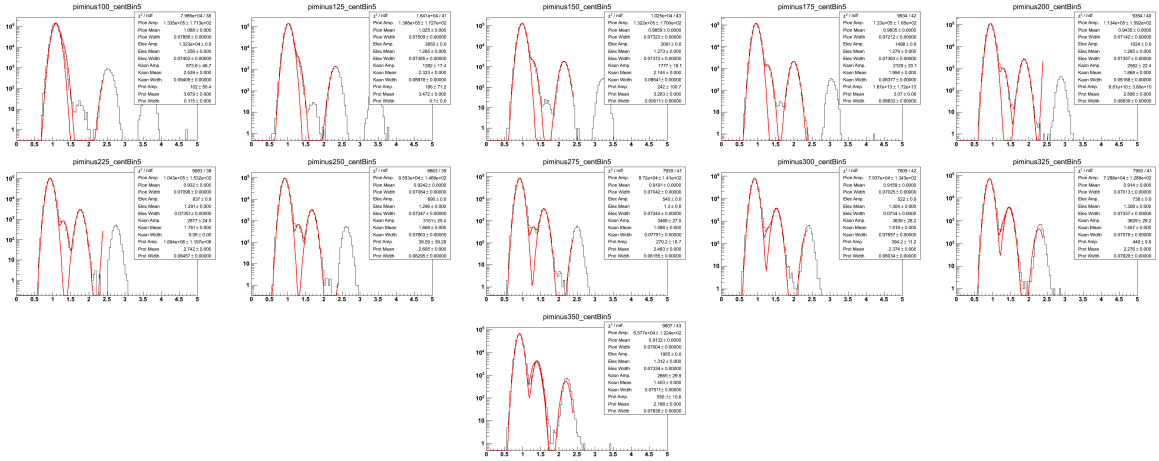

Figure A.63: Negative pion TPC fits for 20%-30% central events $Au+Au\sqrt{s_{NN}} = 19.6$ GeV. These are organized in 25 MeV bins in $m_T - m_\pi$ in a rapidity window of 0.1 units around mid-rapidity, $|y| < 0.05$. The Gaussian fits, drawn in red, are in $\log(10^6 \times dE/dx)$ and are of the $m_T - m_\pi = 0.100$ to 0.500 GeV/c^2 range. The track data are represented in the black histogram.

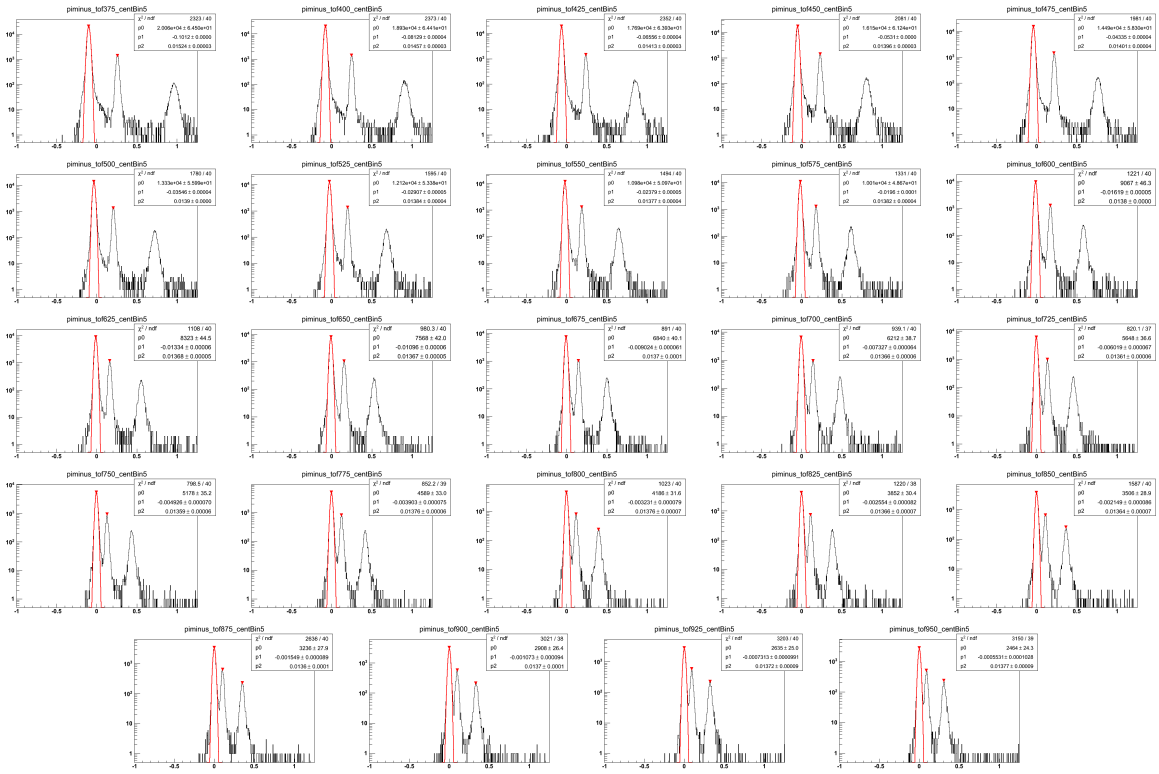

Figure A.64: Negative pion TOF fits for 20%-30% central events $Au+Au\sqrt{s_{NN}} = 19.6$ GeV. These are organized in 25 MeV bins in $m_T - m_\pi$ in a rapidity window of 0.1 units around mid-rapidity, $|y| < 0.05$. The Gaussian fits, drawn in red, are in $\beta^{-1}_{\text{expected}} - \beta^{-1}_{\text{measured}}$ and are of the $m_T - m_\pi =$ 0.350 to 1.0 GeV/c^2 range. The track data are represented in the black histogram.

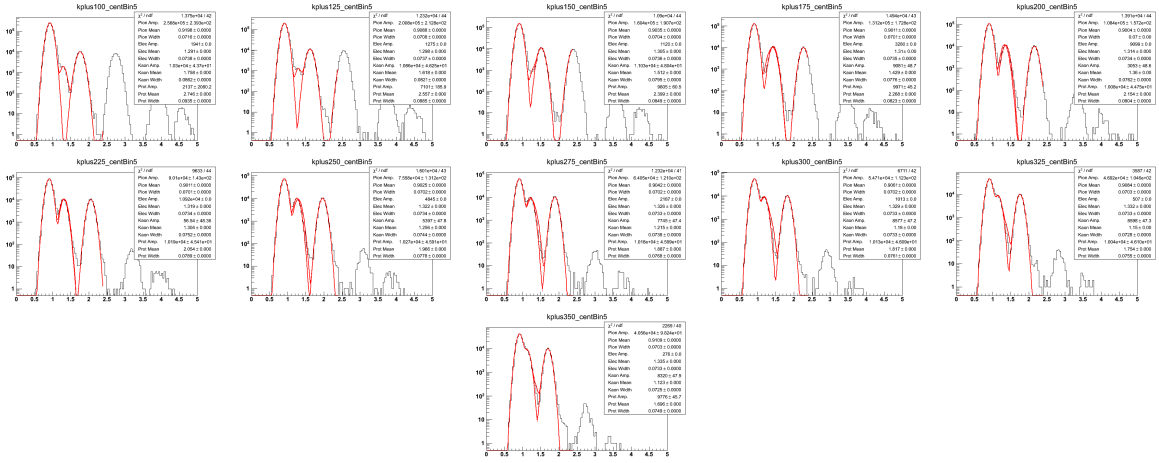

Figure A.65: Positive kaon TPC fits for 20%-30% central events $Au+Au\sqrt{s_{NN}} = 19.6$ GeV. These are organized in 25 MeV bins in $m_T - m_K$ in a rapidity window of 0.1 units around mid-rapidity, $|y| < 0.05$. The Gaussian fits, drawn in red, are in $\log(10^6 \times dE/dx)$ and are of the $m_T - m_K =$ 0.100 to 0.500 GeV/c^2 range. The track data are represented in the black histogram.

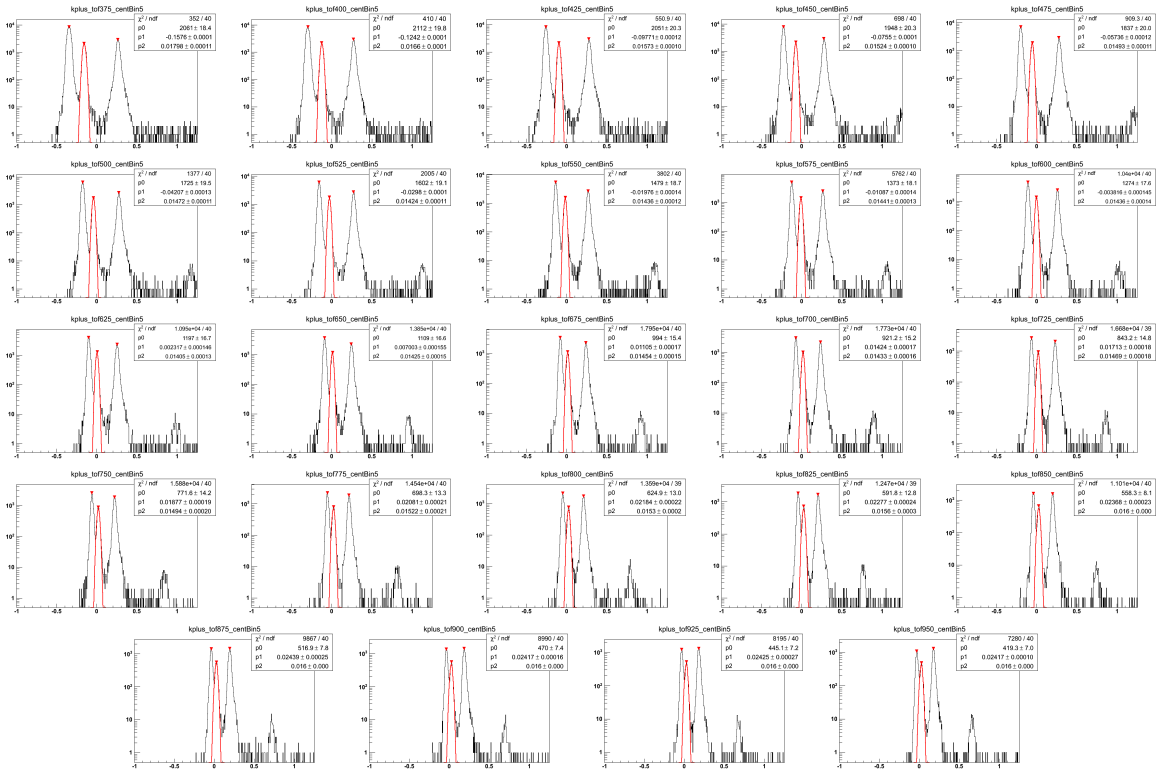

Figure A.66: Positive kaon TOF fits for 20%-30% central events $Au+Au\sqrt{s_{NN}} = 19.6$ GeV. These are organized in 25 MeV bins in $m_T - m_K$ in a rapidity window of 0.1 units around mid-rapidity, $|y| < 0.05$. The Gaussian fits, drawn in red, are in $\beta^{-1}_{\text{expected}} - \beta^{-1}_{\text{measured}}$ and are of the $m_T - m_K =$ 0.350 to 1.0 GeV/c^2 range. The track data are represented in the black histogram.

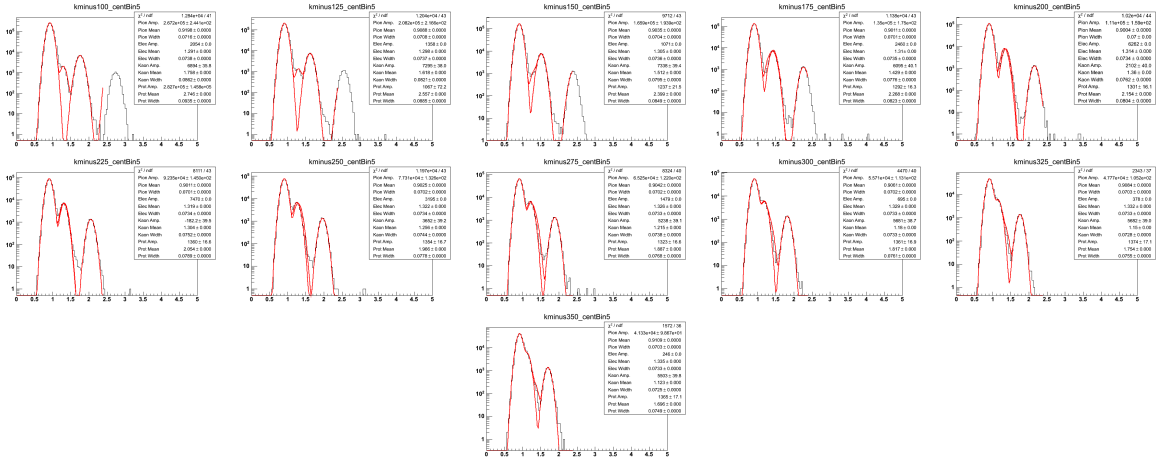

Figure A.67: Negative kaon TPC fits for 20%-30% central events $Au+Au\sqrt{s_{NN}} = 19.6$ GeV. These are organized in 25 MeV bins in $m_T - m_K$ in a rapidity window of 0.1 units around mid-rapidity, $|y| < 0.05$. The Gaussian fits, drawn in red, are in $\log(10^6 \times dE/dx)$ and are of the $m_T - m_K =$ 0.100 to 0.500 GeV/c^2 range. The track data are represented in the black histogram.

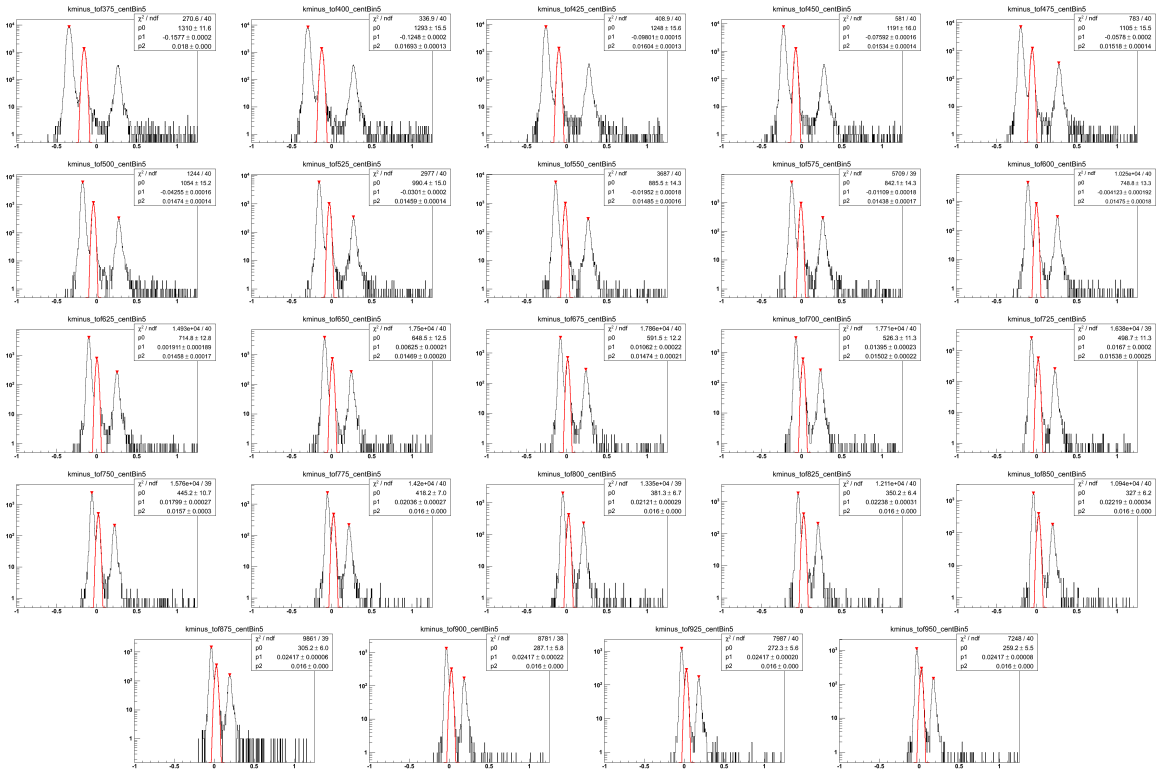

Figure A.68: Negative kaon TOF fits for 20%-30% central events $Au + Au\sqrt{s_{NN}} = 19.6$ GeV. These are organized in 25 MeV bins in $m_T - m_K$ in a rapidity window of 0.1 units around mid-rapidity, $|y| < 0.05$. The Gaussian fits, drawn in red, are in $\beta^{-1}_{\text{expected}} - \beta^{-1}_{\text{measured}}$ and are of the $m_T - m_K = 0.350$ to 1.0 GeV/c^2 range. The track data are represented in the black histogram.

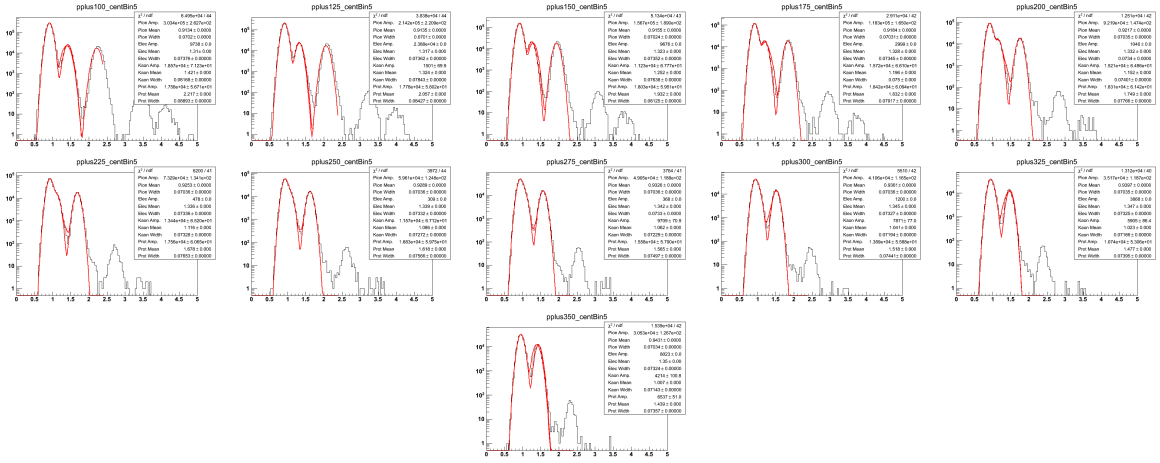

Figure A.69: Positive proton TPC fits for 20%-30% central events $Au + Au\sqrt{s_{NN}} = 19.6$ GeV. These are organized in 25 MeV bins in $m_T - m_p$ in a rapidity window of 0.1 units around mid-rapidity, $|y| < 0.05$. The Gaussian fits, drawn in red, are in $\log(10^6 \times dE/dx)$ and are of the $m_T - m_p = 0.100$ to 0.500 GeV/c^2 range. The track data are represented in the black histogram.

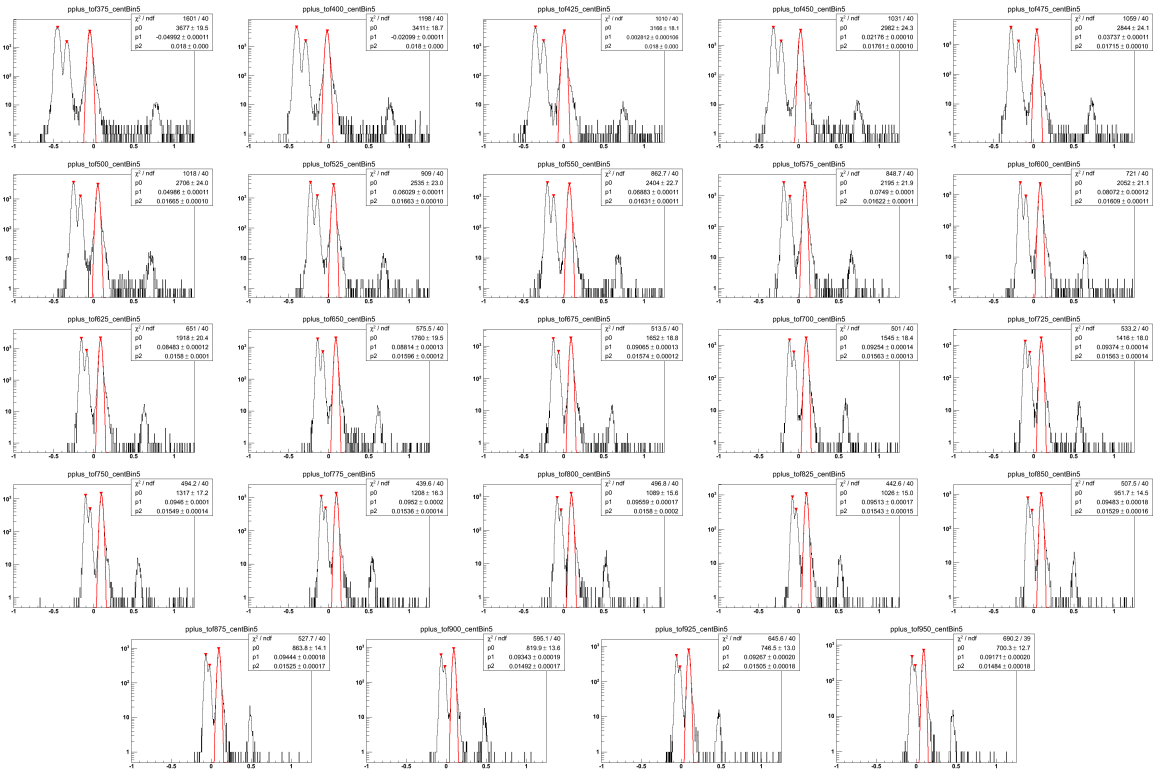

Figure A.70: Positive proton TOF fits for 20%-30% central events $Au + Au\sqrt{s_{NN}} = 19.6$ GeV. These are organized in 25 MeV bins in $m_T - m_p$ in a rapidity window of 0.1 units around mid-rapidity, $|y| < 0.05$. The Gaussian fits, drawn in red, are in $\beta^{-1}_{\text{expected}} - \beta^{-1}_{\text{measured}}$ and are of the $m_T - m_p = 0.350$ to 1.0 GeV/c^2 range. The track data are represented in the black histogram.

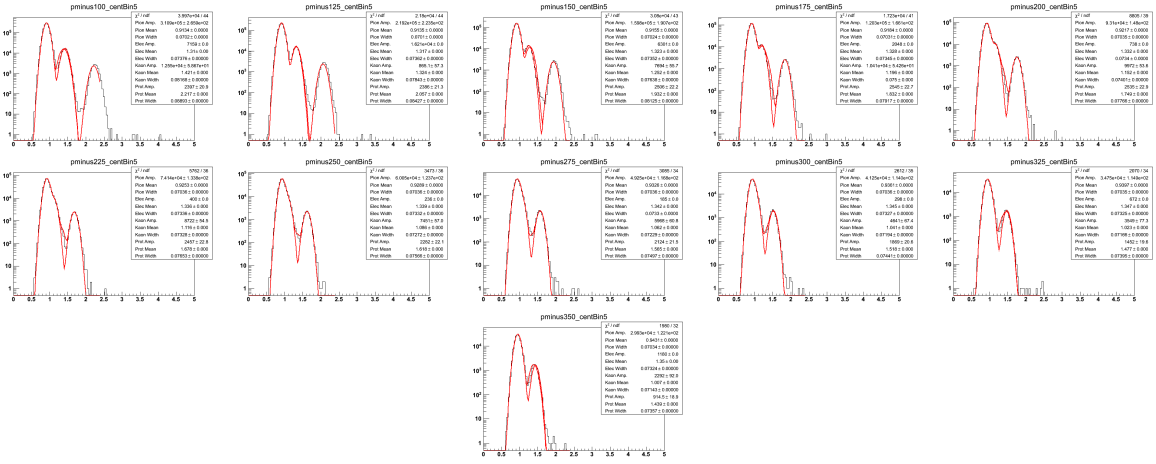

Figure A.71: Negative proton TPC fits for 20%-30% central events $Au + Au\sqrt{s_{NN}} = 19.6$ GeV. These are organized in 25 MeV bins in $m_T - m_p$ in a rapidity window of 0.1 units around mid-rapidity, $|y| < 0.05$. The Gaussian fits, drawn in red, are in $\log(10^6 \times dE/dx)$ and are of the $m_T - m_p = 0.100$ to 0.500 GeV/c^2 range. The track data are represented in the black histogram.

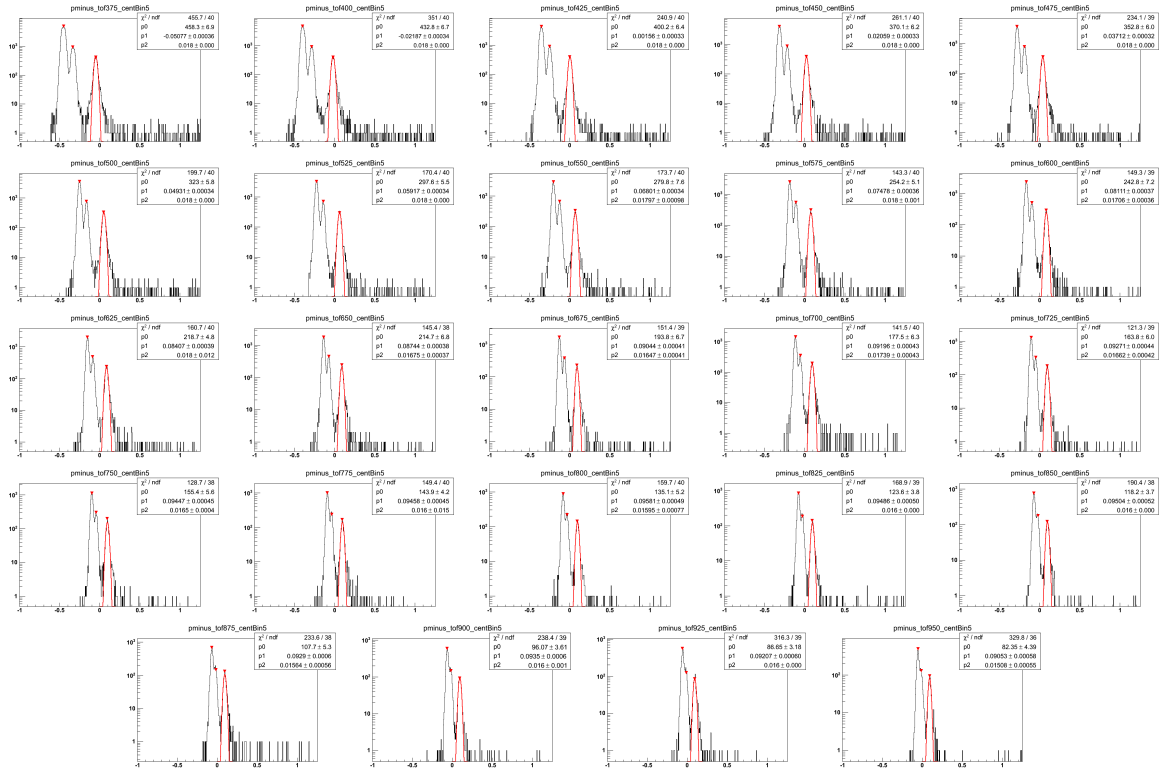

Figure A.72: Negative proton TOF fits for 20%-30% central events $Au + Au\sqrt{s_{NN}} = 19.6$ GeV. These are organized in 25 MeV bins in $m_T - m_p$ in a rapidity window of 0.1 units around mid-rapidity, $|y| < 0.05$. The Gaussian fits, drawn in red, are in $\beta^{-1}_{\text{expected}} - \beta^{-1}_{\text{measured}}$ and are of the $m_T - m_p = 0.350$ to 1.0 GeV/c^2 range. The track data are represented in the black histogram.

A.7 The 10%-20% Centrality Class

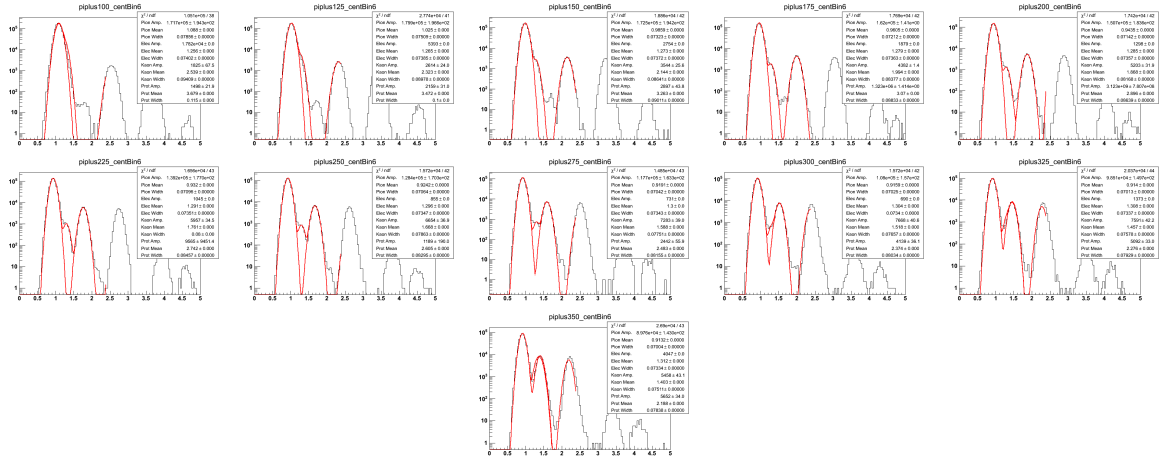

Figure A.73: Positive pion TPC fits for 10%-20% central events $Au+Au\sqrt{s_{NN}} = 19.6$ GeV. These are organized in 25 MeV bins in $m_T - m_\pi$ in a rapidity window of 0.1 units around mid-rapidity, $|y| < 0.05$. The Gaussian fits, drawn in red, are in $\log(10^6 \times dE/dx)$ and are of the $m_T - m_\pi =$ 0.100 to 0.500 GeV/c^2 range. The track data are represented in the black histogram.

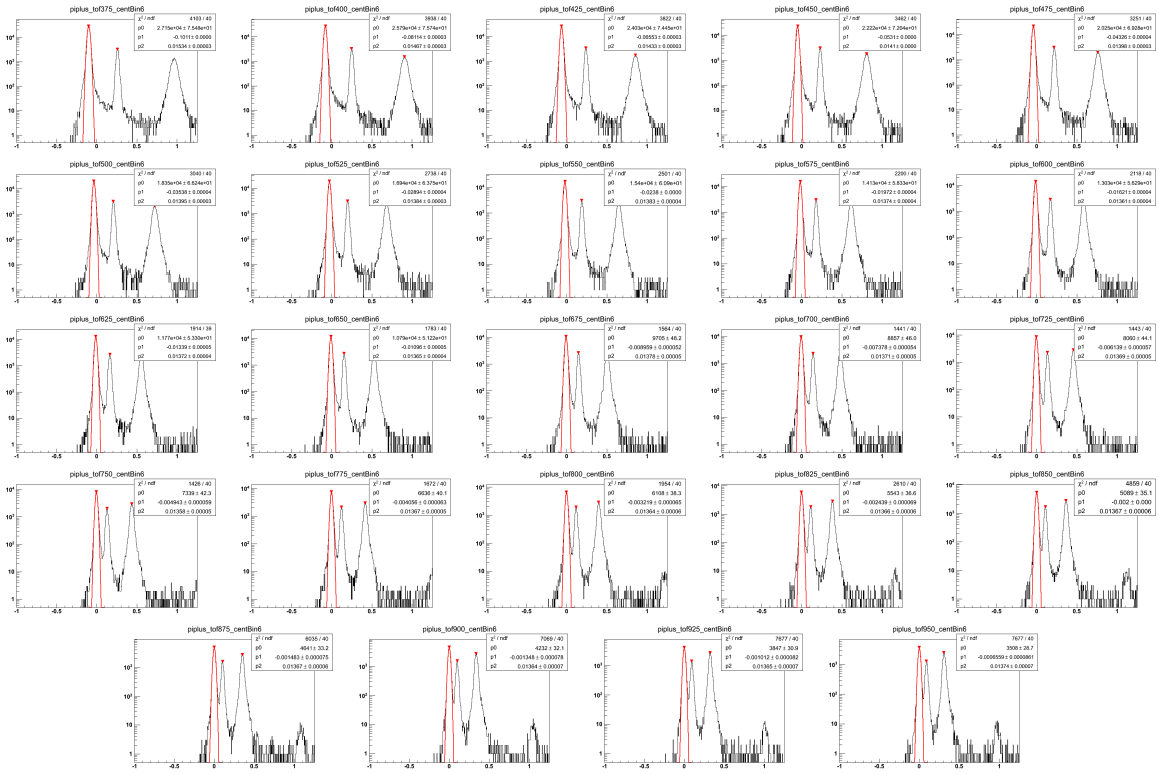

Figure A.74: Positive pion TOF fits for 10%-20% central events $Au+Au\sqrt{s_{NN}} = 19.6$ GeV. These are organized in 25 MeV bins in $m_T - m_\pi$ in a rapidity window of 0.1 units around mid-rapidity, $|y| < 0.05$. The Gaussian fits, drawn in red, are in $\beta^{-1}_{\text{expected}} - \beta^{-1}_{\text{measured}}$ and are of the $m_T - m_\pi =$ 0.350 to 1.0 GeV/c^2 range. The track data are represented in the black histogram.

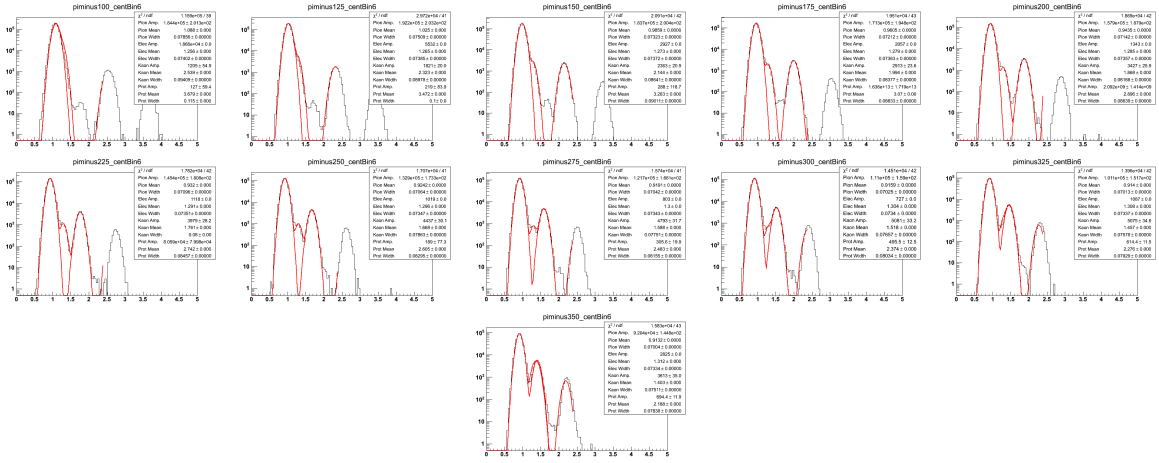

Figure A.75: Negative pion TPC fits for 10%-20% central events $Au+Au\sqrt{s_{NN}} = 19.6$ GeV. These are organized in 25 MeV bins in $m_T - m_\pi$ in a rapidity window of 0.1 units around mid-rapidity, $|y| < 0.05$. The Gaussian fits, drawn in red, are in $\log(10^6 \times dE/dx)$ and are of the $m_T - m_\pi =$ 0.100 to 0.500 GeV/c^2 range. The track data are represented in the black histogram.

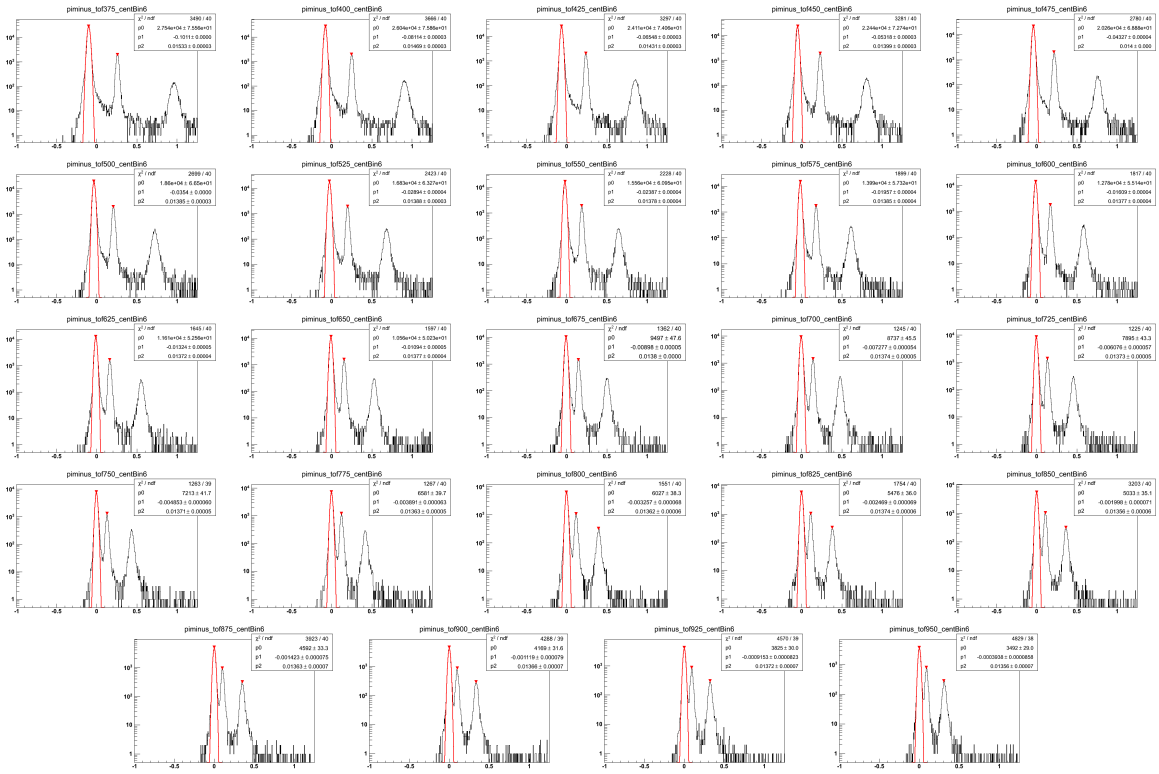

Figure A.76: Negative pion TOF fits for 10%-20% central events $Au+Au\sqrt{s_{NN}} = 19.6$ GeV. These are organized in 25 MeV bins in $m_T - m_\pi$ in a rapidity window of 0.1 units around mid-rapidity, $|y| < 0.05$. The Gaussian fits, drawn in red, are in $\beta^{-1}_{\text{expected}} - \beta^{-1}_{\text{measured}}$ and are of the $m_T - m_\pi =$ 0.350 to 1.0 GeV/c^2 range. The track data are represented in the black histogram.

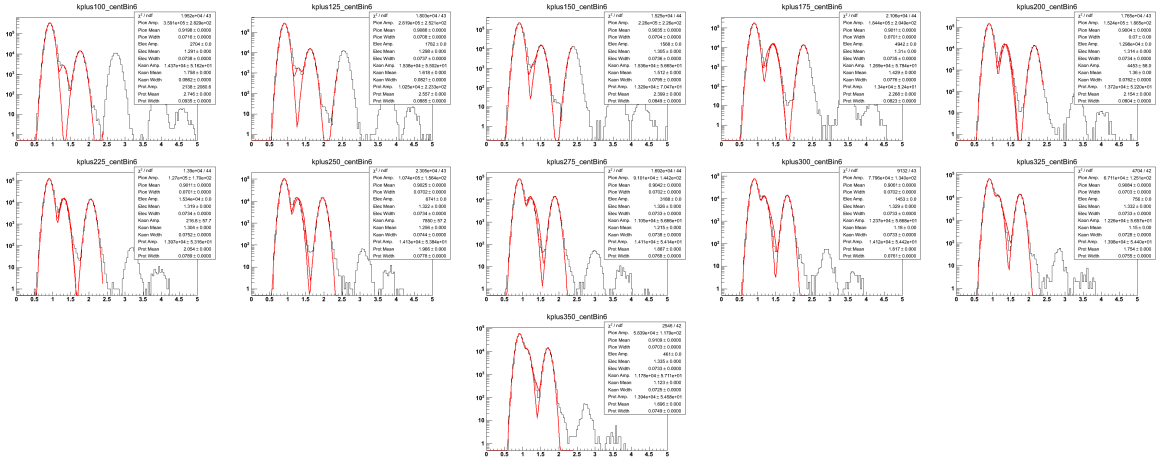

Figure A.77: Positive kaon TPC fits for 10%-20% central events $Au+Au\sqrt{s_{NN}} = 19.6$ GeV. These are organized in 25 MeV bins in $m_T - m_K$ in a rapidity window of 0.1 units around mid-rapidity, $|y| < 0.05$. The Gaussian fits, drawn in red, are in $\log(10^6 \times dE/dx)$ and are of the $m_T - m_K =$ 0.100 to 0.500 GeV/c^2 range. The track data are represented in the black histogram.

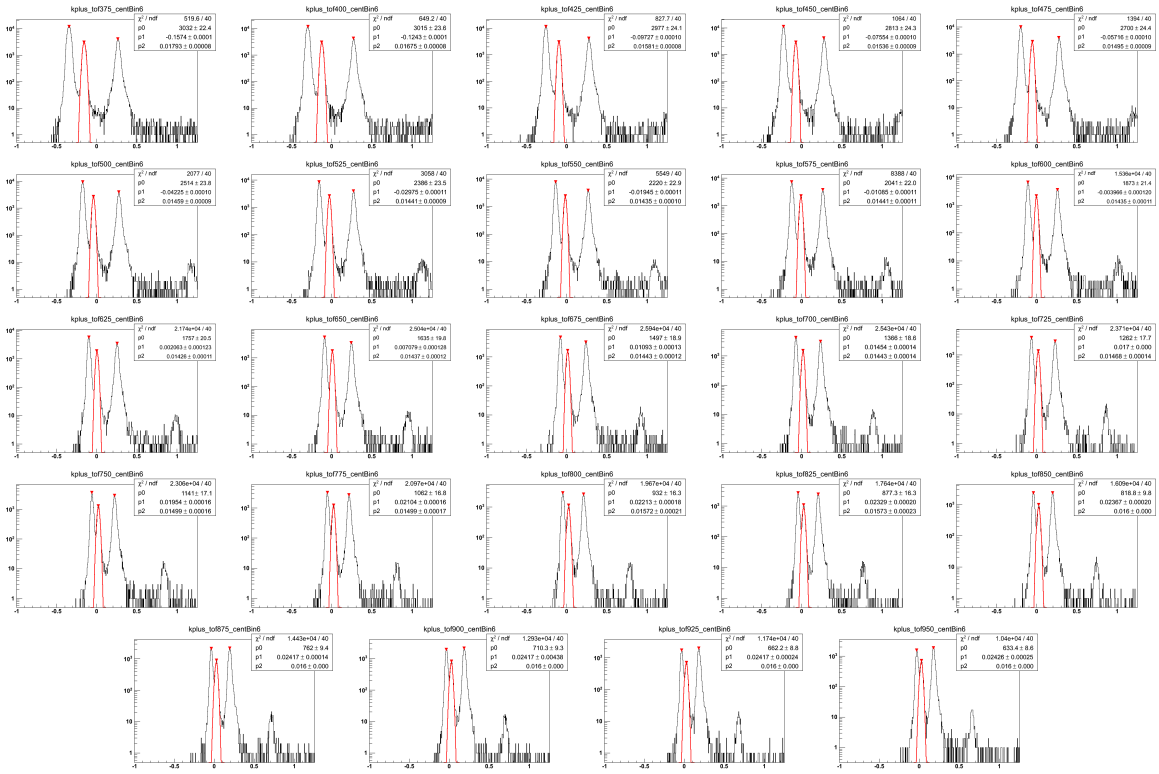

Figure A.78: Positive kaon TOF fits for 10%-20% central events $Au+Au\sqrt{s_{NN}} = 19.6$ GeV. These are organized in 25 MeV bins in $m_T - m_K$ in a rapidity window of 0.1 units around mid-rapidity, $|y| < 0.05$. The Gaussian fits, drawn in red, are in $\beta^{-1}_{\text{expected}} - \beta^{-1}_{\text{measured}}$ and are of the $m_T - m_K =$ 0.350 to 1.0 GeV/c^2 range. The track data are represented in the black histogram.

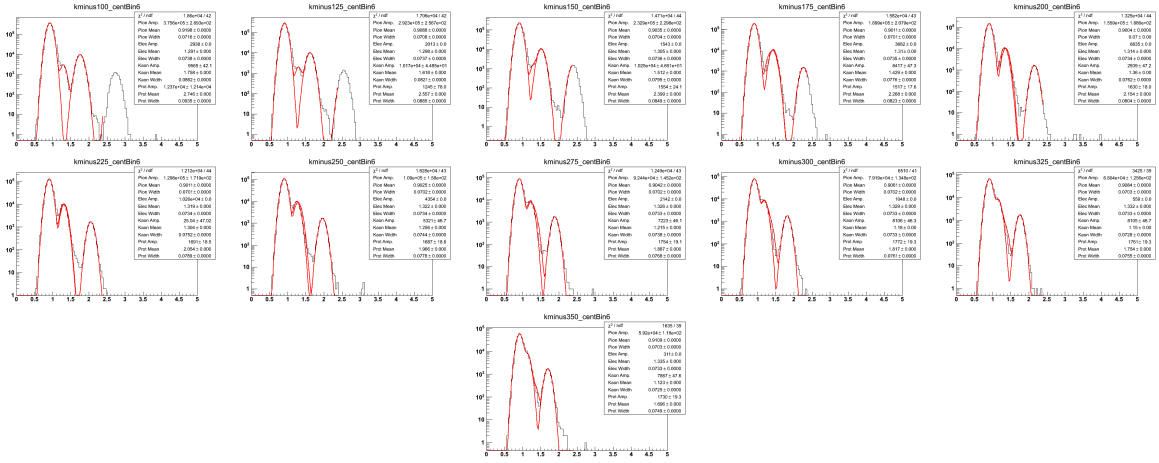

Figure A.79: Negative kaon TPC fits for 10%-20% central events $Au+Au\sqrt{s_{NN}} = 19.6$ GeV. These are organized in 25 MeV bins in $m_T - m_K$ in a rapidity window of 0.1 units around mid-rapidity, $|y| < 0.05$. The Gaussian fits, drawn in red, are in $\log(10^6 \times dE/dx)$ and are of the $m_T - m_K =$ 0.100 to 0.500 GeV/c^2 range. The track data are represented in the black histogram.

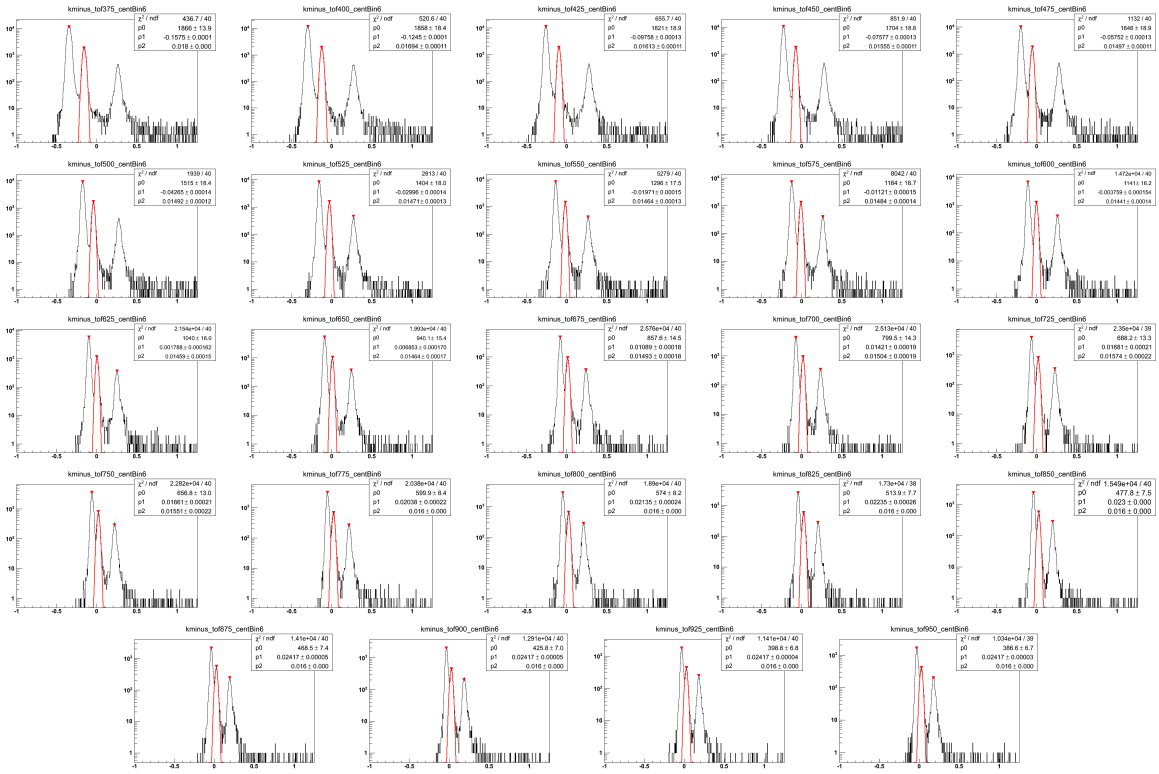

Figure A.80: Negative kaon TOF fits for 10%-20% central events $Au + Au\sqrt{s_{NN}} = 19.6$ GeV. These are organized in 25 MeV bins in $m_T - m_K$ in a rapidity window of 0.1 units around mid-rapidity, $|y| < 0.05$. The Gaussian fits, drawn in red, are in $\beta^{-1}_{\text{expected}} - \beta^{-1}_{\text{measured}}$ and are of the $m_T - m_K = 0.350$ to 1.0 GeV/c^2 range. The track data are represented in the black histogram.

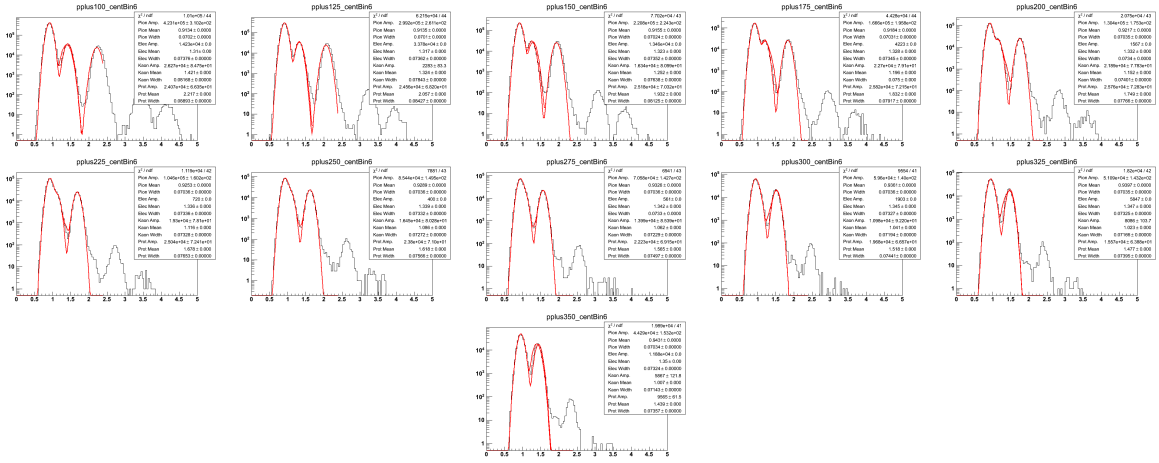

Figure A.81: Positive proton TPC fits for 10%-20% central events $Au + Au\sqrt{s_{NN}} = 19.6$ GeV. These are organized in 25 MeV bins in $m_T - m_p$ in a rapidity window of 0.1 units around mid-rapidity, $|y| < 0.05$. The Gaussian fits, drawn in red, are in $\log(10^6 \times dE/dx)$ and are of the $m_T - m_p = 0.100$ to 0.500 GeV/c^2 range. The track data are represented in the black histogram.

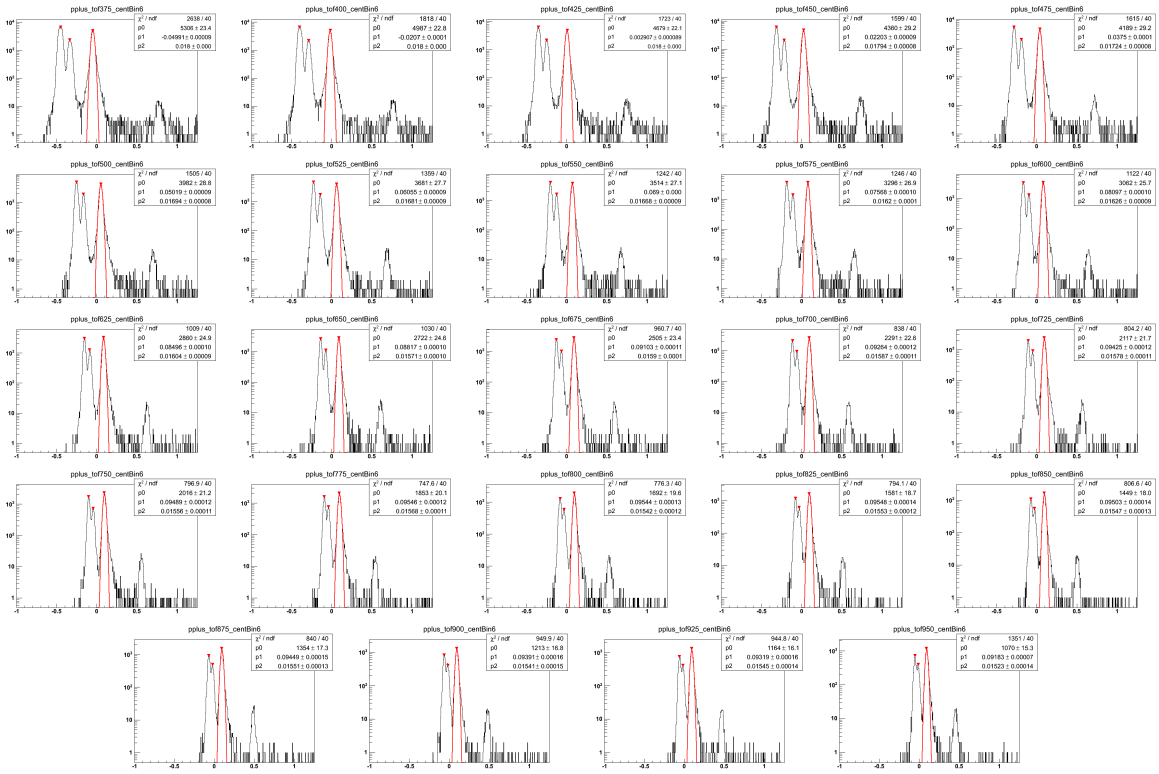

Figure A.82: Positive proton TOF fits for 10%-20% central events $Au + Au\sqrt{s_{NN}} = 19.6$ GeV. These are organized in 25 MeV bins in $m_T - m_p$ in a rapidity window of 0.1 units around mid-rapidity, $|y| < 0.05$. The Gaussian fits, drawn in red, are in $\beta^{-1}_{\text{expected}} - \beta^{-1}_{\text{measured}}$ and are of the $m_T - m_p = 0.350$ to 1.0 GeV/c^2 range. The track data are represented in the black histogram.

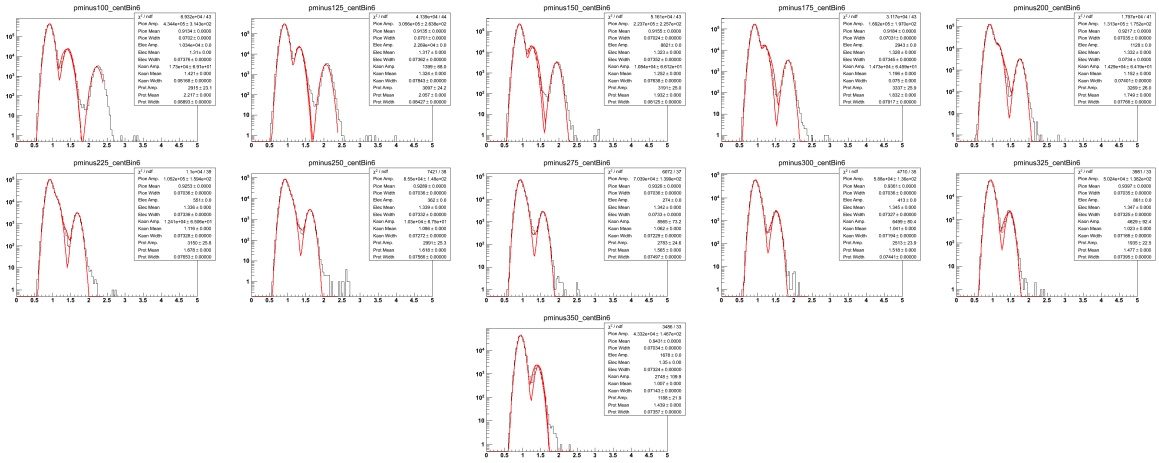

Figure A.83: Negative proton TPC fits for 10%-20% central events $Au + Au\sqrt{s_{NN}} = 19.6$ GeV. These are organized in 25 MeV bins in $m_T - m_p$ in a rapidity window of 0.1 units around mid-rapidity, $|y| < 0.05$. The Gaussian fits, drawn in red, are in $\log(10^6 \times dE/dx)$ and are of the $m_T - m_p = 0.100$ to 0.500 GeV/c^2 range. The track data are represented in the black histogram.

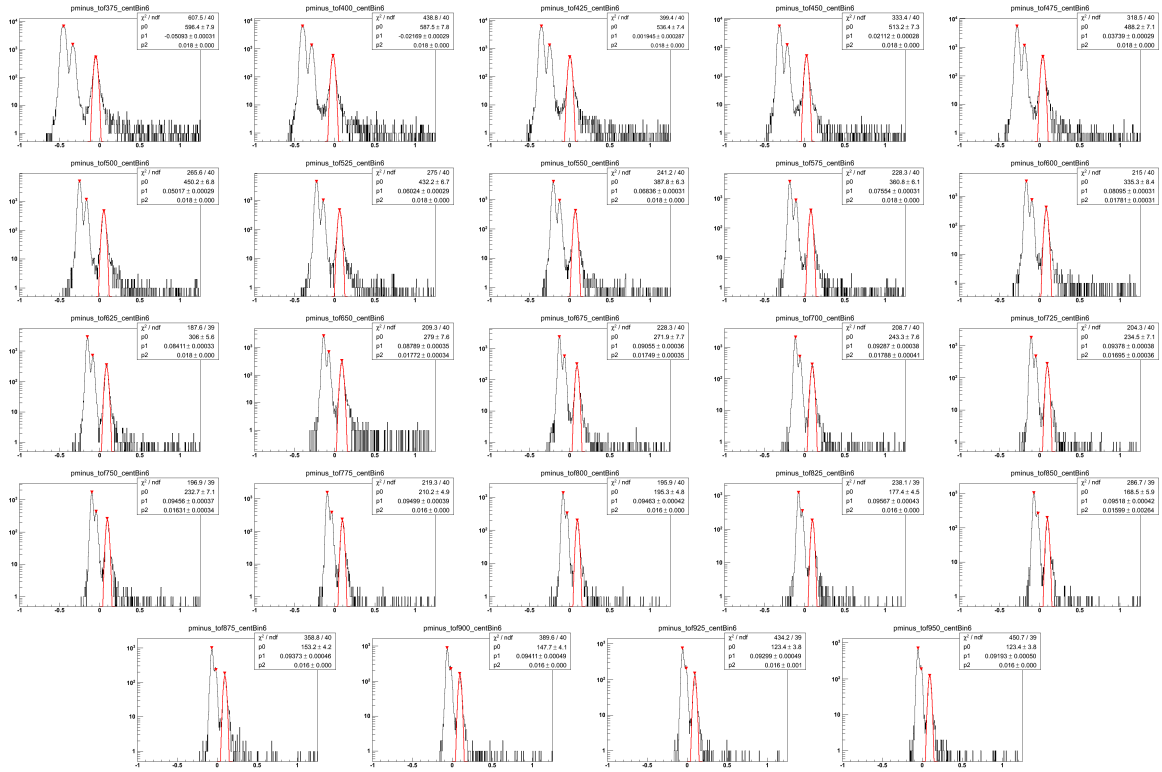

Figure A.84: Negative proton TOF fits for 10%-20% central events $Au + Au\sqrt{s_{NN}} = 19.6$ GeV. These are organized in 25 MeV bins in $m_T - m_p$ in a rapidity window of 0.1 units around mid-rapidity, $|y| < 0.05$. The Gaussian fits, drawn in red, are in $\beta^{-1}_{\text{expected}} - \beta^{-1}_{\text{measured}}$ and are of the $m_T - m_p = 0.350$ to 1.0 GeV/c^2 range. The track data are represented in the black histogram.

A.8 The 5%-10% Centrality Class

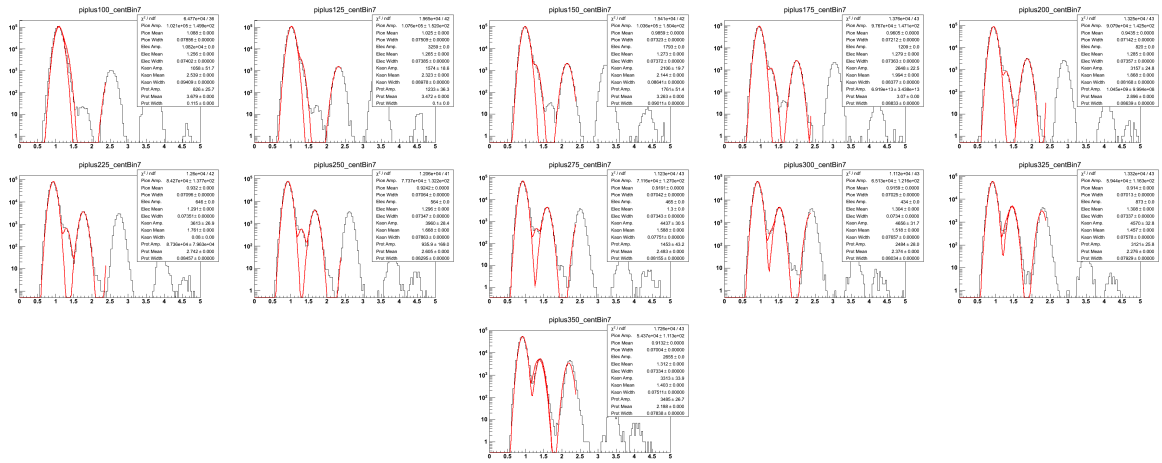

Figure A.85: Positive pion TPC fits for 5%-10% central events $Au+Au\sqrt{s_{NN}} = 19.6$ GeV. These are organized in 25 MeV bins in $m_T - m_\pi$ in a rapidity window of 0.1 units around mid-rapidity, $|y| < 0.05$. The Gaussian fits, drawn in red, are in $\log(10^6 \times dE/dx)$ and are of the $m_T - m_\pi =$ 0.100 to 0.500 GeV/c^2 range. The track data are represented in the black histogram.

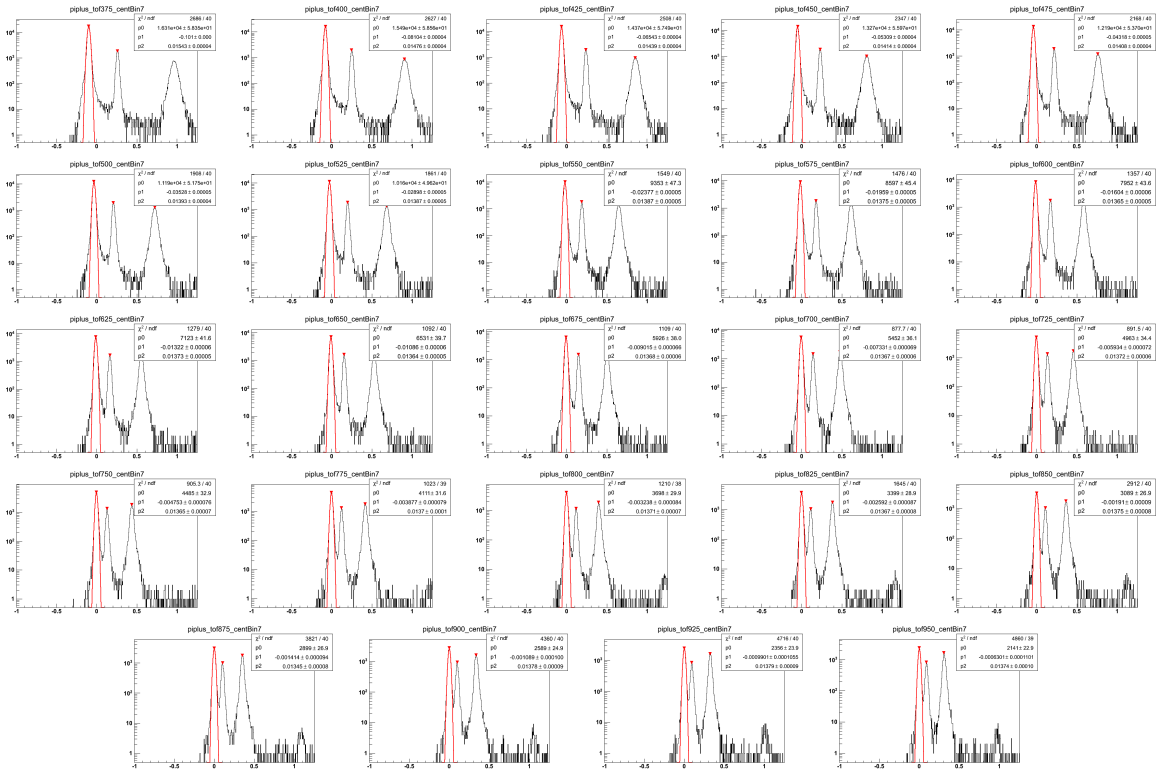

Figure A.86: Positive pion TOF fits for 5%-10% central events $Au+Au\sqrt{s_{NN}} = 19.6$ GeV. These are organized in 25 MeV bins in $m_T - m_\pi$ in a rapidity window of 0.1 units around mid-rapidity, $|y| < 0.05$. The Gaussian fits, drawn in red, are in $\beta^{-1}_{\text{expected}} - \beta^{-1}_{\text{measured}}$ and are of the $m_T - m_\pi = 0.350$ to 1.0 GeV/c^2 range. The track data are represented in the black histogram.

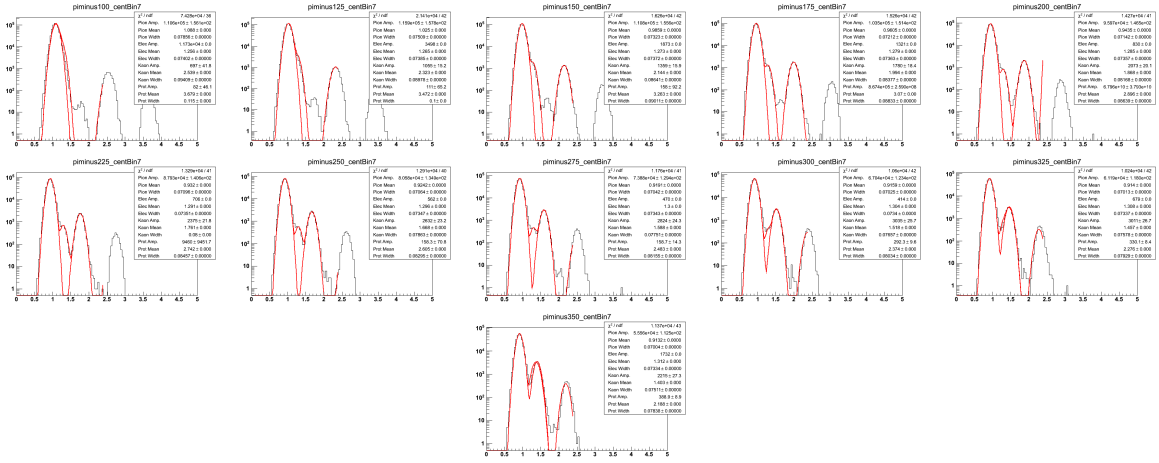

Figure A.87: Negative pion TPC fits for 5%-10% central events $Au+Au\sqrt{s_{NN}} = 19.6$ GeV. These are organized in 25 MeV bins in $m_T - m_\pi$ in a rapidity window of 0.1 units around mid-rapidity, $|y| < 0.05$. The Gaussian fits, drawn in red, are in $\log(10^6 \times dE/dx)$ and are of the $m_T - m_\pi = 0.100$ to 0.500 GeV/c^2 range. The track data are represented in the black histogram.

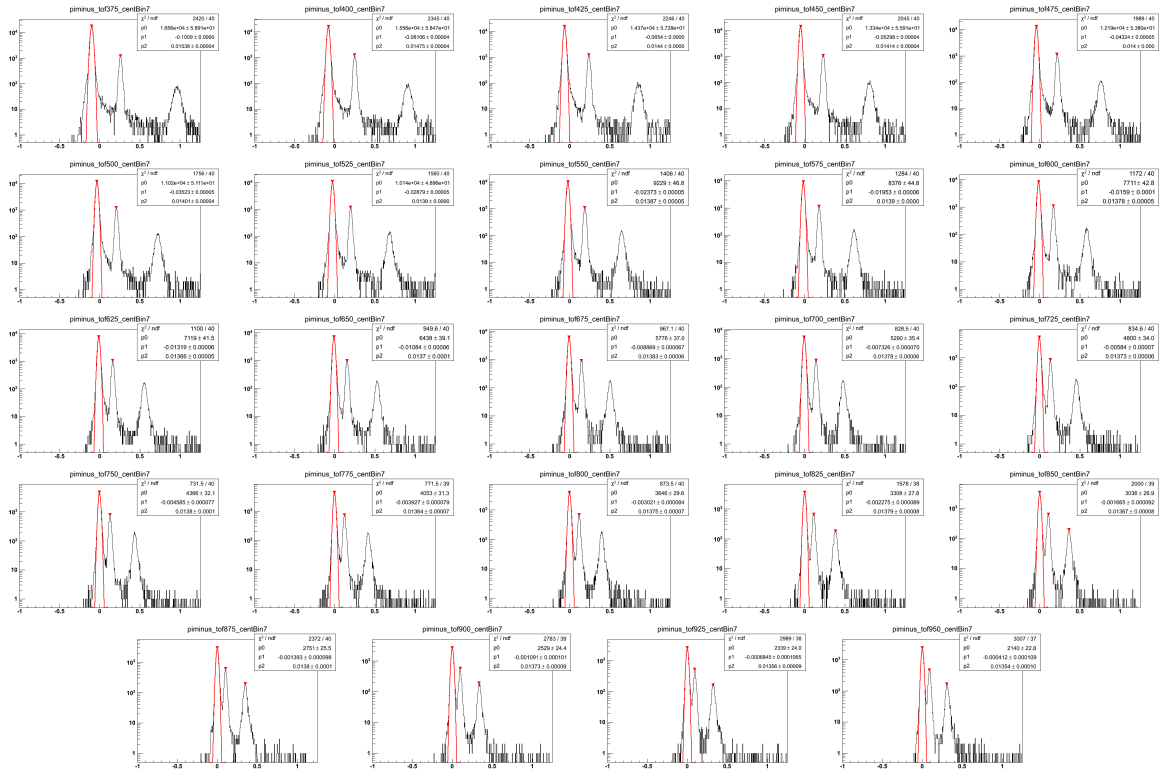

Figure A.88: Negative pion TOF fits for 5%-10% central events $Au+Au\sqrt{s_{NN}} = 19.6$ GeV. These are organized in 25 MeV bins in $m_T - m_\pi$ in a rapidity window of 0.1 units around mid-rapidity, $|y| < 0.05$. The Gaussian fits, drawn in red, are in $\beta^{-1}_{\text{expected}} - \beta^{-1}_{\text{measured}}$ and are of the $m_T - m_\pi =$ 0.350 to 1.0 GeV/c^2 range. The track data are represented in the black histogram.

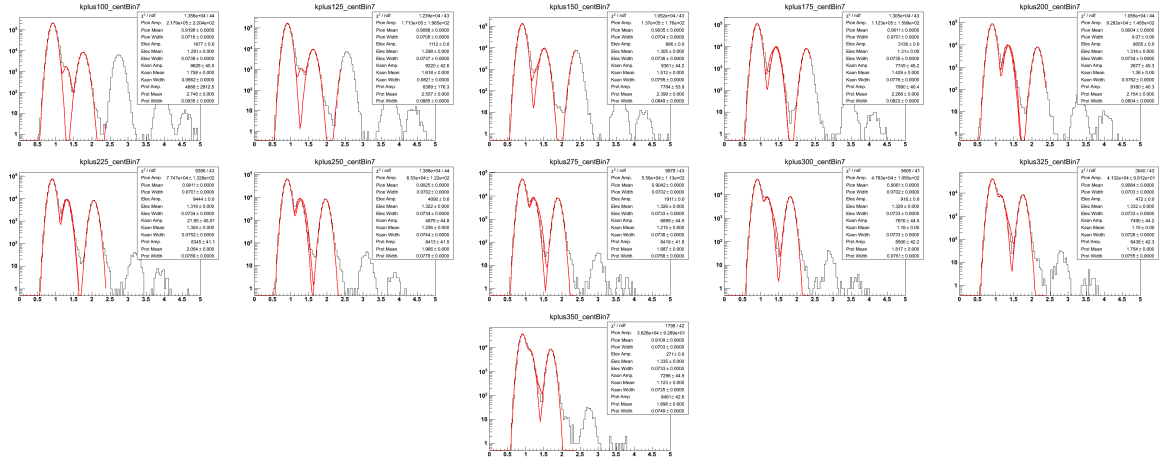

Figure A.89: Positive kaon TPC fits for 5%-10% central events $Au+Au\sqrt{s_{NN}} = 19.6$ GeV. These are organized in 25 MeV bins in $m_T - m_K$ in a rapidity window of 0.1 units around mid-rapidity, $|y| < 0.05$. The Gaussian fits, drawn in red, are in $\log(10^6 \times dE/dx)$ and are of the $m_T - m_K =$ 0.100 to 0.500 GeV/c^2 range. The track data are represented in the black histogram.

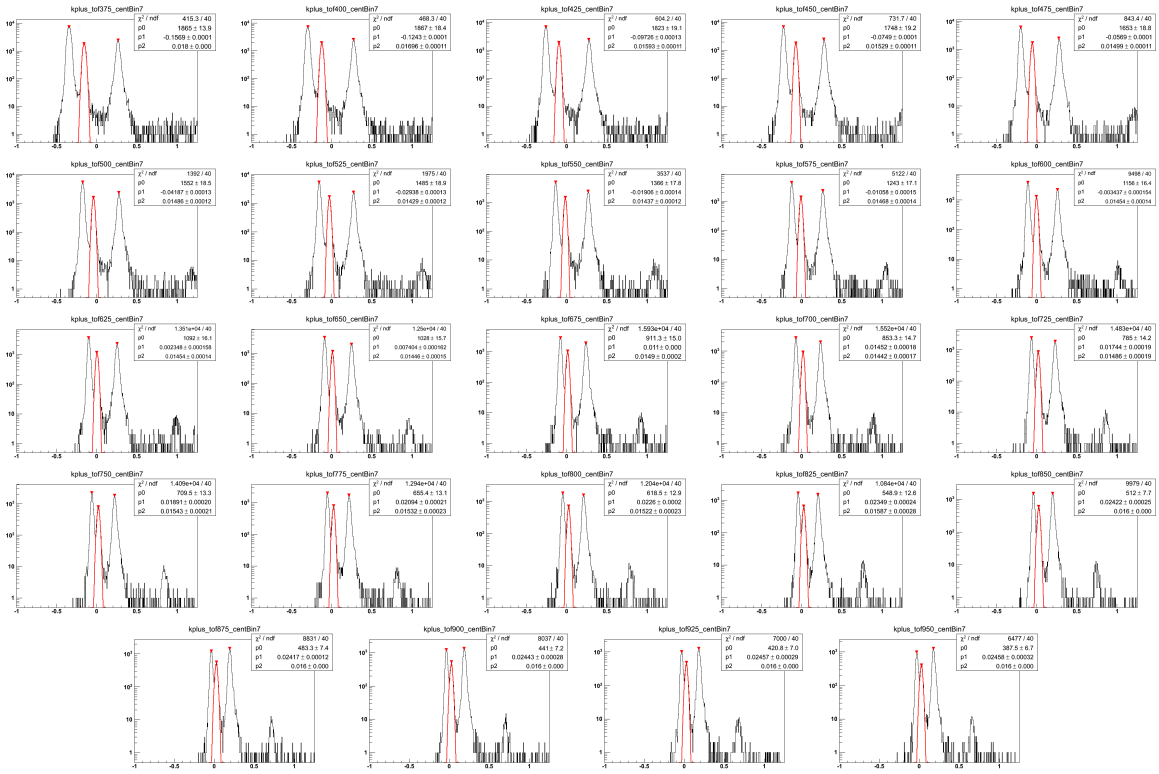

Figure A.90: Positive kaon TOF fits for 5%-10% central events $Au+Au\sqrt{s_{NN}} = 19.6$ GeV. These are organized in 25 MeV bins in $m_T - m_K$ in a rapidity window of 0.1 units around mid-rapidity, $|y| < 0.05$. The Gaussian fits, drawn in red, are in $\beta^{-1}_{\text{expected}} - \beta^{-1}_{\text{measured}}$ and are of the $m_T - m_K =$ 0.350 to 1.0 GeV/c^2 range. The track data are represented in the black histogram.

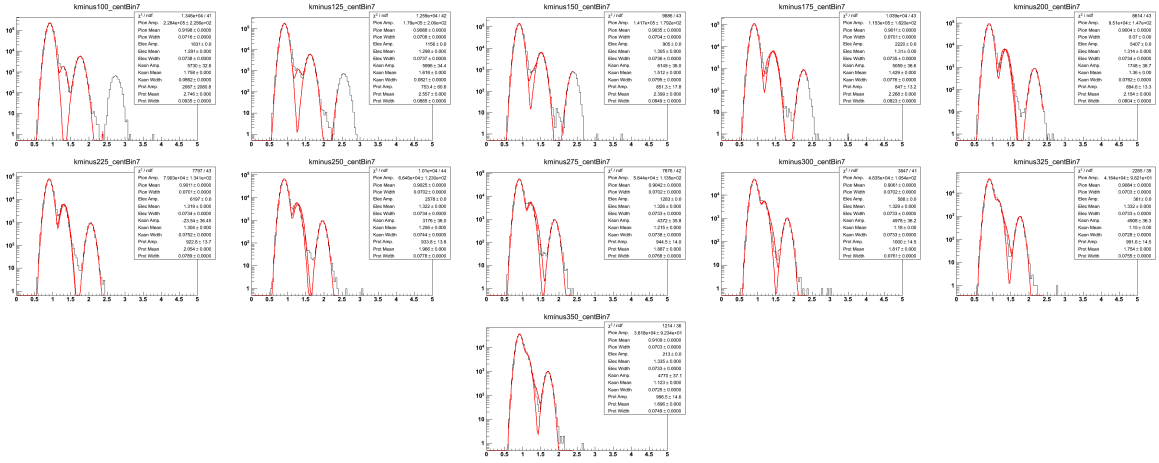

Figure A.91: Negative kaon TPC fits for 5%-10% central events $Au+Au\sqrt{s_{NN}} = 19.6$ GeV. These are organized in 25 MeV bins in $m_T - m_K$ in a rapidity window of 0.1 units around mid-rapidity, $|y| < 0.05$. The Gaussian fits, drawn in red, are in $\log(10^6 \times dE/dx)$ and are of the $m_T - m_K =$ 0.100 to 0.500 GeV/c^2 range. The track data are represented in the black histogram.

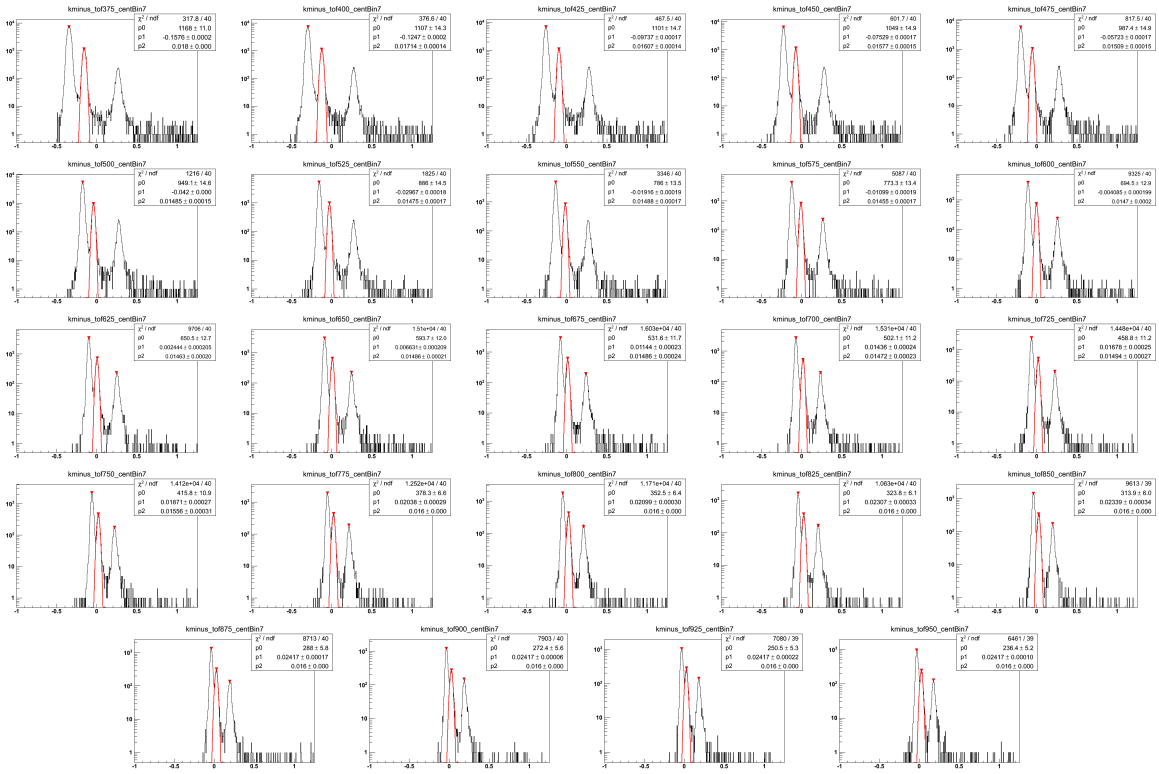

Figure A.92: Negative kaon TOF fits for 5%-10% central events $Au+Au\sqrt{s_{NN}} = 19.6$ GeV. These are organized in 25 MeV bins in $m_T - m_K$ in a rapidity window of 0.1 units around mid-rapidity, $|y| < 0.05$. The Gaussian fits, drawn in red, are in $\beta^{-1}_{\text{expected}} - \beta^{-1}_{\text{measured}}$ and are of the $m_T - m_K =$ 0.350 to 1.0 GeV/c^2 range. The track data are represented in the black histogram.

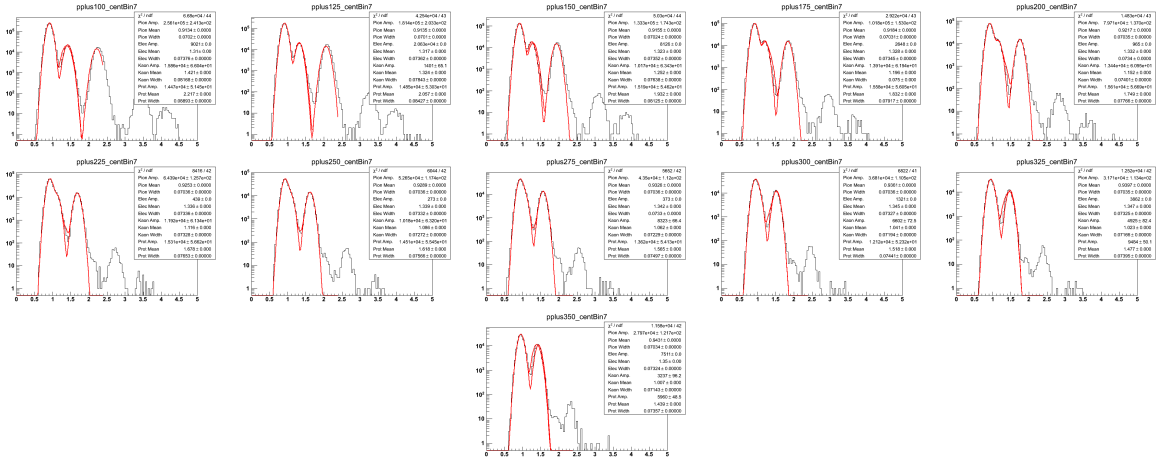

Figure A.93: Positive proton TPC fits for 5%-10% central events $Au+Au\sqrt{s_{NN}} = 19.6$ GeV. These are organized in 25 MeV bins in $m_T - m_p$ in a rapidity window of 0.1 units around mid-rapidity, $|y| < 0.05$. The Gaussian fits, drawn in red, are in $\log(10^6 \times dE/dx)$ and are of the $m_T - m_p =$ 0.100 to 0.500 GeV/c^2 range. The track data are represented in the black histogram.

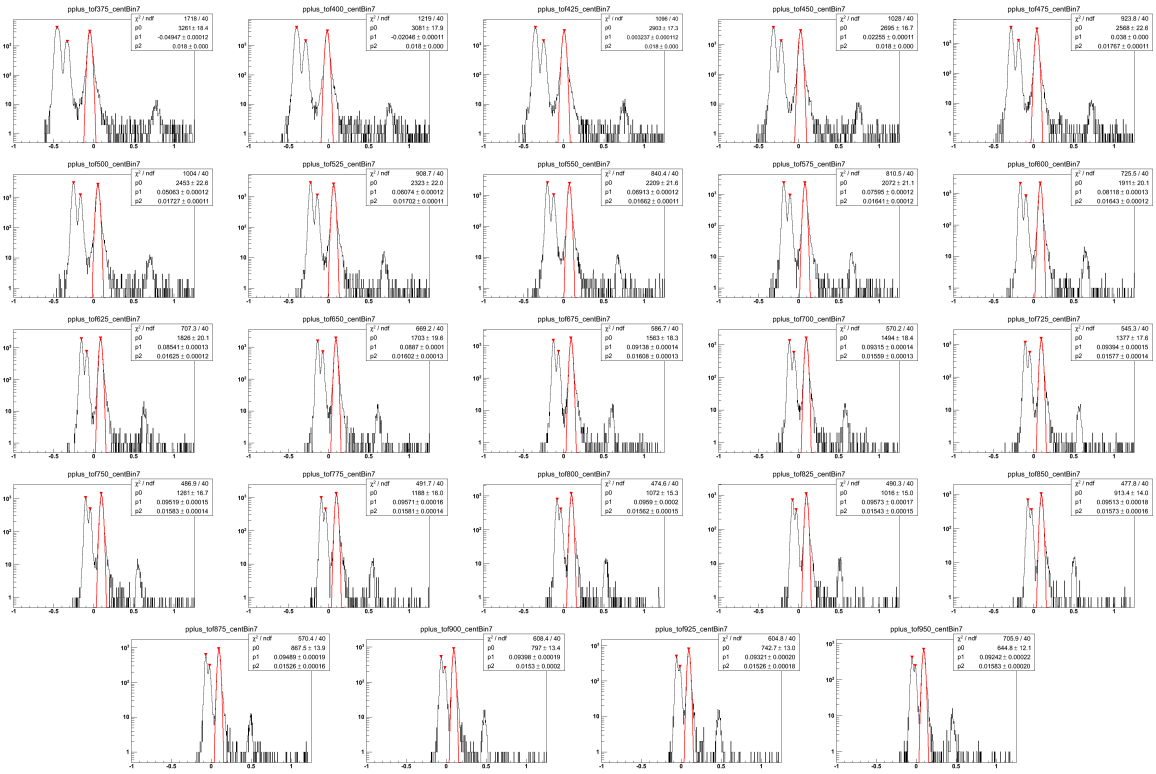

Figure A.94: Positive proton TOF fits for 5%-10% central events $Au + Au\sqrt{s_{NN}} = 19.6$ GeV. These are organized in 25 MeV bins in $m_T - m_p$ in a rapidity window of 0.1 units around mid-rapidity, $|y| < 0.05$. The Gaussian fits, drawn in red, are in $\beta^{-1}_{\text{expected}} - \beta^{-1}_{\text{measured}}$ and are of the $m_T - m_p = 0.350$ to 1.0 GeV/c^2 range. The track data are represented in the black histogram.

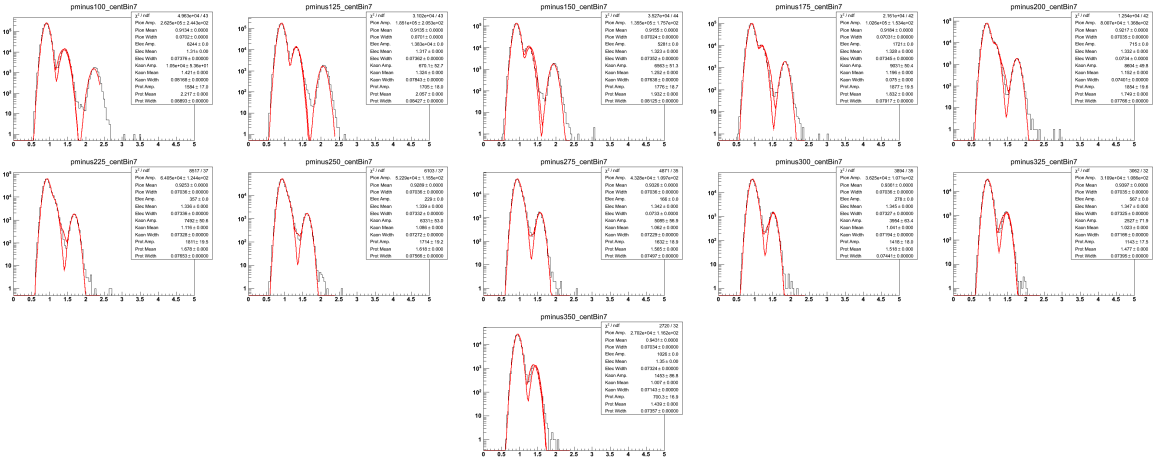

Figure A.95: Negative proton TPC fits for 5%-10% central events $Au + Au\sqrt{s_{NN}} = 19.6$ GeV. These are organized in 25 MeV bins in $m_T - m_p$ in a rapidity window of 0.1 units around mid-rapidity, $|y| < 0.05$. The Gaussian fits, drawn in red, are in $\log(10^6 \times dE/dx)$ and are of the $m_T - m_p = 0.100$ to 0.500 GeV/c^2 range. The track data are represented in the black histogram.

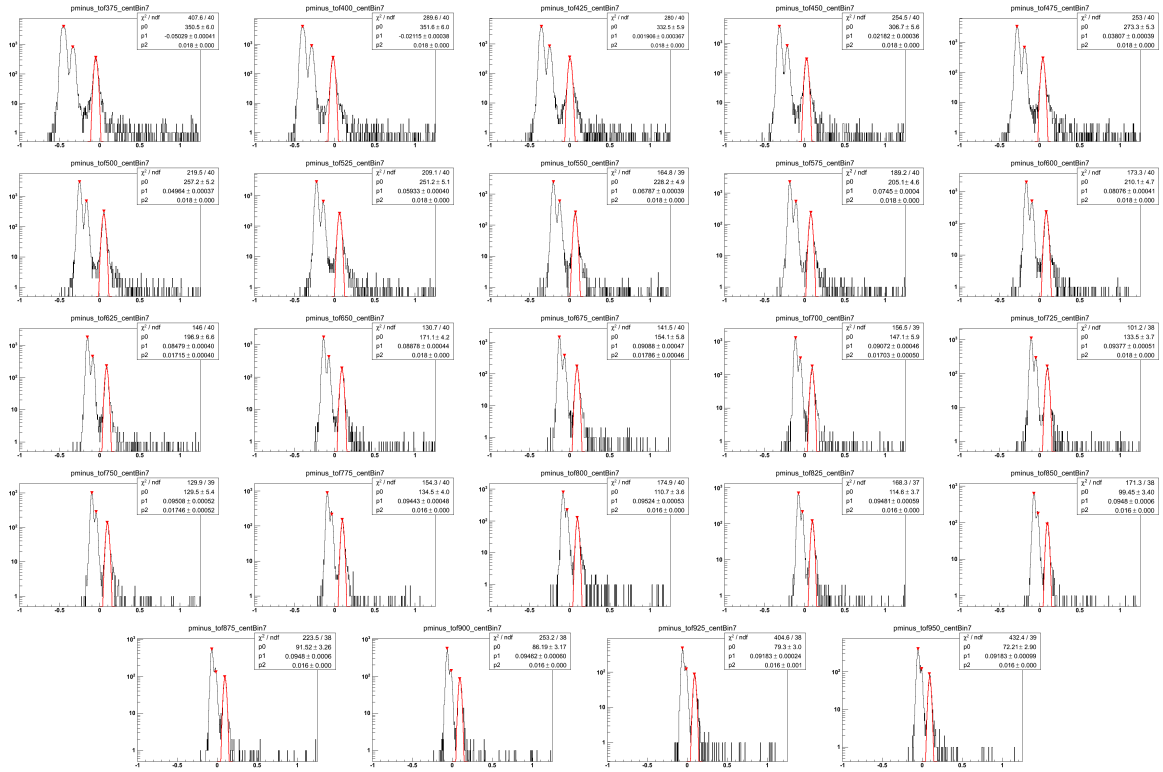

Figure A.96: Negative proton TOF fits for 5%-10% central events $Au + Au\sqrt{s_{NN}} = 19.6$ GeV. These are organized in 25 MeV bins in $m_T - m_p$ in a rapidity window of 0.1 units around mid-rapidity, $|y| < 0.05$. The Gaussian fits, drawn in red, are in $\beta^{-1}_{\text{expected}} - \beta^{-1}_{\text{measured}}$ and are of the $m_T - m_p = 0.350$ to 1.0 GeV/c^2 range. The track data are represented in the black histogram.

A.9 The 0%-5% Centrality Class

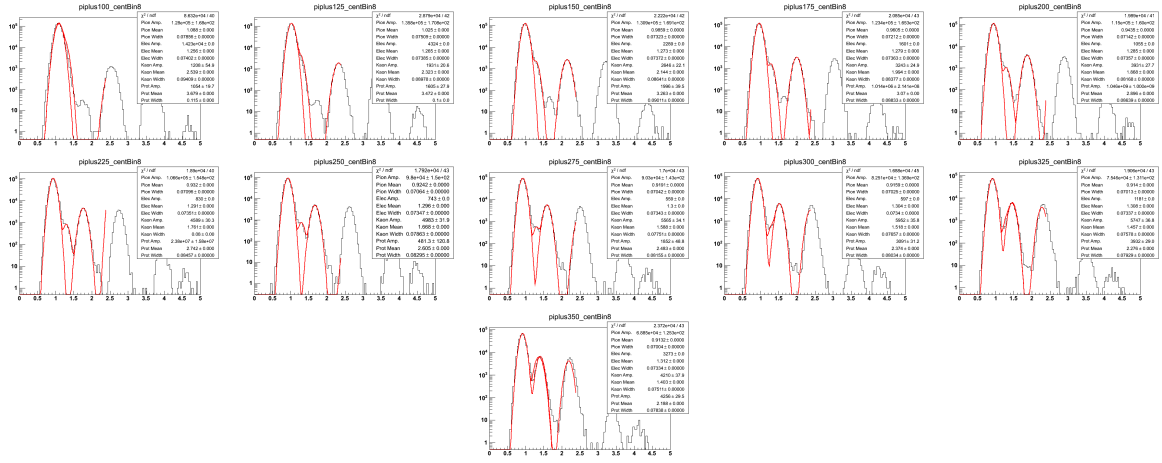

Figure A.97: Positive pion TPC fits for 0%-5% central events $Au + Au\sqrt{s_{NN}} = 19.6$ GeV. These are organized in 25 MeV bins in $m_T - m_\pi$ in a rapidity window of 0.1 units around mid-rapidity, $|y| < 0.05$. The Gaussian fits, drawn in red, are in $\log(10^6 \times dE/dx)$ and are of the $m_T - m_\pi =$ 0.100 to 0.500 GeV/c^2 range. The track data are represented in the black histogram.

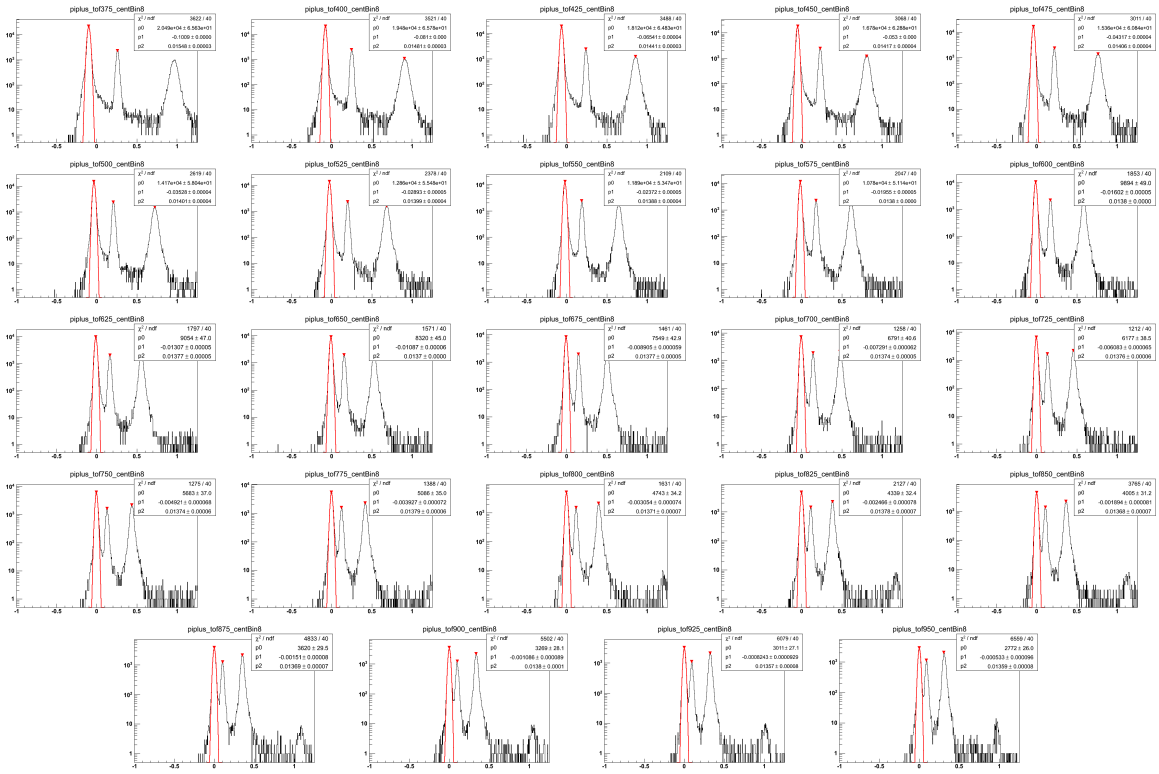

Figure A.98: Positive pion TOF fits for 0%-5% central events $Au + Au\sqrt{s_{NN}} = 19.6$ GeV. These are organized in 25 MeV bins in $m_T - m_\pi$ in a rapidity window of 0.1 units around mid-rapidity, $|y| < 0.05$. The Gaussian fits, drawn in red, are in $\beta^{-1}_{\text{expected}} - \beta^{-1}_{\text{measured}}$ and are of the $m_T - m_\pi =$ 0.350 to 1.0 GeV/c^2 range. The track data are represented in the black histogram.

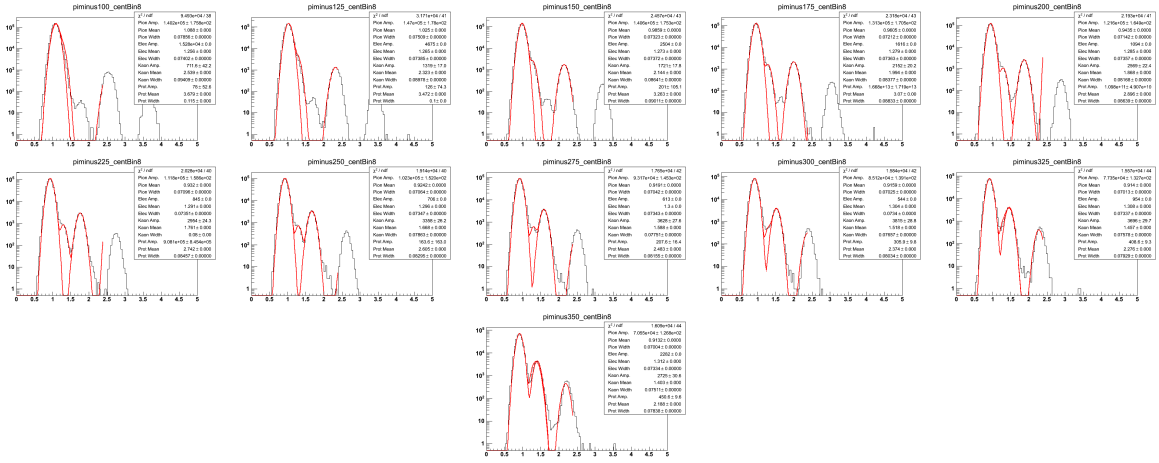

Figure A.99: Negative pion TPC fits for 0%-5% central events $Au + Au\sqrt{s_{NN}} = 19.6$ GeV. These are organized in 25 MeV bins in $m_T - m_\pi$ in a rapidity window of 0.1 units around mid-rapidity, $|y| < 0.05$. The Gaussian fits, drawn in red, are in $\log(10^6 \times dE/dx)$ and are of the $m_T - m_\pi =$ 0.100 to 0.500 GeV/c^2 range. The track data are represented in the black histogram.

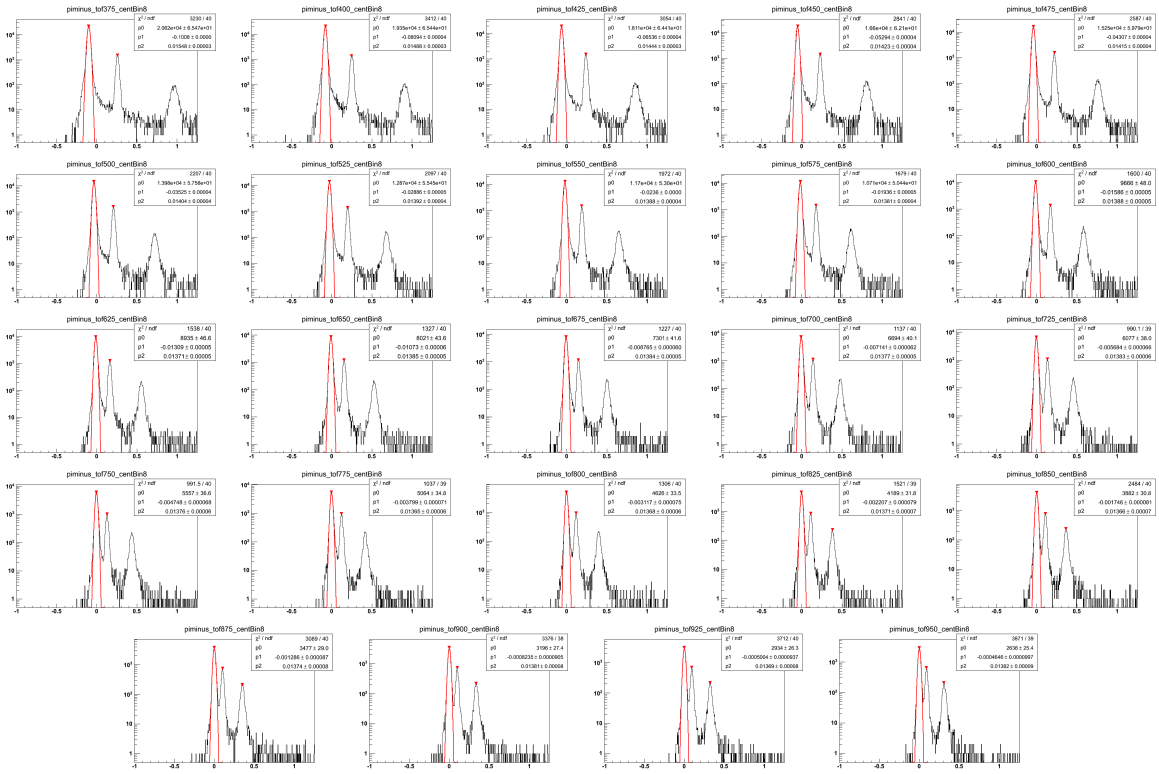

Figure A.100: Negative pion TOF fits for 0%-5% central events $Au+Au\sqrt{s_{NN}} = 19.6$ GeV. These are organized in 25 MeV bins in $m_T - m_\pi$ in a rapidity window of 0.1 units around mid-rapidity, $|y| < 0.05$. The Gaussian fits, drawn in red, are in $\beta^{-1}_{\text{expected}} - \beta^{-1}_{\text{measured}}$ and are of the $m_T - m_\pi =$ 0.350 to 1.0 GeV/c^2 range. The track data are represented in the black histogram.

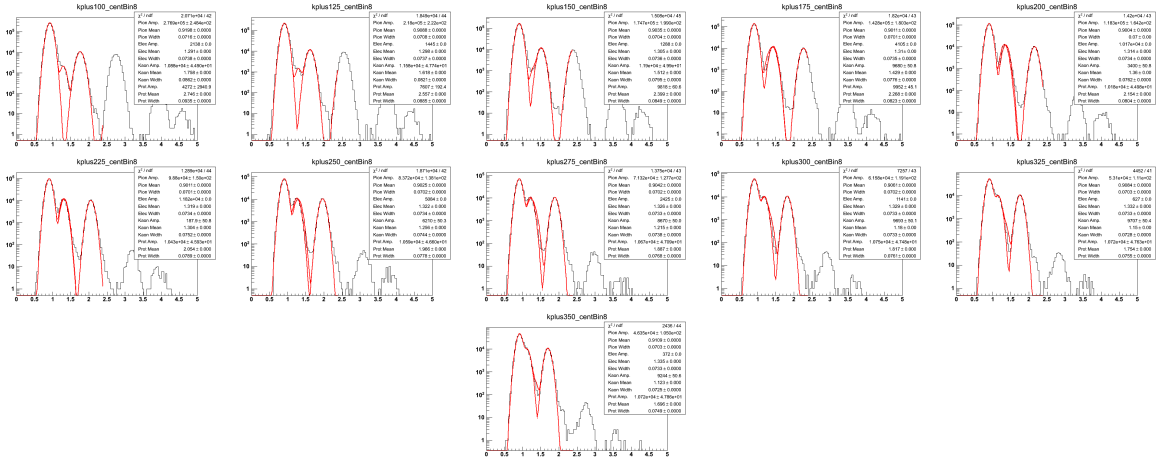

Figure A.101: Positive kaon TPC fits for 0%-5% central events $Au+Au\sqrt{s_{NN}} = 19.6$ GeV. These are organized in 25 MeV bins in $m_T - m_K$ in a rapidity window of 0.1 units around mid-rapidity, $|y| < 0.05$. The Gaussian fits, drawn in red, are in $\log(10^6 \times dE/dx)$ and are of the $m_T - m_K =$ 0.100 to 0.500 GeV/c^2 range. The track data are represented in the black histogram.

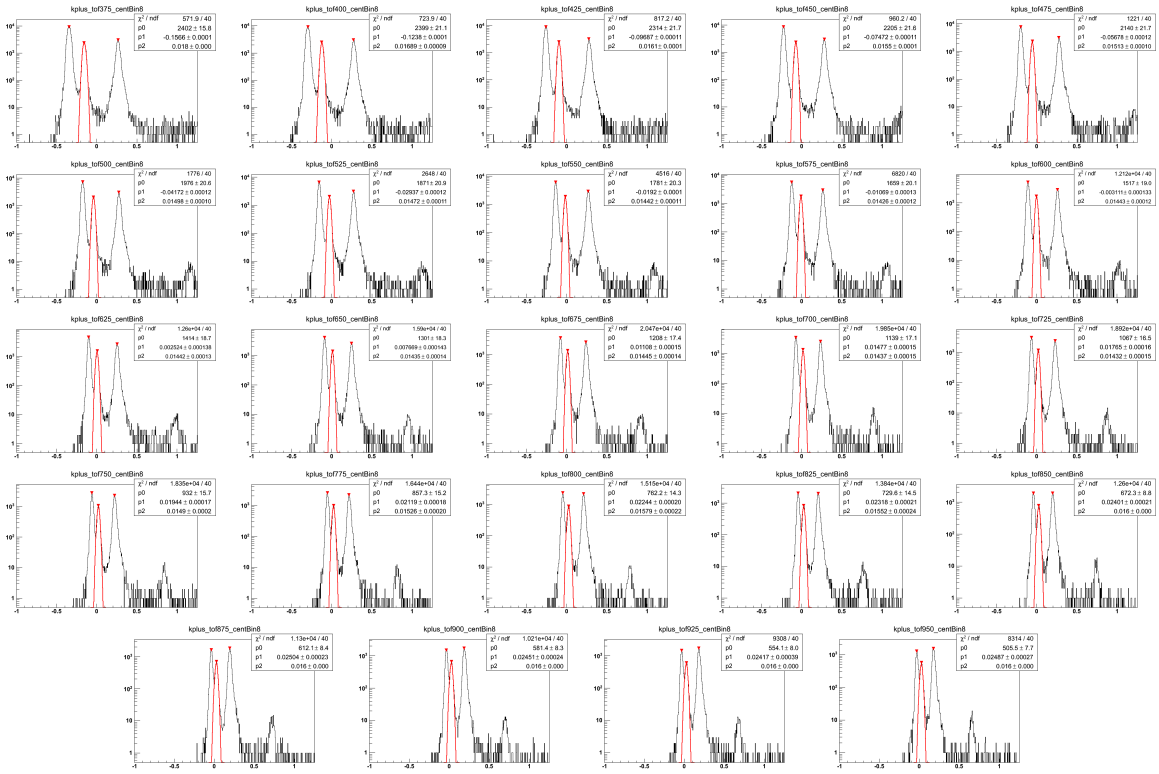

Figure A.102: Positive kaon TOF fits for 0%-5% central events $Au+Au\sqrt{s_{NN}} = 19.6$ GeV. These are organized in 25 MeV bins in $m_T - m_K$ in a rapidity window of 0.1 units around mid-rapidity, $|y| < 0.05$. The Gaussian fits, drawn in red, are in $\beta^{-1}_{\text{expected}} - \beta^{-1}_{\text{measured}}$ and are of the $m_T - m_K =$ 0.350 to 1.0 GeV/c^2 range. The track data are represented in the black histogram.

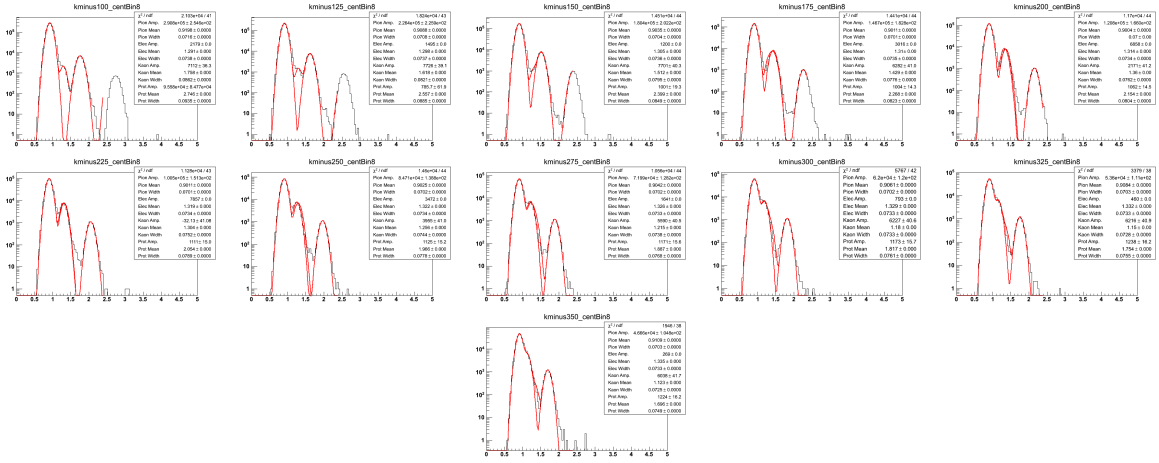

Figure A.103: Negative kaon TPC fits for 0%-5% central events $Au+Au\sqrt{s_{NN}} = 19.6$ GeV. These are organized in 25 MeV bins in $m_T - m_K$ in a rapidity window of 0.1 units around mid-rapidity, $|y| < 0.05$. The Gaussian fits, drawn in red, are in $\log(10^6 \times dE/dx)$ and are of the $m_T - m_K =$ 0.100 to 0.500 GeV/c^2 range. The track data are represented in the black histogram.

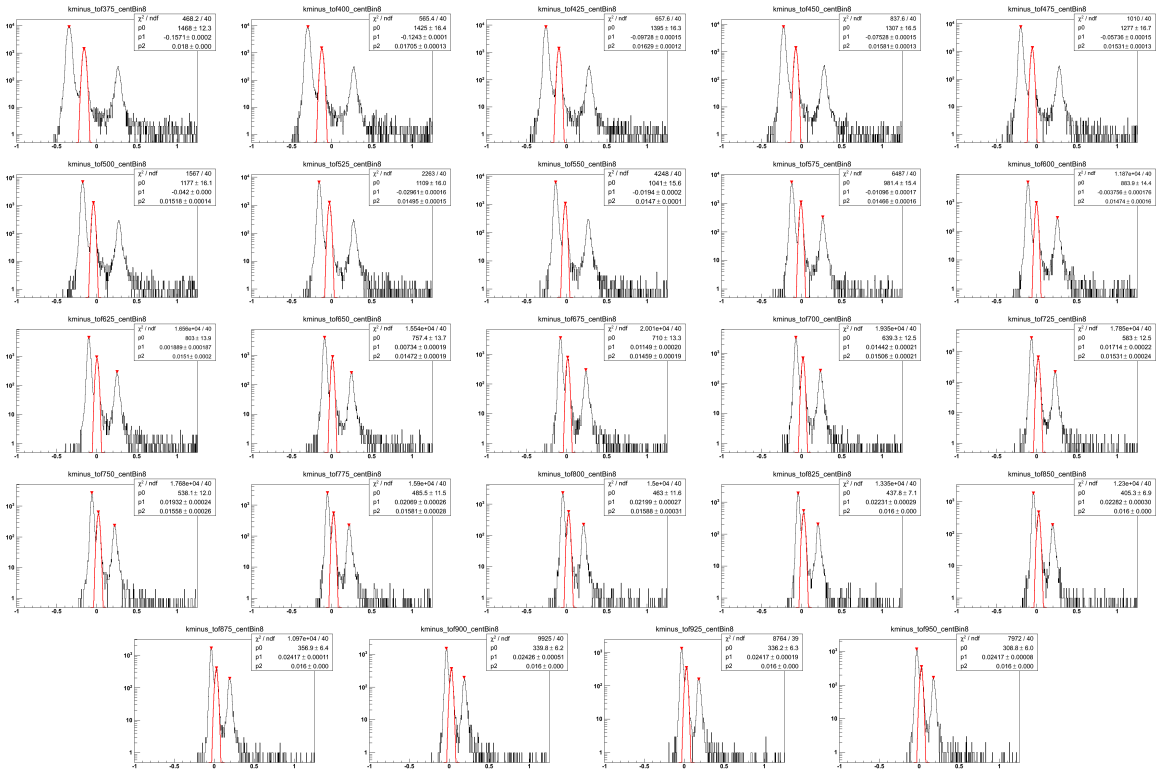

Figure A.104: Negative kaon TOF fits for 0%-5% central events $Au+Au\sqrt{s_{NN}} = 19.6$ GeV. These are organized in 25 MeV bins in $m_T - m_K$ in a rapidity window of 0.1 units around mid-rapidity, $|y| < 0.05$. The Gaussian fits, drawn in red, are in $\beta^{-1}_{\text{expected}} - \beta^{-1}_{\text{measured}}$ and are of the $m_T - m_K =$ 0.350 to 1.0 GeV/c^2 range. The track data are represented in the black histogram.

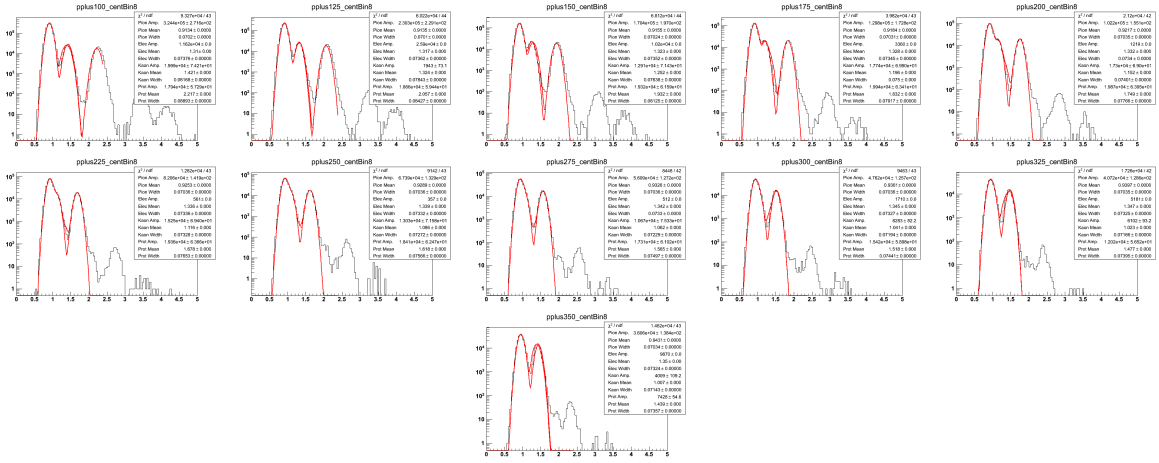

Figure A.105: Positive proton TPC fits for 0%-5% central events $Au + Au\sqrt{s_{NN}} = 19.6$ GeV. These are organized in 25 MeV bins in $m_T - m_p$ in a rapidity window of 0.1 units around mid-rapidity, $|y| < 0.05$. The Gaussian fits, drawn in red, are in $\log(10^6 \times dE/dx)$ and are of the $m_T - m_p = 0.100$ to 0.500 GeV/c^2 range. The track data are represented in the black histogram.

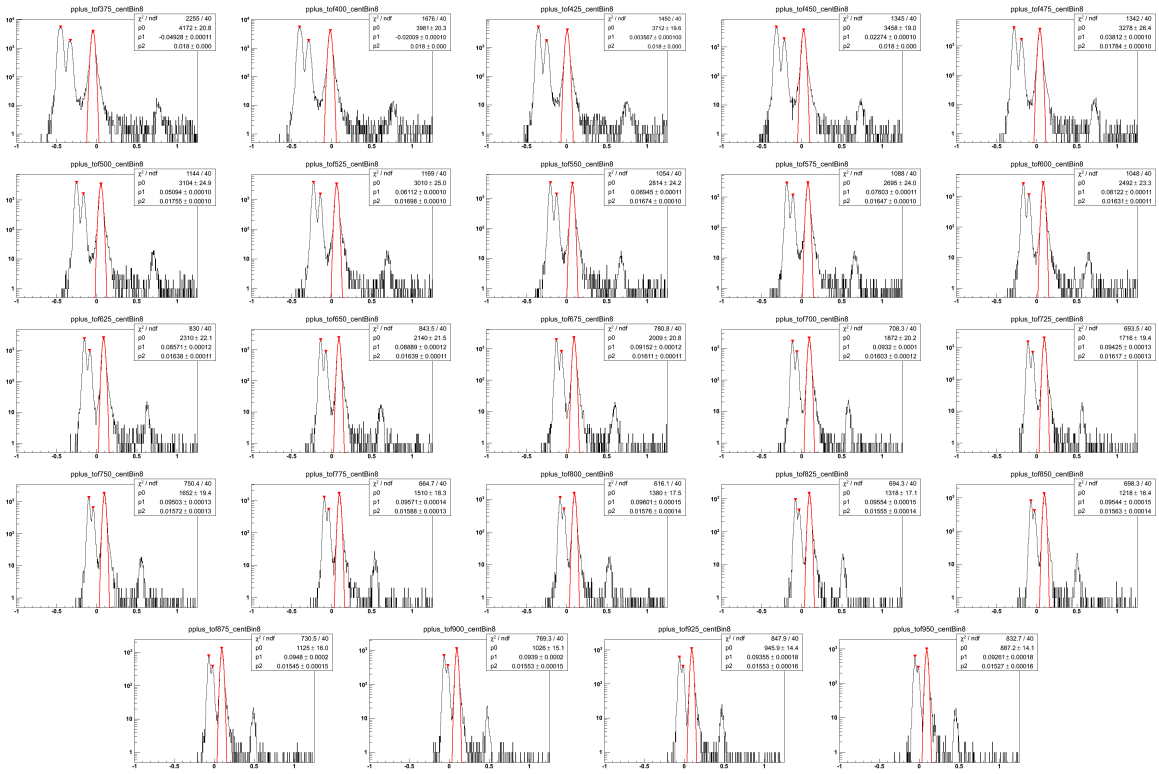

Figure A.106: Positive proton TOF fits for 0%-5% central events $Au + Au\sqrt{s_{NN}} = 19.6$ GeV. These are organized in 25 MeV bins in $m_T - m_p$ in a rapidity window of 0.1 units around mid-rapidity, $|y| < 0.05$. The Gaussian fits, drawn in red, are in $\beta^{-1}_{\text{expected}} - \beta^{-1}_{\text{measured}}$ and are of the $m_T - m_p = 0.350$ to 1.0 GeV/c^2 range. The track data are represented in the black histogram.

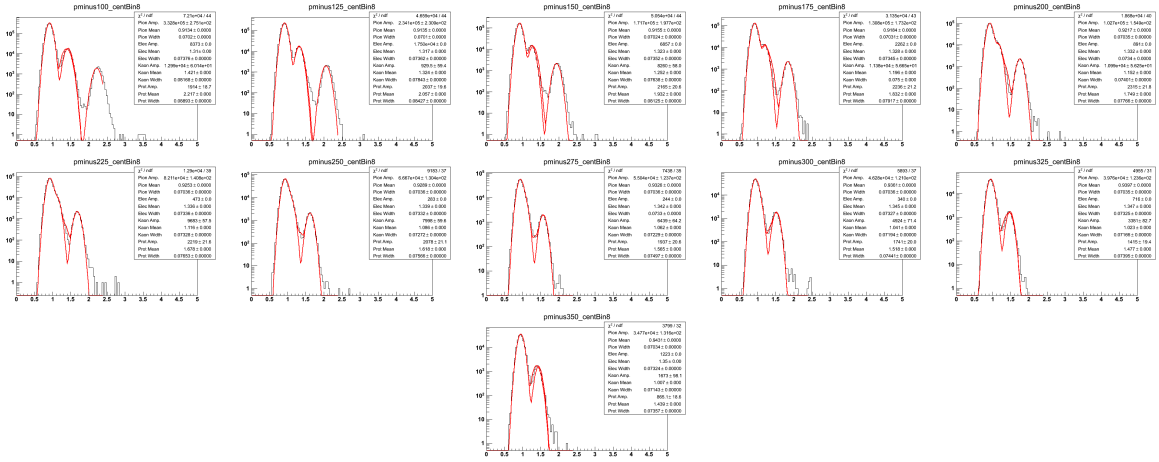

Figure A.107: Negative proton TPC fits for 0%-5% central events $Au + Au\sqrt{s_{NN}} = 19.6$ GeV. These are organized in 25 MeV bins in $m_T - m_p$ in a rapidity window of 0.1 units around mid-rapidity, $|y| < 0.05$. The Gaussian fits, drawn in red, are in $\log(10^6 \times dE/dx)$ and are of the $m_T - m_p = 0.100$ to 0.500 GeV/c^2 range. The track data are represented in the black histogram.

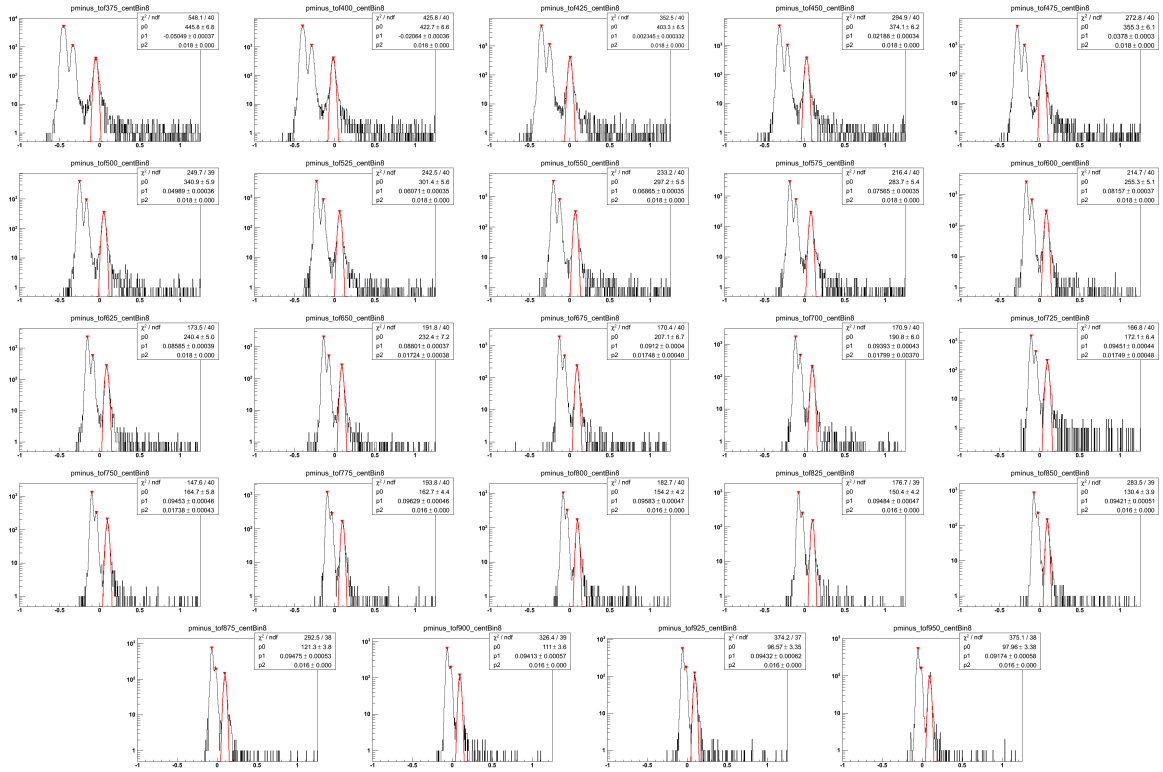

Figure A.108: Negative proton TOF fits for 0%-5% central events $Au + Au\sqrt{s_{NN}} = 19.6$ GeV. These are organized in 25 MeV bins in $m_T - m_p$ in a rapidity window of 0.1 units around mid-rapidity, $|y| < 0.05$. The Gaussian fits, drawn in red, are in $\beta^{-1}_{\text{expected}} - \beta^{-1}_{\text{measured}}$ and are of the $m_T - m_p = 0.350$ to 1.0 GeV/c^2 range. The track data are represented in the black histogram.

Appendix B

Global Properties of Nucleus-Nucleus Collisions

Nucleus-nucleus collisions, A+A, have three main stages of evolution discussed in Chapter 2. These stages each have signatures which survive hadronization and are the signals pulled from all data sets. Discussed in this Appendix are the experimental observables measured by particle detectors relating the theory of the collision.

In the final stage of the collision, hadronization and chemical and kinetic freeze-out occur. In the subsequent hot hadronic gas phase following hadronization, global observables can provide information regarding the initial parameters of the collision. The particle detectors discussed in Chapter 3 collect data on the total number of produced particles (or tracks in the STAR case), specific particle charge, velocity/momentum, position, and energy loss. From kinematic equations and geometry other properties of the collision are determined.

B.1 The Glauber Model

One of the first parameters to determine, outside of specifics to a particular particle, is what class of events one is analyzing. What kind of collision occurred? Central, or peripheral? By answering this type of question, the feasibility of certain analyses on that class of event becomes apparent (meaning, in glancing collisions, an Υ production analysis would be unreasonably difficult). Determining the impact parameter, or the centrality, of the collision

is not by measuring the distance between the centers of each nuclei, but rather through the Glauber Model [33, 34, 180].

Collision geometry plays an important role due to the dependence of the relativistic heavy ion total cross-section on the size of the colliding nuclei. Figure B.1 displays the range of overlap that two colliding nuclei may achieve. A peripheral, or least central collision is represented in (a) while a central, or least peripheral, collision is displayed in (b). The Glauber model takes advantage of this relation to predict, based on the number of participating (or "wounded") nucleons, how many particles will be produced and detected for a given impact parameter. A simplified model does this by assuming each nucleon is a hard sphere populating the nucleus according to the Woods-Saxon nuclear density function,

$$\rho(r) = \rho_0/(1 + e^{(r-R)/z}) \tag{B.1}$$

where ρ_0 is the density in the central region of the nucleus, R is the mean electromagnetic radius of the nucleus (typically the radius when $\rho = \frac{1}{2}\rho_0$), and z describes the surface layer thickness. At RHIC, however, due to the capability of colliding many differing species of nuclei, the Fermi distribution is used [180]:

$$\rho(r) = \rho_0 \frac{1 + w(r/R)^2}{1 + \exp(\frac{r-R}{a})} \tag{B.2}$$

where ρ_0 corresponds to the central nuclear density, R corresponds to the radius of the nucleus, a is the skin depth, and w corresponds to deviations from a spherical nuclear shape. Note for ^{197}Au, $w = 0$ and reduces to the Woods-Saxon distribution. Additionally, the model needs the nucleon-nucleon cross-section which PYTHIA [172] [173] typically estimates from $\sim$ 32 mb to $\sim$ 42 at the range of RHIC energies [180]. This cross section constitutes the only beam-energy dependent variable in the Glauber model which is non-trivial [180]. From there, the analytical Glauber model utilizes the optical-limit approximation [171] [170] for the collision of two nucleons in each of the colliding nuclei. When two nucleons are determined

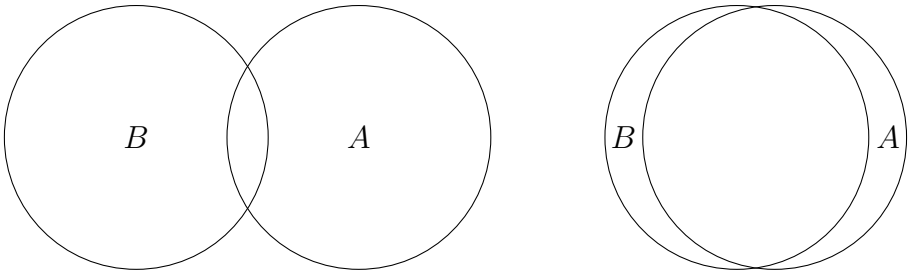

Figure B.1: Different overlap areas of colliding nuclei in (a) a more peripheral collision as the overlap region is smaller compared to (b) a more central collision since the overlap region is very large.

to collide, those nucleons are assumed to have sufficient momentum to continue essentially undeflected as the nuclei pass through each other, and to move independently in the nucleus, thus they will count toward the total number of participating nucleons. The probability that a collision between nucleons will occur diminishes with the number of collisions in which a particular nucleon had already been a participant.

The Glauber Monte Carlo method is quite a bit simpler to obtain the geometrical quantities of interest, namely N_{part} and N_{coll}. The distribution of nucleons occurs according to the Fermi distribution for each nuclei in the collision, and then a random impact parameter is chosen. The computer treats collision of nuclei as independent binary collisions of nucleons, meaning no dependence of the inelastic nucleon-nucleon cross section on the number of collisions a particular nucleon has participated in perviously. A collision between nucleons occurs when their two-dimensional area (calculated either via a Gaussian distribution or the inelastic cross-section) perpendicular to the beam axis overlaps. The averages of the geometrical quantities are then obtained via the repetition of many collisions at these differing impact parameters.

Once the number of participants and the number of collisions are determined via simulation, typical for RHIC, these quantities translate to experimental observables entirely dependent on the experiment and collision system. Typically, to translate between experiment

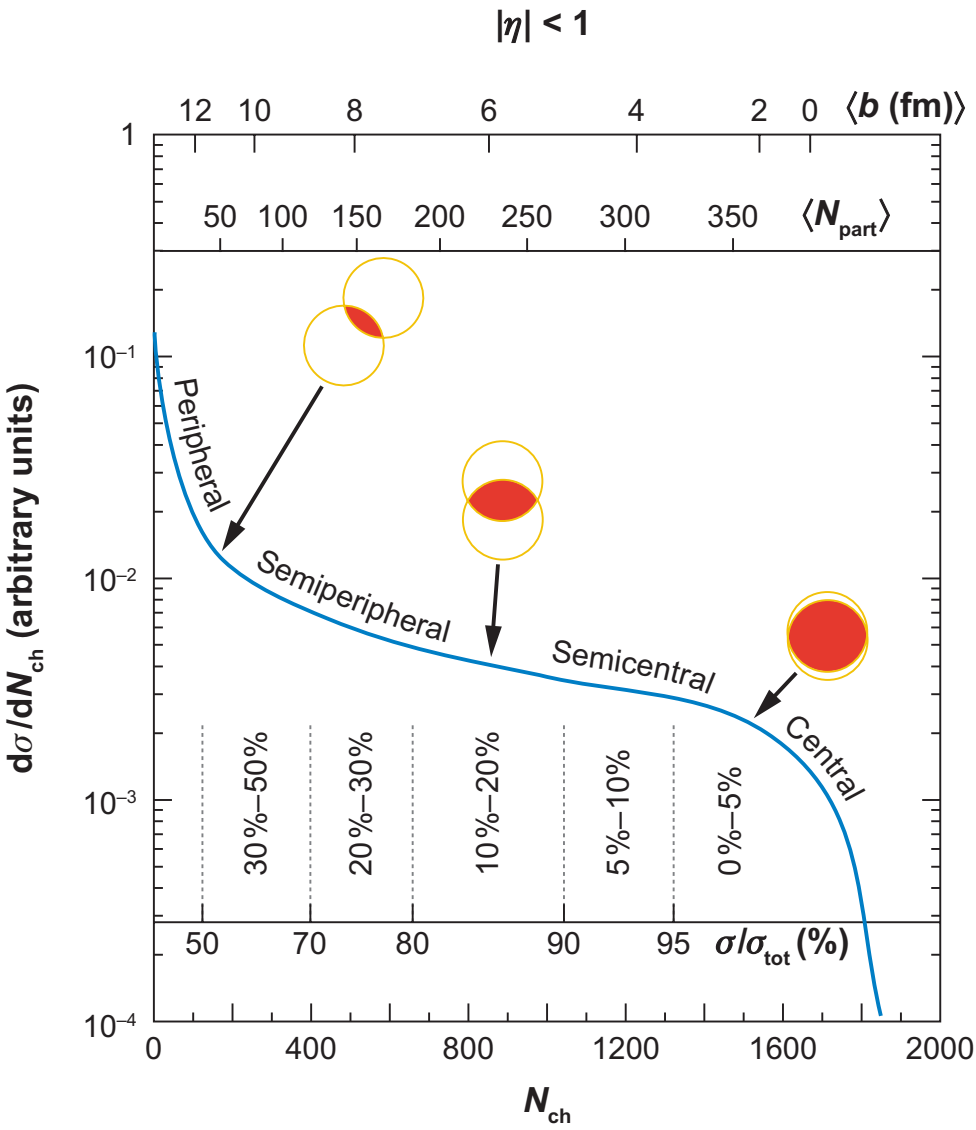

Figure B.2: Taken from Reference [180]. An illustrated example of the correlation of the final-state-observable total inclusive charged-particle multiplicity $N_{\rm ch}$ with Glauber-calculated quantities (b, $N_{\rm part}$). The plotted distribution and various values are illustrative and not actual measurements (T. Ullrich, private communication).

and Glauber, an experimental centrality class distribution is mapped to a similar centrality class distribution from Glauber by equating the mean values from the same centrality class in each distribution. This mapping relies on the basic assumption that the particle multiplicity is a monotonic function of the impact parameter, b, see Figure B.2. The smaller the impact parameter or more central the collision, the larger the number of produced particles we expect (right-hand side of the figure), while the larger the impact parameter or more

peripheral the collision, the smaller the expected number of produced particles (left-hand side of the figure). Centrality classes are defined as a fraction of the total number of events in a distribution of the experimental and Glauber per-event charged particle multiplicity, and a sample binning is given by the dashed lines in the figure. The geometric quantities then are calculated for each centrality class of the Glauber distribution. This Glauber mapping thus provides a relation between the number of experimentally observed charged particles and the (experimentally unmeasurable) impact parameter, b.

Curriculum Vitæ

S. G. Brovko

1140 Alta Vista Ave P.O. Box 741• Big Bear City, CA 92314-0741
Phone: 714-746-7585 • nuclear.ucdavis.edu/~brovko • E-Mail: sgbrovko@ucdavis.edu

SGB

Objective

To find a technically challenging and scientifically interesting career.

Experience

Graduate Student Researcher **April 2011 - Present**

Mentoring junior and undergraduate students in beginning analyses using the STAR framework and considering Ultra-Relativistic Heavy Ion and Quark-Gluon-Plasma physics. Performing a hydrodynamic, statistical and thermal analysis of data measured at STAR. Presenting findings to the Physics Working Group, STAR collaboration and scientific community at large. Complete shift obligations remotely running the STAR detector at Brookhaven National Laboratory on the Relativistic Heavy Ion Collider ring.

Teaching Assistant **September 2008 – March 2011**

Introducing students to physics concepts and guiding students through applications of that knowledge. Experience in laboratory teaching while aiding students in performing advanced physics experiments (Rutherford Scattering, Muon Lifetime) and introductory physics experiments (momentum conservation, boiling water), classroom teaching with discussion questions as well as guided whole-class discussions, grading advanced thermodynamics and introductory general physics assignments and exams.

Temporary Scorer at Pearson Evaluations **January 2011 - Present**

Grading California Subject Examinations for Teachers every two months on a holistic scale. Evaluating candidates based on accomplishing the purpose of the exam, demonstrating subject matter knowledge and giving relevant support to the problem at hand.

Education

Ph.D. University of California, Davis: Nuclear Physics **In Progress**

Block Grant Recipient, STAR Collaborator, Physics Club Graduate Student Advisor, APS, SPS

M.S. University of California, Davis: Physics **10 December 2010**

Physics Club, IAESTE, APS, SPS

B.S. University of California, Davis: Physics **14 June 2008**

Dean's List 2005, Senior Student Award 2008, Physics Club, IAESTE, APS, SPS

Skills

Linux, Unix, Mac OS X, Windows 98, Windows XP, Windows Vista, Windows 7

Large Data Analysis Packages (i.e. ROOT)

Microsoft Office and LaTeX

Data Mining and Data Interpretation

Simulations and UrQMD Simulation Package

Conference and Event Planning

Bash Scripting, C and C++

Critical Thinking and Problem Solving

Publications

The full list of 50 refereed publications is available upon request.

1) Coulomb Effect in Au+Au and Pb+Pb Collisions as a function of collision energy. By D. Cebra et al. arXiv:1408.1369 [nucl-ex].

2) J\psi production at high transverse momenta in p+p and Au+Au collisions at sqrt{s_{NN}} = 200 GeV
By STAR Collaboration (L. Adamczyk et al.). arXiv:1208.2736 [nucl-ex].

3) Inclusive charged hadron elliptic flow in Au + Au collisions at sqrt{s_{NN}} = 7.7 - 39 GeV
By STAR Collaboration (L. Adamczyk et al.). arXiv:1206.5528 [nucl-ex].

Oral Presentations at Scientific Meetings

The full list is available upon request.

1) Ultra-Relativistic Heavy Ion Group (Nuclear Group) at UC Davis
Poster Presentation for Graduate Program Preview Day 2010

2) STAR as a Fixed Target Experiment: Au+Al at 2.8 AGeV
American Physical Society April Meeting April 2011

3) Hadron Production at sqrt{s_{NN}} = 19.6 and 27 GeV Au+Au
STAR Collaboration Analysis Meeting August 2011

4) Hadron Production at sqrt{s_{NN}} = 19.6 GeV Au+Au Collisions at STAR
Division of Nuclear Physics of the American Physical Society October 2011

5) Did You Say Fixed Target At STAR?
STAR Collaboration Analysis Meeting, Junior's Day April 2012

6) Colliding Au+Au at STAR
Physics & Tea for Undergraduates May 2012

7) Hadron Production and Freeze-Out Dynamics in Au+Au at sqrt{s_{NN}} = 19.6 GeV
Division of Nuclear Physics of the American Physical Society October 2012

8) 19.6 GeV Au+Au PID Spectra Update
STAR Collaboration Analysis Meeting November 2012

Publications

Full Publication List for S G Brovko

1. Coulomb effect in Au+Au and Pb+Pb collisions as a function of collision energy
   D. Cebra, S.G. Brovko, C.E. Flores, B.A. Haag, J.L. Klay. Aug 6, 2014. 6 pp.
   e-Print: arXiv:1408.1369 [nucl-ex]
2. Elliptic flow of non-photonic electrons in Au+Au collisions at $\sqrt{s_{NN}}$ = 200, 62.4 and 39 GeV
   STAR Collaboration (L. Adamczyk (AGH-UST, Cracow) *et al.*). May 24, 2014. 10 pp.
   e-Print: arXiv:1405.6348 [hep-ex]
3. Precision Measurement of the Longitudinal Double-spin Asymmetry for Inclusive Jet Production in Polarized Proton Collisions at $\sqrt{s}$=200 GeV
   STAR Collaboration (L. Adamczyk (AGH-UST, Cracow) *et al.*). May 20, 2014. 7 pp.
   e-Print: arXiv:1405.5134 [hep-ex]
4. Measurement of longitudinal spin asymmetries for weak boson production in polarized proton-proton collisions at RHIC
   STAR Collaboration (L. Adamczyk (AGH-UST, Cracow) *et al.*). Apr 28, 2014. 7 pp.
   e-Print: arXiv:1404.6880 [nucl-ex]
5. Observation of $D0$ meson nuclear modifications in Au+Au collisions at $\sqrt{s_{NN}}$ = 200 GeV
   STAR Collaboration (L. Adamczyk (AGH-UST, Cracow) *et al.*). Apr 24, 2014. 7 pp.
   e-Print: arXiv:1404.6185 [nucl-ex]
6. Beam-energy dependence of charge separation along the magnetic field in Au+Au collisions at RHIC
   STAR Collaboration (L. Adamczyk (AGH-UST, Cracow) *et al.*). Apr 5, 2014. 6 pp.
   Published in Phys.Rev.Lett. 113 (2014) 052302
   DOI: 10.1103/PhysRevLett.113.052302
   e-Print: arXiv:1404.1433 [nucl-ex]
7. Event-plane dependent dihadron correlations with harmonic v_n subtraction in Au+Au Collisions at $\sqrt{s_{NN}}$=200 GeV
   STAR Collaboration (H. Agakishiev (Dubna, JINR) *et al.*). Apr 3, 2014. 8 pp.
   Published in Phys.Rev. C89 (2014) 041901
   DOI: 10.1103/PhysRevC.89.041901
   e-Print: arXiv:1404.1070 [nucl-ex]
8. Jet-Hadron Correlations in sqrt{s_{NN}} = 200 GeV p+p and Central Au+Au Collisions
   STAR Collaboration (L. Adamczyk (AGH-UST, Cracow) *et al.*). Feb 25, 2013.
   Published in Phys.Rev.Lett. 112 (2014) 122301
   DOI: 10.1103/PhysRevLett.112.122301
   e-Print: arXiv:1302.6184 [nucl-ex]
9. Beam energy dependent two-pion interferometry and the freeze-out eccentricity of pions in heavy ion collisions at STAR
   STAR Collaboration (L. Adamczyk (AGH-UST, Cracow) *et al.*). Mar 19, 2014. 27 pp.
   e-Print: arXiv:1403.4972 [nucl-ex]
10. Dielectron Azimuthal Anisotropy at mid-rapidity in Au+Au collisions at $\sqrt{s_{NN}}$=200 GeV
    STAR Collaboration (L. Adamczyk (AGH-UST, Cracow) *et al.*). Feb 7, 2014. 13 pp.
    e-Print: arXiv:1402.1791 [nucl-ex]
11. Beam energy dependence of moments of the net-charge multiplicity distributions in Au+Au collisions at RHIC
    STAR Collaboration (L. Adamczyk (AGH-UST, Cracow) *et al.*). Feb 7, 2014. 7 pp.
    e-Print: arXiv:1402.1558 [nucl-ex]

12. Energy Dependence of Moments of Net-proton Multiplicity Distributions at RHIC
STAR Collaboration (L. Adamczyk (AGH-UST, Cracow) *et al.*). Sep 22, 2013. 7 pp.
Published in Phys.Rev.Lett. 112 (2014) 3, 032302
DOI: 10.1103/PhysRevLett.112.032302
e-Print: arXiv:1309.5681 [nucl-ex]

13. Neutral pion cross section and spin asymmetries at intermediate pseudorapidity in polarized proton collisions at s=200□□GeV
STAR Collaboration (L. Adamczyk (AGH-UST, Cracow) *et al.*). Sep 6, 2013. 11 pp.
Published in Phys.Rev. D89 (2014) 1, 012001
DOI: 10.1103/PhysRevD.89.012001
e-Print: arXiv:1309.1800 [nucl-ex]

14. Beam-Energy Dependence of Directed Flow of Protons, Antiprotons and Pions in Au+Au Collisions
STAR Collaboration (L. Adamczyk (AGH-UST, Cracow) *et al.*). Jan 13, 2014. 7 pp.
Published in Phys.Rev.Lett. 112 (2014) 162301
DOI: 10.1103/PhysRevLett.112.162301(2014), 10.1103/PhysRevLett.112.162301
e-Print: arXiv:1401.3043 [nucl-ex]

15. Dielectron Mass Spectra from Au+Au Collisions at $\sqrt{s_{NN}}$ = 200 GeV
STAR Collaboration (L. Adamczyk (AGH-UST, Cracow) *et al.*). Dec 28, 2013. 8 pp.
Published in Phys.Rev.Lett. 113 (2014) 022301
DOI: 10.1103/PhysRevLett.113.022301
e-Print: arXiv:1312.7397 [hep-ex]

16. Suppression of Upsilon Production in d+Au and Au+Au Collisions at sqrt(s_NN) = 200 GeV
STAR Collaboration (L. Adamczyk (AGH-UST, Cracow) *et al.*). Dec 12, 2013. 12 pp.
Published in Phys.Lett. B735 (2014) 127
DOI: 10.1016/j.physletb.2014.06.028
e-Print: arXiv:1312.3675 [nucl-ex]

17. J/ψ polarization in p+p collisions at $\sqrt{s}$ = 200 GeV in STAR
STAR Collaboration (L. Adamczyk (AGH-UST, Cracow) *et al.*). Nov 7, 2013. 9 pp.
WUT-13-01
e-Print: arXiv:1311.1621 [nucl-ex]

18. J/ψ production at low p_T in Au+Au and Cu+Cu collisions at $\sqrt{s_{NN}}$ = 200 GeV at STAR
STAR Collaboration (L. Adamczyk (AGH-UST, Cracow) *et al.*). Oct 14, 2013. 14 pp.
e-Print: arXiv:1310.3563 [nucl-ex]

19. Freeze-out dynamics via charged kaon femtoscopy in $\sqrt{s_{NN}}$ = 200 GeV central Au□+□Au collisions
STAR Collaboration (L. Adamczyk (AGH-UST, Cracow) *et al.*). Feb 13, 2013. 8 pp.
Published in Phys.Rev. C88 (2013) 3, 034906
DOI: 10.1103/PhysRevC.88.034906
e-Print: arXiv:1302.3168 [nucl-ex]

20. Measurement of J/ψ Azimuthal Anisotropy in Au+Au Collisions at $\sqrt{s_{NN}}$ = 200 GeV
STAR Collaboration (L. Adamczyk (AGH-UST, Cracow) *et al.*). Dec 2012. 7 pp.
Published in Phys.Rev.Lett. 111 (2013) 5, 052301
DOI: 10.1103/PhysRevLett.111.052301
e-Print: arXiv:1212.3304 [nucl-ex]

21. Third Harmonic Flow of Charged Particles in Au+Au Collisions at sqrtsNN = 200 GeV
STAR Collaboration (L. Adamczyk (AGH-UST, Cracow) *et al.*). Jan 2013. 11 pp.
Published in Phys.Rev. C88 (2013) 1, 014904
LBNL (2013), LBNL-(2013)

DOI: 10.1103/PhysRevC.88.014904
e-Print: arXiv:1301.2187 [nucl-ex]

22. Elliptic flow of identified hadrons in Au+Au collisions at $\sqrt{s_{NN}}$= 7.7-62.4 GeV
STAR Collaboration (L. Adamczyk (AGH-UST, Cracow) *et al.*). Jan 2013. 25 pp.
Published in Phys.Rev. C88 (2013) 014902
DOI: 10.1103/PhysRevC.88.014902
e-Print: arXiv:1301.2348 [Unknown]

23. System-size dependence of transverse momentum correlations at $\sqrt{s_{NN}}=62.4 and 200 GeV at the BNL Relativistic Heavy Ion Collider
STAR Collaboration (L. Adamczyk (AGH-UST, Cracow) *et al.*). Jan 2013. 11 pp.
Published in Phys.Rev. C87 (2013) 6, 064902
DOI: 10.1103/PhysRevC.87.064902
e-Print: arXiv:1301.6633 [nucl-ex]

24. Experimental studies of di-jets in Au + Au collisions using angular correlations with respect to back-to-back leading hadrons
STAR Collaboration (L. Adamczyk (AGH-UST, Cracow) *et al.*). Dec 2012. 13 pp.
Published in Phys.Rev. C87 (2013) 4, 044903
DOI: 10.1103/PhysRevC.87.044903
e-Print: arXiv:1212.1653 [nucl-ex]

25. Measurement of Charge Multiplicity Asymmetry Correlations in High Energy Nucleus-Nucleus Collisions at 200 GeV
STAR Collaboration (L. Adamczyk (AGH-UST, Cracow) *et al.*). Mar 4, 2013. 26 pp.
Published in Phys.Rev. C89 (2014) 044908
DOI: 10.1103/PhysRevC.89.044908
e-Print: arXiv:1303.0901 [nucl-ex]

26. Fluctuations of charge separation perpendicular to the event plane and local parity violation in $\sqrt{s_{NN}}$=200 GeV Au+Au collisions at RHIC
STAR Collaboration (L. Adamczyk (AGH-UST, Cracow) *et al.*). Feb 15, 2013. 10 pp.
e-Print: arXiv:1302.3802 [nucl-ex]

27. Observation of an energy-dependent difference in elliptic flow between particles and anti-particles in relativistic heavy ion collisions
STAR Collaboration (L. Adamczyk *et al.*). Jan 2013. 7 pp.
Published in Phys.Rev.Lett. 110 (2013) 142301
DOI: 10.1103/PhysRevLett.110.142301
e-Print: arXiv:1301.2347 [nucl-ex]

28. J/ψ production at high transverse momenta in p+p and Au+Au collisions at $\sqrt{s_{NN}}$=200 GeV
STAR Collaboration (L. Adamczyk (AGH-UST, Cracow) *et al.*). Aug 2012. 7 pp.
Published in Phys.Lett. B722 (2013) 55-62
DOI: 10.1016/j.physletb.2013.04.010
e-Print: arXiv:1208.2736 [nucl-ex]

29. Single Spin Asymmetry A_N in Polarized Proton-Proton Elastic Scattering at $\sqrt{s}$=200 GeV
STAR Collaboration (L. Adamczyk (AGH-UST, Cracow) *et al.*). Jun 2012. 11 pp.
Published in Phys.Lett. B719 (2013) 62-69
DOI: 10.1016/j.physletb.2013.01.014
e-Print: arXiv:1206.1928 [nucl-ex]

30. Inclusive charged hadron elliptic flow in Au + Au collisions at $\sqrt{s_{NN}}$ = 7.7 - 39 GeV
STAR Collaboration (L. Adamczyk (AGH-UST, Cracow) *et al.*). Jun 2012. 19 pp.
Published in Phys.Rev. C86 (2012) 054908

DOI: 10.1103/PhysRevC.86.054908
e-Print: arXiv:1206.5528 [nucl-ex]

31. Transverse Single-Spin Asymmetry and Cross-Section for $\pi 0$ and η Mesons at Large Feynman-x in Polarized $p+p$ Collisions at $\sqrt{s}$=200 GeV
STAR Collaboration (L. Adamczyk (AGH-UST, Cracow) *et al.*). May 2012. 7 pp.
Published in Phys.Rev. D86 (2012) 051101
DOI: 10.1103/PhysRevD.86.051101
e-Print: arXiv:1205.6826 [nucl-ex]

32. Longitudinal and transverse spin asymmetries for inclusive jet production at mid-rapidity in polarized $p+p$ collisions at $\sqrt{s}$=200 GeV
STAR Collaboration (L. Adamczyk (AGH-UST, Cracow & AGH-UST, Cracow) *et al.*). May 2012. 18 pp.
Published in Phys.Rev. D86 (2012) 032006
DOI: 10.1103/PhysRevD.86.032006
e-Print: arXiv:1205.2735 [nucl-ex]

33. Measurements of $D0$ and $D*$ Production in $p+p$ Collisions at $\sqrt{s}$=200 GeV
STAR Collaboration (L. Adamczyk (AGH-UST, Cracow) *et al.*). Apr 2012. 14 pp.
Published in Phys.Rev. D86 (2012) 072013
DOI: 10.1103/PhysRevD.86.072013
e-Print: arXiv:1204.4244 [nucl-ex]

34. Di-electron spectrum at mid-rapidity in $p+p$ collisions at $\sqrt{s}$=200 GeV
STAR Collaboration (L. Adamczyk (AGH-UST, Cracow) *et al.*). Apr 2012. 15 pp.
Published in Phys.Rev. C86 (2012) 024906
DOI: 10.1103/PhysRevC.86.024906
e-Print: arXiv:1204.1890 [nucl-ex]

35. Directed Flow of Identified Particles in Au + Au Collisions at $\sqrt{s_{NN}}$=200 GeV at RHIC
STAR Collaboration (L. Adamczyk (Jagiellonian U.) *et al.*). Dec 2011.
Published in Phys.Rev.Lett. 108 (2012) 202301
DOI: 10.1103/PhysRevLett.108.202301
e-Print: arXiv:1112.3930 [nucl-ex]

36. Measurement of the $W \to e\nu$ and $Z/\gamma* \to e+e-$ Production Cross Sections at Mid-rapidity in Proton-Proton Collisions at $\sqrt{s}$ = 500 GeV
STAR Collaboration (L. Adamczyk (Jagiellonian U.) *et al.*). Dec 2011. 14 pp.
Published in Phys.Rev. D85 (2012) 092010
DOI: 10.1103/PhysRevD.85.092010
e-Print: arXiv:1112.2980 [hep-ex]

37. Energy and system-size dependence of two- and four-particle $v2$ measurements in heavy-ion collisions at RHIC and their implications on flow fluctuations and nonflow
STAR Collaboration (G. Agakishiev (Dubna, JINR) *et al.*). Nov 2011. 15 pp.
Published in Phys.Rev. C86 (2012) 014904
DOI: 10.1103/PhysRevC.86.014904
e-Print: arXiv:1111.5637 [nucl-ex]

38. System size and energy dependence of near-side di-hadron correlations
STAR Collaboration (G. Agakishiev (Dubna, JINR) *et al.*). Oct 2011. 17 pp.
Published in Phys.Rev. C85 (2012) 014903
DOI: 10.1103/PhysRevC.85.014903
e-Print: arXiv:1110.5800 [nucl-ex]

39. Identified hadron compositions in p+p and Au+Au collisions at high transverse momenta at $\sqrt{s_{NN}}$=200 GeV

STAR Collaboration (G. Agakishiev (Dubna, JINR) *et al.*). Oct 2011. 6 pp.
Published in Phys.Rev.Lett. 108 (2012) 072302
DOI: 10.1103/PhysRevLett.108.072302
e-Print: arXiv:1110.0579 [nucl-ex]

40. Directed and elliptic flow of charged particles in Cu+Cu collisions at $\sqrt{s_{NN}}$ = 22.4 GeV
STAR Collaboration (G. Agakishiev (Dubna, JINR) *et al.*). Sep 2011. 10 pp.
Published in Phys.Rev. C85 (2012) 014901
DOI: 10.1103/PhysRevC.85.014901
e-Print: arXiv:1109.5446 [nucl-ex]

41. Anomalous centrality evolution of two-particle angular correlations from Au-Au collisions at $\sqrt{s_{NN}}$ = 62 and 200 GeV
STAR Collaboration (G. Agakishiev (Dubna, JINR) *et al.*). Sep 2011. 26 pp.
Published in Phys.Rev. C86 (2012) 064902
DOI: 10.1103/PhysRevC.86.064902
e-Print: arXiv:1109.4380 [nucl-ex]

42. $\rho 0$ Photoproduction in AuAu Collisions at $\sqrt{s_{NN}}$=62.4 GeV with STAR
STAR Collaboration (G. Agakishiev (Dubna, JINR) *et al.*). Jul 2011. 9 pp.
Published in Phys.Rev. C85 (2012) 014910
DOI: 10.1103/PhysRevC.85.014910
e-Print: arXiv:1107.4630 [nucl-ex]

43. Strangeness Enhancement in Cu+Cu and Au+Au Collisions at $\sqrt{s_{NN}}$=200 GeV
STAR Collaboration (G. Agakishiev (Dubna, JINR) *et al.*). Jul 2011. 6 pp.
Published in Phys.Rev.Lett. 108 (2012) 072301
DOI: 10.1103/PhysRevLett.108.072301
e-Print: arXiv:1107.2955 [nucl-ex]

44. Evolution of the differential transverse momentum correlation function with centrality in Au+Au collisions at $\sqrt{s_{NN}}$=200 GeV
STAR Collaboration (H. Agakishiev (Dubna, JINR) *et al.*). Jun 2011. 7 pp.
Published in Phys.Lett. B704 (2011) 467-473
DOI: 10.1016/j.physletb.2011.09.075
e-Print: arXiv:1106.4334 [nucl-ex]

45. Observation of the antimatter helium-4 nucleus
STAR Collaboration (H. Agakishiev (Dubna, JINR) *et al.*). Mar 2011. 20 pp.
Published in Nature 473 (2011) 353, Erratum-ibid. 475 (2011) 412
DOI: 10.1038/nature10079
e-Print: arXiv:1103.3312 [nucl-ex]

46. High pT non-photonic electron production in p+p collisions at $\sqrt{s}$=200 GeV
STAR Collaboration (H. Agakishiev (Dubna, JINR) *et al.*). Feb 2011. 17 pp.
Published in Phys.Rev. D83 (2011) 052006
DOI: 10.1103/PhysRevD.83.052006
e-Print: arXiv:1102.2611 [nucl-ex]

47. Studies of di-jet survival and surface emission bias in Au+Au collisions via angular correlations with respect to back-to-back leading hadrons
STAR Collaboration (H. Agakishiev (Dubna, JINR) *et al.*). Feb 2011. 6 pp.
Published in Phys.Rev. C83 (2011) 061901
DOI: 10.1103/PhysRevC.83.061901
e-Print: arXiv:1102.2669 [nucl-ex]

48. Strange and Multi-strange Particle Production in Au+Au Collisions at $\sqrt{s_{NN}}$ = 62.4 GeV
STAR Collaboration (M.M. Aggarwal (Panjab U.) *et al.*). Oct 2010. 17 pp.

Published in Phys.Rev. C83 (2011) 024901
DOI: 10.1103/PhysRevC.83.024901
e-Print: arXiv:1010.0142 [nucl-ex]

49. Measurements of Dihadron Correlations Relative to the Event Plane in Au+Au Collisions at sNN−−−−√=200 GeV
STAR Collaboration (H. Agakishiev *et al.*). Oct 2010. 41 pp.
e-Print: arXiv:1010.0690 [nucl-ex]

50. Measurement of the parity-violating longitudinal single-spin asymmetry for $W\pm$ boson production in polarized proton-proton collisions at s√=500−GeV
STAR Collaboration (M.M. Aggarwal (Panjab U.) *et al.*). Sep 2010. 6 pp.
Published in Phys.Rev.Lett. 106 (2011) 062002
DOI: 10.1103/PhysRevLett.106.062002
e-Print: arXiv:1009.0326 [hep-ex]

Full Presentation List for S G Brovko

Fixed Target At STAR: Al+Al at 2.8AGeV
Beam Energy Scan Focus Group February 2011
Light Flavor Spectra Physics Working Group March 2011
Gaussian Fits For 19.9 GeV Au+Au
Light Flavor Spectra Physics Working Group September 2011
Hadron Production at 19.6 and 27 GeV Au+Au
STAR Collaboration Analysis Meeting August 2011
27GeV Minimum Bias Quality Analysis
Light Flavor Spectra Physics Working Group July 2011
Au+Al Quality Analysis from 11.5 GeV Au+Au Dataset
Light Flavor Spectra Physics Working Group February 2012
STAR as a Fixed Target Experiment: Au+Al at 2.8 AGeV
American Physical Society April Meeting April 2011
STAR as a Fixed Target Experiment: Au+Al at 2.8 AGeV
STAR Collaboration Analysis Meeting March 2011
Hadron Production at 19.6 GeV Au+Au Collisions at STAR
Division of Nuclear Physics of the American Physical Society October 2011
Hadron Production and Freeze-out Dynamics in Au+Au at 19.6 GeV
Division of Nuclear Physics of the American Physical Society October 2012
Getting Started at STAR
Nuclear Group Quarter Meeting 2009
Did You Say Fixed Target at STAR?
STAR Collaboration Analysis Meeting Junior's Day April 2012
Minuit at 7 GeV
Software and Computing Meeting July 2010
Particle Acceptances in Fixed Target
Beam Energy Scan Focus Group November 2011
STAR Poster
Physics Department Graduate Preview Day March 2010
Charged Particle Spectra For Au+Al Fixed Tareget $\sqrt{S}$ = 2.8 GeV
STAR Collaboration Meeting November 2010
Identified Particle Production in the Beam Energy Scan
STAR Collaboration Meeting November 2011
Particle Ratios & Spectra in $\sqrt{s_{NN}}$ = 19.6 GeV Au+Au Collisions at STAR
STAR Collaboration Meeting November 2011
19.6GeV Pion & Kaon Spectra
Light Flavor Spectra Physics Working Group September 2011
Fast Offline, 27 GeV Au+Au Update
Light Flavor Spectra Physics Working Group August 2011
Efficiency Corrections to 19.6 GeV Au+Au PID Spectra
Light Flavor Spectra Physics Working Group May 2012
π, K, p Spectra at 19.6 GeV Au+Au
Light Flavor Spectra Physics Working Group October 2011
Statistical and Thermal Fits to 19.6 GeV Au+Au PID Spectra
Light Flavor Spectra Physics Working Group June 2012
Colliding Au+Au at STAR
Physics & Tea for Undergraduates May 2012
ToF Matching Efficiency
Light Flavor Spectra Physics Working Group September 2011
19.6 GeV Au+Au PID Spectra Update
Light Flavor Spectra Physics Working Group November 2012
Light Flavor Spectra Physics Working Group December 2012
STAR Collaboration Analysis Meeting November 2012

References

[1] M. Gyulassy, J Phys. G: Nucl. Part. Phys., S911(2004)

[2] J. Adams *et al.* (STAR Collaboration), Phys. Rev. Lett. **91**, 072304 (2003)

[3] C. Adler *et al.* (STAR Collaboration), Phys. Rev. Lett. **90**, 082302 (2003)

[4] J. W. Harris and B. Muller, Annu. Rev. Nucl. Part. Sci. **46**, 71 (1996)

[5] M. Asakawa and K. Yazaki, Nucl. Phys. A **504**, 668 (1989)

[6] F. R. Brown *et al.*, Phys. Rev. Lett. **65**, 2491 (1990)

[7] U. Heinz and G. Kestin, Eur. Phys. J. Special Topics **155**, 75 (2008)

[8] D. H. Rischke, Prog. Part. Nucl. Phys. **52**, 197 (2004)

[9] C. Alt *et al.* (NA49 Collaboration), Phys. Rev. C **77**, 024903 (2008)

[10] Z. Fodor and S. D. Katz, JHEP **0404**, 050 (2004), hep-lat/0402006, http://arxiv.org/abs/hep-lat/0402006

[11] R. V. Gavai and S. Gupta, Phys. Rev. D **71**, 114014 (2005), hep-lat/0412035, http://arxiv.org/abs/hep-lat/0412035

[12] F. Karsch, C. R. Allton, S. Ejiri, S. J. Hands, O. Kaczmarek, E. Laermann, and C. Schmidt, Nucl. Phys. Proc. Suppl. **129**, 614 (2004), hep-lat/0309116, http://arxiv.org/abs/hep-lat/0309116

[13] P. de Forcrand and O. Philipsen, JHEP **01**, 077 (2007), hep-lat/0607017, http://arxiv.org/abs/hep-lat/0607017

[14] Z. Fodor and S. D. Katz, "The phase diagram of quantum chromodynamics," (08 2009), arXiv:0908.3341[hep-ph], 0908.3341, http://arxiv.org/abs/0908.3341

[15] R. V. Gavai and S. Gupta, Phys. Rev. D **78**, 114503 (2008), 0806.2233, http://arxiv.org/abs/0806.2233

[16] C. Schmidt, for RBC-Bielefeld, and H. Collaborations, Nucl. Phys. A **820**, 41c (10 2009), 0810.4024, http://arxiv.org/abs/0810.4024

[17] E. L. Bratkovskaya, M. Bleicher, A. Dumitru, K. Paech, M. Reiter, S. Soff, H. Stöcker, H. Weber, M. van Leeuwen, and W. Cassing, "Review of qgp signatures - ideas versus observables," (2004), arXiv:nucl-th/0401031, nucl-th/0401031, http://arxiv.org/abs/nucl-th/0401031

[18] E. Shuryak, "Interactions between hadrons are strongly modified near the qcd (tri)critical point," (2005), arXiv:hep-ph/0504048, hep-ph/0504048, http://arxiv.org/abs/hep-ph/0504048

[19] M. Gazdzicki, M. I. Gorenstein, and S. Mrowczynski, Phys. Lett. B **585**, 115 (2004), hep-ph/0304052, http://arxiv.org/abs/hep-ph/0304052

[20] M. I. Gorenstein, M. Gazdzicki, and O. S. Zozulya, Phys. Lett. B **585**, 237 (2004), hep-ph/0309142, http://arxiv.org/abs/hep-ph/0309142

[21] P. Kolb *et al.*, Phys. Rev. C **62**, 054909 (2000)

[22] J.-Y. Ollitrault *et al.*, Physical Review D **46**, 229 (1992)

[23] M. Stephanov *et al.*, Physical Review Letters **102**, 032301 (2009)

[24] S. Ejiri, F. Karsch, and K. Redlich, Physics Letters B **633**, 275 (2006), ISSN 0370-2693, http://www.sciencedirect.com/science/article/pii/S0370269305017521

[25] M. Asakawa", Physical Review Letters **101**, 2302 (2008)

[26] M. Stephanov, K. Rajagopal, and E. Shuryak, Phys. Rev. D **60**, 4028 (1999)

[27] M. Gazdzicki, Z. Fodor, and G. Vesztergombi, *Study of Hadron Production in Hadron-Nucleus and Nucleus-Nucleus Collisions at the CERN SPS*, Tech. Rep. SPSC-P-330. CERN-SPSC-2006-034 (CERN, Geneva, 2006)

[28] D. Cebra (for the STAR Collaboration), "Charged hadron results from au+au at 19.6 gev," (03 2009), arXiv:0903.4702[nucl-ex], 0903.4702, http://arxiv.org/abs/0903.4702

[29] L. Kumar (for the STAR Collaboration), J. Phys. G: Nucl. Part. Phys. **36**, 064066 (12 2009), 0812.4099, http://arxiv.org/abs/0812.4099

[30] B. I. Abelev *et al.* (STAR Collaboration), Phys. Rev. C **81**, 024911 (Feb 2010), http://link.aps.org/doi/10.1103/PhysRevC.81.024911

[31] M. M. Aggarwal *et al.* (STAR Collaboration), "An experimental exploration of the qcd phase diagram: The search for the critical point and the onset of de-confinement," (July 2010), arXiv:1007.2613 [nucl-ex]

[32] A. Bialas, M. Bleszynski, and W. Czyz, Nucl. Phys. B **111**, 461 (1976)

[33] R. J. Glauber and G. Matthiae, Nucl. Phys. B **21**, 135 (1970)

[34] R. J. Glauber, Nucl. Phys. A **774**, 3 (2006)

[35] L. Adamczyk *et al.* (STAR Collaboration), *RHIC Beam Use Request For Runs 14 and 15*, Tech. Rep. (Brookhaven National Laboratory, 2013) www.c-ad.bnl.gov/esfd/RMEM_14/star_bur_2014.pdf

[36] N. Cabibbo and G. Parisi, Phys. Lett. B, 67(1975)

[37] J. C. Collins and M. J. Perry, Phys. Rev. Lett. **34**, 1353 (1975)

[38] E. V. Shuryak, Phys. Lett. B **78**, 150 (1978)

[39] J. Beringer *et al.* (Particle Data Group), Phys. Rev. D **86**, 010001 (2012)

[40] K. Wilson, Phys. Rev. D **10**, 2445 (1974)

[41] R. Vogt, *Ultrarelativistic Heavy-Ion Collisions* (Elsevier, Amsterdam, 2007)

[42] F. Karsch, "Recent lattice results on finite temperature and density qcd, part i," ArXiv:[hep-lat]0711.0656

[43] F. Karsch, "Recent lattice results on finite temperature and density qcd, part ii," ArXiv:[hep-lat]0711.0661

[44] I. Montav and G. Munster, *Quantum Fields on a Lattice* (Cambridge University Press, Cambridge, 1994)

[45] F. Karsch, in *Lecture Notes In Physics*, Vol. 583, edited by W. Plessas and L. Mathelitsch (Springer, Berlin, 2002) pp. 209–249

[46] H. J. Rothe, in *Lecture Notes In Physics*, Vol. 59 (World Scientific, Singapore, 1997)

[47] F. Karsch and E. Laermann, in *Quark Gluon Plasma 3*, edited by R. C. Hwa and X.-N. Wang (World Scientific, Singapore, 2004) pp. 1–59

[48] L. D. McLerran and B. Svetitsky, Phys. Lett. B **98**, 195 (1981)

[49] L. D. McLerran and B. Svetitsky, Phys. Rev. D **24**, 450 (1981)

[50] J. Kuti, J. Polónyi, and K. Szlachányi, Phys. Lett. B **98**, 199 (1981)

[51] F. Karsch and E. Laermann, Phys. Rev. D **50**, 6954 (1994)

[52] F. Karsch, E. Laermann, and A. Peikert, Phys. Lett. B **478**, 447 (2000)

[53] J. Bartke, *Introduction to Relativistic Heavy Ion Physics* (World Scientific Co. Pte. Ltd., 2009)

[54] R. Raitio, Nucl. Phys. A **418**, 539c (1984)

[55] U. Heinz, "Concepts of heavy ion physics," (2004), cERN Yellow Report

[56] A. Bialas, M. Chojnacki, and W. Florkowski, J. Phys. G: Nucl. Part. Phys. **35**, 104073 (2008)

[57] J. Rafelski, Phys. Rept. **88**, 331 (1982)

[58] P. Koch, B. Muller, and J. Rafelski, Phys. Rept. **142**, 167 (1986)

[59] T. Matsui and H. Satz, Phys. Lett. B **178**, 416 (1985)

[60] F. Karsch, E. Laermann, and A. Peikert, Nucl. Phys. Proc. Suppl. **94**, 411 (2001)

[61] L. Kluberg and H. Satz, "Color deconfinement and charmonium production in nuclear collisions," (January 2009), arXiv:0901.3831v1

[62] R. Chatterjee, L. Bhattacharya, and D. K. Srivastava, Lect. Notes Phys. **785**, 219 (2010)

[63] J. Alam, B. Sinha, and S. Raha, Phys. Rept. **273**, 243 (1996)

[64] J. Kapusta, P. Lichard, and D. Seibert, Phys. Rev. D **44**, 2774 (1991)

[65] J. Kapusta, P. Lichard, and D. Seibert, Phys. Rev. D **47**, 4171 (1993)

[66] M. M. Aggarwal *et al.* (WA98 Collaboration), Phys. Rev. Lett. **85**, 3595 (2000)

[67] S. S. Adler *et al.* (PHENIX Collaboration), Phys. Rev. Lett. **94**, 232301 (2005)

[68] C. Y. Wong, *Introduction of High Energy Heavy Ion Collisions* (World Scientific, Singapore, 1994)

[69] G. Agakichiev *et al.* (CERES Collaboration), Eur. Phys. J. C **41**, 475 (2005)

[70] D. Adamova *et al.* (NA45 Collaboration), Phys. Rev. Lett. **91**, 042301 (2003)

[71] R. Arnaldi *et al.* (NA60 Collaboration), Phys. Rev. Lett. **96**, 162302 (2006)

[72] C. Adler *et al.* (STAR Collaboration), Phys. Rev. Lett. **87**, 182301 (2001)

[73] C. Adler *et al.* (STAR Collaboration), Phys. Rev. Lett. **89**, 132301 (2002)

[74] C. Adler *et al.* (STAR Collaboration), Phys. Rev. Lett. **90**, 032301 (2003)

[75] S. Esumi *et al.* (PHENIX Collaboration), Nucl. Phys. A **715**, 599 (2003)

[76] S. S. Adler *et al.* (PHENIX Collaboration), Phys. Rev. Lett. **91**, 182301 (2001)

[77] P. Huovinen, P. F. Kolb, U. Heinz, P. Ruuskanen, and S. A. Voloshin, Phys. Lett. B **503**, 58 (2001)

[78] D. Teaney, J. Lauret, and E. V. Shuryak, "A hydrodynamic description of heavy ion collisions at the sps and rhic," (2001), arXiv:nucl-th/0110037

[79] S. Voloshin and Y. Zhang, Z. Phys. C **70**, 665 (1996)

[80] A. M. Poskanzer and S. A. Voloshin, Phys. Rev. C **58**, 1671 (1998)

[81] T. Hirano, N. van der Kolk, and A. Bilandzic, Lect. Notes Phys. **785**, 139 (2010)

[82] E. Schnedermann, J. Sollfrank, and U. Heinz, Phys. Rev. C **48**, 2462 (1993)

[83] P. J. Siemens and J. O. Rasmussen, Phys. Rev. Lett. **42**, 880 (1979)

[84] L. V. Bravina, N. S. Amelin, L. P. Csernai, P. Levai, and D. Strottman, Nucl. Phys. A **566**, 461c (1994)

[85] L. V. Bravina, L. P. Csernai, P. Levai, and D. Strottman, Phys. Rev. C **50**, 2161 (1994)

[86] D. H. Rischke, Y. Puersuen, J. A. Maruhn, H. Stoecker, and W. Greiner, "The phase transition to the quark-gluon plasma and its effect on hydrodynamic flow," (1995), cU-TP-695, arXiv:nucl-th/9505014

[87] L. P. Csernai and D. Rohrich, Phys. Lett. B **458**, 454 (1999)

[88] A. Adare *et al.* (PHENIX Collaboration), Phys. Rev. Lett. **98**, 162301 (2007)

[89] A. Capella and E. G. Ferreiro, Phys. Rev. C **75**, 024905 (2007)

[90] C. Alt *et al.* (NA49 Collaboration), Phys. Rev. C **68**, 034903 (2003)

[91] J. Adams *et al.* (STAR Collaboration), Phys. Rev. Lett. **95**, 122301 (2005)

[92] J. Adams *et al.* (STAR Collaboration), Phys. Rev. Lett. **92**, 052302 (2004)

[93] H. Sorge, Phys. Rev. Lett. **82**, 2048 (1999)

[94] J. Adams *et al.* (STAR Collaboration), Phys. Rev. Lett. **92**, 182301 (2004)

[95] S. Sakai (for the PHENIX Collaboration), J Phys. G: Nucl. Part. Phys. **32**, S551 (2006)

[96] J. Adams *et al.* (STAR Collaboration), Nucl. Phys. A **757**, 102 (2005)

[97] D. Hardtke *et al.* (STAR Collaboration), Nucl. Phys. A **715**, 272 (2003)

[98] J. D. Björken, Phys. Rev. D **27**, 140 (1983)

[99] W. Florkowski and W. Broniowski, Acta Phys. Polon. B **35**, 2895 (2004)

[100] F. Retiere and M. A. Lisa, "Observable implications of geometrical and dynamical aspects of freeze-out in heavy ion collisions," ArXiv:nucl-th/0312024

[101] W. Broniowski and W. Florkowski, Phys. Rev. Lett. **87**, 272302 (2001)

[102] W. Broniowski and W. Florkowski, Phys. Rev. C **65**, 064905 (2002)

[103] C. Hoehne *et al.* (NA49 Collaboration), Nucl. Phys. A **774**, 35 (2006)

[104] M. Gazdzicki and M. I. Gorenstein, Acta Phys. Polon. B **30**, 2705 (1999)

[105] M. I. Gorenstein, M. Gazdzicki, and K. A. Bugaev, Phys. Lett. B **567**, 175 (2003)

[106] H. Peterson and M. Bleicher, "Longitudinal flow and onset of deconfinement," Nucl-th/0611001

[107] E. Fermi, Prog. Theor. Phys. **5**, 570 (1950)

[108] M. Gazdzicki, Z. Phys. C **66**, 659 (1995)

[109] A. Rustamov, Cent. Eur. J. Phys **10**, 1267 (2012)

[110] L. D. Landau, Izv. Akad. Nauk **17**, 51 (1953)

[111] E. V. Shuryak, Yad. Fiz. **16**, 395 (1972)

[112] G. Baym and P. Braun-Munzinger, Nucl. Phys. A **610**, 286c (1996)

[113] W. Beneson *et al.*, Phys. Rev. Lett. **43**, 683 (1979)

[114] K. L. Wolf *et al.*, Phys. Rev. Lett. **42**, 1448 (1979)

[115] S. Nagamiya *et al.*, Phys. Rev. C **24**, 971 (1981)

[116] K. L. Wolf *et al.*, Phys. Rev. C **26**, 2572 (1982)

[117] M. Gonin *et al.* (E802/E866), Nucl. Phys. A **566**, 601c (1994)

[118] F. Videbaek *et al.* (E866), Nucl. Phys. A **590**, 249c (1995)

[119] L. Ahle *et al.* (E802 Collaboration), Nucl. Phys. A **610**, 139c (1996)

[120] L. Ahle *et al.*, Phys. Rev. C **57**, R466 (1998)

[121] C. Muentz, Acta Phys. Polon. B **29**, 3253 (1998)

[122] K. H. Ackermann *et al.*, Nucl. Instr. Meth. A **499**, 624 (2003)

[123] J. M. Landgraf *et al.*, Nucl. Instr. Meth. A. **499**, 762 (2003)

[124] M. Beddo *et al.*, Nucl. Instr. Meth. A **499**, 725 (2003)

[125] C. E. Allgower *et al.*, Nucl. Instr. Meth. A **499**, 740 (2003)

[126] M. Anderson *et al.*, Nucl. Instr. Meth. A **499**, 679 (2003)

[127] K. H. Ackermann *et al.*, Nucl. Instr. Meth. A **499**, 713 (2003)

[128] L. Kotchenda *et al.*, Nucl. Instr. Meth. A **499**, 703 (2003)

[129] H. S. Matis *et al.*, Nucl. Instr. Meth. A **499**, 802 (2003)

[130] J. Abele *et al.*, Nucl. Instr. Meth. A **499**, 692 (2003)

[131] C. Adler *et al.*, Nucl. Instr. Meth. A **499**, 778 (2003)

[132] A. Braem *et al.*, Nucl. Instr. Meth. A **499**, 720 (2003)

[133] M. M. Aggarwal *et al.*, Nucl. Instr. Meth. A **499**, 751 (2003)

[134] D. Reichhold *et al.*, Nucl. Instr. Meth. A **499**, 792 (2003)

[135] L. Arnold *et al.*, Nucl. Instr. Meth. A **499**, 652 (2003)

[136] R. Bellwied *et al.*, Nucl. Instr. Meth. A **499**, 640 (2003)

[137] M. Anderson, Nucl. Instr. Meth. A **499**, 659 (2003)

[138] F. S. Bieser, Nucl. Instr. Meth. A **499**, 766 (2003)

[139] F. Bergsma *et al.*, Nucl. Instr. Meth. A **499**, 633 (2003)

[140] A. Schmah (for the STAR Collaboration), J. Phys. G: Nucl. Part. Phys. **38**, 124049 (2011)

[141] S. Margetis and D. Cebra, *Main Vertex Reconstruction in STAR*, Tech. Rep. 89 (STAR Note, http://drupal.star.bnl.gov/ST AR/starnotes/public/sn0089, 1994)

[142] H. Bichsel, *Energy loss in thin layers of argon*, Tech. Rep. 418 (STAR Note, http://www.star.bnl.gov/star/starlib/doc/www/sno/ice/sn0418.html, 2000)

[143] H. Bichsel, *Comparison of Bethe-Bloch and Bichsel Functions*, Tech. Rep. 439 (STAR Note, http://www.star.bnl.gov/star/starlib/doc/www/sno/ice/sn0439.html, 2001)

[144] W. J. Llope *et al.*, Nucl. Instr. Meth. A **522**, 252 (2004)

[145] E. C. Zeballos *et al.*, Nucl. Instr. Meth. A **374**, 132 (1996)

[146] M. C. S. Williams *et al.*, Nucl. Instr. Meth. A **478**, 183 (2002)

[147] B. Bonner *et al.*, Nucl. Instr. Meth. A **508**, 181 (2003)

[148] L. Ruan, *Pion, Kaon, Proton and Antiproton Spectra in d+Au and p+p Collisions at* $\sqrt{s_{NN}} = 200$ *GeV at the Relativistic Heavy Ion Collider*, Ph.D. thesis, University of Science and Technology of China (September 2004)

[149] C. Adler, A. Denisov, E. Garcia, M. Murray, H. Stroebele, and S. White, Nucl. Instr. Meth. A **470**, 488 (2001)

[150] A. J. Baltz, C. Chasman, and S. N. White, Nucl. Instr. Meth. A **417**, 1 (1998)

[151] H. Appelhauser *et al.* (NA49 Collaboration), Eur. Phys. J. A **2** (1998)

[152] R. Reed *et al.*, J. Phys.: Conf. Ser. **219**, 032020 (2010)

[153] K. S. Krane, *Introductory Nuclear Physics* (John Wiley and Sons, 1988)

[154] S. A. Bass *et al.*, Prog. Part. Nucl. Phys. **41**, 225 (1998)

[155] M. Bleicher *et al.*, J. Phys. G: Nucl. Part. Phys. **25**, 1859 (1999)

[156] J. Engelage *et al.*, *STAR Trigger-DAQ Interface Specification Version 1.4*, STAR

[157] A. Wagner *et al.* (KaoS Collaboration), Phys. Lett. B **420**, 20 (1998)

[158] M. Heffner, *Hadron Spectra in Au+Au Collisions at the BNL AGS*, Ph.D. thesis, University of California, Davis (2000)

[159] J. L. Klay *et al.* (E895 Collaboration), Phys. Rev. C **68**, 054905 (2003)

[160] L. Ahle *et al.* (E866 and E917 Collaborations), Phys. Lett. B **476**, 1 (2000)

[161] I. G. Beardon *et al.* (NA44 Collaboration), Phys. Rev. C **66**, 044907 (2002)

[162] H. Boggild *et al.* (NA44 Collaboration), Phys. Lett. B **372**, 339 (1996)

[163] S. V. Afanasiev *et al.* (NA49 Collaboration), Phys. Rev. C **66**, 054902 (2002)

[164] M. M. Aggarwal *et al.* (WA98 Collaboration), Phys. Rev. C **67**, 014906 (2003)

[165] M. M. Aggarwal (WA98 Collaboration), Eur. Phys. J. C **48**, 343 (2006)

[166] D. Pelte *et al.* (FoPi Collaboration), Z. Phys. A **357**, 215 (1997)

[167] W. Reisdorf *et al.* (FoPi Collaboration), Nucl. Phys. A **781**, 459 (2007)

[168] F. Retiere *et al.* (WA98 Collaboration), Nucl. Phys. A **681**, 149c (2001)

[169] L. Rosselet *et al.* (WA98 Collaboration), Nucl. Phys. A **698**, 647c (2002)

[170] T. Wibig and D. Sobczynska, J. Phys. G **24**, 2037 (1998)

[171] J. Chauvin, D. Bebrun, A. Lounis, and M. Buenerd, Phys. Rev. C **28**, 1970 (1983)

[172] T. Sjostrand, S. Mrenna, and P. Z. Skands, JHEP **0605** (2006)

[173] J. P. Guillaud and A. Sobol, *Simulation of diffractive and non-diffractive processes at the LHC energy with the PYTHIA and PHOJET MC event generators.*, Tech. Rep. LAPP-EXP 2004–06 (CNRS Tech. Rep., CNRS, Paris, France, 2004)

[174] P. Braun-Munzinger *et al.*, Nucl. Phys. A **697**, 902 (2002)

[175] E. V. Shuryak, PoSCPOD2006:026(2006)

[176] U. Heinz and A. Kuhlman, Phys. Rev. Lett. **94**, 132301 (2005)

[177] *The Physics of the Quark Gluon Plasma*, edited by S. Sarkar, H. Satz, and B. Sinha (Springer, Heidelberg, 2010)

[178] B. Muller, *The Physics of the Quark Gluon Plasma* (Springer, Heidelberg, 1985)

[179] R. C. Hwa, *Quark Gluon Plasma*, Vol. 1, 2 (World Scientific, 1990 and 1995)

[180] M. Miller *et al.*, Annu. Rev. Nucl. Part. Sci. **57**, 205 (2007)

[181] L. Kumar, *Identified Particle Production, Fluctuations and Correlations Studies in Heavy Ion Collisions at RHIC Energies*, Ph.D. thesis, Panjab University (2009)